Generation of a Drug-incorporated Membrane for Biomedical Applications

Rosemond Attaa Mensah

Submitted to the University of Hertfordshire in Partial Fulfilment of the requirements for the degree of Doctor of Philosophy

May 2022

ACKNOWLEDGMENT

I am eternally grateful to Almighty God for His immense grace, blessings, and strength during my research and thesis writing.

I would like to express my sincere gratitude to my principal supervisor, Dr. David Chau for allowing me to do the research and for providing valuable guidance throughout this research and thesis preparation. I am extremely grateful for His continuous support, patience, and motivation. I could not have imagined having a better supervisor and my Ph.D. study. Also, it is a genuine pleasure to express my deep sense of thankfulness to my co-supervisors Dr. Michael Cook, Dr. Victoria Hutter and Dr. Stewart Kirton for their dedication, encouragement and intellectual guidance. Though it was daunting to write this thesis, the combined efforts of the research team motivated me to complete the course.

A special mention to the team of Eastman Dental Institute, University College London, Professor Hae-Won Kim and team at UCL Eastman-Korea Dental Medicine Innovation Centre and Institute of Tissue Regeneration Engineering., Dr Kyong Jin Cho and the team at Department of Ophthalmology, Dankook University College of Medicine, Dankook Cheonan, Republic of Korea, Dr Laura Sidney of Faculty of Medicine and Health Sciences, University of Nottingham and Dr Decio Alves of Lima Department of Engineering, Lancaster University, Lancaster, UK. Your collaboration indeed made this work complete.

Dr. Sara Shafaie, Dr Ewelina Hoffman, Dr Loanna Styliari and Dr Kapil Patel deserve special mention for their pivotal in the thesis' development. I would like to recognise the UH technicians, Mr James Stanley, Mr Lee Nixon and Mr Steven Tonks, and UCL technicians, Dr Nicola Mordan and Dr George Georgiou for their laboratory support. I would like to appreciate the administration staff at the UH Doctoral college, Miss Elizabeth Day and Miss Kathy Lee. Many thanks to my friends and research colleagues Dr Deborah Ogbeni, Dr Linda Ameh, Dr John Dauda and Dr Perezimor Etifa for offering me their friendship, experiences and constant encouragement.

This endeavour would not have been possible without my parents who prepared and educated me for my future. Although they are no longer with me, they continue to be an inspiration to me. Words cannot express my gratitude to my husband and sons for their sacrifices, tremendous prayers, love, moral and financial support.

I express my thanks to my siblings, aunts and uncles for their support and valuable prayers. My special thanks to Bishop Elijah-Ben and his wife, Reverend Colleen, the pastors and the entire congregation of Salvation Clinic International Ministries, your prayers worked. To my friends Dr Patricia Kpalam, Dr Gyanwa Opare-Addo, Sylvia, Efua, Annalisa, Akwasi and Charity Marfo, Mr Richmond and Ivy Asiedu-Darkwah, and Dr Felix and Joyce Oppong, thank you for your encouragement, support and keen interest to get the thesis done

Finally, my thanks go to all the people who have supported me to complete the research work directly or indirectly.

ABSTRACT

Current approach for ocular wound healing involves bandages combined with repeated administration of therapeutic eye drops. There is a need to develop ocular medicated bandages as a convenient and cost-effective strategy for wound healing. This project aimed to develop a controlled release biocompatible bandage consisting of 10-50 µm drug–incorporated poly (lactic-co-glycolic acid) (PLGA) microparticles (MP) and eggshell membrane (ESM) for ocular wound healing application. The eggshell membrane is a natural material with unique physical and biological properties. No studies have demonstrated nor reported its potential as a novel ocular wound dressing yet. ESM samples were isolated from the eggshell by either manual peeling (ESMstrip) or, via extraction, using in-house developed acetic acid or ethylenediaminetetraacetic acid, EDTA, protocols Energy-dispersive X-ray spectroscopy (EDS) confirmed that the ESM samples contained carbon, nitrogen, oxygen, and sulphur, with no traces of calcium residues from the extraction process. The extraction method (acetic acid and EDTA) did not alter the chemical bonding structures of the ESM, and the chemical composition of the fibrous proteins of the ESM was further clarified using Fourier transform infrared (FTIR) spectroscopy. The ESM has a three-layer composite structure, according to scanning electron microscopy (SEM) analyses: an inner layer that is continuous, dense, and non-fibrous (limiting membrane), a middle layer with a network of fibres (inner shell membrane), and an outer layer (outer shell membrane) with larger fibres. Furthermore, optical transparency, porosity, fluid absorption/uptake, thermal stability, mechanical/physical profiling of the ESM samples were performed and showed suitable profiles for translational applications. Biological *in vitro* studies using SV40 immortalised corneal epithelial cells (ihCEC) and corneal mesenchymal stromal cells (C-MSC) demonstrated excellent biocompatibility. A sub-study presented a design of experiment technique (DOE) known as Taguchi Design for the generation of a formulation model for optimizing the various factors shown to affect MP size when fabricated using the solvent emulsion technique and to produce the most appropriate MP for topical drug delivery. The first optimization step using the L12 design showed that all parameters significantly influenced the particle size of the fabricated MP with exception of the concentration of PVA in the hardening bath. In contrast, the L18 design results showed that the molecular weight of PLGA does not significantly affect the particle size. The optimized formulation was identified to be run 16 from the L18 OA design. The mean particle size was found to be 23.0 µm. that falls under the required range that is 10 – 50 µm. The results from this study showed that the application of Taguchi design can be used to predict and determine the best combination of process parameters that can provide the optimal response condition- in this case, to identify the most appropriate microparticle size for topical application. Additional studies were conducted with the formulation model to fabricate BSA-loaded PLGA-MP as well as their characterization using microscopy, size distribution and drug release profile. The MP were successfully attached onto the ESM using a chemical method (NaOH). The presence of the loaded MP did not compromise the transparency of the bandage. The FTIR spectra reveal the crosslink of the ESMs absorption peak with the absorption peak of the MP. The 2 in 1 bandage consisting of MP and ESM demonstrated high biocompatibility, durability, flexibility, fluid absorption capacity, thermal stability and a sustained drug release profile. These findings show that the ESM could be used in a variety of regenerative medical and/or biotechnological applications, such as ocular and skin wound dressings.

RESEARCH OUTPUTS

PAPERS:

1. Eggshell membrane-A versatile biological material for translational application: A review (incomplete)
2. Rosemond A. Mensah, Seung-Bin JO, Hoon Kim, Sung-Min Park, Kapil D. Patel, Kyong-Ji Cho, Michael T. Cook, Stewart B. Kirton, Victoria Hutter, Laura E. Sidney, Decio Alves-Lima, Hungyen Lin, Jung-Hwan Lee, Hae-Won Kim, David Y.S. Chau (2021). 'The eggshell membrane: a potential biomaterial for corneal wound healing' Journal of Biomaterial for corneal wound healing 0(0) https://doi.org/10.1177/08853282211024004
3. Rosemond A. Mensah, Seung-Bin JO, Hoon Kim, Sung-Min Park, Kapil D. Patel, Kyong-Ji Cho, Michael T. Cook, Stewart B. Kirton, Victoria Hutter, Laura E. Sidney, Decio Alves-Lima, Hungyen Lin, Jung-Hwan Lee, Hae-Won Kim, David Y.S. Chau 'The in vitro and in vivo characterization of decellularized chicken eggshell membrane for translational regenerative applications.' eCM Periodical, 2020, Collection 1, 2020 TERMIS EU Abstracts (page P77)
4. Mensah RA, Kirton SB, Cook MT, Styliari ID, Hutter V, Chau DYS (2019) 'Optimising poly (lactic-co-glycolic acid) microparticle fabrication using a Taguchi orthogonal array design-of experiment approach.' PLoS ONE 14(9): e0222858. https: //doi.org /10.1371 /journal. pone .0222858
5. RA Mensah, EA Hoffman, MT Cook, SB Kirton, V Hutter, DYS Chau 'Development and characterization of a novel drug-loaded PLGA microparticle bandage for topical wound healing applications.' eCM Meeting Abstracts 2018, Collection 4, page 67

ORAL CONFERENCE PRESENTATIONS:

1. Rosemond Mensah, Stewart Kirton, Ioanna Styliari, Victoria Hutter, Michael Cook, David Chau 'A bandage containing drug-loaded microparticles for ocular application'. Africans in STEM, 2019, Cambridge University, UK.
2. Rosemond Mensah, Stewart Kirton, Ioanna Styliari, Victoria Hutter, Michael Cook, David Chau 'Drug-loaded microparticle-based bandage for ocular wound healing. UKICRS Symposium and Industrial Workshop, 2019, Liverpool John Moores University, UK.

3. Rosemond Mensah 'Breakfast waste can cure you'. 3 Minutes Thesis Competition (first heat), 2018, University of Hertfordshire, UK.
4. R.A. Mensah M.T. Cook, S.B. Kirton, V. Hutter, D.Y.S. Chau 'Development of a novel drug-loaded bandage for wound healing applications. Ghanaian Scholars' Research Conference, 2018, Coventry, UK.
5. Mensah, R.A., Kirton, S.B., Cook, M.T., Hutter, V., and Chau, D.Y.S. 'Optimising the manufacturing process of poly (lactic-co-glycolic) microparticles using Taguchi L12 orthogonal array design'. Life and Medical Sciences Research Conference, 2018, University of Hertfordshire, UK.

POSTER CONFERENCE PRESENTATIONS:

1. Rosemond Mensah, Michael Cook, Victoria Hutter, Stewart Kirton, David Chau. Design and evaluation of microparticle loaded eggshell membrane as a wound bandage for ophthalmic applications. 10th APS International Pharmsci Conference, 2019, University of Greenwich, UK.
2. Rosemond Mensah, Stewart Kirton, Ioanna Styliari, Victoria Hutter, Michael Cook, David Chau 'Physio-mechanical evaluation of a novel medicated ocular bandage for wound repair'. Africans in STEM, 2019, Cambridge University, UK.
3. Rosemond Mensah, Stewart Kirton, Ioanna Styliari, Victoria Hutter, Michael Cook, David Chau 'Physico-mechanical evaluation of medicated bandage for wound repair.' UKICRS Symposium and Industrial Workshop, 2019, Liverpool John Moores University, UK.
4. Mensah, R.A., Styliari, ID, Kirton, S.B., Cook, M.T., Hutter, V., and Chau, D.Y.S. 'Preparation and characterization of eggshell membrane for ocular wound healing application. Life and Medical Sciences Research Conference, 2019, University of Hertfordshire, UK.
5. Rosemond A. Mensah, Stewart B. Kirton, Michael T. Cook, Victoria Hutter, David Y.S. Chau 'Optimization of the process parameters for PLGA microparticle formulation based on Taguchi design'. Young Modellers' Forum, 2018, Old Naval College, University of Greenwich, UK.
6. Rosemond Attaa Mensah 'From waste to a biological material'. Postgraduate Conference, 2018 (Vision and Voice competition), University of Hertfordshire, UK.
7. R.A Mensah, E.A. Hoffman, M.T. Cook, S.B. Kirton, V. Hutter, D.Y.S. Chau 'Development and characterization of a novel drug loaded PLGA microparticle

bandage for topical wound healing applications. 1. Tissue and Cell Engineering Society (TCES) Annual Meeting, 2018, Keele University, UK.

8. Rosemond Mensah, Stewart Kirton, Ioanna Styliari, Victoria Hutter, Michael Cook, David Chau 'Taguchi design for the optimization of manufacturing process of PLGA microparticles for topical controlled drug delivery'. UKICRS Symposium and Industrial Workshop, 2018, Queen's University Belfast, UK. Mensah, R.A., Kirton, S.B., Cook, M.T., Hutter, V., and Chau, D.Y.S 'Development and mechanical characterization of novel biomaterial for wound- healing applications. Postgraduate Conference, 2017, University of Hertfordshire, UK.
9. Mensah, R.A., Cook, M.T., Hutter, V., Kirton, S.B., Chau, D.Y.S The preparation and evaluation of PLGA microparticles: implication in the development of a novel, controlled release, membrane for ophthalmic application. 8th APS International PharmSci Conference, 2017, University of Hertfordshire, UK.
10. R.A Mensah, S. Shafaie, E. Hoffman, M.T. Cook, S.B. Kirton, V. Hutter, D.Y.S. Chau. Evaluation of novel PLGA microparticles-incorporated biomimetic membranes as potential ocular drug-controlled release system. Tissue and Cell Engineering Society (TCES) Annual Meeting, 2017, Manchester Metropolitan University, UK.
11. Mensah, R.A., Kirton, S.B., Cook, M.T., Hutter, V., and Chau, D.Y.S. Optimising the manufacturing process of poly (lactic-co-glycolic) microparticles using Taguchi L12 orthogonal array design. Life and Medical Sciences Conference, 2017, University of Hertfordshire, UK.

TABLE OF CONTENTS

ABBREVIATIONS

AgNP	Silver nanoparticles
ANOVA	Analysis of variance
ARPE-19	Arising retinal pigment epithelia cell line
ATCC	American type culture collection
BCA	Bicinchoninic acid
BCL	Bandage contact lenses
BS	Burst strength
BSA	Bovine serum albumin
CAB	Cacodylate buffer
CA	Contact angle
CAM	Chorioallantoic membrane
CO_2,	Carbon dioxide
$CaCO_3$	Calcium carbonate
DAF	Dissolved air floatation
DCM	Dichloromethane
DDLD	Dry dispersion laser diffraction
DI	Deionised
DMEM	Dulbecco's Modified eagle Media
DOE	Design of experiment
EAc	Ethyl acetate
ECM	Extracellular matrix
EDS	Energy dispersive X-ray spectroscopy
EDTA	Ethylenediaminetetraacetic acid
EDX	Energy dispersive x-ray analysis

EE	Entrapment efficiency
ES	Eggshell
ESM	Eggshell membrane
EW	Weight of water across each membrane
FA	Fluid adsorption
FBM	Fluorescein isothiocyanate labelled bovine serum loaded microparticles
FDA	Food and Drug Administration
FESEM	Field emission scanning electron microscope
FITC-BSA	Fluorescein isothiocyanate labelled bovine serum
FTIR	Fourier-transform infrared spectroscopy
GAG	Glycosaminoglycan
GTR	Guided tissue regeneration
HAM	Human amniotic membrane
HIC	Hydrochloric acid
HIV	Human immunodeficiency virus
HKGS	Human keratinocyte growth supplement
HMDS	Haematological malignancy diagnostic service
ihCEC	Immortalised corneal epithelial cell line
IM	Inner shell membrane
IR	Infrared rays
IU/ml	International Unites per millilitre
L12	Level 12
L18	Level 18
LC	Loading capacity
LD	Laser diffraction

LDH	Lactate dehydrogenase
LESM	Inner layer of eggshell membrane
LM	Limiting membrane
LOD	Limit of detection
LOQ	Limit of quantification
LZM	Lysozyme
ml	Millilitre
MP	Microparticles
MPa	Megapascals
MRSA	Methicillin-resistant Staphylococcus aureus
MSC-C	Mesenchymal stem cell- corneal stromal (MSC-C
MTS	3-(4,5-dimethylthiazol-2-yl)-5-(3-carboxymethoxyphenyl)-2-(4-sulfophenyl)-2H-tetrazolium
MW	Molecular weight
OA	Orthogonal array
OESM	Outer layer eggshell membrane
OM	Outer shell membrane
C_{opt}	Optical concentration
PBS	Phosphate buffered saline
PDI	Polydispersity
PLA	Poly(lactide)
PLG	Poly(glycoside)
PLGA	Poly (lactic-co-glycolic acid)
PMMA	Polymethyl-methacrylate
PRK	Phototherapeutic keratectomy

PVA	Polyvinyl alcohol
S	Slope
s	seconds
SD	Sprague Dawley
SEM	Scanning electron microscope
SEP	Soluble eggshell membrane protein
SI	Swelling index
Ra	Arithmetical mean deviation
TA	Texture analyser
TCP	Tissue culture plates
TGA	Thermogravimetric analyser
TMP	Tympanic membrane perforation
UV	Ultraviolet
VEGF	Vascular endothelial growth factor
VM	Vascular endothelial growth factor loaded microparticles
VMD	Volume mean diameter
WDLD	Wet dispersion laser diffraction
X10	10^{th} percentile
X50	50^{th} percentile
X90	90^{th} percentile
ε	Porosity
σ	Standard deviation
%	Percent
°C	Degree Celsius

LIST OF FIGURES

LIST OF TABLES

CHAPTER 1:
GENERAL INTRODUCTION

1.0 CHAPTER 1: GENERAL INTRODUCTION

1.1 LITERATURE REVIEW

1.1.1 Anatomy and physiology of the human eye

The human eye is one of the most complex sensory organs which react to light, it allows vision, and consists of various structures and layers at different parts with specific functions (as seen in Figure 1.2A below). The surface part comprises of the sclera, which protects the eye, and it is covered with a thin delicate membrane known as the conjunctiva, and the cornea which is transparent and covers the iris. The coloured part of the eye includes: the iris which is circular and controls the size of the pupil and the amount of light reaching the retina, the pupil - an adjustable opening found at the centre of the iris through which light enters the eye and the ciliary body - a small ring-like found behind the iris which produces a clear intraocular fluid known as the aqueous humour (Oyster, 1999). This fluid flows behind the iris or through the pupil, fills a chamber behind the cornea known as anterior chamber and the fluid leave the eye by absorption into the bloodstream through the drainage system (known as drainage angle) of the eye. A normal level of pressure in the eye is needed for its health, therefore, the drainage system must function properly and there must be a balance in the amount of fluid that is produced and leaves the eye (Herndon, Brunner and Rollins, 2006).

The posterior chamber of the eye is made up of hydrogel substance knowns as vitreous humour which contains salt, proteins, collagen and hyaluronic acid which helps to hold the retina in place by propelling it against the choroid. The posterior part of the eye includes: the retina which is a light-sensitive sheet of tissue that shapes the back end of the eye, the choroid, a layer behind that contains blood vessels responsible for nourishing the retina, the optic nerves connect the eye to the brains and the macula, a small area found at the centre of the retina (Oyster, 1999).

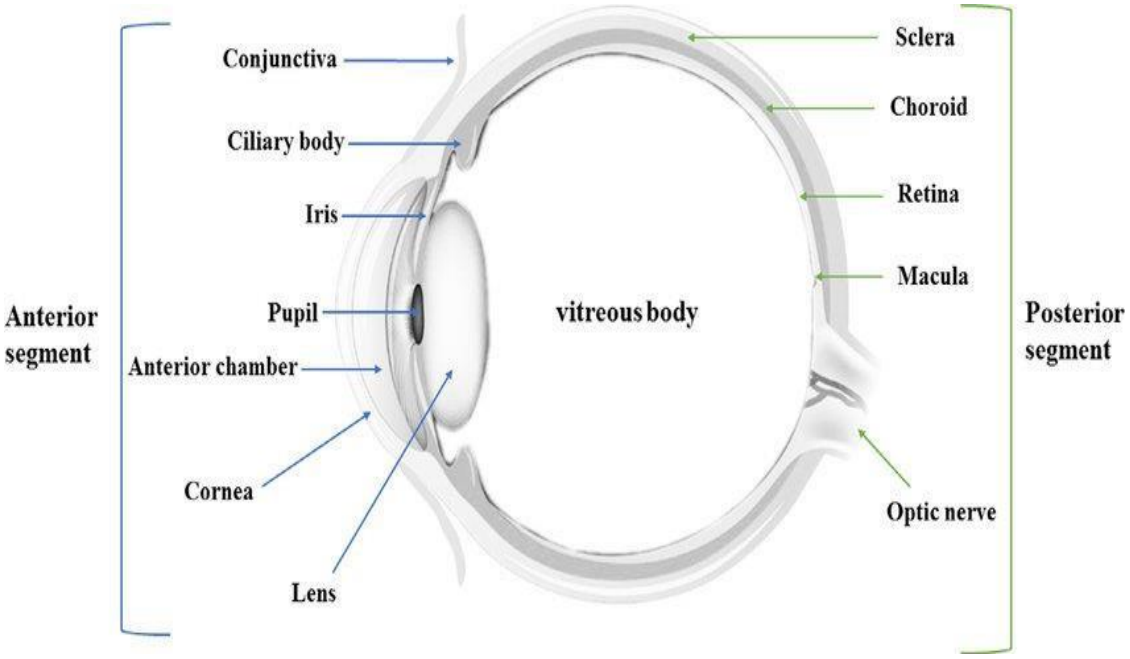

Figure 1.1A. Schematic diagram of the Anatomy of Human Eye
This diagram shows the inside look of the eye displaying the various anterior and posterior segments. The anterior segment is made of the cornea, iris, conjunctiva, lens, pupil, anterior chamber and ciliary body. The posterior consists of the sclera, choroid, retina, macula and optic nerve (Adapted from Wu et al., 2018).

1.1.2 The cornea

The cornea is the anterior-most part of the eye and the primary light–focusing structure. It is reported to be the most powerful optical refracting surface and it accounts for about 70% of its refractive power (Nishida, 2003). The cornea functions by maintaining a tough, physical and impermeable barrier between the eye and the environment. The cornea is lipophilic, tough and transparent (Cavanagh, 1989 and Marfurt et al., 2010). These characteristics provide its ability to guarantee that light is focused and conveyed without scattering through the lens and onto the retina. Hence, the mechanical integrity of the cornea is essential for clear vision.

The cornea is prone to eye injuries such as physical or chemical trauma or severe infections due to its exposure to the environment (Cavanagh, 1989). Therefore, the cornea structure needs to be restored rapidly after injury to prevent cornea diseases that can cause permanent loss of

vison. The human cornea is made of 78% water, 15% collagen (of which 50-55% is Type I, 15% Type II, 8-10% is Type v and 25-30% is Type VI), 5% of other proteins which includes 0.7% of keratin sulphate, 0.3% chondroitin/dermatan sulphate and hyaluronic acid, and salts (1%). The cornea consists of six layers, the outer layer of the cornea or epithelial layer, the middle layer termed the stroma, a single layer of cells called the endothelium, fourth layer knowns as Dua's layer found between the cornea stroma and the Descemet's membrane (firth layer) and lastly the Bowman's layer (Figure 1.2B). (Corneal anatomy, 1999 and Dua et al., 2013). From the anterior to posterior, five layers comprise the cornea except the Dua's layer. The Dua's layer has been suggested as an essential addition to the list, but its unclear nature means it remains a distinct classification for now.

The complicated structure of the cornea allows it to perform various functions. The strength, elasticity and thickness of the cornea primarily due to the stromal layer, allow for a mechanically tough barrier that withstands the intraocular pressure and protects the eye from slight mechanical damage (Marfurt et al., 2010). The primary structural component of the cornea is collagen. Collagen is found mainly in the Bowman's layer and in the corneal stroma and it is the primary source of the corneal tensile strength (William and Wilson, 2006). Unlike most tissues in the body, the cornea contains no blood vessels (avascular) to nourish or protect it against infection. Instead, the cornea receives its nourishment from tears and the aqueous humour (Smolin and Thoft, 1983 and Lens, Nemeth and Ledford, 2008).

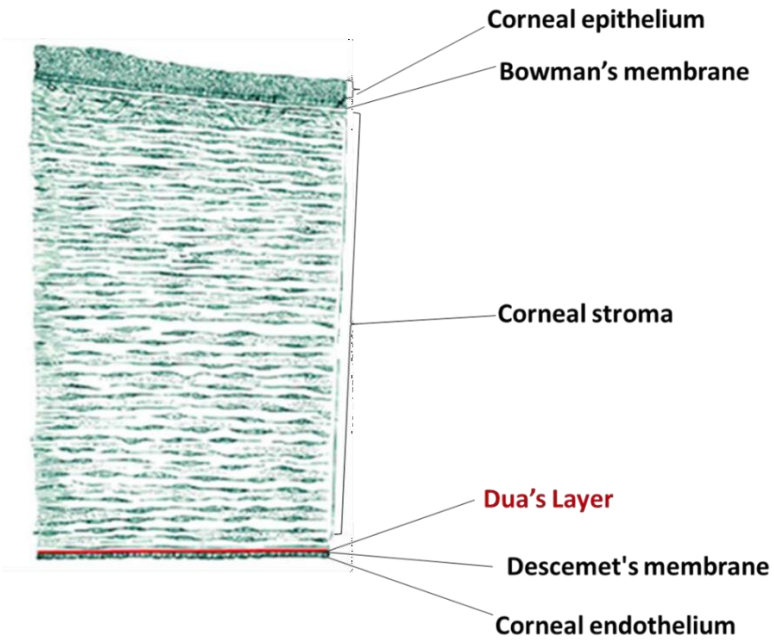

Figure 1.1B. Histology of the Human cornea
The cornea consists of 6 layers: corneal epithelium, bowman's membrane, corneal stroma, Dua's layer, Descemet's membrane and corneal endothelium. The Dua's layer, the fourth layer was discovered in 2013. (Image reproduced from Dua et al., 2013)

1.1.3 Ocular wound healing

There are various diseases which affect both the eye and cornea like redness, dryness and corneal swelling (keratitis, Figure 1.3) and even more acute diseases like corneal dystrophies and keratoconus (thinning and weakening of the cornea) (Kwok et al, 2019 and Martin et al, 2019). Additionally, injuries such as scrapes, burns (chemical and thermal) and punctures (mechanical) into the eye may damage the cornea. Diseases affecting the cornea may be infectious or non-infectious, and the two may lead to severe visual impairments requiring intervention (Willman, Fu, and Melanson, 2022). On the other hand, the incidence and epidemiology of corneal diseases change from area to area. From the use of traditional eye medicines (which is currently regarded as an important risk factor for corneal ulceration) to hydration cross-linking, which has lately been accepted by the US Food and Drug Administration (FDA) to fortify the cornea, the best aim in corneal therapy is to use minimally invasive procedures that may restore or preserve eyesight (Jeng et al., 2016).

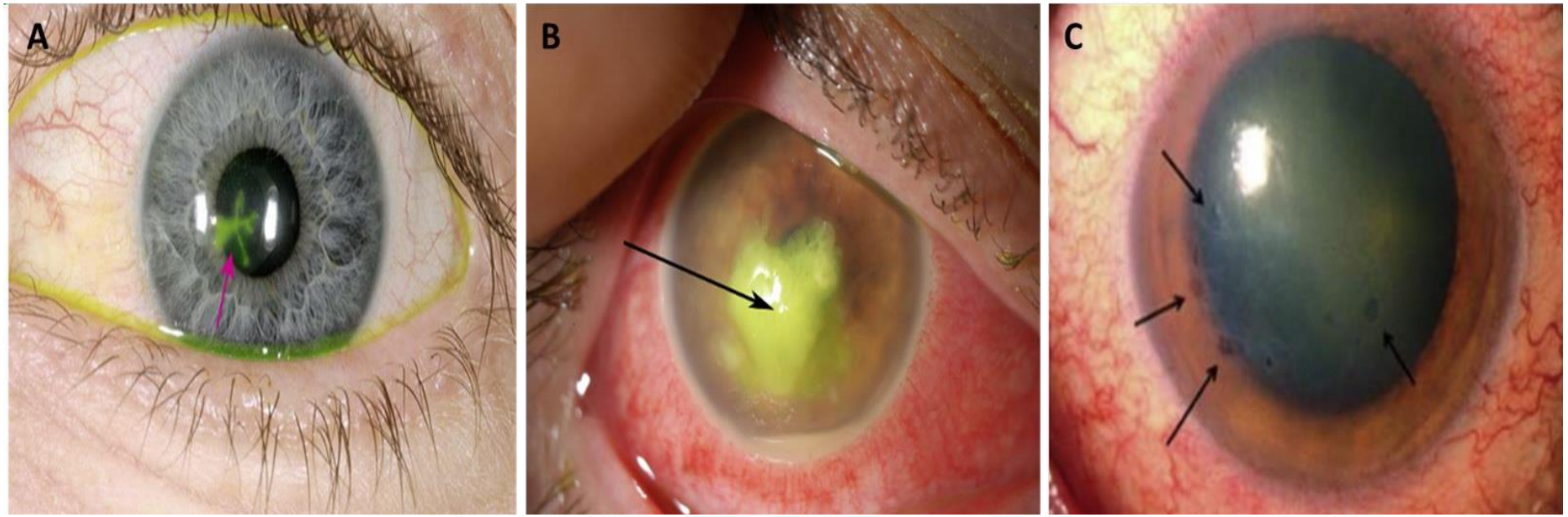

Figure 1.2. Images of cornea disorders.
(A) Herpes simplex keratitis. The arrow displayed in the image is the injury to the cornea. To identify the injury, fluorescein eye drops are put on the eye. (B) Bacterial cornea ulcer. The arrow reveals the lack of transparency in the cornea due to the bacterial infection. (C) Bullous keratopathy. Arrows show blisters on the surface of the cornea (Adapted from Roat, 2020).

The most remarkable progress in the medical treatment of corneal disorders over recent decades has been corneal transplantation and, today, the cornea would be the most frequently transplanted tissue worldwide. Corneal transplantations are broken up into two major categories depending upon the sum of surgically substituted tissue i.e., keratoplasty and keratoprosthesis (Singh, Gupta, Vanathi and Tandon, 2019). Nonetheless, in a more recent process known as lamellar keratoplasty, just the damaged layers are replaced using a donor graft, along with the healthful region of the retina is left undamaged. In lamellar keratoplasty, the integrity of the cornea and the surrounding cells are maintained, consequently, better visual progress is usually attained. Regrettably, there are occasionally poor outcomes due to graft rejection or late graft failure. Throughout the past couple of decades, the lack of donor cell has quickened the research on locating an alternate remedy to transplantation, along with a synthetic cornea or keratoprosthesis was suggested as an alternative (Avadhanam, Smith and Liu, 2015).

Historically, Guillaume Pellier de Quengsy, Jr. was the primary individual who suggested a lean silver-rimmed convex glass disk as a synthetic cornea, as long ago as 1789 (Mannis and Mannis, 1999). At that moment, the initial priority was to select clear and non-irritating substances, however as time went by other investigators focused on designing a synthetic cornea that was capable to encourage better integration of the synthetic tissue using the host tissue. Glass and quartz would be the options for the transparent region of the prosthesis and organic polymers such as gutta-percha and casein were added into the artificial retina layout. Afterwards, gold bands and platinum rings have been utilized to attain much better incorporation with all the host corneas. Further research on artificial corneas led to replacing quartz and glass with lighter substances such as plastics. At the start of the twentieth century, attention was redirected from artificial corneas into transplantation of donor corneal following the first powerful keratoplasty (Zirm, 1989).

Despite some clinical achievements in utilizing artificial corneas, the device refusal remains comparatively large. The existence of corneal epithelial stem cells, that are situated in the basal epithelial layer of the corneal limbus (the boundary between the cornea and the sclera), has contributed some hope for improved integration and healing. Hence, many researchers have concentrated on using new biomaterials to mimic the corneal structure, which might allow much better corneal self-repair (Holland et al, 2021). The absence of donors and related side effects like rejection makes corneal transplant less achievable (Fernández-Pérez et al., 2020 and Mathews et al., 2018).

Similar to the skin, corneal healing entails a succession of events such as inflammation, myofibroblast differentiation, extracellular matrix (ECM) deposition, tissue remodeling and fibrosis (Singh et al., 2013) (Yu et al., 2010). On the other hand, the cornea distinguishes itself with an angiogenic and immune privilege, whereby the cornea is oblivious of any bloodstream or cerebral vasculature (Singh et al., 2013, Cursiefen et al.,2007 and Ambati et al., 2006). Consequently, the cornea does not react to minor accidents with angiogenesis, as blood vessel formation interferes with corneal transparency and may result in vision loss (Li et al., 2020 and Bukowiecki et al., 2017). On account of the avascular nature of the retina, it's the epithelium that modulates the flow of materials in and outside of the cornea, such as growth factors and cytokines necessary for wound healing (Spadea et al., 2015, Yu et al., 2010 and Bazan et a., 2002) (Katz et al., 1981). The resistant benefit describes the absence of inflammation in the cornea, and this can be essential in ensuring transparency, minimal scarring and rapid wound healing and corneal re-epithelisation (Zarrintaj et al., 2018 and Bian et al., 2017).

Cornea healing mechanism is in place to aid in proper repair and the preservation of comea structure after injury. Wound healing is a dynamic and cell-mediated response, in the initial inflammatory stage to ECM remodeling and scar formation. After corneal injury, instant keratocyte apoptosis happens to prevent excessive corneal inflammation and opacification

(Ambrósio et al., 2009 and Wilson et al., 1996). The stromal cell population is replenished to reestablish the collagen organisation dropped in the accident site (Zarrintaj et al., 2018). On the other hand, the collagen generated during the early stages of fix is more irregular in size, composition and arrangement that could result in permanent opacification and scarring (Knupp et al., 2009) (Hart et al., 1969) (Maurice et al., 1957). It's, therefore, essential to overcome up with a membrane that has the best topography, biomolecular composition, (Islam et al., 2015) chemistry and architectural gathering (Mobaraki et al., 2019) (Fagerholm et al., 2014) to help improve and accelerate wound healing. This has caused the development of treatments which not only hide the wound but also make certain that the pharmacokinetic, mechanical and pharmacological requirements are fulfilled (Mobaraki et al., 2019).

1.2 BANDAGES FOR OCULAR WOUND HEALING

1.2.1 Bandage Contact lens

For more than a century, bandage contact lenses (BCLs) have been used in ophthalmology for therapeutic purposes (Sabell, 1997, Buckley, 2002 and Gassett and Kaufman in 1970). During this time, contact lenses have changed in their therapeutic indications and the materials from which they are manufactured (Ambroziak, Szaflik and Szaflik, 2004). Therapeutic contact lenses are the norm today for treating a variety of anterior segment ocular conditions. The main goal of therapeutic contact lenses is to help heal injured or diseased eye tissue or relieve pain and discomfort. Specific aims of using BCLs include aiding the regenerative process, stimulating corneal metabolism, increasing epithelial adhesion, maintaining stable corneal hydration, reducing collagenase accumulation, reducing oedema, and improving corneal hydration (Ambroziak, Szaflik and Szaflik, 2004 and Szaflik et al, 2002). The BCLs protect the cornea not only from potential exterior source of injury, but also from patient' eye lids

(Ehrich, 1993). The classes of BCL are based on the type of biomaterial ie., silicon hydrogel, hydrogel and collagen shield (Figure 1.4). BCLs can be made up of natural or synthetic biomaterials.

Figure 1.3. Bandage contact lenses.

1.2.1.1 Hydrogel

Hydrogels are the main component of ocular bandage lenses because of their hydrophilic nature and cross-linked polymeric networks that have high water absorption capability (Zidan et al, 2018, Gorbet et al, 2014 and Lin, Chen and Boahnke, 1998). Hydroxyethyl methacrylate (HEMA,) and poly (hydroxyethyl methacrylate) (p-HEMA) are used in the preparation of soft contact lenses. These lenses are very thin and flexible to conform to the surface of the eye. Hydrogel contact lenses were first introduced in the early 1970s and became much more popular due to their improved comfort and ease of use. When it comes to dry and delicate eyes, hydrogel materials are often the most suitable choice due to their unique biocompatibility with the human

eye (Zidan et al, 2018).

Hydrogel lenses are formed when chains of water-loving monomeric units are cross-linked into a matrix-like polymer. Each polymer has its own unique attributes that are determined by the interaction of chemical groups and the degree of crosslinking (Zhao et al, 2021 and Zidan et al, 2018). HEMA and p-HEMA), and other hydrophilic monomers are added to improve wetting and enhance oxygen transport. Adding substances such as methacrylic acid or higher proportions of hydrophilic neutral groups can increase the water content in contact lenses. (Curtis and Watters, 2019 and Childs et al, 2016). The U.S. Food and Drug Administration (FDA) divided contact lenses into four groups in 1985 based on the ionicity and water content of the lenses. Group 1 consists of low-water content non-ionic polymers. Group 2 includes non-ionic polymers with a high-water content. Group 3 consists of lenses with ionic polymers and low water content, and group 4 includes lenses with ionic polymers and high-water content (Zhao et al, 2021).

1.2.1.2 Silicon Hydrogel

Silicone hydrogels are advanced soft lenses that have enhanced oxygen permeability combined with a water content that is optimal for comfort and therapeutic effect (Kim and Chauhan, 2016 and Zhao et al, 2021). The most significant benefit of silicone hydrogels is that they allow up to five times more oxygen to reach the cornea than regular hydrogel lenses (Zhao et al, 2021). Without a healthy supply of oxygen, the ocular surface can become dry and itchy, and vision may begin to blur - a condition known as Hypoxia. The enhanced transmissibility of silicone hydrogels keeps the ocular surface healthy and comfortable for longer, making them a great fit for extended application. Ambroziak, Szaflik and Szaflik (2004) evaluated the clinical effects of silicon hydrogel contact lens as a continuous wear bandage and revealed that the lens is an effective and well tolerated bandage lens.

1.2.1.3 Collagen shield

Collagen was introduced as a wound-healing agent in the management of burns and skin ulceration in the 1970s and the biocompatibility and biodegradability of collagen, along with its ability to support corneal epithelial cells in culture, led to the development of collagen corneal shields as an ocular surface bandage (Poland and Kaufman, 1988, Lee, Singla and Lee, 2001 and Aghan et al, 2016). Collagen corneal shield was developed as a cornea bandage lens by Fyodorov in 1984 (Poland and Kaufman, 1988). Studies using animal and human subjects have investigated collagen shields as a drug delivery device and in the promotion of corneal epithelial and stromal healing. Collagen shields are currently indicated for ocular surface protection following surgery and in traumatic and nontraumatic corneal conditions. Collagen shields are currently manufactured from porcine scleral tissue or bovine corium (dermis) collagen and contain mainly type I collagen and some type III collagen. They are shaped like a contact lens and are supplied in a dehydrated form requiring rehydration prior to insertion (Greenwald and Kleinmann, 2008 and Zhao et al, 2021).

1.2.1.4 Limitations of BCLs

The BCLs are designed to protect the wounded cornea from the mechanical rubbing of the blinking eyelids thereby controlling pain and promoting healing of the wound (Aasuri and Sreedhar, 1997 and Nessim et al., 2008). Murali and Sreedhar (1997) reviewed the medical reports of 129 patients (138 eyes) fitted with BCL between 1992 and 1999 and concluded that BCL was safe and effective in improving symptoms and promoting healing of the cornea diseases. However, the lack of biological designs limits the ability of the BCL to form an optimum environment for wound healing (Shimazaki et al 2016). Shimazaki et al. showed that BCL had no significant benefit in wound healing, re-epithelization and pain depletion. Although these hydrogel lenses are soft and flexible, they have low gas permeability and must therefore be removed daily (Zhao et al, 2021). Silicone hydrogels are also slightly firmer than hydrogels, making them easier to handle and still be comfortable on the eye. However, adding

silicon to the hydrogel can increase the build-up of lipid deposits and reduce the number of water molecules in the lens (Zidan et al, 2018, Gorbet et al, 2014). Many manufacturers have introduced wetting agents to combat this problem and keep the lens moist for longer. (Zhao et al, 2021 and Zidan et al, 2018). Collagen shields have been commercially available for over 10 years, yet they are not widely utilised due to the variations in collagen crosslinking induced by ultraviolet light (UV) (Zhao et al, 2021).

1.2.2 Amniotic membrane bandages

The human amniotic membrane (HAM) is a useful tool in ophthalmic disease treatment and is widely used in the treatment of ophthalmic diseases due to its biocompatible, absorbable and non-toxic features. It is one of the oldest biological materials used as scaffolds in tissue engineering (Malhotra, 2014). The HAM is used as a naturally occurring biomaterial in tissue grafting to acts as a substrate and ocular bandage to promote re-epithelialisation in chronic cornea wound healing (Malhotra, 2014 and Elhassan, 2019).

1.2.2.1 Structures and properties

The HAM (Figure 1.5a) is one of the thickest membranes (0.02-0.05 mm) in the body (Malhotra, 2014). The membrane consists of three layers which are the epithelium, the basement membrane and stroma (Figure 1.5b). The epithelium is a single layer of cuboidal or columnar cells with surface microvilli projecting into the amniotic fluid (Malhotra, 2014). Studies by Malhotra (2014) and Anton-Sales et al (2020), revealed that the epithelium, the inner layer of the HAM is smooth and shiny and has no fibres. (Figure 1.5c). The basement membrane is composed of reticular fibres, and it is one of the thickest basement membranes discovered in the human body and can withstand cryopreservation (Malhotra, 2014 and Elhassan, 2019). The stroma consists of three layers - compact, fibroblast, and spongy. The compact layer is the strongest layer of amnion and can withstand inflammation and oedema.

The fibroblast layer is thick and composed of fibroblasts within reticular tissue which occasionally display phagocytic potential. The stroma, the outermost layer is spongy, gelatinous-like, and made up of collagen fibres (Bourne, 1962, Malhotra, 2014 and Rahman et al, 2009). The various layers contain epithelium matrix proteins such as collagens, cell–adhesion (proteoglycans, fibronectin, laminins and glycosaminoglycan), cytokines and a myriad of growth factors (Figure 1.5b) which are beneficial in the wound healing process (Rahman et al, 2009 and Bourne, 1962). The collagen and elastin found in the extracellular matrix of the membrane provide the stiffness and elasticity for HAM.

HAM has the following advantageous characteristics: anti-inflammatory effect due to the production of anti-inflammatory factors such as hyaluronic acid, suppression of inflammatory cytokines, antibacterial properties by molecules such as β-defense and elafin , anti-fibrotic properties due to TGF-β downregulation and its receptor expression, hypogenicity, immunomodulatory properties as a result of factors secreted by epithelial cells are macrophages and it inhibits the migration of natural killer cells and prevents maternal immune attack (Friel et al, 2016, Lee et al, 2012 and Leal-Marin, 2020). The mechanical properties of HAM such as elasticity, stiffness, and tensile strength, are dependent on the composition of the placenta (Leal-Marin, 2020). The alignment of collagen fibrils in the ECM is responsible for tensile strength, while elastic deformation is related to the presence of elastin fibres, laminin, hyaluronic acid, and glycosaminoglycan (Gholipourmalekabadi et al, 2016 and Leal-Marin, 2020). Some research has shown that the shear modulus of the amniotic membrane is between 100 and 400 Pa, with the measurement differences relating to the state of the HAM used. Decellularized HAM has a higher shear modulus than native because the denudation process dehydrates the membrane and thus reduced their thickness. It has been found that the elasticity of the HAM decreases with increasing thickness Leal-Marin, 2020).

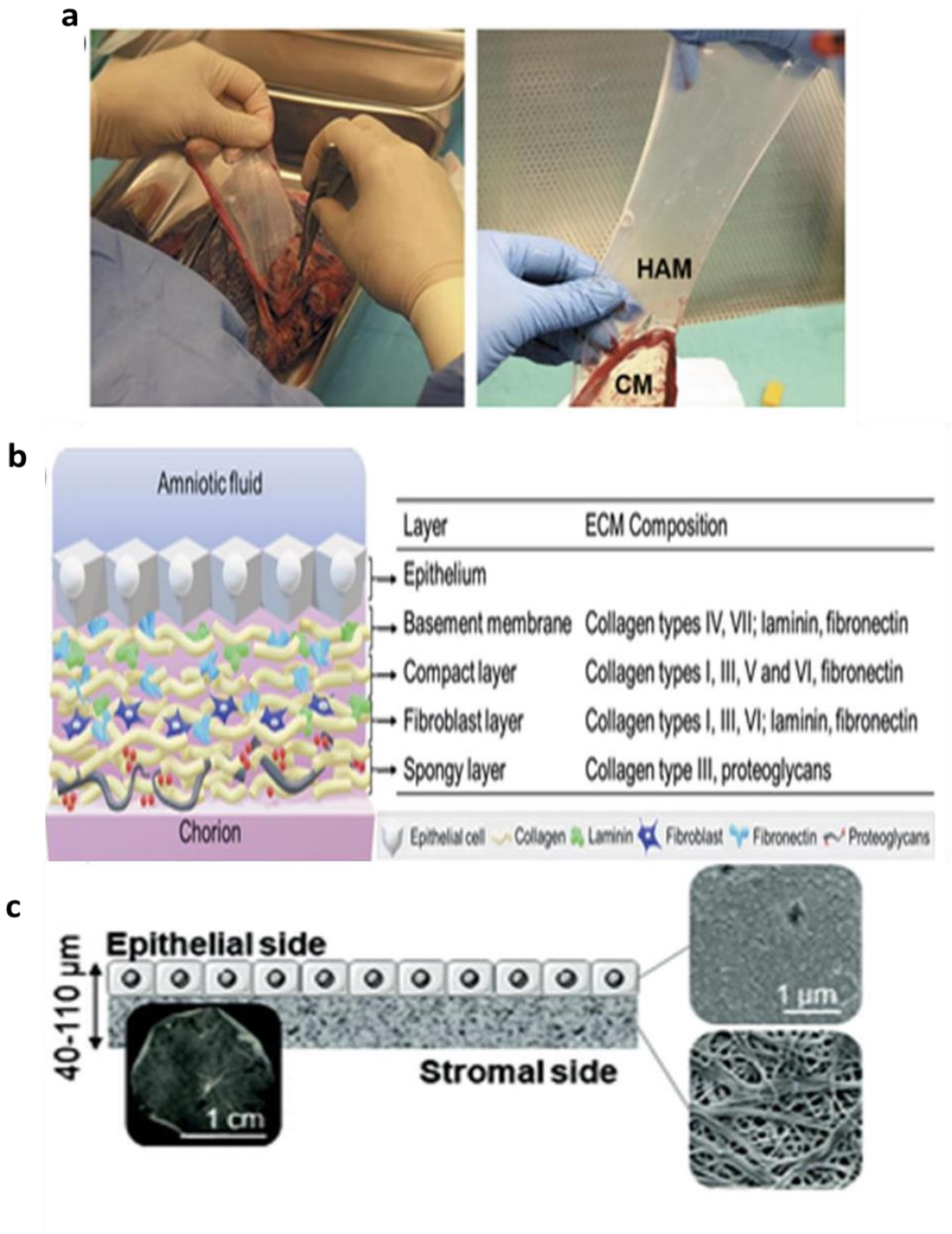

Figure 1.4. Human Amniotic membrane
(A) Photograph of Human amniotic membrane separated from the placenta. The HAM is a thin translucent layer attached to the chorionic membrane (CM) (Reproduced from Leal-Marin et al., 2020) (B) Schematic representation of the cross-section of the human Amniotic Membrane showing the extracellular –matrix composition of each layer (Image reproduced from Leal-Marin et al., 2020). (C) Micro and nano structure of the bandage materials tested. Each material presents two differentiated sides, which are illustrated schematically and with SEM micrographs (Anton-Sales et al., 2020)

1.2.2.2 Amniotic membrane preparation

The placentae are obtained from mothers who have had caesarean section and the donors are serologically negative for Human immunodeficiency virus (HIV), hepatitis B and C viruses, and Syphilis. The placenta obtained after vaginal delivery is not used due to possible containment with bacteria from the vagina (Tsubota et al, 1996). There are two main types of processing and preservation techniques for HAM: cryopreservation and dehydration (Cooke et al., 2014). Cryopreservation of HAM involves slow freezing at -80 ºC using Dulbecco's Modified Eagle Media (DMEM) and glycerol media to allow for slow rate freezing without ice formation. The preservation method maintains the biochemical components of the HAM which promote wound healing of the corneal. The HAM is stored in a -80 ºC refrigerator and thawed to room temperature when needed (Tan et al., 2014, Adds, 2001 and Cooke et al., 2014). The dehydration technique involves preserving the HAM using a vacuum with low-temperature heat to retain the cellular components. The dehydrated HAM is stored at room temperature and rehydrated for clinical use (Cooke et al., 2014 and Tan et al., 2014).

1.2.2.3 Application of HAM

The abilities of HAM to facilitate repair and healing of wound, decrease scarring and inflammation, and its antimicrobial properties makes it one of the best biomaterials for chronic wounds (Niknejab et al, 2008). HAM is used in ocular surface reconstruction as a substrate or scaffold for the growth of epithelial cells by incorporating it into the cornea or conjunctiva (Baradaran-Rafii et al, 2008). It also functions as a biological bandage to protect the underlying healing epithelial surface with the intention of the membrane to be removed over a period (Rahman et al, 2009). Several research have shown the use of HAM as treatment options in many eye conditions. These include glaucoma, tumours, dry eye, conjunctival reconstruction pterygium, corneal epithelial defects, cornea limbal stem deficiency and oedema (Fujishima et

al, 1998, Dalla Pozza et al, 2005, Barabino et al, 2003, Azuara-Blanco et al, 1999 and Tsubota et al, 1996).

In ophthalmology, transplantation of frozen or fresh HAM is commonly used for pterygium excision, conjunctival resurfacing (e.g., after symblephar on lysis), reepithelialisation of corneal ulcers, or temporary closure of perforated corneas (Fan, Wang and Zhong, 2016). It is most used to improve healing of corneal ulcers. Transplantation techniques can be classified into three main types: graft, patch, and sandwich. In grafting, the HAM is placed with the epithelium facing up the defect tissue, such as the cornea. Before transplantation, the surrounding layer of the host cornea is removed. The regenerating epithelium grows on the membrane, while HAM is mainly incorporated into the host tissue. In deep-rooted corneal ulcers, multilayer grafts inlays can be sutured (Meller et al, 2011). In the patch (or overlay) technique, the membrane is sewn to the surrounding conjunctiva. The membrane is larger than the underlying defect, so the host epithelium is present below the membrane. The epithelium side is commonly placed facing the defect tissue. Therefore, the fragile epithelium can grow under membrane protection. The sandwich technique combines the graft and patch techniques. The inner layers are attached as a graft, and for protection, an outer layer is fixed as a patch. The epithelium is expected to grow under the patch but over the inlay graft that is nearest the surface. The layers are attached to the cornea with non-absorbable sutures, or to other tissue with absorbable and non-absorbable sutures. A contact lens is often inserted for the protection of the thin HAM (Leal-Marin et al, 2021).

Currently, the HAM bandages produced are classified under the two types of preservation techniques. Prokera® (Bio-tissue) is the only cryo-pressed HAM bandage produced for effective cornea wound healing. This form of bandage is approved by the U.S. FDA for protective, wound healing and anti-inflammatory effects. Morkin and Hamrah, (2018)

evaluated the efficacy, safety and tolerability of Prokera® for the treatment of neuropathic corneal pain (NCP) in 9 patients and observed sustained pain control after the application of the lenses. AmbioDiskTM (IOP Ophthalmic), ArilTM (Seed Biotech) and BioDOptix® are dehydrated HAM bandages approved by FDA for wound coverage (Murube, 2006, Foulks 2014 and Chau et al, 2012).

1.2.2.4 Limitations

Nonetheless, HAM is affected by some limitations and controversies such as variation of the thickness, mechanical strength and transparency of the membrane at different parts of the membrane, racial variations between donors and different pieces of the membrane from same donor can possibly have diverse effects (Dua, Maharajan and Hopkinson, 2018, and Lai and Ma, 2013). However, Chau et al., 2012 demonstrated that cross-linking HAM with tissue transglutaminase enhances the mechanical properties and does not impair the transparency. Furthermore, processing and preservation of HAM by the different techniques can affect the membrane differently and can significantly alter the membrane (Hao et al., 2000, Lai, 2014 and Al-Mosallamy, 2015). Furthermore, the cost of serological testing, processing and preserving the HAM is relatively expensive. As a result, novel biomaterials able to overcome these limitations are currently explored to generate cornea wound bandage. (Murube 2006 and Chau et al, 2012).

1.3 CHICKEN **(GALLUS GALLUS)** EGGSHELL MEMBRANE

Eggshell membrane (ESM) is a protein-based fibrous tissue that lies in between the mineralized eggshell (ES) and the albumen to protect against bacterial invasion (Figure 1.6) (Ahlborn and Sheldon, 2006 and Wang, Chen and Huang, 2014). The utilisation of ESM has long been underestimated because it was considered as a waste material, however environmental reduction of waste is a major concern of society. Despite its unique properties and fascinating structure, only a handful of studies have been done (Choi et al, 2021). Devi et al, (2012) proposed the use of ESM in combination of gold nanoparticles for the recovery of precious metals from chemical and industrial waste. Wang, Wei and Huang generated a new bio-sorbent material from eggshell membrane via thiol functionalization method. They concluded that ESM is an ideal material for producing a column for wastewater purification (Wang, Wei and Huang, 2013).

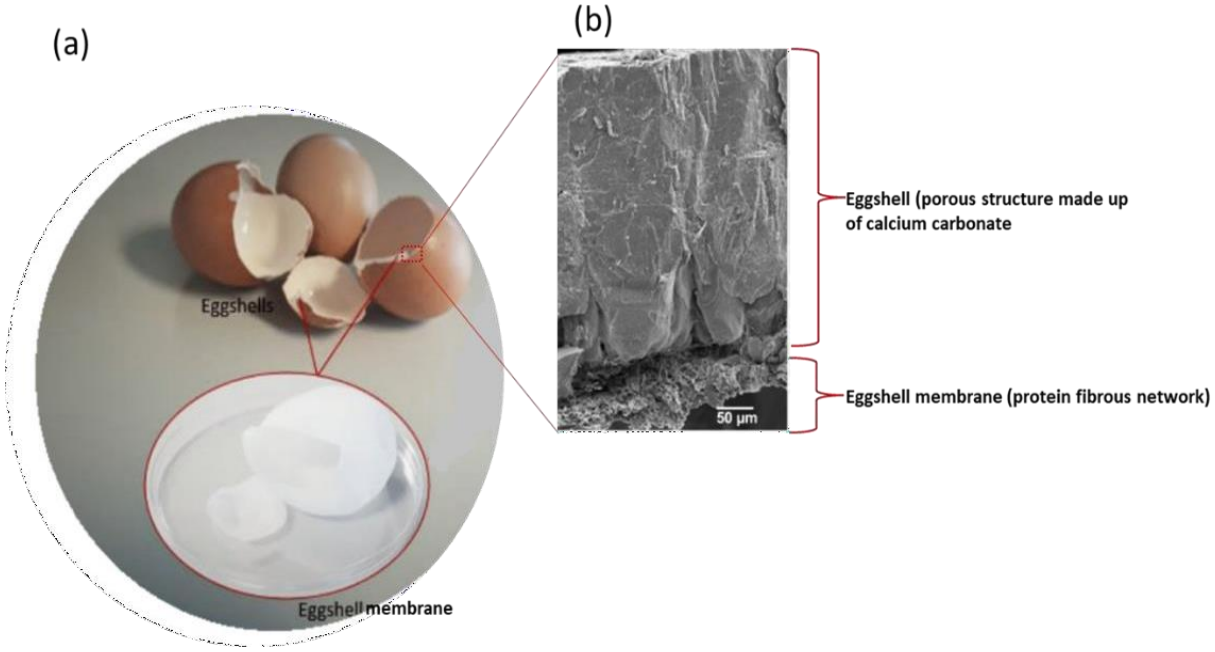

Figure 1.5. Photograph of Chicken (gallus gallus) eggshell.
Inset shows (a) a photograph of the eggshell membrane separated from cross-sectional of eggshell (Image adapted from Jonchere et al., 2010).

1.3.1 Structure and properties

The ESM can be divided into three substructures: the outer shell membrane (OSM), the inner shell membrane (ISM) and the limiting membrane, LM (Figure 1.7a) (Bellairs and Boyde, 1969, Lee et al., 2009). The inner and outer shell membranes are the first layers of ECM covering the egg (yolk and whites) (Creger et al. 1976). The outer ESM is located just under the ES and its fibres range in thickness between 1 and 7 μm (Figure 1.7b). The fibres of the OSM extend into the mammillary knobs of the shell. The thickness of the whole outer membrane layer is approximately 50 to 70 μm (Torres et al., 2010 and Shi, Zhou, Guyonnet, Hincke and Mine, 2021). The inner ESM is separated from the outer ESM by the space filled with air, which is the biggest in the air cell (Figure 1.7a). In comparison with the outer one, the fibres of the ISM are smaller in diameter, their thickness ranges from 0.1 to 3 μm and in addition the whole inner membrane layer is thinner (its thickness is between 15 and 26 μm) (Baláž, 2014). The fibres of the inner ESM are interlaced with the outer membrane. The LM represents the innermost very thin structure of the ESM, which surrounds the egg white (Baláž, 2014 and Torres et al., 2010). Bellairs and Boyde (1969) reported that after staining eggshell membrane with fluorescein isothiocyanate (FITC), the LM appears as particles that fill the spaces between the inner membrane fibres, several microns outward from the level at which the inner membrane fibres first appear.

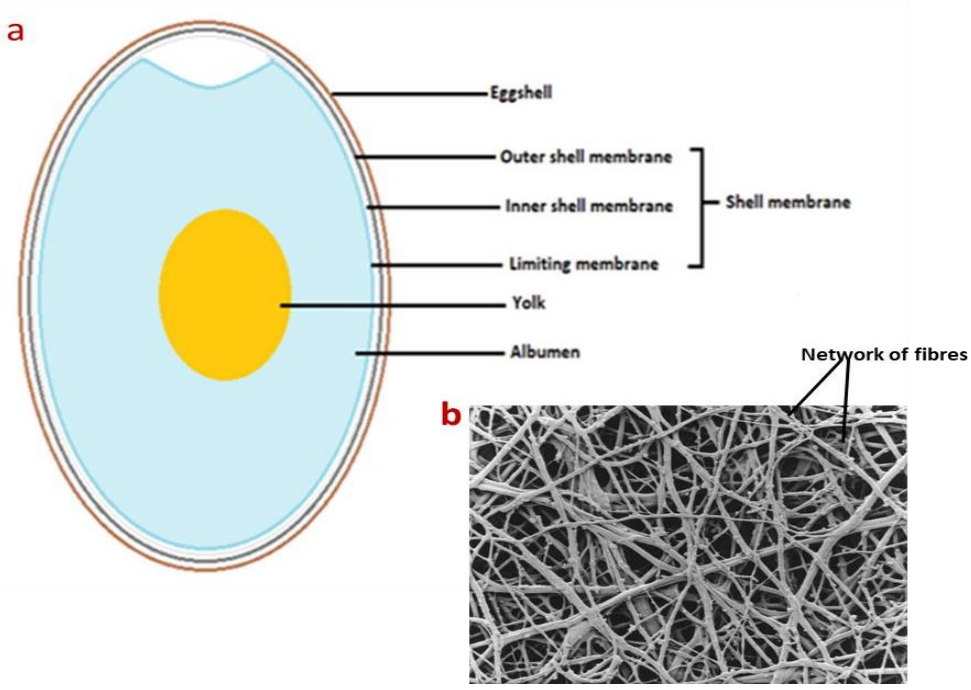

Figure 1.6. Schematic diagram showing the anatomy of Chicken egg.
(a) The Chicken egg consists of the eggshell, shell membranes consisting of three-layers: outer shell membrane, inner shell membrane and the limiting membrane, the yolk and albumen. (Mensah et al., 2021). (b) SEM of outer membrane from the shell of chicken's egg (Lee et al., 2009)

The ESM is exceptionally protein-rich and comprises a high number of pure glycoproteins like collagens, hyaluronic acid and glucosamine (Table 1.1). The collagens provide the thermal stability, wound healing and optimum mechanical strength of the ESM (Ahmed, Suso, Maqbool and Hincke, 2019). The presence of the hyaluronic acid plays a role in improving angiogenesis and tissue morphogenesis and retaining water in the ESM (Khanmohammadi et al, 2014, Vulganova and Urgeova, 2013). The separate layers of the eggshell have been analysed and found to contain several types of collagens (types X, I, V). The outer membrane is predominantly made of type I collagen, whereas the inner membrane consists mainly of type V collagen (Wong et al. 1984). In addition, type X collagen has been reported to occur in both membrane structures (Arias et al. 1991).

ESM amino acid profiles have also shown high concentrations of arginine, glutamic acid, histidine, cystine, and proline (Britton and Hale 1977). The presence of the chemical components as well as the antibacterial properties enables the ESM to maintain homeostasis and act as a protective barrier and nutritional supplement provider to the growing embryo (Sah et al., 2016). For instance, Sah et al., recognised antibacterial enzymes like lysozymes and β-N-acetylglucosaminidase from the ESM letting it behave as a bacterial filter (Sah et al., 2016) (Lifshitz et al., 1964).

Corneal wound management depends on the maintenance of a sterile barrier against the abrasive forces through blinking to protect the wound from further disease and harm (Li et al., 2019) (Ljubimov et al., 2015). Hence, the antibacterial and antifungal properties of this ESM together with the highly pressurised, porous, exceptionally collagenised construction, make the ESM a very attractive biomaterial for corneal wound healing (Benson et al., 2012) (Mine et al., 2003) (Poland et al., 2001). Meanwhile, the high surface area, porosity, biological attributes and non-toxic character, make the ESM a perfect scaffold to encourage cell growth and migration, and this can be improved by the biocompatibility and protein-cellular interactions which happen in the ESM port (Yi et al., 2004) (Maeda et al., 1982). Likewise, the high surface area of the ESM serves as an adsorbent of drugs, nanoparticles or microparticles to improve tissue regeneration via controlled drug release (Chai et al., 2013) (Benson et al., 2012) (Yang et al., 2003). Unlike the AM, the ESM has improved mechanical properties and can be an economical, excess industrial waste merchandise connected with minimal ethical issues (Sah et al., 2016) (Tsai et al., 2006). The similarity of the ESM to native tissue, along with its elevated protein and glycoprotein content, renders it a highly valued source in biomedical technology and wound healing, capable of providing the best environment for tissue regeneration and healing (Ahmad et al. 2017) (Yang et al., 2003).

Table 1.1. Composition of Eggshell membrane and their utility for tissue regeneration

Composition	Advantages	References
Collagen type I	A key constituent of mammalian connective tissue (30% of human protein) Fibres incorporate into the new tissue matrix Unique biocompatibility and biodegradable properties Adhesive	WeGlowacki and Mizuno, 2008, Kadler, 2008
Collagen type V	Non-cartilaginous connective tissues e.g., skin dermis, bone, tendon, cornea Collagen type I assembly Responsible for tensile strength	WeGlowacki and Mizuno, 2008, Kadler, 2008, Anstrup et al., 2011,
Collagen type X	Network forming collagen Human cartilage Bio-mineralization	Cen et al., 2008, Rucklidge, Milne and Robins, 1996
Fibronectin	Cell adhesive Cell growth, migration, and differentiation Cell binding to ECM Wound healing	Williams, 2011
Other Glycoproteins	Cell adhesive Cell signaling	Raunest, Hötzinger and Bürrig, 1994
Proteoglycans	Connective tissue Contain glycosaminoglycans (GAGs) such as hyaluronic acid, dermatan sulphate and chondroitin sulphate Form porous hydrated gels	Baker and Balch, 1962, Raunest, Hötzinger and Bürrig, 1994

1.3.2 Method of separation

One important process for the use of ESM as a biomaterial is its separation from the ES. Several reports have demonstrated how to extract the membrane from the ES. One of the methods is simply peeling of the membrane out of the shell. This process has been claimed to be efficient even though the outer membrane is strongly bounded by the shell (Torres et al., 2010 and Li et al., 2011). Another method to loosen the outer membrane embedded in the shell is treating the outer membrane with acids including dilute acetic acid, hydrochloric acid (HCl) and ethylenediaminetetraacetic acid (EDTA) (Torres-Mansilla and Delgado-Meijia, 2017). The acidic treatment method applied to ES acts on the surface to either dissolve the calcium carbonate ($CaCO_3$) in the ES or loosen the interfacial bonding between the outer membrane and ES, thereby producing an intact ESM (Guo et al., 2011, Sah, and Rath, 2016).

During the acid treatment process, several factors such as the incubation temperature, reaction time, moisture content, and type of acid used will impact the effectiveness of this separation stage. (Marcet, Salvadores, Rendueles and Díaz, 2018: Zhang et al, 2016). Accordingly, the whole ESM could be separated manually (Guo et al., 2011, Sah, and Rath, 2016).

A new mechanical technique known as dissolved air floatation (DAF) recently developed by ESM Technologies, LLC (Carthage, MO, USA) has proven to recover efficiently and successfully 96% of ESM within 2 hours of processing ES waste (Sah and Rath, 2016). Other mechanical processes include the use of microwave to separate the ESM from the ES. The principle behind this method is that the ESM has a higher water content than the shells and absorbs more energy from electromagnetic waves, resulting in differentiated heating of the two components, followed by membrane expansion, weakening of physical connections between the shells and membranes, and separation (Hussain et al, 2010). Finally, the passage of ES fragments through a series of drills in an aqueous environment heated by steam, followed by separation in a cyclone, is another mechanical method of separation (Adams, 2010). Generally, the mechanical techniques produce fragments of ESM. Table 1.2 presents some of the different processing methods for the extraction of ESM from ES and the limitations associated with method.

Table 1.2. Separation method of eggshell membrane from eggshell

Method	Limitations	References
Immersed overnight in 0.5M HCl followed by mechanical stripping from eggshells	Denaturation of collagen and loss of acid-soluble collagen due to strong acid treatment	Ishikawa, Suyama and Satoh, 1999
Immersed in 5% EDTA at room temperature for 1 hour (Resulting in the partial loosening of membrane from the shell) followed by manual stripping.	Need for the manual separation of the loosened membrane	Soledad Fernandez et al., 2001
Pneumatically removal of ESM from crushed eggshell small particles collected to a valve	Loss of membrane still attached to the shell particle, contamination of membrane with shell particles	Thoroski, 2004
Kept in 5% Na-EDTA at 26±2 °C for 24 hours followed by hexane (half the quantity of EDTA solution) for 3 min	Drawbacks not found, milder treatments such as EDTA/hexane don't affect the protein quality of the membrane, minimal contamination from shell particles	Sachindra, Bhaskar and Mahendrackac, 2014

1.3.3 Applications of Eggshell membrane

1.3.3.2 Skin wound healing

Millions are estimated to suffer from acute and chronic skin wounds yearly and these various wounds invariably bring along obvious health, potential emotional and financial implications to patients (Langemo and Brown, 2006, Shankaran, Brooks and Mostow, 2013). The centre of interest in intensive research on acute and chronic wounds is to find an effective treatment.

The many proteins and peptides found in ESM make it an ideal candidate for wound healing. The application of chicken ESM for skin wound healing was first attempted by Maeda and Sasaki (1982). The initially study was conducted using rabbits. The results revealed that ESM was a suitable material for wound healing. Consequently, the ESM was applied as a skin graft in a patient and after seven days, the wound was well epithelialized. ESMs were further used

in two cases, a 3-year-old female child with a severe burn on foot and a 3-year-old female child with a scald burn on elbow joint. In both cases, satisfactory epithelialisation was observed.

In wound management, the dressing must prevent bacterial infection, and stimulate angiogenesis and re-epithelialisation (Raja, 2007, Kim, 2018). A membrane consisting of polydopamine-modified ESM nano/microfibres with KR-12 antimicrobial peptide and HA was generated by Lui et al (2019). Accordingly, the *in vitro* biological results showed that the membrane had remarkable antibacterial activity and stopped the formation of methicillin-resistant Staphylococcus aureus (MRSA) biofilm on the membrane surface. In addition, the membrane increased the proliferation of keratinocytes and human umbilical vein endothelial cells and enhanced the secretion of vascular endothelial growth factor (VEGF). The *in vivo* animal model study revealed that the membrane is a suitable material for wound dressings.

In a quest to generate a cost-effective wound healing product with anti-inflammatory properties, PEP has been explored in several studies (Morooka et al., 2009, Vuong et al, 2018, Cree and Pliya, 2019, Ahmed, Suso and Hincke, 2019). Morooka et al, 2009 analysed the effect of processed knitted fabric with soluble eggshell membrane on human skin. The results indicated that the presence of the ESM in the fabric did not affect the water content, water evaporation and water absorption of the human skin. This support the theory that ESM is an appropriate material for skin wound healing. Guarderas et al, 2016 evaluated the effectiveness of chicken ESM dressing on wound healing. The findings suggested that ESM significantly improves cutaneous wound healing. Vuong et al, 2018 studied the effect of PEP on matrix metalloproteinase (MMP) activities in vitro dermal fibroblast cell culture and in vivo mouse skin wound healing models. The PEP treatments in both models increased the activity of MMP and the regulation of early cellular functions during wound healing. Ahmed, Suso and Hincke, 2019 conducted a study to evaluate PEP for advancement of skin wound healing. A mouse

wound model was implemented to assess the impact of the PEP on wound healing. The histopathological assessment of the wound at day 3, 7 and 10 showed that the PEP significantly enhanced the wound closure. Additionally, the histological studies revealed that the granulation tissue in the PEP treated wounds were significantly thicker than the non-treated controls. Furthermore, higher amount of collagen was deposited in PEP treated wound with minimal inflammatory responses. A study conducted by Choi, Kim, Suh and Han, 2021 discovered that ESM treated with carboxylic acid could improve skin wound healing. By introducing a simple approach for crosslinking with a carboxylic acid, the modified ESM was produced to promote wound healing. Biocompatibility of the surfaces of the ESM was obtained using an improved approach of immersing the surfaces in 0.5 M acetic acid and 0.5 M citric acid. As a result, the modified ESM exhibited appropriate physicochemical qualities and flexibility, making it excellent for wound healing on the skin. The modified ESM increased hDF cell adhesion, proliferation, and secretion of wound-healing related cytokines and growth factors in the *in vitro* tests. Furthermore, an *in vivo* study utilising a skin damage rat model, the modified ESM greatly encouraged full-thickness skin wounds.

1.3.3.3 Bone, cartilage, and nerve

A huge interest has been generated in neural tissue repair and regeneration strategies because it specifically influences the quality of human life (Schmidt and Leach, 2003, Ninov and Yun, 2015, Kim, 2020). The design of a cost effective bioactive organic-inorganic hybrid materials containing osteogenic activity in bone tissue engineering has generated a substantial curiosity (Yoshikawa et al., 2001, Tohma et al., 2011). Arias et al, 2008 sufficiently proved the effectiveness of ESM as a biodegradable bone regeneration inhibitor material. Dried Extracted ESM got dried and interposed in the osteomy site of rabbit ulna. A histological examination of the ulna osteotomised regions after 1-16 weeks. After histological and fluorescence microscopy and radiological evaluation, the research will reveal firstly that ESMs as an interposed material

in rabbit osteotomized ulnar experiments played out as an effective obstacle against bone bridging. (Farjah, Naeimi and Saberi, 2016) exhibited the efficient use of ESM to boost nerve regeneration and encourage the operational improvement in an injured sciatic nerve of rat. This study contrasted the use of ESM tube conduit with autograft. It was noticed on the 90th day, post operations created a greater nerve regeneration in the ESM group as compared to the autograft.

The ESM which has been garnered from locally obtainable single comb white leghorn hen eggs was probed for its ability to back adhesion and proliferation of human meniscal cells in the current research (Pillai et al, 2015). Autoclaving was applied on the extracted ESM and matched with raw ESM for meniscal cell growth. Raw ESM was cationic in nature and the surface was covered with a mucilaginous coating. Nevertheless, autoclaved ESM exhibited almost neutral surface charge without any mucilaginous coating. An enhanced defiance of the autoclaved ESM to biodegradation when compared to raw ESM became apparent. The main human meniscal cells planted into the stringy side of both ESM exhibited cell adhesion and proliferation in autoclaved ESM than raw ESM. ECM released into the cultured medium by the adhered cells was higher with autoclaved ESM than raw ESM. Cell attachment, DNA content on the scaffold, cell proliferation index, cytotoxicity and biodegradation studies also established that autoclaved ESM scaffolds supports better cell attachment and growth of meniscal cells when compared to raw ESM. Hence, autoclaved ESM can be a potential and interesting natural scaffold matrix for meniscal tissue engineering.

Chen et al, (2019) proved the use of a versatile biomimetic mineralisation procedure to generate ESM/hydroxyapatite composite with the ESM as the model. The findings showed that both sides of ESM proved exceptional biomimetic mineralisation ability, with the hydrophilicity and thermal stability of ESM got efficiently better by the insertion of HA. Furthermore, in vitro

experiments on MC3T3-E1 cells showed that the inmost side of the ESM benefited cell proliferation and adhesion than the outer side. Incredibly, the processes of proliferation, adhesion and multiplying, along with the alkaline phosphatase (ALP) activity and demonstration of bone-related genes and proteins (runt-related transcription factor 2, ALP, collagen type I, and osteocalcin) on both sides of the ESM composites showed a suggestively advanced as compared to those of the original ESM. These results indicated that ESM-HA composites attained employing biomimetic mineralisation potentially could be new materials for future bone tissue repair.

1.3.3.4 Oral and maxillofacial surgery

Periodontitis is a primary cause of tooth loose in adults and it affect 5 to 15 % people worldwide (Peterson, 2003). Guided tissue regeneration (GTR) is a technique employed in the regeneration of damaged periodontal tissues (Gentile et al, 2011). This technique involves the use of a barrier membrane to eliminate epithelial cells from the damaged surface and repopulate the periodontal ligament cells (Salonen and Persson, 1990, Dupoirieux et al, 2001 and Jun et al, 2012). Synthetic GTR membranes have been shown to have poor biocompatibility and inflammatory effect due to the acidic degradation products (AlGhamdi and Ciancio, 2009). The biological and biochemical properties of natural ESM inspired Jun et al (2012) to use SEP/PLGA nanofibers as a GTR membrane to enhance the cell proliferation, spreading and proliferation. Several biocompatibility tests such as oral mucous membrane irritation, acute toxicity, haemolysis and cytotoxicity were performed to determine the biocompatibility of the SEP. This study showed SEP/PLGA as a potential GTR membrane (Figure 1.8). However, the natural ESM was not applied in this study due to the results obtained by Dupoirieux et al, (2011) which indicated that natural form is not favourable for guided bone regeneration.

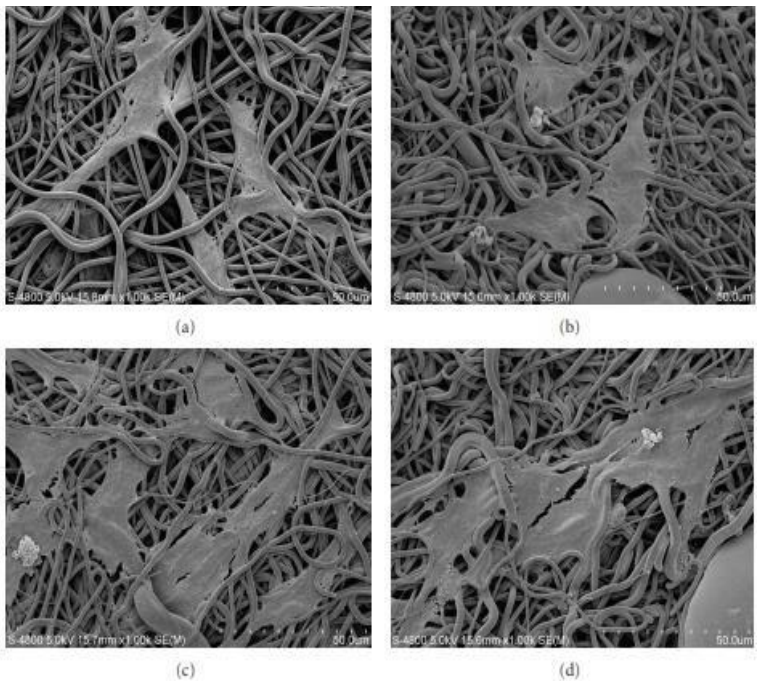

Figure 1.8. SEM photographs of cellular growth on different groups of nanofibers.
(a) pristine PLGA, (b) SEP/PLGA = 90: 10, (c) SEP/PLGA = 70: 30, (d) SEP/PLGA = 50: 50.
(Adapted from Jun et al., 2012)

1.3.3.5 Neurosurgery

In neurosurgical operations, it is important to protect the brain tissue from the hazardous effect of the metallic microsurgical instruments (Cokluk and Aydin, 2007, Spetzger, von Schilling, Brombach and Winkler, 2011). The experimental study of Gokyar Cokluk and Kuruoglu (2017) evaluated the use of raw ESM as a therapeutic intervention for the protection of naked brain tissue. In their study, 13.3 % of the uncovered fresh cadaveric cow brains operated with ESM were minimally damaged as compared to 60 % of the brains without it. According to the findings, ESM has some promising effects as a material for brain tissue protection and essential in neurosurgery.

1.3.3.6 Otolaryngology

ESM has been shown as an effective patch for the treatment of moderate to large traumatic tympanic membrane perforation (TMP) in human (Jong et al, 2017). TMP, a hole in ear drum is a condition that can be caused by infection or trauma (Afolabi, Aremu, Alabi and Segun-Busari, 2009). In clinical practice, most TMPs have tendencies to heal on their own.

Nonetheless, in large perforation, the spontaneous healing fails (Lou, Tang and Yang, 2011). Jong et al, 2017 evaluated the effects of ESM patches on the healing time for TMP. Sterilized round disc ESM patches moisturised with saline were placed on the surface of perforation in patients. After 3 months, the healing time for patients with the ESM patches were significantly improved as compared to patients that received perforation edge approximation.

1.3.3.7 Ophthalmology

In ophthalmology, ESM was first utilized by Coover in 1899 for four different eye injuries namely symblepharon, burns on eyeball, cornea ulcer and iritis. Before then, the ESM was not used due to fear of infection. Raw ESM obtained by manually peeling from the shell was applied in each case study. In the case of symblepharon, after 10 days, the eyeballs and lids of the patients were smooth with no adhesions. Similar results were observed in patients with burns on eyeballs. The use of ESM in patients with corneal ulcers experienced no pain or irritation during the treatment. The ulcers were suitably healed after two weeks. Finally, ESM was employed in iridectomy for recurrent iritis and resulted in an effective wound healing with no infection. No further studies have reported on the use of ESM in ophthalmic surgery or other eye applications despite the promising report.

1.4 OCULAR DRUG DELIVERY SYSTEM

In the ophthalmic world, the most widely used non-invasive mode of administering drugs to the eye to treat diseases is topical instillation. Convectional drug formulations such as eye drops, ointments, gels, intraocular injections and lacriserts are used. One of the most important functions of the structure of the eye is to protect it against any foreign substance by removing them instantly. This poses as the main challenge in the conventional delivery system because the drugs must stay in the eye for a long period before they are absorbed into target site of action (Ferreira et al, 2012).

About 90% of the ophthalmic pharmaceutical formulations are in the form of topical eye drops due to their ease of administration and patient compliance. The instillation of these drugs has low bioavailability and ocular adverse effects due to the washing of the drops by mechanisms like reflex blinking and tear dilution and turnover), the absence of control release properties and the presences of several barriers (cornea, conjunctiva, retinal pigment epithelium and blood-retinal barriers) (Shell, 1985). The presence of these barriers makes it difficult to achieve the therapeutic concentration of a topical drop to the various posterior tissues of the eye. Moreover, the topical eye drop therapy has the failure to deliver insoluble and lipophilic molecules to the eye tissues (Gower et al., 2016).

The use of control drug delivery systems like hydrogels, nanoparticles, microparticles, implants, dendrimers, microneedles, mucoadhesive polymers and iontophoresis are the strategies being used to overcome some of the problems associated with conventional therapy. They are used to improve the bioavailability and therapeutic efficiency of ophthalmic pharmaceutical formulations that causes little toxicity and minimal side effects (Ankit, Rishabha and Pramod, 2011). One of the strategies showing promising results through various researches is microparticles.

1.4.2 Microparticles

Microparticles (MP), being one of the novel ocular drug delivery systems, have various advantages, ability to provide controlled and sustained release of the drugs, increase drug bioavailability and protect the incorporated drug, person another organ to organ from direct toxic exposure. Additionally, the side effects associated with conventional dosage is overcome by using Microparticles which increases accurate dosage. In addition, the therapeutic effects of ocular drugs are improved, offer relief and better patient's adherence to the use of the drug treatments (Chau et al, 2010). Some commercial drugs that have being successfully loaded in MP for ophthalmic purposes are outlined in Table 1.3 below.

Table 1.3. Commercial ophthalmic drug incorporated microparticle products

Drug	Polymer	Evaluation	Reference
Norfloxacin (ophthalmic solution is known as chibroxin)	Ethylcellulose and hhydroxypropyl methylcellulose	The in vitro release study demonstrated a super case II transport diffusion of Norfloxacin from the microparticles. The prepared microparticles indicated sustained drug release of a period of 10 h and buoyant release of 12h.	Ramesh, Balachandra and Chinnaiah, 2013
Gentamicin	PLA and PLGA	The encapsulation efficiencies of the spray method and the double emulsion methods were 45% and 13% respectively. The results obtained in the study showed that spray drying techniques for the preparation of the microparticles may be the appropriate delivery system.	Prior et al., 2009
Dexamethasone	PLGA	The drug-loaded particle was prepared using the o/w solvent emulsion method and the encapsulation efficiency was 72.97%.	Bracia et al.,2009

1.4.2.2 Formulation materials for microparticles

In pharmaceutical applications, the biodegradability and biocompatibility properties of polymers are of critical importance to consider. In the body, biodegradable materials degrade to nontoxic degradation products that do not cause problem of carrier toxicity (Alagusundaram et al., 2009). When biocompatible materials are exposed to the body or bodily fluids, they do not produce toxic or immune response but non-biocompatible can pose permanent injuries to body tissues (Tapan Kumar et al., 2010).

The polymers used for MP are classified into two types, natural polymers obtained from different sources like collagen, gelatin, chitosan, agarose, starch, dextran and starch. The other being synthetic polymers (Figure 1.9) includes, poly(lactide) (PLA), poly(glycolide) (PLG) and their copolymers PLGA (Chau et al., 2010, Alagusundaram et al., 2009, Alberton et al.,1996, Berthold, Cremer and Kreuter, 1998, Ko, Sfeir and Kumta 2010, Keppeler, Ellis and Jacquier, 2009, Ai-min et al., 2011, Bachelder et al., 2010 and Balmayor et al., 2009).

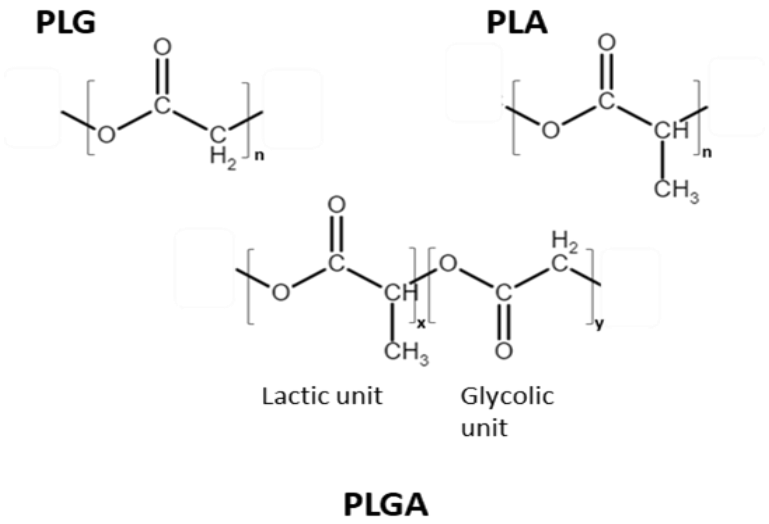

Figure 1.8. Chemical structures of PLG, PLA and PLGA polymers.
The n represents the number of repeat units in PLG and PLA. The x and y represent a number of lactic and glycolic units in the PLGA respectively.
The fabrication of MP depends on the choice of suitable polymeric materials (Giri et al., 2013).

One of the synthetic polymers mostly used is PLGA due to its biodegradable and biocompatible properties, control release, target delivery and therapeutic effects (Chau et al., 2010 and Nihant et al., 1995). In the body, PLGA undergoes hydrolysis to slowly generate low concentrations of lactic and glycolic acid which do not cause carrier toxicity or immunological response and explains the success of PLGA as a biodegradable polymeric material (Patil, Papadimitrakopoulos and Burgess, 2004 and Alagusundaram, Madhu, Umashankari and Badarinath, 2009). When used for drug delivery, this hydrolysis leads to the degradation of the PLGA matrix and any drug incorporated within is liberated in a time-dependent fashion, typically over several weeks. PLGA has a tailored biodegradation rate, and this is dependent on the copolymer ratio (Makadia and Siegel, 2011). PLGA of different lactide/glycolide (copolymer) ratios, 50:50, 65:35, 75:25 and 85:15 lactide/glycolide are available. The 65:35, 75:25 and 85:15 lactide/glycolide copolymers have extended degradation half-lives as compared to 50:50 lactide/glycolide copolymers that have the fastest degradation half-life of about 60 days (Alagusundaram, Madhu, Umashankari and Badarinath, 2009, Chau et al., 2010 and Tamboli, Mishra and Mitra, 2012).

1.4.2.3 Method of preparation

Various techniques such as solvent emulsion evaporation (single or double), spray drying, polymerization and phase separation are employed in the preparation of microparticles (Giri et al., 2013, Lai and Tsiang, 2005, Bible et al, 2009, Chau et al, 2009 and Nalla, 2017). These techniques must fulfil certain standards such as the ability to integrate high drug concentration, biocompatibility with a reliable biodegradability and predisposition to chemical modification. Also, the method should not affect the stability of the product after the preparation, have clinically suitable shelf-life, desired size range and finally, the drug encapsulation efficiency should be high (Yadav, 2013).

The spraying drying method is when the polymer is dissolved in an organic solvent which is volatile such as acetone, dichloromethane etc. This method is based on the drying of the

polymer and the drug loaded MP made of PLA and PLGA containing gentamicin sulphate were obtained by spray drying and w/o/w double emulsion process for the treatment of Brucella infections. The encapsulation efficiencies of the spray method and the double emulsion methods were 45% and 13% respectively (Prior et al, 1999).

Comparative studies have shown that the single or double emulsion evaporation (a simple beaker-stirrer laboratory method) is economical, convenient and robust (Lai and Tsiang, 2005, Khaled et al., 2010 and Nalla, 2017). Again, this technique is well controlled which gives preliminary ideas about the controlled parameters to produce microparticles on a large scale (Nalla, 2017).

The single emulsion method involves oil-in-water (o/w) emulsification. The o/w emulsion system consists of an organic phase comprised of a solvent (for example dichloromethane (DCM), chloroform and ethyl acetate) with dissolved polymer and the drug to be encapsulated, emulsified in an aqueous phase containing a dissolved surfactant (polyvinyl alcohol, PVA). A surfactant is included in the aqueous phase to prevent the organic droplets from coalescing once they are formed. The polymer-solvent-drug solution is emulsified (with suitable stirring and temperature conditions) to produce an o/w emulsion. The emulsion is formed by using a magnetic bar for mixing the organic and aqueous phases. Once the emulsion is created it is subjected to solvent removal by either evaporation or extraction process to solidify the polymer droplets (Airavind Chakrapan, 2006). The summary of the formulation process is presented in Figure 1.10. This method is not efficient for the encapsulation of hydrophilic drugs because the drug rapidly dissolves into the aqueous phase of the emulsion (Bodmeier and McGinity, 1987).

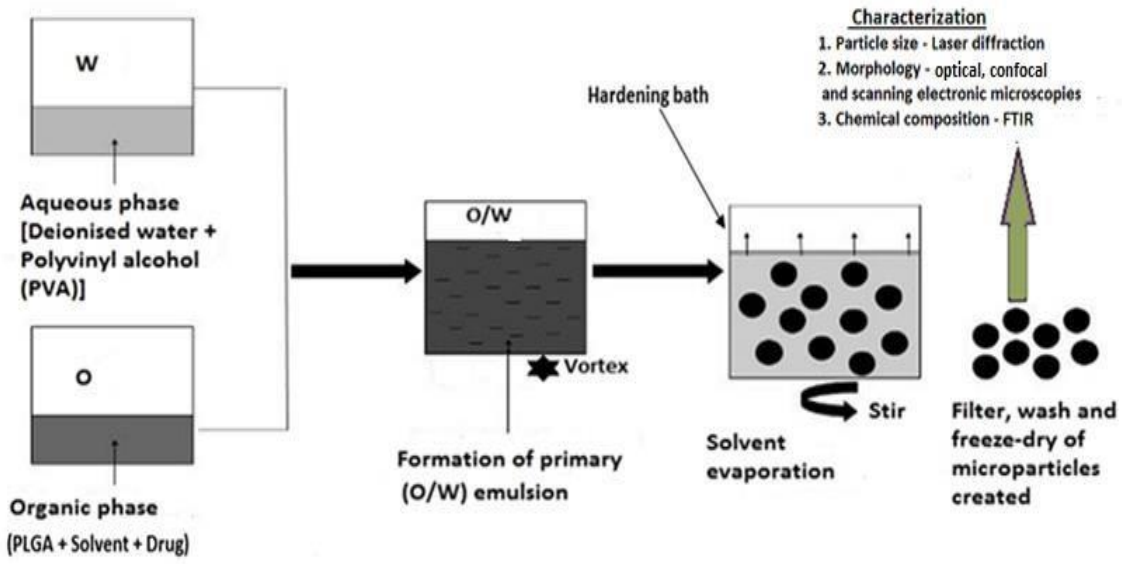

Figure 1.9. Schematic diagram of single o/w emulsion method.
This technique involves displaying the various steps in creating microparticles (Mensah et al., 2019, Bible et al., 2009).

The double emulsion solvent technique involves the formation of double or multiple emulsions of type o/w/o (oil in water in oil), w/o/o (water in oil in oil) and w/o/w (water in oil in water) for the preparation of the microparticles. The w/o/w emulsion solvent is the suitable methods used for the incorporation of drugs in microparticles (Figure 1.11) (Vikrant et al, 2012). This method is employed to overcome the limitation associated with the use of a single solvent emulsion method for the encapsulation of hydrophilic water-soluble soluble drugs). Lai and Tsiang (2005) prepared acetaminophen loaded PLA microparticles by three emulsion solvent evaporation methods: o/w emulsion method, o/w co-solvent method and w/o/w double emulsion method. The encapsulation efficiency in the w/o/w emulsion method was three times more as compared to the o/w emulsion method. Moreover, the microparticles prepared by the w/o/w double emulsion method showed good, controlled release characteristics.

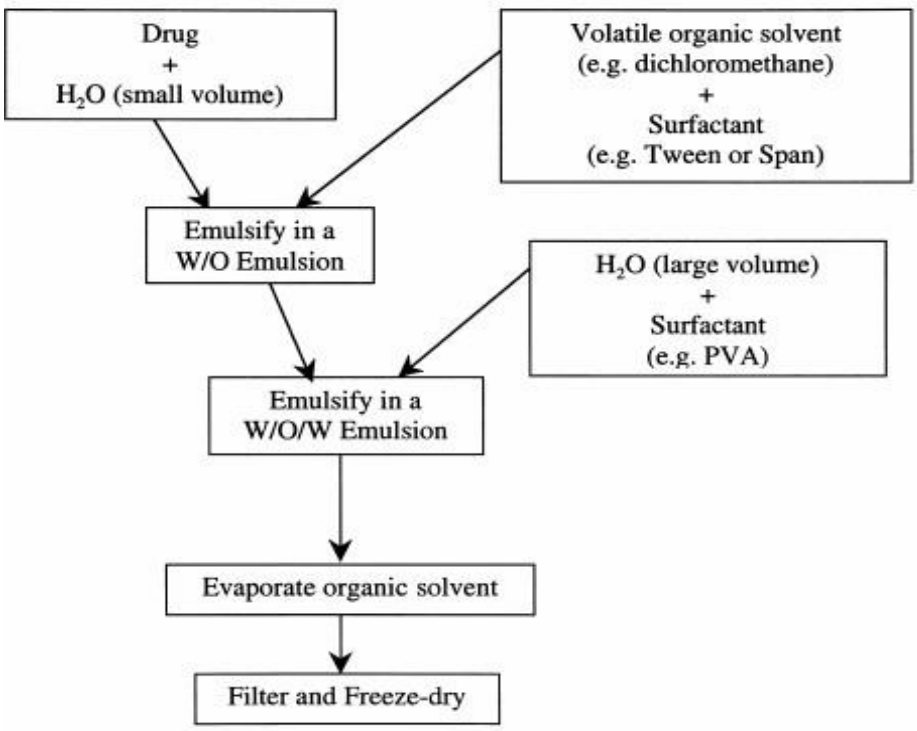

Figure 1.10. Flow chart outlining the steps in the w/o/w double emulsion method. (Kerr, 1987)

1.4.3 Physicochemical evaluation

The prerequisite for the effective use of MP is the evaluation of its characteristics. This also helps to determine the appropriate carrier for drug delivery. Different reviews have described a collective method of characterising microparticles, which includes the particle size and shape, morphology, size distribution, encapsulation efficiency, and *in vitro* dissolution (Alagusundaram et al, 2009).

To understand the role of MP, the size needs to be measured accurately. The performance of a drug, duration of drug release and mode of application are dependent on the MP size. The particle size analysis is important as to prevent tissue irritation (Ferreira et al, 2012 and Yadav and Jat, 2013). The particle size and shape of the MP can be measured by visualisation technique example the optic microscopy (OM) and scanning electron microscopy (SEM). They both determine the size and the microparticles' outer structure. However, SEM determines the

double -walled and the surface after particles are cross-sectioned. On the contrary, SEM provides a higher resolution than OM (Matthews and Nixon, 1974).

Particle size distribution of MP can be measured using different methods such as dynamic light scattering (<1 nm to > 1 µm), laser diffraction (<100 nm to 2 mm) and automated imaging (<1 µm to 3 mm) (Stanley-Wood and Lines, 2007). Laser diffraction, a well-established technique is one of the widely used particle size analysis method. It can generate results in less than a minute, large numbers of particles can be sampled in each measurement, and finally it has a wide dynamic range (Mori, Yoshida and Masuda, 2012). Laser diffraction measures particle size distribution by measuring the angular variation the in intensity of light scattered as a laser beam passes through a dispersed MP sample. Large particles scatter light at small angles relative to the laser beam and small particles scatter light at large angles. The angular scattering intensity data is then analysed to evaluate the size of the particles responsible for creating the scattering pattern. The particle size is reported as a volume mean diameter (Ross, 1973 and Mori, Yoshida and Masuda, 2012).

Hence, there is a need for careful selection of the process factors in order to fabricate the most appropriate MP size. Several methods are used to measure MP size, including dry dispersion laser diffraction (DDLD), wet dispersion laser diffraction (WDLD) and optical microscopy measurements. However, the method that is increasingly used is DDLD (Jaffari et al., 2013). DDLD method is desirable to measure the particle size and particle size distribution of wider range of particle (20nm – 2000 µm) (Keck and Muller, 2008). In DDLD, sample is dispersed in compressed air (dry) and a beam of monochromatic light is passed through this dispersion. The type of light intensity distribution patterns produced by particles of various sizes are deduced based on Mie scattering theory (Keck and Muller, 2008). The Mie theory assumes that the particle being measured is spherical. Therefore, the equivalent sphere diameter of particles is calculated. DDLD does not require the calibration of the measurements signal response, however pressure titration is required

to be developed to define the instruments parameters to provide accurate and precise MP size (ISO 13320:2009,2022 and Jaffari et al., 2013).

Fourier Transform Infrared Spectroscopy (FTIR) is used to determine the chemical composition and the degradation of the polymeric matrix of the carrier. The FTIR provides information about the microparticles' surface composition dependant on the fabricating techniques and conditions. (Capan et al, 2003). Fu et al, (1999) used FTIR to evaluate the secondary structures of bovine serum albumin (BSA) and chicken egg-white lysozyme (LZM).

The encapsulation efficiency drug-loaded MP can be evaluated by allowing the washed MP to undergo lysis (the breakdown of a cell by rupture of the cell wall or cell membrane (Thermofisher.com, 2017). The encapsulation efficiency percentage is calculated by using the following equation:

$$\%\, Entrapment = \frac{Actual\ \ content}{Theoritical\ \ content}\ X\ 100 \qquad \text{Equation 1.1}$$

In vitro and in vivo techniques have been described to determine the release characteristics and permeability of drugs through the cell membrane. In pharmaceutical production, in vitro drug release studies have been used as a quality control procedure. Mahboubian et al, (2010) prepared PLGA MP containing triptorelin and investigated the in vitro controlled release characteristics of the microparticles. Spherical PLGA MP with a 90% encapsulation efficiency and prolonged triptorelin release over 45 days were obtained.

1.5 THESIS OVERVIEW AND HYPOTHESIS

The World Health Organisation, (WHO) projected that at least 2.2 billion people worldwide suffer from near or far vision impairment and blindness (Vision and Blindness impairment, 2021). The majority of people with vision impairment or blindness are over 50 years old, however, vision loss can affect people of all ages. Vision impairment invariably bring, aside the obvious issues, potential emotional and financial implication to patients. It is estimated that the United States of America (USA) and the United Kingdom (UK) alone spend roughly $51.4 billion and £28.1 billon respectively on tackling the effects of vision impairment (CDC.gov, 2021 and Pezzullo et al, 2018). The fourth leading cause of blindness is ocular surface and cornea disorders, and this comes after glaucoma, cataracts and age-related macular degeneration (Vision and Blindness impairment, 2021). The centre of interest in intensive research on acute and chronic wounds is to find an effective treatment.

The location of the cornea makes it susceptible to injuries/damages. Corneal injuries can result from a variety of influences, such as burns, physical or chemical trauma, or exposure to ultraviolet light (UV) (Willman, Fu, and Melanson, 2022). The degree of injury will directly correlate to the length of recovery time and treatment method. Minor cornea damages heal quickly whereas more severe wounds take relatively longer to heal and can cause pain, irritation, tearing and redness (Zidan et al., 2018, Kwok et al., 2019 and Slaughter et al., 2019). Improper healing of the cornea tissues after injury or abrasion can cause serious corneal complication, blindness and the need for corneal transplantation. It is, therefore, crucial to manage and enhance corneal wound healing as the lack of donors and associated side effects such as rejection makes corneal transplants less accessible (Fernández Pérez et al., 2020 and Mathews et al., 2018).

The go-to treatment of chronic cornea disorders is the application of protein-based bandages (Zidan et al, 2018 and Antons-Salea et al, 2020). In general, an ideal biomaterial for ocular bandage should be biocompatible, non-toxic, transparent, comfortable for the patient, easy and quick to

apply, adhere to the ocular tissue, quickly seal the injured area, mimic the mechanical properties of the tissue, be permeable to nutrients and gases, and have a microbial barrier (Santiago et al., 2019, Grinstaff, 2007 and Miki et al., 2002). Additional desirable characteristics includes cost-effectiveness, long storage stability, and the ability to incorporate drugs or biological compounds (Santiago et al., 2019 and Chae et al., 2014). Currently, the most widely used bandage which is made up of natural biomaterial is human amniotic membrane (HAM) (Foulks, 2014, Chau et al, 2012, Rolando et al, 2005 and Zidan et al, 2018). Notwithstanding its clinical outcome, the availability of HAM remains lilted due to its allogeneic nature which causes rejections, extremely expensive, the reliance on donor tissues, presence of tissue banks and medical infrastructures (Lai and Ma, 2013, Murube 2006, Chau et al., 2012 and Leal-Marin et al., 2020). Consequently, there is an active quest for biomaterials to generate an ocular bandage for cornea wound healing.

Unlike the HAM, the Chicken eggshell membrane (ESM) has better mechanical properties and is an inexpensive, excess industrial waste product associated with minimal ethical concerns (Sah et al.,2016). Chicken ESM is a natural biomaterial obtained from chicken egg and it has good biocompatibility, biodegradability and wound-healing properties, and ability to promote cell adhesion (Ohto-Fujita et al., 2018 and Yoo et al., 2015). The soluble and intact ESM has been exploited as a biomaterial for skin wound healing (Choi et al, 2021). The resemblance of the ESM to native tissue, and its high protein and glycoprotein content, make the ESM a highly valued resource in wound healing and capable of providing an ideal environment for tissue healing (Ahmad et al. 2017). Based on these characteristics, the ESM can be exploited as a potential biomaterial for ocular bandage for ocular wounds.

The global demand for chicken eggs is growing rapidly, while production is also increasing. In 2018, global production of eggs was 76.7 million tons, an increase of 14.95% over the past 10 years (Chi et al., 2022 and Shahbandeh, 2020). In 2018, China produced a total of 26.9 million tons of food and agriculture products (Food and Agriculture Organization, 2020). In the same year, the

United States produced 6.46 million tons of eggs, followed by India (5.23 million tons), Mexico (2.87 million tons), Brazil (2.66 million tons) and Japan (2.62 million tons). The increase in egg production worldwide is due to its high global consumption and egg consumption is estimated to rise by 50% up to 2035. This is due to its lower price compared to other protein sources and the perceived health benefits (Sass et al., 2021 and Chi et al., 2022). Consequently, its essential to exploit the use of eggs outside the food industry so as to minimize waste.

The treatment for ocular wound generally requires the combination of ocular bandages and repeated administration of eye drops at regular time intervals for a longer duration. The major problems with eye drops are poor retention in the eye, low bioavailability across the cornea and ocular adverse effects including wound-healing complications. Polymer-based microparticulate systems are often used in therapeutic applications as controlled and sustained release carriers for drugs and growth factors to improve the duration of effect and may be combined within a bandage to allow a prolonged retention at the site of action (Williams, 2009).

Poly lactic-co-glycolic acid (PLGA) is a synthetic polymer that has been widely studied and used in the formulation microparticles for the controlled and sustained release of drugs (Bible et al, 2009). The single emulsion oil-in-water (O/W) evaporation method is often used for the preparation of MP, but with many processing variables present, it is difficult to predict the size of the final products. Particle size is a significant characteristic as it determines the profile of the drug release and dictates the routes of administration (e.g., topical or injection) (Bible et al,2009). Taguchi design is a statistical technique used to optimize parameters with interrelationships and its design protocol attempts to identify controllable factors that minimize the effect of "noise" (i.e., uncontrollable factors) (Montgomery, 1999).

Notwithstanding these promising results, the application of ESM to heal the cornea remain generally unexploited. Therefore, based on the impact of ESM as biomaterial in skin wound healing application, physical and chemical characteristics similarities with HAM, ESM was

exploited in this thesis as a potential biomaterial for ocular/cornea bandage. This study aimed to formulate and evaluate a potential novel bandage comprised of drug-incorporated MP and ESM for ocular wound healing applications (Figure 1.1).

Chapter 1 of the thesis reviews the literature on the ocular wound healing application and ocular drug delivery. Chapter 2 entails development and characterization of ESM to be used as a wound bandage. Chapter 3 concentrates on the fabrication and optimisation, consequently, engage in the fabrication of drug – incorporated microparticles to achieve the desired release profile. The formation of wound bandage consisting of the drug–incorporated microparticles and the ESM is shown in chapter 4. Finally, chapter 5 presents the summary discussion and conclusion of the research described in the thesis and recommendations for future work

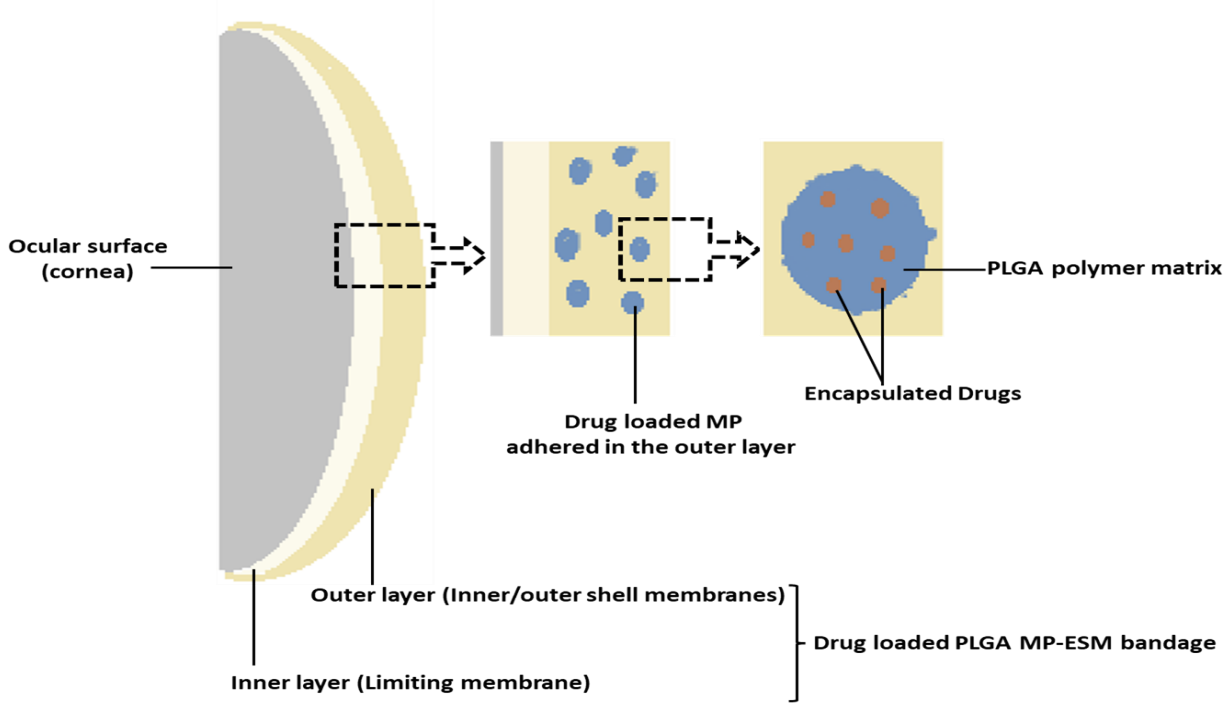

Figure 1.11. Schematic representation of the proposed biomedical bandage
This diagram illustrates the objective of the study. It shows the generated bandage for ocular wound healing consisting of drug loaded PLGA microparticles and Eggshell membrane. MP – microparticles, ESM -eggshell membrane and PLGA- Poly lactic-co-glycolic acid.

1.6 **REFERENCES**

Aagaard-Tillery, K., Silver, R. and Dalton, J. (2006). Immunology of normal pregnancy. Seminars in Fetal and Neonatal Medicine, 11(5), pp.279-295.

Ahlborn, G. and Sheldon, b. (2006). Identifying the components in eggshell membrane responsible for reducing the heat resistance of bacterial pathogens. Journal of food protection, 69(4), pp.729-738.

Ahlborn, G., Clare, D., Sheldon, B. and Kelly, R. (2006). Identification of Eggshell Membrane Proteins and Purification of Ovotransferrin and β-NAGase from Hen Egg White. The Protein Journal, 25(1), pp.71-81.

Airavind Chakrapan, M. (2006). Processing and characterization of polymer microparticles for controlled drug delivery systems. Ph.d. The ohio state university.

Aran, K. (2012). Development of microfluidic platform for continuous extraction of diagnostics plasma proteins from whole blood during cardiac surgery.

Arias, J., Gonzalez, A., Fernandez, M., Gonzalez, C., Saez, D. and Arias, J. (2008). Eggshell membrane as a biodegradable bone regeneration inhibitor. Journal of Tissue Engineering and Regenerative Medicine, 2(4), pp.228-235.

Armbruster, C., Schneider, M., Schumann, S., Gamerdinger, K., Cuevas, M., Rausch, S., Baaken, G. and Guttmann, J. (2009). Characteristics of highly flexible PDMS membranes for long-term mechanostimulation of biological tissue. Journal of Biomedical Materials Research Part B: Applied Biomaterials, 91B(2), pp.700-705.

Avadhanam VS, Smith HE, Liu C. Keratoprostheses for corneal blindness: a review of contemporary devices. Clin Ophthalmol. 2015 Apr 16;9:697-720. doi: 10.2147/OPTH.S27083. PMID: 25945031; PMCID: PMC4406263.

Baker, J. and Balch, D. (1962). A study of the organic material of hen's-egg shell. Biochemical Journal, 82(2), pp.352-361.

Baláž, M. (2014). Eggshell membrane biomaterial as a platform for applications in materials science. Acta Biomaterialia, 10(9), pp.3827-3843.

Balazs, E. (1973). The Vitreous. International Ophthalmology Clinics, 13(3), pp.169-187.

Bélanger, M. and Marois, Y. (2001). Hemocompatibility, biocompatibility, inflammatory andin vivostudies of primary reference materials low-density polyethylene and polydimethylsiloxane: A review. Journal of Biomedical Materials Research, 58(5), pp.467-477.

Belhamri, S. and Hamdadou, N. (2016). Concentration influence on structural and optical properties of SnO2 thin films synthesized by the spin coating technique. Journal of Physics: Conference Series, 758, p.012007.

Bellairs, R. and Boyde, A. (1969). Scanning electron microscopy of the shell membranes of the hen's egg. Zeitschrift for Zellforschung und Mikroskopische Anatomie, 96(2), pp.237-249.

Benson, K., Ruff, K. and Jensen, G. (2012). Effects of Natural Eggshell Membrane (NEM) on Cytokine Production in Cultures of Peripheral Blood Mononuclear Cells: Increased Suppression of Tumor Necrosis Factor-αLevels After In VitroDigestion. Journal of Medicinal Food, 15(4), pp.360-368.

Bible, E., Chau, D., Alexander, M., Price, J., Shakesheff, K. and Modo, M. (2009). Attachment of stem cells to scaffold particles for intra-cerebral transplantation. Nature Protocols, 4(10), pp.1440-1453.

Bible, E., Chau, D., Alexander, M., Price, J., Shakesheff, K. and Modo, M. (2009). Attachment of stem cells to scaffold particles for intra-cerebral transplantation. Nature Protocols, 4(10), pp.1440-1453.

Bodmeier, R. and McGinity, J. (1988). Solvent selection in the preparation of poly(dl-lactide) microspheres prepared by the solvent evaporation method. International Journal of Pharmaceutics, 43(1-2), pp.179-186.

Bourke, S., Al-Khalili, M., Briggs, T., Michniak, B., Kohn, J. and Poole-Warren, L. (2003). A photo-crosslinked poly(vinyl alcohol) hydrogel growth factor release vehicle for wound healing applications. AAPS PharmSci, 5(4), pp.101-111.

Cao, J. and Jager, M. (2015). Animal Eye Models for Uveal Melanoma. Ocular Oncology and Pathology, 1(3), pp.141-150.

Cen, L., Liu, W., Cui, L., Zhang, W. and Cao, Y. (2008). Collagen Tissue Engineering: Development of Novel Biomaterials and Applications. Pediatric Research, 63(5), pp.492-496.

Chang-Lin, J., Attar, M., Acheampong, A., Robinson, M., Whitcup, S., Kuppermann, B. and Welty, D. (2011). Pharmacokinetics and Pharmacodynamics of a Sustained-Release Dexamethasone Intravitreal Implant. Investigative Opthalmology and Visual Science, 52(1), p.80.

Chang-Lin, J., Burke, J., Peng, Q., Lin, T., Orilla, W., Ghosn, C., Zhang, K., Kuppermann, B., Robinson, M., Whitcup, S. and Welty, D. (2011). Pharmacokinetics of a Sustained-Release Dexamethasone Intravitreal Implant in Vitrectomized and Nonvitrectomized Eyes. Investigative Opthalmology and Visual Science, 52(7), p.4605.

Chau, D., Brown, S., Mather, M., Hutter, V., Tint, N., Dua, H., Rose, F. and Ghaemmaghami, A. (2012). Tissue transglutaminase (TG-2) modified amniotic membrane: a novel scaffold for biomedical applications. Biomedical Materials, 7(4), p.045011.

Chau, D., Tint, N., Collighan, R., Griffin, M., Dua, H., Shakesheff, K. and Rose, F. (2010). The visualisation of vitreous using surface modified poly(lactic-co-glycolic acid) microparticles. British Journal of Ophthalmology, 94(5), pp.648-653.

Chiang, W. and Chang, D. (1995). Preparation and characterization of polyurethanes/allyl novolac resin simultaneous interpenetrating network. European Polymer Journal, 31(8), pp.709-714.

Coates, N. (1988). Determinants of Japan's business success: Some Japanese executives. Academy of Management Executive, 2(1), pp.69-72.

Dalrymple, J. (1989). The anatomy of the human eye. Birmingham, Ala.: Classics of Ophlthalmology Library, Division of Gryphon Editions.

Devi, P., Banerjee, S., Chowdhury, S. and Kumar, G. (2012). Eggshell membrane: a natural biotemplate to synthesize fluorescent gold nanoparticles. RSC Advances, 2(30), p.11578.

Dua, H., Faraj, L., Said, D., Gray, T. and Lowe, J. (2013). Human Corneal Anatomy Redefined. Ophthalmology, 120(9), pp.1778-1785.

Dupps, W. and Wilson, S. (2006). Biomechanics and wound healing in the cornea. Experimental Eye Research, 83(4), pp.709-720.

Exploratorium: the museum of science, art and human perception. (2017). Science of Eggs: Making Naked Eggs Activity | Exploratorium. [online] Available at: https://www.exploratorium.edu/cooking/eggs/activity-naked.html [Accessed 21 Aug. 2017].

Eze, B.I., Chuka-Okosa, C.M. and Uche, J.N. Traditional eye medicine use by newly presenting ophthalmic patients to a teaching hospital in south-eastern Nigeria: socio-demographic and clinical correlates. BMC Complement Altern Med 9, 40 (2009). https://doi.org/10.1186/1472-6882-9-40

Furgiuele, F. (1978). Eye and Eyelid Infections. Drugs, 15(4), pp.310-316.

Giri, T., Choudhary, C., Ajazuddin, Alexander, A., Badwaik, H. and Tripathi, D. (2013). Prospects of pharmaceuticals and biopharmaceuticals loaded microparticles prepared by

double emulsion technique for controlled delivery. Saudi Pharmaceutical Journal, 21(2), pp.125-141.

Glowacki, J. and Mizuno, S. (2008). Collagen scaffolds for tissue engineering. Biopolymers, 89(5), pp.338-344.

Guo, X., Zhang, F., Peng, Q., Xu, S., Lei, X., Evans, D. and Duan, X. (2011). Layered double hydroxide/eggshell membrane: An inorganic biocomposite membrane as an efficient adsorbent for Cr(VI) removal. Chemical Engineering Journal, 166(1), pp.81-87.

Holland, Gráinne & Pandit, Abhay & Sánchez-Abella, Laura & Haiek, Andrea & Loinaz, Iraida & Dupin, Damien & Gonzalez, Maria & Larra, Eva & Bidaguren, Aritz & Lagali, Neil & Moloney, Elizabeth & Ritter, Thomas. (2021). Artificial Cornea: Past, Current, and Future Directions. Frontiers in Medicine. 8. 770780. 10.3389/fmed.2021.770780.

Hickey, T., Kreutzer, D., Burgess, D. and Moussy, F. (2002). Dexamethasone/PLGA microspheres for continuous delivery of an anti-inflammatory drug for implantable medical devices. Biomaterials, 23(7), pp.1649-1656.

Hiroshi, Y. 1986. The Strength and Aging of Human Body. Qing Hai People Publishing House, pp. 169–170.

Ishikawa, S., Suyama, K. and Satoh, I. (1999). Biosorption of Actinides from Dilute Waste Actinide Solution by Egg-Shell Membrane. Applied Biochemistry and Biotechnology, 78(1-3), pp.521-534.

Ishikawa, S., Suyama, K. and Satoh, I. (1999). Biosorption of Actinides from Dilute Waste Actinide Solution by Egg-Shell Membrane. Applied Biochemistry and Biotechnology, 78(1-3), pp.521-534.

Kadler, K. (2008). Extracellular matrix (ECM) research. Methods, 45(1), p.1.

Kemala, T., Budianto, E. and Soegiyono, B. (2012). Preparation and characterization of microspheres based on blend of poly(lactic acid) and poly(ε-caprolactone) with poly(vinyl alcohol) as emulsifier. Arabian Journal of Chemistry, 5(1), pp.103-108.

K, D. (1987). Microparticulate Drug Delivery Systems as an Adjunct to Cancer Treatment. Cancer Drug Delivery, 4(1), pp.55-61.

Khaled, K., Sarhan, H., Ibrahim, M., Ali, A. and Naguib, Y. (2010). Prednisolone-Loaded PLGA Microspheres. In Vitro Characterization and In Vivo Application in Adjuvant-Induced Arthritis in Mice. AAPS PharmSciTech, 11(2), pp.859-869.

Kim, K., Kim, S. and Kim, H. (2005). Applying the Taguchi method to the optimization for the synthesis of TiO2 nanoparticles by hydrolysis of TEOT in micelles. Colloids and Surfaces A: Physicochemical and Engineering Aspects, 254(1-3), pp.99-105.

Krishnamoorthy, K. and Mahalingam, M. (2015). Fabrication and optimization of camptothecin loaded Eudragit S 100 nanoparticles by Taguchi L4 orthogonal array design. International Journal of Pharmaceutical Investigation, 5(3), p.147.

Lai, M. and Tsiang, R. (2005). Microencapsulation of acetaminophen into poly(L-lactide) by three different emulsion solvent-evaporation methods. Journal of Microencapsulation, 22(3), pp.261-274.

Langer, R. and Vacanti, J. (1993). Tissue engineering. Science, 260(5110), pp.920-926.

Lee, S., Grass, G., Kim, G., Dresbach, C., Zhang, L., Gösele, U. and Knez, M. (2009). Low-temperature ZnO atomic layer deposition on biotemplates: flexible photocatalytic ZnO structures from eggshell membranes. Physical Chemistry Chemical Physics, 11(19), p.3608.

Lens, A., Nemeth, S. and Ledford, J. (2008). Ocular anatomy and physiology. Thorofare, NJ: SLACK.

Li, N., Niu, L., Qi, Y., Yiu, C., Ryou, H., Arola, D., Chen, J., Pashley, D. and Tay, F. (2011). Subtleties of biomineralisation revealed by manipulation of the eggshell membrane. Biomaterials, 32(34), pp.8743-8752.

López-Alemany, A., Compañ, V. and Refojo, M. (2002). Porous structure of Purevision™ versus Focus® NightandDay™ and conventional hydrogel contact lenses. Journal of Biomedical Materials Research, 63(3), pp.319-325.

Los, L. (2008). The rabbit as an animal model for post-natal vitreous matrix differentiation and degeneration. Eye, 22(10), pp.1223-1232.

Lutolf, M., Weber, F., Schmoekel, H., Schense, J., Kohler, T., Müller, R. and Hubbell, J. (2003). Repair of bone defects using synthetic mimetics of collagenous extracellular matrices. Nature Biotechnology, 21(5), pp.513-518.

Mahomed, A., Wolffsohn, J. and Tighe, B. (2016). Structural design of contact lens-based drug delivery systems, in vitro and in vivo studies of ocular triggering mechanisms. Contact Lens and Anterior Eye, 39(2), pp.97-105.

Mindel, J. and Mittag, T. (1977). Variability of choline acetyltransferase in ocular tissues of rabbits, cats, cattle and humans. Experimental Eye Research, 24(1), pp.25-33.

Mohan, R., Bajaj, A. and Gundappa, M. (2017). Human amnion membrane: Potential applications in oral and periodontal field. Journal of International Society of Preventive and Community Dentistry, 7(1), p.15.

Montgomery, D. (1999). Experimental Design for Product and Process Design and Development. Journal of the Royal Statistical Society: Series D (The Statistician), 48(2), pp.159-177.

Mori, Y., Yoshida, H. and Masuda, H. (2012). Particle Size Analysis by Laser Diffraction Method Using Reference Particles. Advanced Materials Research, 508, pp.33-37.

Mori, Y., Yoshida, H. and Masuda, H. (2012). Particle Size Analysis by Laser Diffraction Method Using Reference Particles. Advanced Materials Research, 508, pp.33-37.

Nair, V., Hansen, M. and Shi, J. (2000). statistics in Advanced Manufacturing. Journal of the American Statistical Association, 95(451), pp.1002-1005.

Nalla, A. (2017). Novel herbal drug delivery system - an overview. World Journal of Pharmacy and Pharmaceutical Sciences, pp.369-395.

Narayanan, R., Mungcal, J., Kenney, M., Seigel, G. and Kuppermann, B. (2006). Toxicity of Triamcinolone Acetonide on Retinal Neurosensory and Pigment Epithelial Cells. Investigative Opthalmology and Visual Science, 47(2), p.722.

Nihant, N., Schugens, C., Grandfils, C., Jerome, R. and Teyssie, P. (1995). Polylactide Microparticles Prepared by Double Emulsion-Evaporation. Journal of Colloid and Interface Science, 173(1), pp.55-65.

Ouchi, T., Sasakawa, M., Arimura, H., Toyohara, M. and Ohya, Y. (2004). Preparation of poly[dl-lactide-co-glycolide]-based microspheres containing protein by use of amphiphilic diblock copolymers of depsipeptide and lactide having ionic pendant groups as biodegradable surfactants by W/O/W emulsion method. Polymer, 45(5), pp.1583-1589.

Oyster, C. (2006). The human eye. Sunderland, Mass.: Sinauer Associates.

Patil, S., Papadimitrakopoulos, F. and Burgess, D. (2004). Dexamethasone-Loaded Poly(Lactic-Co-Glycolic) Acid Microspheres/Poly(Vinyl Alcohol) Hydrogel Composite Coatings for Inflammation Control. Diabetes Technology and Therapeutics, 6(6), pp.887-897.

Peppas, N. (1989). Ophthalmic drug delivery: Pharmaceutical, technological and clinical aspects. Journal of Controlled Release, 8(3), pp.275-276.

Pinsky, P.M., Datye, D.V., 1991. A microstructurally based finite element model of the incised

human cornea. Journal of Biomechanics 24, 907–922.

Raunest, J., Hötzinger, H. and Bürrig, K. (1994). Magnetic resonance imaging (MRI) and arthroscopy in the detection of meniscal degenerations: Correlation of arthroscopy and MRI with histology findings. Arthroscopy: The Journal of Arthroscopic and Related Surgery, 10(6), pp.634-640.

Ross, A. (1973). Particle detection and shape discrimination using a laser diffraction method. Optics and Laser Technology, 5(1), p.13.

Rucklidge, G., Milne, G. and Robins, S. (1996). Collagen Type X: A Component of the Surface of Normal Human, Pig, and Rat Articular Cartilage. Biochemical and Biophysical Research Communications, 224(2), pp.297-302.

Sah, M. and Rath, S. (2016). Soluble eggshell membrane: A natural protein to improve the properties of biomaterials used for tissue engineering applications. Materials Science and Engineering: C, 67, pp.807-821.

Sanchez, I., Martin, R., Ussa, F. and Fernandez-Bueno, I. (2011). The parameters of the porcine eyeball. Graefe's Archive for Clinical and Experimental Ophthalmology, 249(4), pp.475-482.

Science of Amniotic Tissue. (2013). [online] Available at: http://www.afcellmedical.comimagesamnioticfluid_chart_large.jpg [Accessed 12 Nov. 2016].

Shapiro, L. and Cohen, S. (1997). Novel alginate sponges for cell culture and transplantation. Biomaterials, 18(8), pp.583-590.

Sharma, A., Pirouzmanesh, A., Patil, J., Estrago-Franco, M., Zacharias, L., Pirouzmanesh, A., Andley, U., Kenney, M. and Kuppermann, B. (2011). Evaluation of the Toxicity of

Triamcinolone Acetonide and Dexamethasone Sodium Phosphate on Human Lens Epithelial Cells (HLE B-3). Journal of Ocular Pharmacology and Therapeutics, 27(3), pp.265-271.

Shi, D. and Gu, H. (2008). Nanostructured Materials for Biomedical Applications. Journal of Nanomaterials, 2008, pp.1-2.

Singh R, Gupta N, Vanathi M, Tandon R. Corneal transplantation in the modern era. Indian J Med Res. 2019 Jul;150(1):7-22. doi: 10.4103/ijmr.IJMR_141_19. PMID: 31571625; PMCID: PMC6798607.

Smolin, G. and Thoft, R. (1983). THE CORNEA-SCIENTIFIC FOUNDATIONS AND CLINICAL PRACTICE. Optometry and Vision Science, 60(11), p.931.

Soledad Fernandez, M., Moya, A., Lopez, L. and Arias, J. (2001). Secretion pattern, ultrastructural localization and function of extracellular matrix molecules involved in eggshell formation. Matrix Biology, 19(8), pp.793-803.

Stanley-Wood, N. and Lines, R. (2007). Particle Size Analysis. [Place of publication not identified]: Royal Society of Chemistry.

Steinberg, D. and Hunter, W. (1984). Experimental Design: Review and Comment. Technometrics, 26(2), p.71.

Torkaman, R., Soltanieh, M. and Kazemian, H. (2010). Optimization of Parameters for Synthesis of MFI Nanoparticles by Taguchi Robust Design. Chemical Engineering and Technology, 33(6), pp.902-910.

Torres, F., Troncoso, O., Piaggio, F. and Hijar, A. (2010). Structure–property relationships of a biopolymer network: The eggshell membrane. Acta Biomaterialia, 6(9), pp.3687-3693.

Travers, B. (1986). A synopsis of the diseases of the eye, and their treatment. Birmingham,

Ala.: The Classics of Ophthalmology Library.

Tsai, W., Yang, J., Lai, C., Cheng, Y., Lin, C. and Yeh, C. (2006). Characterization and adsorption properties of eggshells and eggshell membrane. Bioresource Technology, 97(3), pp.488-493.

Tsai, W., Yang, J., Lai, C., Cheng, Y., Lin, C. and Yeh, C. (2006). Characterization and adsorption properties of eggshells and eggshell membrane. Bioresource Technology, 97(3), pp.488-493.

Wang, S., Wei, M. and Huang, Y. (2013). Biosorption of Multifold Toxic Heavy Metal Ions from Aqueous Water onto Food Residue Eggshell Membrane Functionalized with Ammonium Thioglycolate. Journal of Agricultural and Food Chemistry, 61(21), pp.4988-4996.

Wang, W., Chen, B. and Huang, Y. (2014). Eggshell Membrane-Based Biotemplating of Mixed Hemimicelle/Admicelle as a Solid-Phase Extraction Adsorbent for Carcinogenic Polycyclic Aromatic Hydrocarbons. Journal of Agricultural and Food Chemistry, 62(32), pp.8051-8059.

Wenstrup, R., Smith, S., Florer, J., Zhang, G., Beason, D., Seegmiller, R., Soslowsky, L. and Birk, D. (2011). Regulation of Collagen Fibril Nucleation and Initial Fibril Assembly Involves Coordinate Interactions with Collagens V and XI in Developing Tendon. Journal of Biological Chemistry, 286(23), pp.20455-20465.

Wenstrup, R., Smith, S., Florer, J., Zhang, G., Beason, D., Seegmiller, R., Soslowsky, L. and Birk, D. (2011). Regulation of Collagen Fibril Nucleation and Initial Fibril Assembly Involves Coordinate Interactions with Collagens V and XI in Developing Tendon. Journal of Biological Chemistry, 286(23), pp.20455-20465.

Williams, D. (2009). On the nature of biomaterials. Biomaterials, 30(30), pp.5897-5909.

Williams, P. (2011). Renewable resources for functional polymers and biomaterials. Cambridge: Royal Society of Chemistry.

Wilson, C. (2004). Topical drug delivery in the eye. Experimental Eye Research, 78(3), pp.737-743.

Woo, S.Y., Kobayashi, A.S., Lawrence, C., Schlegel, W.A., 1972. Nonlinear material properties of intact cornea and sclera. Experimental Eye Research 14, 29–39.

Wormald, R. (1995). Assessing the prevalence of eye disease in the community. Eye, 9(6), pp.674-676.

Xu, Q., Hashimoto, M., Dang, T., Hoare, T., Kohane, D., Whitesides, G., Langer, R. and Anderson, D. (2009). Preparation of Monodisperse Biodegradable Polymer Microparticles Using a Microfluidic Flow-Focusing Device for Controlled Drug Delivery. Small, 5(13), pp.1575-1581.

Yadav, T. (2013). MICROSPHERES AS AN OCULAR DRUG DELIVERY SYSTEM- A REVIEW. Journal of Drug Delivery and Therapeutics, 3(1).

Yang, R., Mather, R. and Fotheringham, A. (2011). The influence of processing parameters on the structural and mechanical properties of drawn polypropylene fibres: A factorial design approach. Journal of Applied Polymer Science, 124(5), pp.3606-3616.

CHAPTER 2: DEVELOPMENT, OPTIMIZATION & CHARACTERIZATION OF EGGSHELL MEMBRANE

2.0 CHAPTER 2: DEVELOPMENT, OPTIMIZATION & CHARACTERIZATION OF EGGSHELL MEMBRANE

2.1 INTRODUCTION

The cornea is responsible for maintaining a tough, physical barrier between the eye and the environment. The cornea is susceptible to eye injuries caused by physical, chemical trauma or severe infections which can lead to permanent damage to the tissue and potential blindness. (Cavanagh, 2002; Foulks, 2014; Litwiniuk and Grzela, 2014). Therefore, it is important to restore the cornea structure quickly after injury to prevent permanent loss of vision. The most used biological material to repair or regenerate the cornea is the human amniotic membrane. (HAM). However, the use of HAM has some limitations such as variation in thickness, mechanical strength and transparency of the membrane in different parts of the membrane, differences between donors and donors, use of drugs/anti-rejection therapy, ethics and local regulatory constraints (Fujishima et al, 1998; Dalla Pozza et al, 2005; Barabino et al, 2003; Azuara-Blanco et al, 1999 and Tsubota et al, 1996). In addition, the cost of serological testing, processing and preserving of the AM is relatively expensive.

The ESM is a unique biomaterial with many benefits that are often undervalued. However, researchers have made important findings in studying this biomaterial due to its unique properties and specific structure (Boonprasert and Tangboriboon, 2018; Chi and Zhao, 2009; Ahmed et al, 2019; Wu et al, 2004; Chen, Kang and Sukigara, 2014; Choi, Kim, Su and Han 2021 and Tan et al. 2011). The ESM is a highly collagenised semi-permeable membrane composed of insoluble protein fibres, mainly composed of collagen types I, V and X, forming a lattice network (Choi et al.,2017) (Torres et al., 2010) (Yi et al., 2004). The ESM plays a vital role in the mineralisation of the eggshell while preventing the mineralisation of the inner egg content (Hincke, 2012) (Arias et al., 199). The ESM is insoluble due to the inter-fibrillar

crosslinks, allowing the ESM to support the embryo during development (Yi, et al.,2005) (Takahashi et al. 1996) (Starcher et al., 1980).

As discussed in chapter 1, the ability to separate ESM successfully from the ES is a vital procedure for its extensive use as a biomaterial (Chi and Zhao, 2009; Tang et al, 2014 and Torres et al, 2010). The extraction of the membrane from the ES has been investigated in several reports: direct manual peeling of membrane from the shell is one of the methods reported to be efficient in preparing ESM despite the fact that the outer membrane remains strongly bonded to the shell (Rolando et al, 2005; Zidan et al, 2018 and Rahman et al, 2009). Alternatively, the ES could be exposed to a solvent- essentially, an acidic treatment could be applied to the ES which acts on its surface by dissolving the calcium carbonate within the shell and loosening the interfacial bonding between outer shell membrane and the ES. These methods generate ESM in its intact form to aid in manipulation into preferred size and shape.

Translational applications of the ESM as a biomaterial can be supported by its chemical composition and physical/mechanical characteristics. However, the uptake of its use as a wound healing agent, in the form of a bioactive dressing for ocular applications, has been limited to date. Despite a very limited summary on the first use of the ESM in ophthalmology in 1899, when Coover successfully used it in a surgical procedure as a bandage for corneal ulcer, to date, no other research data or studies on the direct use of ESM in ophthlamic application have been reported. Accordingly, with the increase incidents of ocular disease, trauma, tissue replacement and pharmaceutical drug development, the exploitation of the ESM for corneal wound healing may have been overlooked. As such, this chapter emphases on investigating the development of a novel protocol, using acetic acid and ethylenediaminetetraacetic acid (EDTA), to extract the eggshell membrane and, thereafter, to evaluate their physical, mechanical and biological properties in the context of translational ocular surface (cornea) therapeutic applications.

2.2 MATERIALS

Free-range, brown, chicken eggs (British Blacktail, gallus galuus) were purchased from a local supermarket (Waitrose, London, UK). Acetic acid, ≥99% was purchased from Fisher Scientific limited (Loughborough, Leicester, UK). Ethylenediaminetetraacetic acid (EDTA), hexamethyldisilane, ≥99%, (HMDS), cacodylate buffer, 0.1M (CAB), 0.25% (v/v) trypsin-EDTA, 100mM L-glutamine, Antibiotic-Antimycotic (AbAm), M199 medium, Giemsa stain and May-Grunwald stain were obtained from Merck (Poole, Dorset, UK). Glutaraldehyde was supplied by Agar Scientific (Stansted, Essex, UK). Epilife Medium with calcium and Human Keratinocyte Growth Supplement (HKGS) were purchased from Invitrogen Life Technologies (ThermoFisher, Leicester, UK). SV40 Immortalised Corneal Epithelial Cell Line (ihCEC) and mesenchymal stem cell- corneal stromal (MSC-C) were in-kind contributions provided Dr Laura Sidney (Tissue Culture Bank, Faculty of Medicine and Health Sciences, Queen's Medical Centre Nottingham University, Nottingham, UK). Immortalised human retinal pigment epithelial cells, ARPE-19 (ATCC® CRL-2302™) were purchased from LGC Standards (Teddington, Middlesex, UK). CellTiter 96® AQueous One Solution Cell Proliferation assay (i.e., MTS Tetrazolium assay) and the CytoTox-ONE™ Homogeneous Membrane Integrity assay kits (i.e., LDH assay) were obtained from Promega (Southampton, Hampshire, UK). Fertilized hens' eggs were purchased from Henry Stewart and Co Ltd (Norfolk, UK). All other reagents and chemicals were obtained from Merck (Poole, Dorset, UK) unless otherwise stated.

2.3 METHODS

2.3.1 Membrane extraction

A preliminary study was performed to obtain the optimised concentrations of the acidic solutions and durations for the extraction of ESM. Fresh eggs were washed carefully with DI water before incubating them at room temperature (~19 °C), submerged, in 0.5 M, 0.9 M or 1.8 M acetic acid or 0.2 M, 0.5 M or 0.9 M EDTA. After the complete dissolution of the calcium carbonate shell by visual observation, the extracted membranes (Table 2.1 and 2.2) were collected and washed in DI thoroughly to remove the albumen and yolk (Figure 2.1). As a control, the ESM was stripped off manually from the eggshell using tweezers (ESMstrip) (Figure 2.1). All resulting extracted ESM samples were fully immersed in Phosphate buffered saline (PBS) in order to avoid dehydration and stored in a refrigerator (4 ºC) before use. All experiments were performed with ESM samples that had not been stored for longer than 72 hours.

Table 2.1. Extraction of Eggshell membrane by different concentration of acetic acid

Molarity (M)	Acetic acid (v/v)	Name of extracted ESM
0.5	3%	ESM- A0.5
0.9	5%	ESM- A0.9
1.8	10%	ESM- A1.8

Table 2.2. Extraction of Eggshell membrane by different concentration of EDTA

Molarity (M)	EDTA (w/v)	Name of extracted ESM
0.2	6%	ESM- E0.2
0.5	15%	ESM- E0.5
0.9	26%	ESM- E0.9

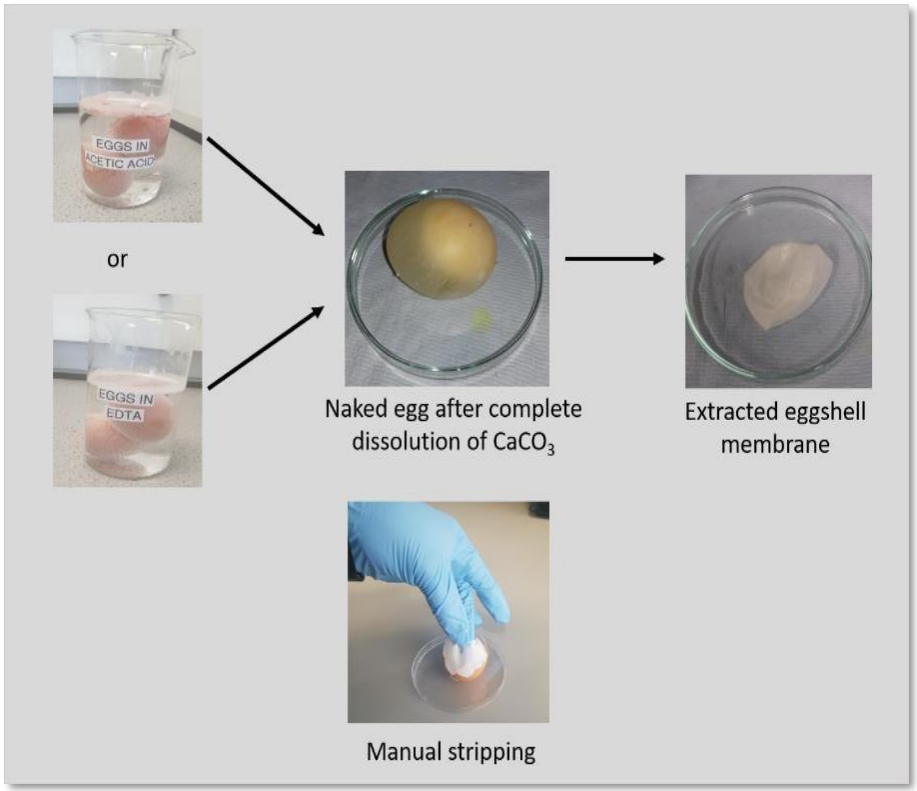

Figure 2.1. Photographic overview of the different protocol.
Unfertilised chicken egg was immersed in acetic acid or EDTA for complete dissolution of the $CaCO_3$ in the shell to expose the naked membrane. The yolk and albumen removed and washed with DI water. The manual stripping method involves carefully removing the shell with tweezers. All these processes were done at room temperature (~19° C).

2.3.2 Membrane characterisation

2.3.2.1 Thickness

The thickness of the extracted membranes was measured by placing the membranes (dabbed "dry" using paper towel to remove excess water) between two microscopic slides of known thickness. The measurements of the total sandwich were taken to the nearest 0.01 mm using Moore and Wright Outside micrometre (Zoro, Leicester, UK) (Figure 2.2). The thickness of each membrane was measured at six random locations and the average values were reported to be the membrane thickness.

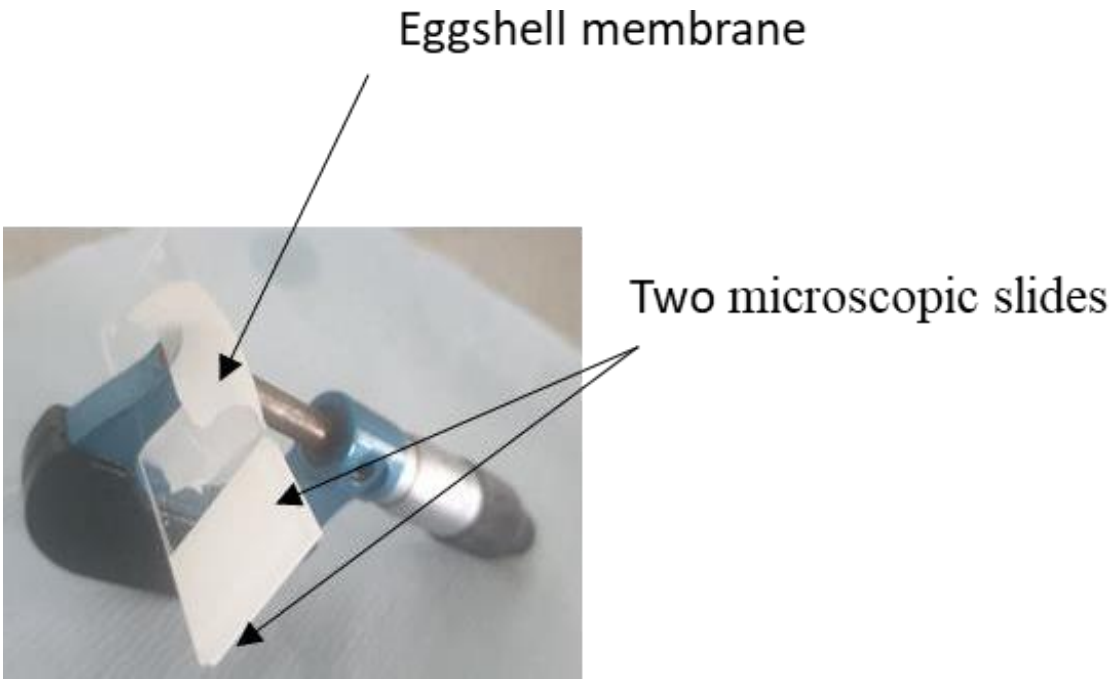

Figure 2.2. Set up for the measurement of thickness of the extracted membranes.
The wet ESM samples were placed between two microscopic slides with known thickness. The total thickness was taken, and the thickness of the ESM samples was deduced by subtracting the thickness of the two microscopic slides from the total thickness measured.

2.3.2.2 Optical properties

ESM samples were soaked in PBS for 24 hours to equilibrate before their transparency characteristics were assessed using two different techniques. In the first case, wet membranes were placed over a standardised waterproof test card and the images of the inner and outer surfaces of each membrane were taken using a 12 MP Super Speed Dual Pixel AF sensor

camera (OIS, FOV: 77˚, Dual Aperture: F1.5 mode/ F2.4 mode) on the Samsung Galaxy S9 plus cell phone (protocol adapted from Chau et al, 2012). In contrast, the second assessment technique was based on the measurement of light transmittance through the wet membranes and determined using a T80 UV-VIS spectrophotometer (PG instrument Ltd., Leicester, UK) at a wavelength range from 400 to 1000 nm. The setup is shown in Figure 2.3 below.

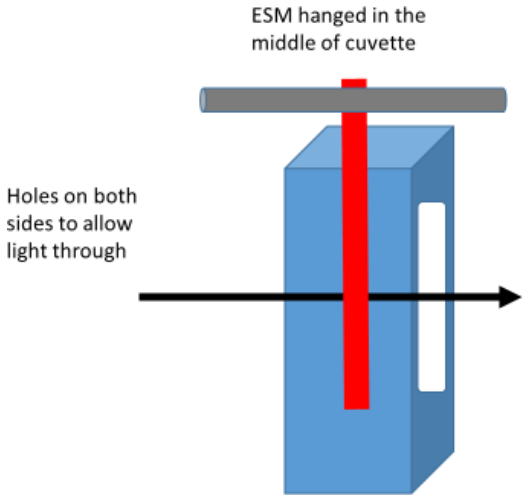

Figure 2.3. Setup for the measurements of light transmittance through extracted membrane. Holes were created in both sides of a cuvette to allow the transmit of light through the wet ESM samples. The samples were attached to the middle of the cuvette. The light transmitted through the holes and the ESM samples was measured using a T80 UV-VIS spectrophotometer (PG instrument Ltd., Leicester, UK) at wavelengths ranging from 400 to 1000 nm.

Structural and morphological analysis

The surface morphologies and characteristics of the outer and inner sides of each extracted membranes were obtained using field emission scanning electron microscope, FESEM, (Philips XL30, UK) with operation voltage of 5kV, spot size 3. Before examination, membranes were fixed in 3% (w/v) glutaraldehyde in 0.1 M cacodylate buffer for 24 hours at 4º C (Figure 2.4a). The fixed membranes were then dehydrated in a series of graded ethyl alcohol solutions for 2 minutes each: 1 x 70%, 1 x 90% and 3 x 100%. Thereafter, the membranes were critical point dried by immersing in Hexamethyldisilane (HMDS) for 2 minutes. The dried membranes were attached onto adhesive 12 mm carbon tabs (Agar Scientific, Stansted, UK)

which were pre-mounted onto 0.5 aluminium spectrum stubs (Agar Scientific, UK) before being sputter-coated with gold/palladium (Polaron E500, Quorum Technology, UK) (Figure 2.4b and c). Morphologies of the membranes were analysed at magnification of 500x and 2000x. The surface roughness and fibre diameter were analysed via Fiji-ImageJ software and OriginLab Origin software 2021.

Figure 2.4. Photographs of treatment of ESM samples for Scanning electronic microscopy
a) ESM samples fixed in 3% (w/v) glutaraldehyde in 0.1 M cacodylate buffer for 24 hours at 4º C. b) Critical point dried ESM samples mounted onto 0.5 aluminium spectrum stubs. c) Gold/palladium coated ESM samples loaded in the field emission scanning electron microscope for image analysis.

In addition, the elemental composition of each of inner and outer sides of the extracted membranes was analysed by FESEM with energy dispersive X-ray (EDX) attachment operating at an accelerating voltage of 15 kV, spot size 5. The ESM samples loaded in the FESEM were bombarded with electron beam. The x-rays released from the samples were detected to characterise the elemental composition of the ESM samples. The spectrum of x-ray emitted were counted at 6 different sites of interest on each ESM samples (Figure 2.5)

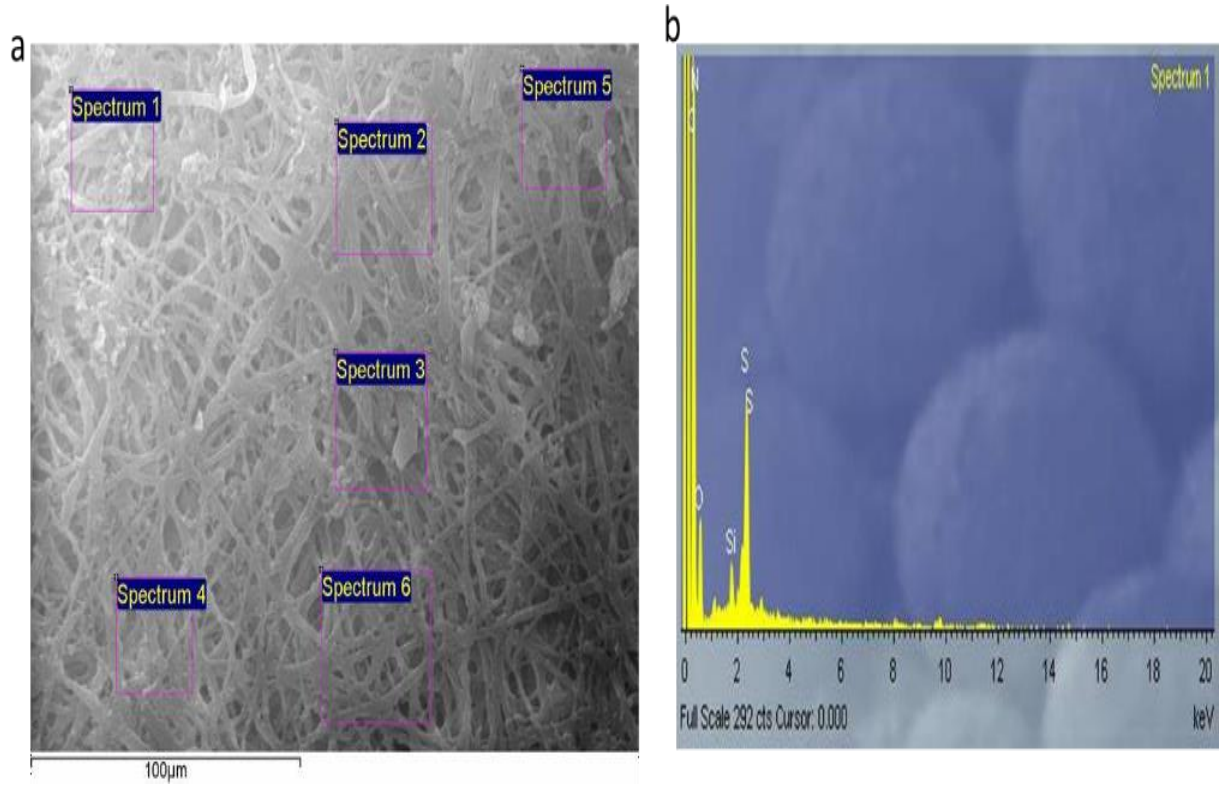

Figure 2.5. Energy dispersive spectroscopy
(a) SEM image of the outer side (fibrous network) of extracted membranes showing the inner shell membrane and the 6 site of interest for taking the spectrum of the emitted x-ray. (b) example of the spectrum generated at site interest 1 to evaluate the elemental chemical composition of the ESM samples.

2.3.2.3 Fourier-transform infrared spectroscopy.

The elements and functional groups of the ESM samples were determined using PerkinElmer Fourier-transform infrared spectroscopy (FTIR) operating in the Attenuated Total Reflectance mode (SensIR Technologies, UK). The samples were scanned in the IR range from 600 to

4000 cm^{-1} (scan rate) and determined at 20 ºC. The spectrometer was calibrated by taking a background spectrum before analysing the extracted membranes.

2.3.2.4 Texture analysis

2.3.2.4.1 Compression properties.

The burst strength of the wet membranes was measured by attaching a film support rig to the Texture Analyser TA. XT (StableMicro Systems Ltd, Surrey UK) (Figure 2.6a). The test membrane (the outer and inner sides of each membrane) was supported between plates which exposed a circular section of the membrane (size = 2 cm^2). The test was performed by initially moving the ball probe at a pre-test speed at 2 mm/s. When the probe reached the surface of the membrane and a trigger force of 5 g was obtained, the speed of the probe was changed to 1 mm/s which initiated the actual test protocol. As the probe deflected the test membrane, the forced was increased until the rupture of the membrane was achieved. The maximum force representing the burst strength was recorded and the distance to burst was recorded as the displacement (Gocek and Adanur, 2012). All experiments were replicated 6 times and conducted at room temperature (~19 °C).

2.3.2.4.2 Tension properties.

The ultimate tensile strength, elongation at break and Young's modulus of the ESM samples were measured using a tensile grip (Figure 2.6b) attached to Texture Analyser TA. XT (StableMicro Systems Ltd, Surrey UK) with a 5 Kg load cell at 1, 3 or 10 mm/sec and *Texture Exponent* software 32 for data evaluation. Prior to analyses, samples were cut into a bone shape with height and length as 25 x 10 mm respectively. Each test membrane was supported by a standard sandpaper to enhance friction and to prevent slipping in between the grips during the analyses before being carefully placed in between the two grips and the sandwich was then screwed tightly together. The extension of test sample caused an increase in force. Data were recorded when the force equaled the trigger force (Torres et al, 2010; Mallakpour and Madani, 2016; Strinkova et al, 2016). The tensile properties and ultimate tensile strength were obtained

from the TA machine and Young's modulus was calculated using equation 2.1 as stated below (Ahmed and Boateng, 2018).

$$\text{Young's modulus (MPa)} = \frac{\text{Slope}}{\text{Membrane thickness x speed (mm/sec)}} x100 \qquad \text{Equation 2.1}$$

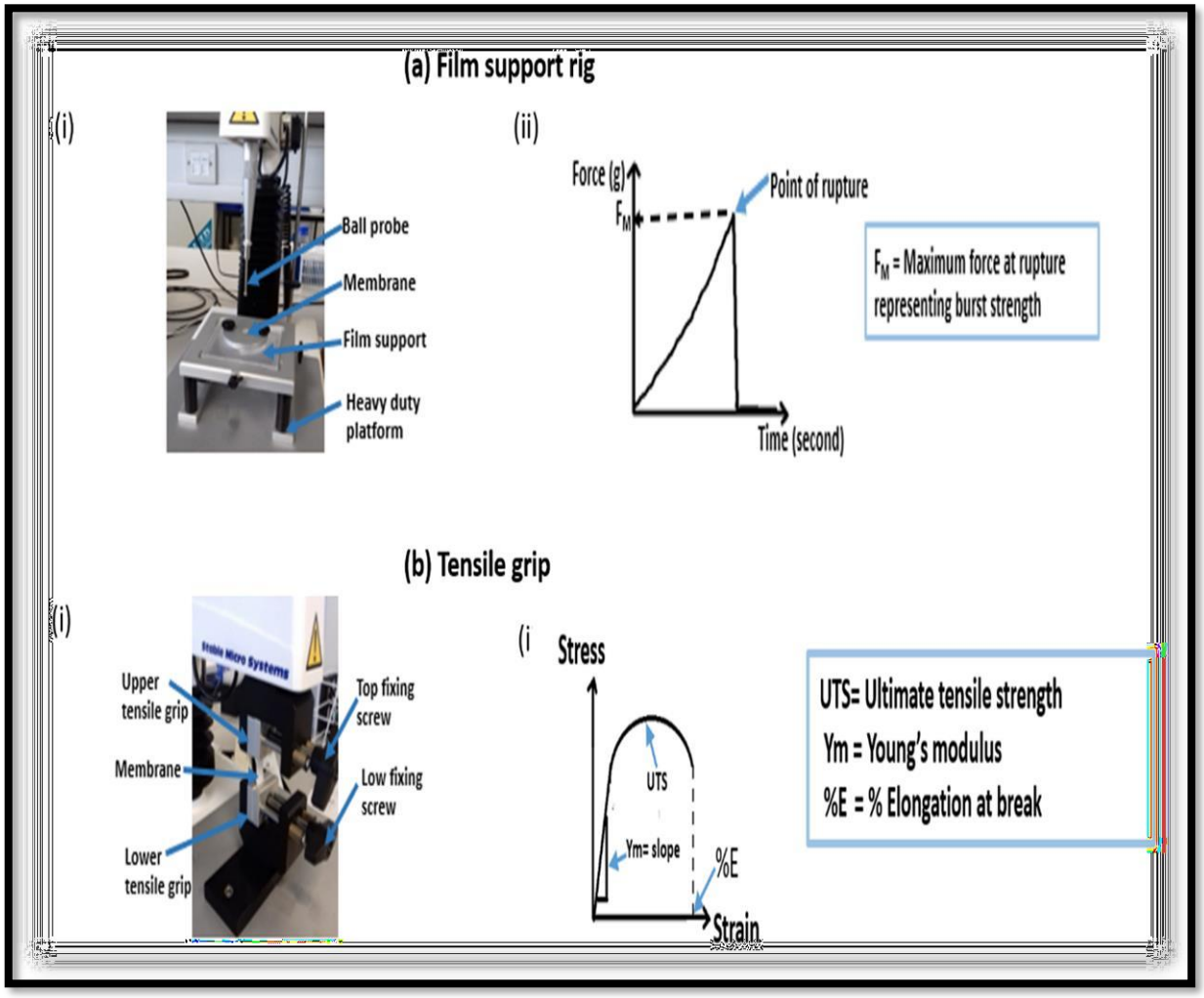

Figure 2.6. Mechanical properties measurements.
(ai) A film support rig attached to TA. XT instrument (StableMicro Systems Ltd, Surrey UK) measured the burst strength of the membranes. The rig is aligned with the ball probe to ensure the probe moves carefully through the test membrane without touching the film support rig. As the probe deflected the test membrane, the forced increased till the rupture of the test membrane. The maximum force representing the burst strength was recorded. (a ii) Graphical representation of a typical burst strength test from texture analyser film support rig. (b i) Tensile grip attached to TA. XT instrument measured the tensile strength and the extensibility of the test membranes. The test membranes were clamped securely. Data were recorded when the force equaled the trigger force. (b ii) Graphical representation of typical stress and strain curve generated from tensile measurement.

2.3.2.5 Porosity.

The fluid handling property of the membranes were assessed by determining the porosity using displacement method described by Ahmed and Boateng, 2018 with a slight modification. Membranes were air dried, at room temperature (~19 °C), for 24 hours and weighed. The dried samples were then immersed in 5 ml of PBS, at 34 ºC, for 24 hours and weighed after dabbing the surfaces with paper towel. The average thickness (mm) and effective area (mm^2) of the membranes were employed to determine the total pore volume. The membrane porosity (ε) was calculated using equation 2.2 as stated below (n=6).

$$\text{Porosity}, \varepsilon\ (\%) = \frac{(Wet\ weight - Dry\ weight)}{(Density\ of\ PBS\ x\ total\ pore\ volume)}\ x100 \qquad \text{Equation 2.2}$$

2.3.2.6 Fluid absorption

The extracted membranes were cut into 2 x 2 cm squares and air dried at room temperature (~19 °C) for 24 hours. Membranes were weighed to the nearest 0.1 mg. The fluid absorption (FA) of each membrane was determined by immersing the samples in 5 ml of PBS, at 34 ºC, for an hour and 24 hours. After 1 h and 24 h, the membranes were carefully blotted using paper towel to remove excess PBS and weighed. Each measurement was repeated 6 times. The FA was calculated using equation 2.3 as stated below:

$$Fluid\ absorption, FA\ (\%) = \frac{(Wet\ weight - Dry\ weight)}{(Dry\ weight)}\ x100 \qquad \text{Equation 2.3}$$

2.3.2.7 Thermogravimateric analysis.

The thermal decomposition profile of the extracted membranes was analysed using a 2050 TA thermogravimetric analyser (TGA) (TA instruments, Crawley, UK). The weighed membranes (5-10mg) were placed into aluminium pans and then deposited within the TGA instrument sample chamber. Each membrane was subjected to a heating profile of 17 to 150 ºC at a rate of 10 ºC/min, under 20 ml/min nitrogen flow. Weight loss of each membrane was deduced from a standardised TGA analysis protocol (Gohari et al, 2014).

2.2.3.9 Contact angle measurements.

Hydrophilicity of the ESM samples was determined by measuring the contact angles (CA) of both the outer and inner surfaces using the static sessile drop method as previously described (Gohari et al, 2014). In short, a small droplet of PBS solution (~2.0 µL) was deposited on the horizontal membrane surface and a side view photo was taken using 200 CAM optical contact angle meter (KSV Instruments Ltd, Finland) at room temperature (~19° C) to measure the contact angle at 10 seconds (Figure 2.6). The experiments were repeated three times and mean value calculated.

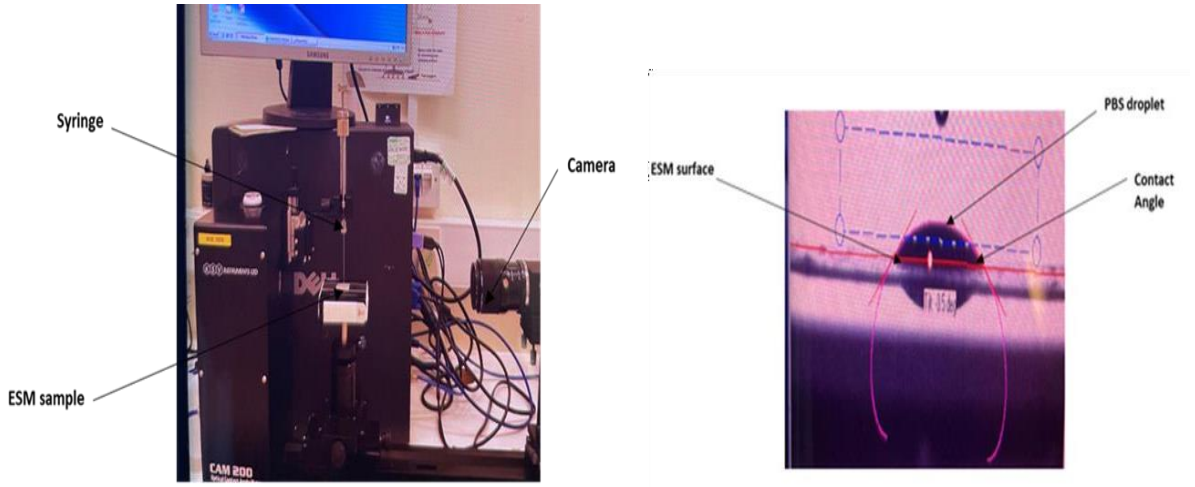

Figure 2.7. Photograph hydrophilicity test using the sessile drop method
(a) KSV 200 CAM optical contact angle meter showing the mounted ESM sample. (b) the sessile drop measurement. at room temperature (~19 °C).

2.3.3 Characterisation of ESM generated from optimised protocol

2.3.3.1 Structural/ Morphology

Using the FESEM images at Magnification of 500x produced for the inner layer: LESMstrip, LESM-A0.5 and LESM-E0.9 and outer layer OESMstrip, OESM-A0.5 and OESM-E0.9, the surface roughness was examined. Surface topography and surface roughness plots were generated using Fiji-ImageJ software. Based on the surface topography and profile plots, the

surface roughness (Arithmetical mean deviation, Ra) was evaluated via SurfCharJ 1q plugin in the Fiji-ImageJ software. In addition, the fibre diameters of the outer layer of the ESM were evaluated via Fiji-ImageJ software and OriginLab Origin 2021.

2.3.3.2 Swelling index.

The swelling index (SI) of each membrane was performed by immersing the ESM samples (ESMstrip, ESM-A0.5 and ESM-E0.9) obtained from the optimised method. into 5 ml of PBS, at 34º C, and any change in the weight of the swollen membrane recorded at 2-minute intervals for a total of 10 minutes before being monitored every 10 minutes afterwards until 1-hour total time. The SI was calculated using equation 2.4 as stated below (n=6).

$$Swelling\ index,\ SI\ (\%) = \frac{(Swollen\ weight - Dry\ weight)}{(Dry\ weight)} x100 \qquad \text{Equation 2.4}$$

2.3.3.3 Water drying profile.

Membrane water drying profile of were determined using terahertz (THz) sensing (Alves et al, 2020). Compared to conventional gravimetric analysis, this technique can be performed without physical contact on the sample of interest. The transmission geometry of the technique differs to reflection geometry (Chau et al, 2016; Vynckier et al, 2015) by allowing water content to be quantified. To ensure full hydration, the membranes ((ESMstrip, ESM-A0.5 and ESM-E0.9) obtained by the optimised method were immersed in distilled water for 24 hours. Prior to measurement, excess surface water was removed. By monitoring the relative THz intensities, weight of water across each membrane (EW) can be estimated as a function of drying time using Beer-Lambert Law, under the assumption of constant water density and uniformity. In particular, equation 2.5 was used to convert the measured intensities into estimated weight:

$$Weight = \frac{A_{membrane}}{A_{camera}} \sum_{pixel=1}^{100} \frac{-(l_{pixel})^2 \rho \ln(\frac{I_{pixel}}{I_{0,pixel}})}{\alpha} \qquad \text{Equation 2.5}$$

2.3.4 Biological Characterisation

2.3.4.1 Optimization of sterilization methods

The OESM-A0.5 was selected for preliminary study to obtain the optimal sterilization method to use for *in vitro* and *in vivo* analyses. The membrane samples were sterilized with five different methods: soaking in 100 IU/ml penicillin-100 µg/ml streptomycin solution for 24 hours, exposure to UV radiation in laminar cell culture flow hood (Thermo Scientific, Germany) for 2 hours, the combination of penicillin- streptomycin and UV radiation and soaking in 70% v/v ethanol for 24 hours for complete evaporation of the ethanol. The thickness of the samples was measured using Moore and Wright Outside micrometre (Zoro, Leicester, UK).

To determine the sterilisation method with the ideal mechanical properties for cytotoxicity analysis, the burst strength of the sterile OESM samples was measured. The burst strength of the membranes was measured using a film support rig attached to a TA. XT instrument (StableMicro Systems Ltd, Surrey, UK). The rig is aligned with the ball probe to ensure that the probe moves carefully through the test membrane without coming into contact with the film support rig. As the probe deflected the test membrane, the force increased until the test membrane ruptured. The maximum force (g) which represented the burst strength, was measured. The control was untreated OESM sample.

2.3.4.2 The *In vitro* cytotoxicity evaluation of the ESM obtained from the optimised protocol.

Human tissue for research was obtained from Manchester Eye Bank subject to a Materials Transfer Agreement and stored and disposed according to the tenets of the UK Human Tissue Act. Corneal- Mesenchymal stem cell (C-MSC) was isolated from corneoscleral rims as previously described (Sidney et al, 2015). C-MSC were cultured in M199 medium supplemented with 20% (v/v) FBS, 1% (v/v) AbAm and 2 mM L-glutamine. The SV40 Immortalised Corneal Epithelial Cell Line (ihCEC) was cultured using Epilife medium supplemented with 5 ml HKGS and 1% (v/v) AbAm. Routine

cell culture involved the use of Corning T-75 flasks (Corming Life Sciences, UK), standard trypsinisation protocol (i.e., 0.25% (v/v) trypsin-EDTA) and placement within a humidified incubator, at 37 ^{o}C and 5% CO_2. Sample membranes (i.e., ESMstrip, ESM-A0.5 and ESM-E0.9) were cut into 14 mm (diameter) discs using a circular craft punch (Figure 2.8a). The samples were then placed into Corning CostarTM Ultra-Low Attachment 24-well tissue culture plates, TCP, (Merck, Poole, UK) and sterilised using 1% (v/v) AbAm, in PBS, for 24 h before an additional treatment of UV radiation, for 2 h, in the laminar cell culture flow hood (Thermo Scientific, Germany) (Figure 2.8b).

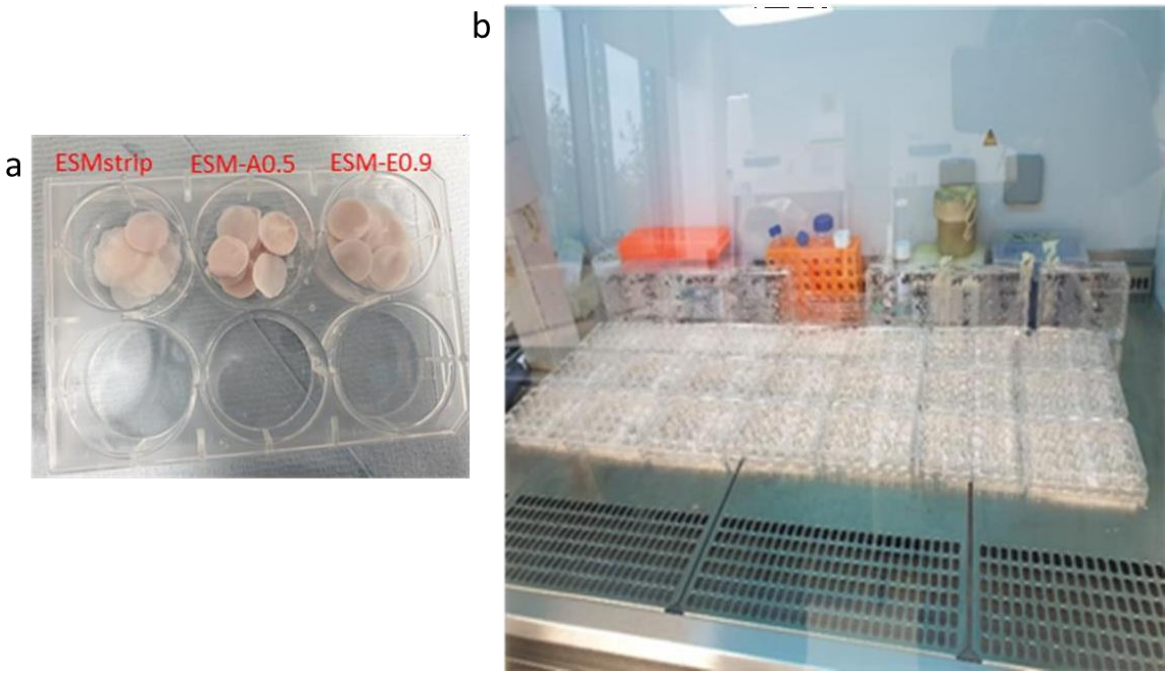

Figure 2.8. Pre-treatment of the ESM obtained from the optimised method
(a) Samples of 14 mm diameter discs of outer and ESMstrip, ESM-A0.5 and ESM-E0.9 in 6-well tissue culture plate. (b) Photograph of the Ultraviolet (UV) radiation treatment of OESMstrip, OESM-A0.5, OESM-E0.9, LESMstrip, LESM-A0.5, and LESM-E0.9 samples (previously sterilized for 24 hours in 1 % (v/v) AbAm, in PBS) in laminar cell culture flow hood (Thermo Scientific, Germany) for 2 hours.

Thereafter, 200 mL of complete growth media were added to each sample in the well and incubated for 30 min to allow for "prewetting" of the membrane samples. The ihCEC or C-MSC cells were seeded on the inner sides of the samples (LESMstrip, LESM-A0.5 and LESM-

E0.9), outer sides (OESMstrip, OESM-A0.5 and OESM-E0.9) or TCP at a density of 10^4 cells/cm^2, respectively, in 200 mL of the complete growth media and incubated for one, three or seven - days under standard cell culture conditions (5% CO_2, 37 ^oC). Control groups using TCP, the inner sides or outer sides of samples with media only were also included. Each sample group had six replicate studies. The metabolic activities of the cells were evaluated using the CellTiter 96 AQueous One Solution Cell Proliferation assay (Promega, Southampton, UK) according to the manufacturer's protocol. In brief, after one, three- or seven-days incubation, 50 mL of the culture media from the wells of three samples in each group were transferred to new 96 well plate and retained for the lactate dehydrogenase (LDH) assay as described below.

Following on, 30 mL of the CellTiter One reagent was then added to each well and incubated at 37 ^oC for 3 h. Subsequently, 100 mL of the media were transferred from the wells in each group into a new 96 well plate and absorbance were read at 492 nm using a BioTek micro plate reader (BioTek, Swindon, UK). For each time point, samples with media only controls were used as the background control. To quantify LDH release from the cells, the CytoTox-One Homogeneous Membrane Integrity assay kit was used. 50 mL of the CytoTox-One reagent were added to the 50 mL culture media (removed as mentioned above) in the 96 well plate and incubated, in the dark/covered in foil, at room temperature (19 ^oC) for 10 min. Thereafter, 10 mL of stop solution was added to each well and the sample plate read immediately using the BioTek micro plate reader (525 nm excitation wavelength and 560–590 nm emission wavelength). Samples with media only controls (background control) were subtracted from the corresponding wells to attain the corrected fluorescent reading.

2.3.4.3 Cell attachment and spreading.

The attachment and spreading characteristics of the cell on the membranes were evaluated using an adapted version of the protocol previously described by Shafaie et al, 2017. Media from three sample wells from each group (i.e., samples with cells) were aspirated and cells

were then washed twice with 100 mL of PBS solution. Sequential addition of 100 mL 3.7% (w/v) paraformaldehyde in PBS solution for 15 min, followed by a PBS wash step, and then 100 mL of 1% (v/v) Triton X-100, for 15 min, were used to fix and permealise the cells at room temperature (19 ^{o}C), respectively. Thereafter, 100 mL of 0.25% May–Grunwald stain, in methanol, were used to treat at room temperature for 15 min. 100 mL of Giemsa stain, in methanol, (1:20 dilution with distilled water) were added to stain the nuclear membranes of the cells. Stains were removed following a 20-min incubation time, at room temperature (19 ^{o}C), before being washed once with distilled water and air dried for 2 h, at room temperature (19 ^{o}C). Cell samples were visualised and imaged using an optical Meiji EMT microscope (Meiji Techno, Somerset, UK) and GX 6 CAM digital camera, and also the FESEM (Philip XL30, UK) with operation voltage of 5 kV, spot size 3 and 100 magnification.

2.3.4.4 Angiogenic properties

The *in ovo* chicken embryo Chorioallantoic membrane (CAM) assay (Figure 2.9) was used to ascertain the angiogenic potential of the (inner and outer sides) of the extracted membranes using a slightly modified version of the protocol previously described by Chau *et al.*, 2012. Briefly, fertilised Dekalb White chicken eggs (Henry Stewart and Co *Ltd*, Norfolk, UK) were incubated in a Brinsea Eco incubator for 4 days at 37 ^{o}C and 80% relative humidity. On the 4th day, 5 ml of the egg white was taken out using a blunt 18-gauge needle through a hole to decrease the volume space within the egg and result in a lower/detachment of the CAM from the top part of the eggshell. A square window opening (~2 x 2 cm^{2}) was cut in each egg and covered with a transparent low adhesion tape. The eggs were incubated for an additional day. On the 5th day, sterilised samples of the inner and outer sides of each membrane type (3 x 3 mm^{2} in size) were placed on the CAM. For controls, pre-sterilised with 70% ethanol, 3 x 3 mm Whatman #1 fiter paper squares, 20 µL PBS and 10ng/ml vascular endothethial growth factor (VEGF)-loaded samples were used. All samples were carefully placed on the CAM, under

sterile conditions, before the windows of the eggs were sealed. Eggs were then kept in the incuator for additional 5 days and monitored on a daily basis. On the 10th day, the tape/seal were removed, and images taken using GX CAM digital camera at X1 magnification. Blood vessels were quantified, assessed and characterised using the AngioQuant software (MATLAB, UK) (Niemisto et al, 2005).

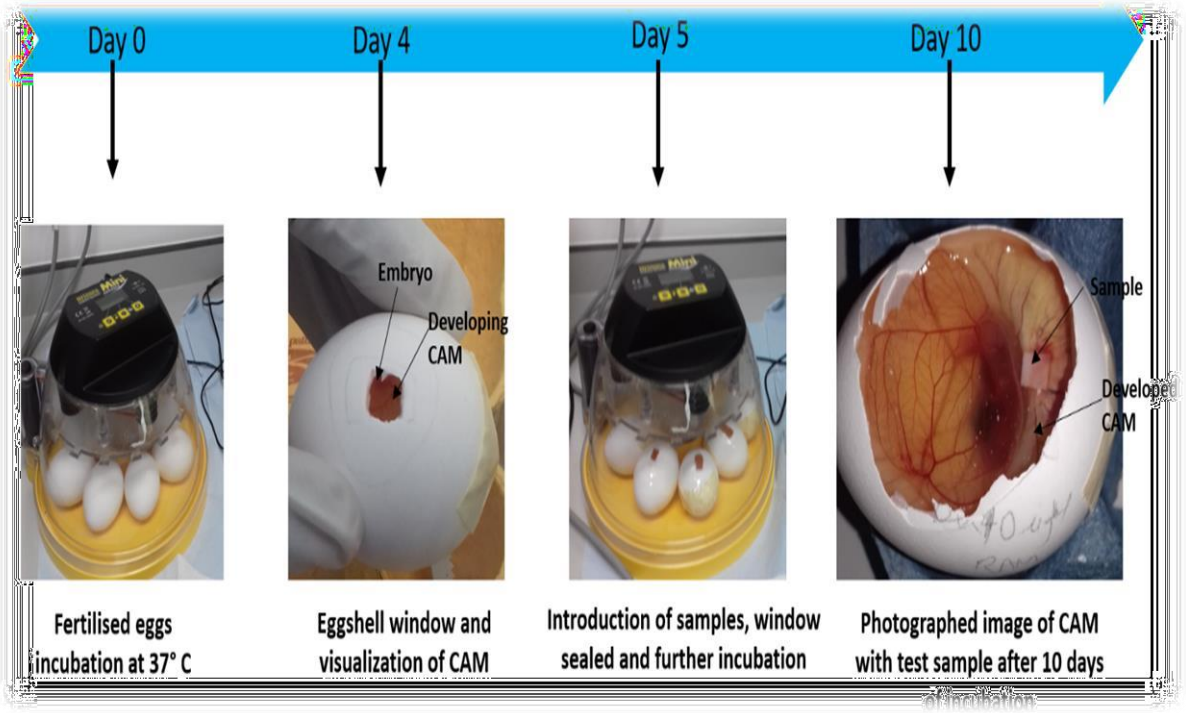

Figure 2.9. Chorioallantoic membrane assay
Fertilized eggs were incubated for 10 days to access the developed CAM in order to observe and compare the angiogenic responses of extracted eggshell membrane membranes.

2.3.5 Statistical analysis

All data were statistically analysed using PRISM (GraphPad software, version 9). The data were evaluated by 1-way, or 2-way analysis of variance (ANOVA) combined with Bonferroni's Multiple post-test, Tukey's and Dunnett's Multiple Comparison Test ($p<0.05$). Data presented were expressed as mean and standard deviation. All experiments were performed in triplicate, and data were denoted as mean standard deviation for n=3 unless otherwise specified.

2.4 RESULTS & DISCUSSION

2.4.1 Membrane extraction

Chicken eggshell membrane (ESM) is a biomaterial firmly attached to the eggshell and its made up of two layers the inner and outer (Baláž, 2014 and Torres et al., 2010). The inner layer is the limiting membrane (LM), and outer layer consists of two components: the inner shell membrane (IM) and the outer shell membrane (OM). The ESM must be separated to achieve its purpose as a biomaterial. The method of extracting ESM from the shell can have a significant impact on the physical, mechanical and biological properties (Guo et al., 2011, Sah, and Rath, 2016, Thoroski, 2004, Zhang et al., 2016 and Choi et al., 2021). The use of manual detachment-the simplest form or separation with dilute acids such acetic acid and EDTA produces a whole membrane. The main objective of the study was to identify an optimal method in extracting an intact ESM with the ideal conditions to fulfil the purpose as a bandage for ocular wound healing.

Two dilute chemicals namely acetic acid and EDTA were employed in the experiment and compared to the peeling method. During the incubation of the egg in the solvents, they break apart the calcium carbonate that make up the shell thereby exposing the naked ESM. An optimised extraction method for the ESM was achieved by immersing the eggshell in acetic acid at three different concentration (0.5, 0.9 and 1.8 M) and EDTA at three different contraction (0.2, 0.5 and 0.9 M). From the results (Table2.3), the extraction time obtained, listing from the shortest time to the longest time for the complete dissolution of the $CaCO_3$ are as follows; ESM-A1.8, ESM-E0.9, ESM-A0.9, ESM-E0.5, ESM-A0.5 and ESM-E0.2. It can be observed that the higher the concentration, the lesser the duration for the extraction.

Table 2.3. The extraction time for membranes extracted with different acetic acid and EDTA.

Sample	Extraction time (hours)
ESM-A0.5	44
ESM-A0.9	31
ESM-A1.8	18
ESM-E0.2	84
ESM-E0.5	36
ESM-E0.9	20

2.4.2 Thickness

The measured thicknesses of the extracted membranes are shown in Figure 2.10. From the results, the thickness of the manually peeled membrane; ESMstrip has an average thickness of 96 ± 5 µm, acetic acid: ESM-A0.5, ESM-A0.9 and ESM-A1.8 have averages of 124 ± 15, 127 ± 2 and 129 ± 16 µm respectively and the average thickness of EDTA extracted membranes: ESM-E0.2, ESM-E0.5 and ESM-E0.9 are 123 ± 14, 127 ± 15 and 122 ± 14 µm respectively. As seen in Figure 2.10, the results document that the thickness of the ESMstrip is significantly less than that of the membrane samples extracted with acetic acid (ESM-A0.5, ESM-E0.2 and ESM-E0.9 $p<0.05$) and EDTA (ESM-A0.9, ESM-A1.8 and ESM-E0.5, $p<0.01$) whereas no significant differences can be observed between all the membranes extracted with acetic acid (ESM-A0.5, ESM-A0.9 and ESM-A1.8) and EDTA (ESM-E0.2, ESM-E0.5 and ESM-E0.9) ($p>0.05$).

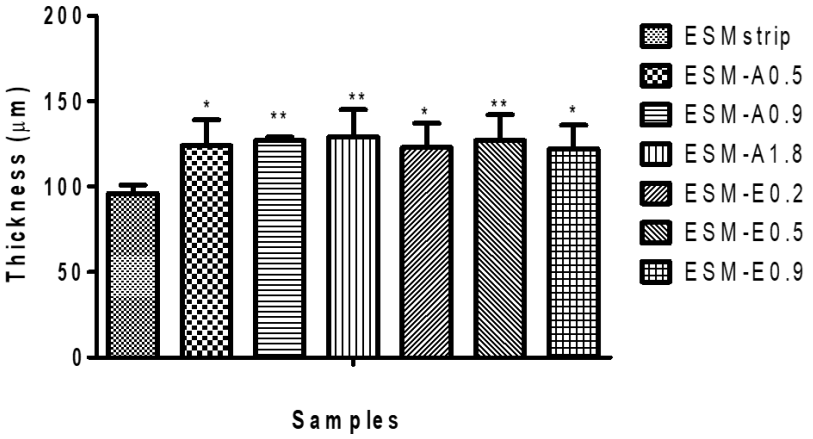

Figure 2.10. Thickness measurements of extracted membranes.
All values are expressed as mean ± σ for n=6. 1-way ANOVA with Bonferroni's Multiple Comparison post Test ($p>0.05$), the average thickness of ESM-A0.5, ESM-A0.9, ESM-A1.8, ESM-E0.2, ESM-E0.5 and ESM-E0.9 are significantly higher than the ESMstrip ($^{*}p<0.05$ and $^{**}p<0.01$). No significant difference is observed among ESM-A0.5, ESM-A0.9, ESM-A1.8, ESM-E0.2, ESM-E0.5 and ESM-E0.9, $p>0.05$.

A simple explanation for this relies on the fact the ESM consists of three distinct layers: The limiting membrane, inner shell membrane and the outer shell membrane. The manually peeled membrane results in the isolation of a membrane composing of two layers, the limiting membrane and the inner shell membrane. In contrast, owing to the fact that the outer shell membrane is firmly attached to the ESM and this layer can only be obtained by chemically treating the shell thereby releasing the membrane after the dissolution of the $CaCO_3$ (Ahmed et al, 2019 and Wu et al, 2004). Previous studies have reported on the thicknesses of the three layers and have shown that each layer has a different and distinct thickness (Ahmed et al, 2019 and Farrar, Barone and Morgan, 2010). Wong Liong and colleagues (2016), using confocal scanning laser microscopy, reported that the average thicknesses of the limiting membrane, inner shell membrane and the outer shell membrane were 3.6 µm, 21 µm and 59 µm. In addition, other thicknesses have been reported in literature depending on how the membranes were prepared and the egg varieties assessed. Strnkova et al. (2016) measured the thickness of manually peeled ESM from hen, goose and Japanese quails by using a digital micrometer and obtained ranges of 22-170 µm, 33-110 µm and 40-90 µm, respectively (Alves-Lima et al,

2020). As such, these results obtained here are consistent with prior studies from existing literature.

2.4.3 Transparency evaluation

The cornea is the transparent window which plays a major role in the visual pathway and, accordingly, any material placed on it must be transparent in order not to compromise its principal role and function (Sidney et al, 2015 and Niemisto et al, 2005). Furthermore, during the application of dressing for wound healing, the transparency of the material is crucial for the visual observations of the wound healing process (Liong, Frank and bailey, 1997).

The results of the visual observation of the inner and outer sides of each extracted membrane can be seen in Figure 2.11. The sample text can be clearly seen in the visual images from the inner side samples (LESMstrip, LESM-A0.5, LESM-A0.9, LESM-A1.8, LESM-E0.2, LESM- E0.5 and LESM-E0.9). In the case of the outer side membrane samples, the visibility of the text in the OESMstrip, OESM-A0.5, OESM-A0.9, OESM-A1.8, OESM-E0.2, OESM-E0.5and OESM-E0.9 are reduced although they can still be considered to be visually transparent overall. This concurs with results produced by Bellairs and Boyde, 1969 that the outer side of ESM is rough while the inner side is smooth which would directly impact visual clarity.

Figure 2.11. Transparency results

Images rep Figure 2.10a resenting the visual transparency of the outer and inner sides of the ESM samples

Moreover, transparency of both sides of the membranes were further assessed by measuring light transmittance using UV-VIS spectrophotometer and this data is summarised in Figure 2.12. The light transmittance values for membranes samples extracted by peeling, acetic acid and EDTA (400–700 nm wavelengths) are all above 80%. Three is no significant difference between the inner sides and the outer sides of the membrane's samples extracted with the different methods ($p>0.05$). Again, no significant difference exited among the OESMstrip, OESM-A0.5, OESM-A0.9, OESM-A1.8, OESM-E0.2, OESM-E0.5, OESM-E0.9, LESMstrip, LESM-A0.5, LESM-A0.9, LESM-A1.8, LESM-E0.2, LESM-E0.5 and LESM-E0.9 membrane samples ($p>0.05$).

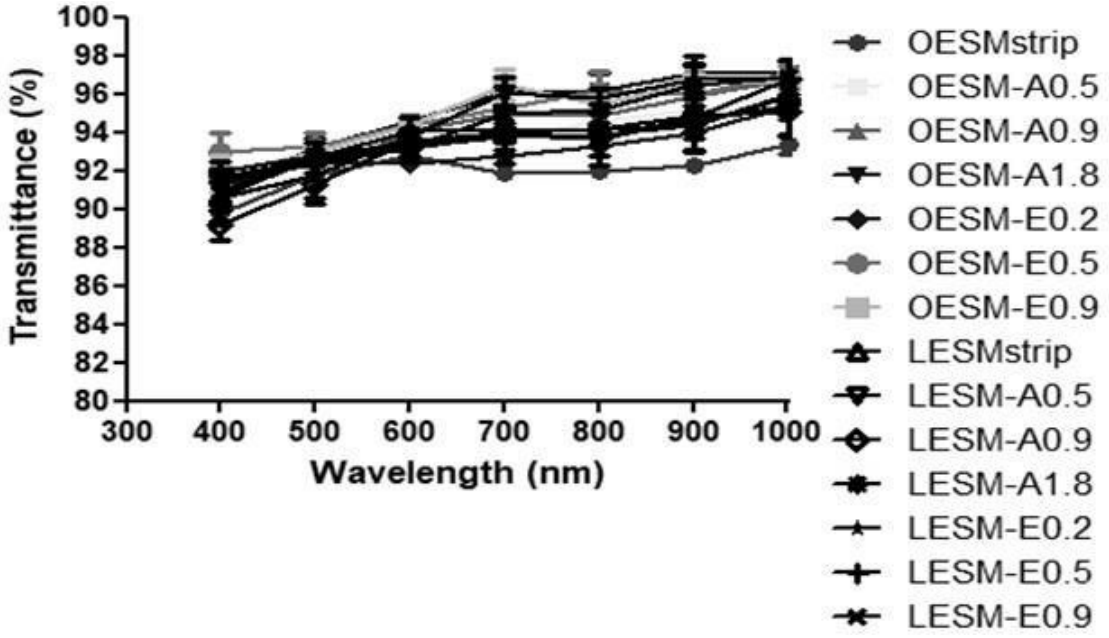

Figure 2.12. Light transmission analysis

UV light transmittance profiles of membranes outer sides (OESMstrip, OESM-A0.5, OESM-A0.9, OESM-A1.8, OESM-E0.2, OESM-E0.5 and OESM-E0.9) and the inner side (LESMstrip, LESM-A0.5, LESM-A0.9, LESM-A1.8, LESM-E0.2, LESM-E0.5 and LESM-E0.9). O: outer side membrane, L: limiting (inner) membrane. All values are expressed as mean ± σ for n=6. 1 way ANOVA with Tukey's Multiple Comparison post Test ($p>0.05$). The transparency of both sides of the ESM extracted manually or acetic or EDTA immersion method was different ($p>0.05$).

2.4.4 Morphology

Field energy scanning electronic microscopy (FESEM) was utilised in visualising the surface morphology of the outer and inner sides of extracted membranes at magnifications of 500x and 2000x. The collated images can be seen in Figures 2.13 and 2.14. It can be noted that both sides of the ESM samples show different structural characteristics: the outer sides of the membranes Figure 2.13 (a, b, c, d, e, f and g) contain macroporous structures within networks of interwoven fibres. However, inner side of the membranes, LESMstrip, LESM-A0.5, LESM-A0.9, LESM-A1.8, LESM-E0.2, LESM-E0.5 and LESM-E0.9 (Figure 2.14 (h) to (n)) display a continuous dense structure with no other significant differences. On further analysis, the outer side of the OESMstrip (Figure 2.13a) which represents the inner shell membrane, displays similar fibrous structures to the samples OESM-A0.5, OESM-A0.9, OESM-A1.8, OESM-E0.2, OESM-E0.5 and OESM-E0.9 (Figure 2.13 (a) to (g)) which are located as the outer shell. In comparison, the fibres of inner shell membrane appear to be much thinner than the outer shell membrane. Interestingly, these results are in conformity with previous reports in the literature (Ahlbom and Sheldon, 2006, Marshalll, Kanezler and Oreffo, 2020 and Devi et al, 2012).

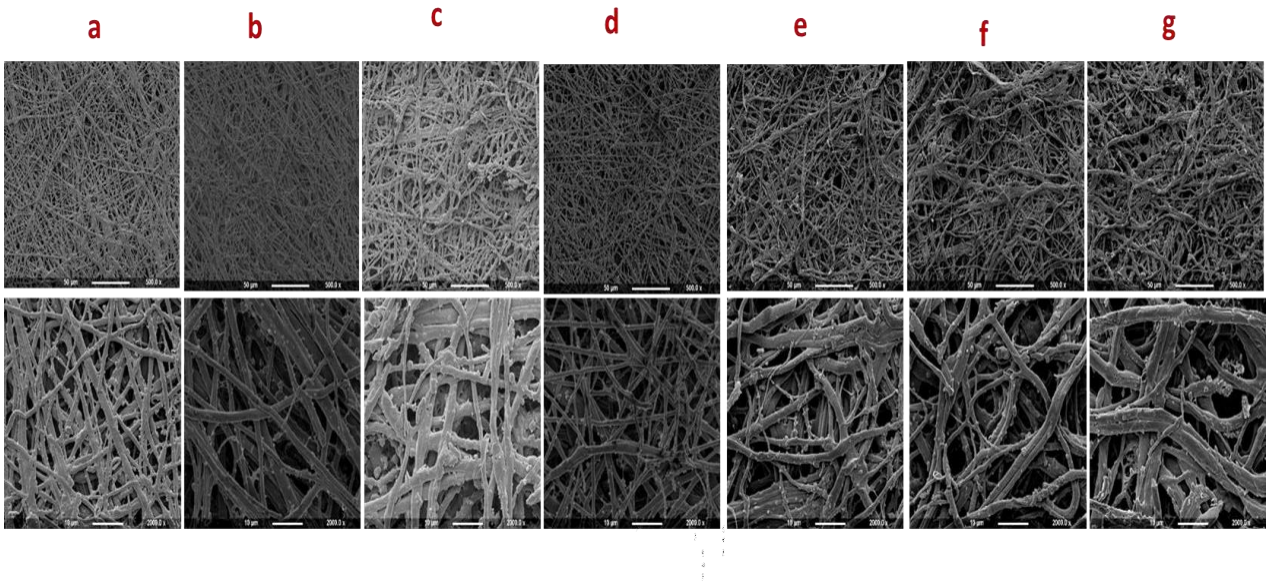

Figure 2.13. FESEM images of the outer side (fibrous network) of extracted membranes showing the inner shell membrane of (a) OESMstrip; outer shell membrane of (b) OESM-A0.5; (c) OESM-A0.9; (d) OESM-A1.8; (e) OESM-E0.2; (f) OESM-E0.5; (g) OESM-E0.9 Magnification at 500x and 2000x.

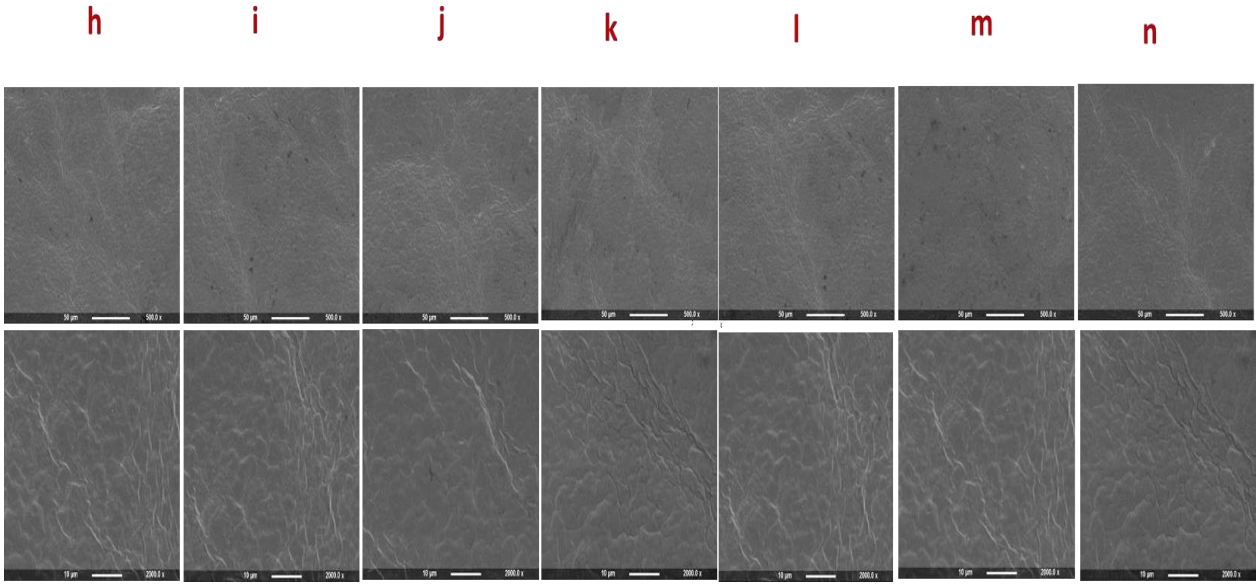

Figure 2.14. FESEM images the inner side– (continuous dense) Limiting membrane of (h) LESMstrip; (i) LESM-A0.5; (j) LESM-A0.9; (k) LESM-A1.8; (l) LESM-E0.2; (m) LESM-E0.5; (n) LESM-E0.9 Magnification at 500x and 2000x.

2.4.5 Elemental/chemical composition

Following the extraction process, EDX analysis was utilised to identify the elemental composition of the membranes in order to profile any remaining residues. The ESM membranes are made up of carbon, nitrogen, oxygen, and sulphur, as shown in the data (Table 2.4). Again, EDX analysis of the individual inner and outer sides of the extracted membranes reveals no calcium content, which is most likely owing to the solvent treatment completely dissolving the $CaCO_3$ (i.e., acetic acid or EDTA). In summary, these findings show that the bulk elemental composition of both sides of the ESM is the same and that there is no layered change due to membrane thickness/distinct layering. This corroborates the data stated by Tsai and colleagues that natural ESM is made up of the elements C, N, O and S (Du, Huang and Feng, 2017). In short, these results demonstrate that both sides of the ESM contain the same bulk elemental composition and that there is no stratified variation based on the membrane thickness/distinct layering.

Table 2.4. Elemental chemical composition (weight %) of inner and outer sides of extracted membranes.

Element	**OESMstrip**	**OESM-A0.5**	**OESM-A0.9**	**OESM-A1.8**	**OESM-E0.2**	**OESM-E0.5**	**OESM-E0.9**
Carbon	65.51 ± 4.61	61.62 ± 4.39	62.79 ± 4.88	63.87 ± 2.33	64.68 ± 3.66	63.05 ± 6.04	63.06 ± 3.12
Nitrogen	2.52 ± 5.10	6.38 ± 5.40	6.15 ± 5.25	4.18 ± 3.96	4.66 ± 3.65	5.78 ± 7.58	3.39 ± 2.98
Oxygen	27.64 ± 2.83	28.39 ± 2.37	27.30 ± 2.02	27.49 ± 1.73	26.67 ± 2.45	27.43 ± 1.37	25.46 ± 1.39
Sulphur	4.32 ± 0.96	3.60 ± 0.28	3.76 ± 0.64	4.46 ± 0.99	3.98 ± 0.65	3.74 ± 0.48	3.68 ± 1.02
Calcium	-	-	-	-	-	-	
Element	**LESMstrip**	**LESM-A0.5**	**LESM-A0.9**	**LESM-A1.8**	**LESM-E0.2**	**LESM-E0.5**	**LESM-E0.9**
Carbon	64.02 ± 3.13	63.86 ± 2.32	61.96 ± 1.92	62.39 ± 4.84	64.25 ± 2.63	61.37 ± 3.82	63.05 ± 6.04
Nitrogen	4.64 ± 3.77	4.17 ± 3.96	6.77 ± 2.06	6.27 ± 5.95	4.17 ± 2.74	7.81 ± 4.24	5.78 ± 7.58
Oxygen	27.43 ± 1.84	27.49 ± 1.72	27.67 ± 1.99	27.08 ± 1.98	27.75 ± 1.81	27.31 ± 2.25	27.42 ± 1.36
Sulphur	3.90 ± 0.28	4.46 ± 0.99	3.60 ± 0.89	4.26 ± 1.24	3.83 ± 0.44	3.51 ± 0.46	3.73 ± 0.48
Calcium	-	-	-	-	-	-	

All values are expressed as mean ± σ for n=6. 1-way ANOVA with Tukey's Multiple Comparison post Test ($p>0.05$)

FTIR spectroscopy was implemented to characterise the extracted membranes. Referring to Figure 2.15, the spectra of the inner and outer sides of each of the membranes are similar. The characteristic bands associated with the structural unit of proteins are identified in each spectrum (Ahmed et al, 2019 and Balaz, 2014). This supports the evidence in the literature that the fibres of ESM are mainly made up of proteins (Chi and Zhao, 2009, Ahmed et al, 2019, Wu et al, 2004, Chen, Kang and Sukigara, 2014, Tsang et al, 2011 and Farrar, Barone and Morgan, 2010). The amide A band, identified at 3325 cm^{-1}, corresponds to the N-H stretching and O-H groups, however the strong absorption of water has overlapped the band. The peak resolved at 2977 cm^{-1} represents amide B which is mainly associated the stretching vibration of C-H bonds found in =C-H and =CH functional groups (Devi et al, 2012 and Hsieh et al, 2013). The peak at 1652 cm^{-1} (C=O) is associated to amide I band, 1530 cm^{-1}, which corresponds to C≡N stretching, and N-H can be assigned to amide II band and the peak evidenced at 1241 cm^{-1} (Farrar, Barone and Morgan, 2010 and Marshall, Kanezler and Oreffo, 2020). Baláž reported that these three lower peaks of the ESM spectrum correspond to the amide I, II and III vibrations of the glycoproteins found in the fibres of the ESM (Farrar, Barone, Morgan, 2010). As such, the FTIR profiles suggest that the acetic acid and the EDTA extraction protocols did not alter the chemical composition of the (organic) structure of the ESM.

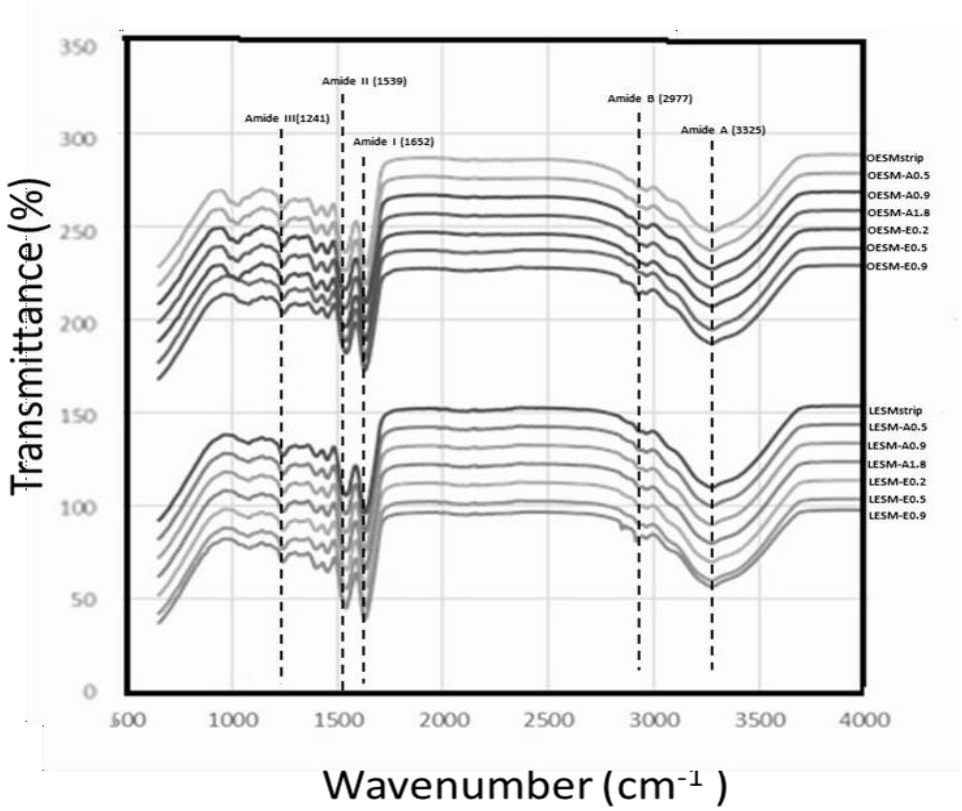

Figure 2.15. FTIR spectra summarising the chemical bonding structure of the extracted ESM samples.

2.4.6 Tensile properties

The mechanical behaviours of potential biomaterials are crucial to their performance (Parodi et al, 1999 and Wang et al, 2017). The mechanical properties were evaluated in aid to select the extraction method that produces the ideal ESM with desirable properties for wound healing application. The stiffness of the inner and outer sides of each membrane were evaluated and compared in context of the compression properties. The burst strength, a measure of resistance to rapture was recorded for the inner and outer sides of each membrane, and is dependent on the tensile strength, and the porosity of the material (Ahmed and Boateng, 2018).

The uniaxial tension and uniaxial compression were employed for the measurement of tensile strength/Young's modulus/ percentage elongation at break and burst strength of the fabricated membranes, respectively. Figure 2.16 and Table 2.5 show the results obtained for the burst strength and distance to burst of both the inner side (LESMstrip, LESM-A0.5, LESM-A0.9 LESM-A1.8, LESM-E0.2, LESM-E0.5, LESM-E0.9) and outer side (OESMstrip, OESM-A0.5, OESM-A0.9, OESM-A1.8, OESM-E0.2, OESM-E0.5 and OESM-E0.9) of each extracted membrane. The outer side of the membrane (OESMstrip, OESM-A0.5, OESM-A0.9, OESM-A1.8, OESM-E0.2, OESM-E0.5, and OESM-E0.9) requires high forces to break and has slight expandable properties, whereas the inner side (LESMstrip, LESM-A0.5, LESM-A0.9, LESM-E0.2, LESM-E0.5, LESM-E0.9). However, no significant differences ($p>0.05$) were observed when comparing the OESMstrip, OESM-A0.5, OESM-A0.9, OESM-A1.8, OESM-E0.2, OESM-E0.5, and OESM-E0.9, with the exception of OESM-A0.5/OESM-A0.9($p<0.01$), OESM-A0.5/OESM-A1.8 ($p<0.0010$), OESM-A0.9/ESM-E0.9($p<0.01$), OESM-A1.8/OESM-E0.9 ($P<0.010$) and OESM-A1.8/ESM-E0.9 ($p<0.01$) (Table 2.6).

In respect of the inner sides of the membranes, the differences between LESMstrip/LESM-A0.9, LESMstrip/LESM-A1.8, LESMstrip/LESM-E0.5, LESMstrip/LESM-E0.9, LESM-A0.5/LESM-A0.9, LESM-A0.5/LESM-E0.2, LESM-A0.5/LESM-E0.5, LESM-A0.5/LESM-

E0.9, LESM-A0.9/LESM-A1.8, LESM-A0.9/LESM-E0.2, LESM-A0.9/LESM-E0.5, LESM-A1.8/LESM-E0.2, LESM-A1.8/LESM-E0.5 and LESM-E0.5/LESM-E0.9 ($p>0.05$) were determined not to be significant whereas differences were observed in these sample pairs LESMstrip/LESM-A0.5 ($p<0.05$), LESMstrip/LESM-E0.5($p<0.05$), LESMstrip/LESM-E0.9 ($p<0.05$), LESM-A0.9/LESM-E0.9($p<0.05$) and LESM-E0.2/LESM-E0.9($p<0.05$) samples (Table 2.5).

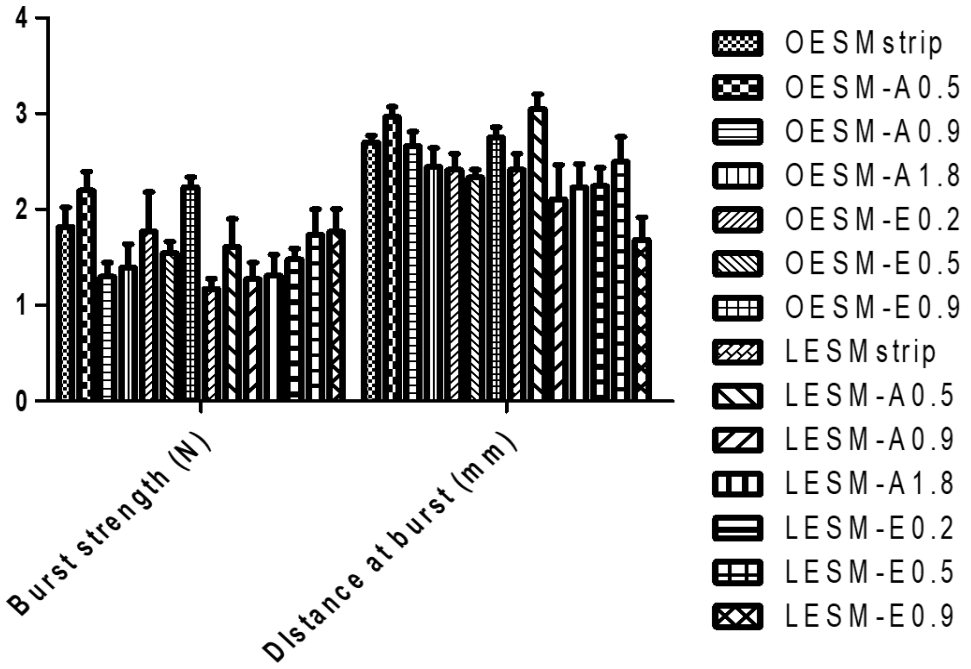

Figure 2.16. Compression profile (burst strength and distance at burst)
for inner side (LESMstrip, LESM-A0.5, LESM-A0.9 LESM-A1.8, LESM-E0.2, LESM-E0.5, LESM-E0.9) and outer side (OESMstrip, OESM-A0.5, OESM-A0.9, OESM-A1.8, OESM-E0.2, OESM-E0.5 and OESM-E0.9).

Table 2.5. Results of 2-way ANOVA with Bonferroni's multiple comparison post-test ($p > 0.05$).

Samples	BS/N	D /mm	Samples	BS/N	D /mm	Samples	BS/N	D /mm
OESMstrip vs OESM-A0.5	ns	ns	OESM-A0.9 vs LESM-A1.8	ns	ns	OESM-E0.5 vs LESM-E0.9	**	*
OESMstrip vs OESM-A0.9	ns	ns	OESM-A0.9 vs LESM-E0.2	ns	ns	OESM-E0.9 vs LESMstrip	***	ns
OESMstrip vs OESM-A1.8	ns	ns	OESM-A0.9 vs LESM-E0.5	ns	ns	OESM-E0.9 vs LESM-A0.5	**	ns
OESMstrip vs OESM-E0.2	ns	ns	OESM-A0.9 vs LESM-E0.9	ns	ns	OESM-E0.9 vs LESM-A0.9	**	ns
OESMstrip vs OESM-E0.5	ns	ns	OESM-A1.8 vs OESM-E0.2	ns	ns	OESM-E0.9 vs LESM-A1.8	***	ns
OESMstrip vs OESM-E0.9	ns	ns	OESM-A1.8 vs OESM-E0.5	ns	ns	OESM-E0.9 vs LESM-E0.2	**	ns
OESMstrip vs LESMstrip	*	*	OESM-A1.8 vs OESM-E0.9	**	*	OESM-E0.9 vs LESM-E0.5	*	ns
OESMstrip vs LESM-A0.5	*	ns	OESM-A1.8 vs LESMstrip	ns	ns	OESM-E0.9 vs LESM-E0.9	*	ns
OESMstrip vs LESM-A0.9	ns	ns	OESM-A1.8 vs LESM-A0.5	ns	ns	LESMstrip vs LESM-A0.5	*	ns
OESMstrip vs LESM-E0.2	*	ns	OESM-A1.8 vs LESM-A1.8	ns	ns	LESMstrip vs LESM-A1.8	ns	ns
OESMstrip vs LESM-E0.9	*	*	OESM-A1.8 vs LESM-E0.5	ns	ns	LESMstrip vs LESM-E0.5	*	ns
OESM-A0.5 vs OESM-A0.9	**	ns	OESM-A1.8 vs LESM-E0.9	**	ns	LESMstrip vs LESM-E0.9	*	ns
OESM-A0.5 vs OESM-A1.8	***	ns	OESM-E0.2 vs OESM-E0.5	ns	ns	LESM-A0.5 vs LESM-A0.9	ns	ns
OESM-A0.5 vs OESM-E0.5	*	ns	OESM-E0.2 vs LESMstrip	ns	ns	LESM-A0.5 vs LESM-E0.2	ns	ns
OESM-A0.5 vs LESMstrip	***	ns	OESM-E0.2 vs LESM-A0.9	ns	ns	LESM-A0.5 vs LESM-E0.9	ns	**
OESM-A0.5 vs LESM-A0.5	**	ns	OESM-E0.2 vs LESM-A1.8	ns	ns	LESM-A0.9 vs LESM-A1.8	ns	ns
OESM-A0.5 vs LESM-A0.9	*	ns	OESM-E0.2 vs LESM-E0.2	ns	ns	LESM-A0.9 vs LESM-E0.2	ns	ns
OESM-A0.5 vs LESM-A1.8	*	ns	OESM-E0.2 vs LESM-E0.5	ns	ns	LESM-A0.9 vs LESM-E0.5	ns	ns
OESM-A0.5 vs LESM-E0.2	*	ns	OESM-E0.2 vs LESM-E0.9	ns	ns	LESM-A0.9 vs LESM-E0.9	*	ns
OESM-A0.5 vs LESM-E0.5	*	ns	OESM-E0.5 vs OESM-E0.9	**	*	LESM-A1.8 vs LESM-E0.2	ns	ns
OESM-A0.5 vs LESM-E0.9	ns	*	OESM-E0.5 vs LESMstrip	ns	ns	LESM-A1.8 vs LESM-E0.5	ns	ns
OESM-A0.9 vs OESM-E0.5	ns	ns	OESM-E0.5 vs LESM-A1.8	ns	ns	LESM-E0.2 vs LESM-E0.9	*	*
OESM-A0.9 vs OESM-E0.9	**	ns	OESM-E0.5 vs LESM-E0.2	ns	ns	LESM-E0.5 vs LESM-E0.9	ns	*

All values are expressed as mean ± σ for n=6. (*$p < 0.05$, **$p < 0.01$ ***$p < 0.001$; ns: no significant difference).

The results of the uniaxial tension tests of the extracted membranes at three different velocity (1, 3 and 10 mm/sec) are listed in Table 2.6 and Figures 2.17, 2.18 and 2.19). Statistically, changing the test velocity had no influence on the ultimate tensile strength, elongation at break and Young's modulus measurements (Tables 2.7, 2.9 and 2.10 respectively) for samples ESMstrip, ESM-A0.5, ESM-A0.9, ESM-A1.8, ESM-E0.2, ESM-E0.5 and ESM-E0.9. No statitstical differences ($p < 0.05$) were observed among the ultimute tensile strength of the different methods of extraction except ESMstrip/ESM-E0.9 ($p < 0.05$) and ESM-E0.2/ESM-E0.9 ($p<0.05$) (Table 2.8). From the data, significant differences were observed between the ESMstrip and ESM-E0.2 ($p<0.001$) at the three test velocities, ESMstrip and ESM-E0.5 (1 mm/sec:$p<0.05$, 3 mm/sec:$p<0.01$ and 10 mm/sec:$p<0.001$).

Comparing the measurements of the elongation at break (Table 2.8) between ESM-A0.5 and EDTA-extracted membranes, they were variations at 1 mm/sec (ESM-E0.2: $p<0.05$) and 10 mm/sec (ESM-E0.2:$p<0.001$, ESM-E0.5:$p<0.001$ and ESM-E0.9:$p<0.01$). Also, at a test velocity of 10 mm/sec, the measurements for this interaction were different i.e., ESM-A0.9/ESM-E0.2 ($p<0.01$), ESM-A0.9/ESM-E0.5 ($p<0.01$) and ESM-A0.9/ESM-E0.9 ($p<0.01$).

Table 2.9 presents the Young's modulus of ESMstrip, ESM-A0.5, ESM-A0.9, ESM-A1.8, ESM-E0.2, ESM-E0.5 ESM-A0.5, ESM-A0.9, ESM-A1.8 and ESM-E0.9 measured at test speed 1, 3 and 10 mm/sec. No significant differences were observed between the manually extracted membrane ESMstrip and the acetic acid -extracted membranes (ESM-A0.5, ESM-A0.9 and ESM-A1.8). However, compared to the EDTA-extracted membrane, ESMstrip had a significantly lower Young's modulus.

Primarily, the components and interactions in the respective side of the ESM samples dominate the strength to burst and may be related to their structural characteristics - as previously stated, the outer side of ESM is composed of fibres whereas the inner side has significantly less (Ahmed

et al, 2019, Wu et al, 2004 and Bellairs and Boyde, 1969).Tensile strength is defined as the maximum stress that a material can withstand while being stretched, it can often be associated with (or defined) as the toughness/strength of a material. In contrast, the measure of stiffness is derived from the Young's modulus value (Guarderas et al, 2016). As such, it can be proposed that the mechanical behaviour of ESM is influenced by the distortion of the (alignment) proteins within the fibres of the membrane (Alves-Lima et al, 2020). The values obtained for these ESM membranes seemingly contribute to the evidence reported in literature that ESM are tough and stiff materials (Parodi et al, 1999; Ahmed, Suso and Hincke 2019 and Gocekand Adanur, 2012). From the analysis, the membranes obtained from 0.5 M acetic acid (ESM-A0.5) and 0.9 M EDTA (ESM-E0.9) techniques were selected as membranes with the appropriate mechanical characteristics for wound bandage

Table 2.6. Tension profile of extracted membrane (Mean ± σ, n=6)

Test velocity (mm/sec)	Ultimate Tensile strength (MPa)						
	ESMstrip	**ESM-A0.5**	**ESM-A0.9**	**ESM-A1.8**	**ESM-E0.2**	**ESM-E0.5**	**ESM-E0.9**
1	0.945 ± 0.272	1.340 ± 0.162	1.002 ± 0.274	1.099 ± 0.249	0.971 ± 0.412	1.151 ± 0.278	1.442 ± 0.262
3	1.013 ± 0.268	1.243 ± 0.142	1.125 ± 0.088	0.931 ± 0.313	1.162 ± 0.467	1.163 ± 0.454	1.370 ± 0.455
10	1.020 ± 0.203	1.099 ± 0.532	0.884 ± 0.274	0.960 ± 0.050	0.955± 0.179	1.044 ± 0.329	1.256 ± 0.598
Test velocity (mm/sec)	**Elongation at break (%)**						
	ESMstrip	**ESM-A0.5**	**ESM-A0.9**	**ESM-A1.8**	**ESM-E0.2**	**ESM-E0.5**	**ESM-E0.9**
1	22.567 ± 5.312	40.453 ± 5.270	30.200 ± 8.222	30.560 ± 7.788	31.549 ± 5.215	32.277 ± 3.298	37.612 ± 2.723
3	22.750 ± 5.990	37.414 ± 6.348	32.774 ± 4.814	29.914 ± 5.457	32.134 ± 2.446	37.942 ± 2.597	39.785 ± 5.414
10	21.976 ± 3.996	36.606 ± 2.959	32.420 ± 5.617	32.042 ± 6.119	37.974 ± 3.436	37.712 ± 4.765	40.180 ± 8.401
Test velocity (mm/sec)	**Young's modulus (MPa)**						
	ESMstrip	**ESM-A0.5**	**ESM-A0.9**	**ESM-A1.8**	**ESM-E0.2**	**ESM-E0.5**	**ESM-E0.9**
1	4.165 ± 0.422	3.649 ± 0.639	3.328 ± 0.335	3.322 ± 0.213	1.992 ± 0.951	2.770 ± 1.398	2.832 ± 0.629
3	4.554 ± 1.003	3.616 ± 0.801	3.475 ± 0.428	3.363 ± 0.423	2.404 ± 1.052	2.658 ± 1.151	3.059 ± 1.858
10	4.673 ± 0.686	4.632 ± 1.253	4.364 ± 1.427	3.653 ± 0.473	2.511 ± 0.179	2.396 ± 0.979	2.708 ± 1.357

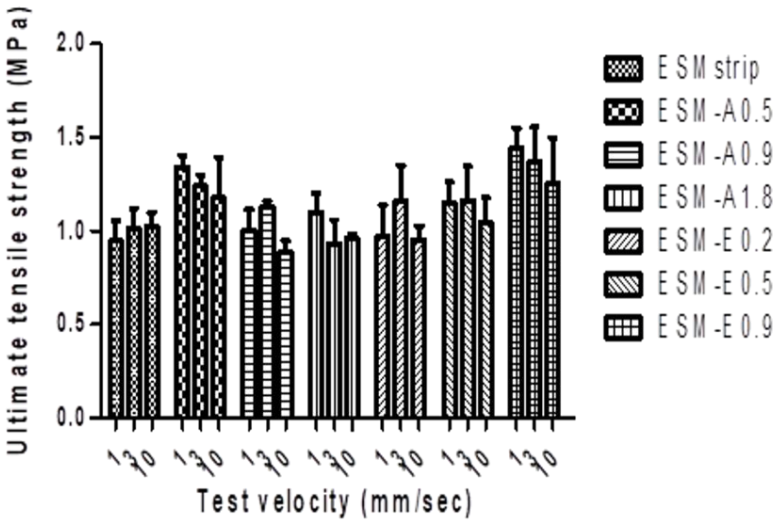

Table 2.7 Results of 2-way ANOVA with Bonferroni's Multiple Comparison post Test ($p>0.05$).

Test velocity (mm/sec)	1	3	10
ESM strip vs ESM-A0.5	ns	ns	ns
ESM strip vs ESM-A0.9	ns	ns	ns
ESM strip vs ESM-A1.8	ns	ns	ns
ESM strip vs ESM-E0.2	ns	ns	ns
ESM strip vs ESM-E0.5	ns	ns	ns
ESM strip vs ESM-E0.9	*	ns	ns
ESM-A0.5 vs ESM-A0.9	ns	ns	ns
ESM-A0.5 vs ESM-A1.8	ns	ns	ns
ESM-A0.5 vs ESM-E0.2	ns	ns	ns
ESM-A0.5 vs ESM-E0.5	ns	ns	ns
ESM-A0.5 vs ESM-E0.9	ns	ns	ns
ESM-A0.9 vs ESM-A1.8	ns	ns	ns
ESM-A0.9 vs ESM-E0.2	ns	ns	ns
ESM-A0.9 vs ESM-E0.5	ns	ns	ns
ESM-A0.9 vs ESM-E0.9	ns	ns	ns
ESM-A1.8 vs ESM-E0.2	ns	ns	ns
ESM-A1.8 vs ESM-E0.5	ns	ns	ns
ESM-A1.8 vs ESM-E0.9	ns	ns	ns
ESM-E0.2 vs ESM-E0.5	ns	ns	ns
ESM-E0.2 vs ESM-E0.9	*	ns	ns
ESM-E0.5 vs ESM-E0.9	ns	ns	ns

Figure 2.17. Ultimate tensile strength recorded at different test speed.
Samples: ESMstrip, ESM-A0.5, ESM-A0.9. ESM-A1.8, ESM-E0.2, ESM-E0.5 and ESM-E0.9. All values are expressed as mean ± σ for n=6. ((*$p<0.05$, ns: no significant difference)

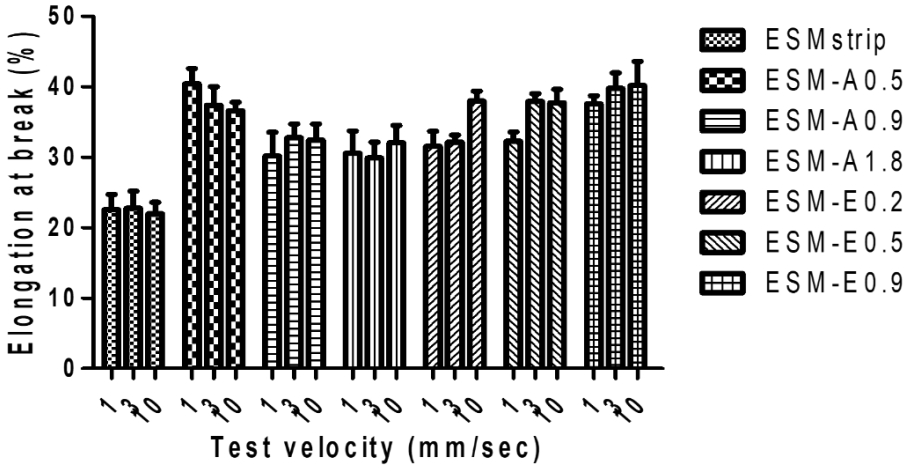

Table 2.8. Results of 2-way ANOVA with Bonferroni's Multiple Comparison post Test ($p>0.05$).

Test velocity (mm/sec)	1	3	10
ESM strip vs ESM-A0.5	ns	ns	ns
ESM strip vs ESM-A0.9	ns	ns	ns
ESM strip vs ESM-A1.8	ns	ns	ns
ESM strip vs ESM-E0.2	***	***	***
ESM strip vs ESM-E0.5	*	**	***
ESM strip vs ESM-E0.9	ns	*	**
ESM-A0.5 vs ESM-A0.9	ns	ns	ns
ESM-A0.5 vs ESM-A1.8	ns	ns	ns
ESM-A0.5 vs ESM-E0.2	*	ns	***
ESM-A0.5 vs ESM-E0.5	ns	ns	***
ESM-A0.5 vs ESM-E0.9	ns	ns	**
ESM-A0.9 vs ESM-A1.8	ns	ns	ns
ESM-A0.9 vs ESM-E0.2	ns	ns	**
ESM-A0.9 vs ESM-E0.5	ns	ns	**
ESM-A0.9 vs ESM-E0.9	ns	ns	*
ESM-A1.8 vs ESM-E0.2	ns	ns	ns
ESM-A1.8 vs ESM-E0.5	ns	ns	ns
ESM-A1.8 vs ESM-E0.9	ns	ns	ns
ESM-E0.2 vs ESM-E0.5	ns	ns	ns
ESM-E0.2 vs ESM-E0.9	ns	ns	ns
ESM-E0.5 vs ESM-E0.9	ns	ns	ns

Figure 2.18. Elongation at break recorded at different test speed.
Samples: ESMstrip, ESM-A0.5, ESM-A0.9. ESM-A1.8, ESM-E0.2, ESM-E0.5 and ESM-E0.9.
All values are expressed as mean ± σ for n=6. (*p<0.05, **p<0.01, (***p<0.001 ns: no significant difference).

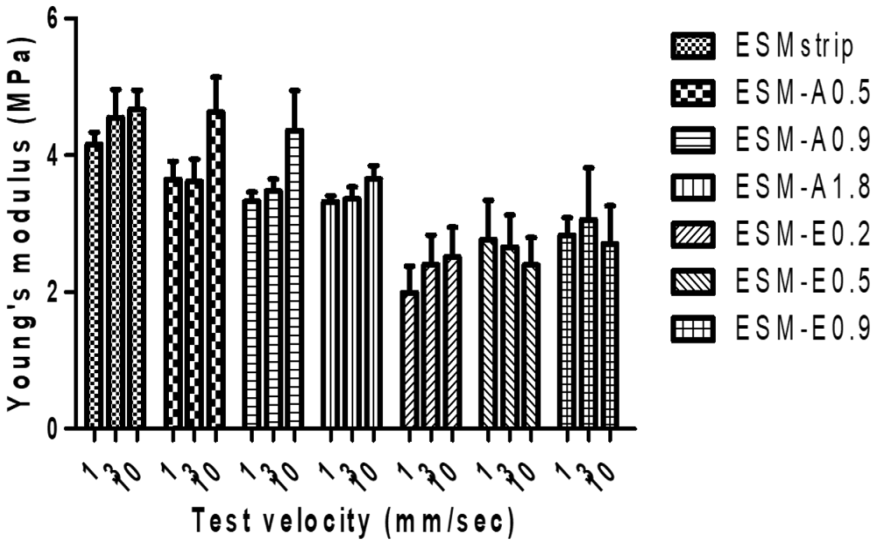

Table 2.9. Results of 2-way ANOVA with Bonferroni's Multiple Comparison post Test ($p>0.05$).

Test velocity (mm/sec)	1	3	10
ESM strip vs ESM-A0.5	ns	ns	ns
ESM strip vs ESM-A0.9	ns	ns	ns
ESM strip vs ESM-A1.8	ns	ns	ns
ESM strip vs ESM-E0.2	***	***	***
ESM strip vs ESM-E0.5	*	**	***
ESM strip vs ESM-E0.9	ns	*	**
ESM-A0.5 vs ESM-A0.9	ns	ns	ns
ESM-A0.5 vs ESM-A1.8	ns	ns	ns
ESM-A0.5 vs ESM-E0.2	*	ns	***
ESM-A0.5 vs ESM-E0.5	ns	ns	***
ESM-A0.5 vs ESM-E0.9	ns	ns	**
ESM-A0.9 vs ESM-A1.8	ns	ns	ns
ESM-A0.9 vs ESM-E0.2	ns	ns	**
ESM-A0.9 vs ESM-E0.5	ns	ns	**
ESM-A0.9 vs ESM-E0.9	ns	ns	*
ESM-A1.8 vs ESM-E0.2	ns	ns	ns
ESM-A1.8 vs ESM-E0.5	ns	ns	ns
ESM-A1.8 vs ESM-E0.9	ns	ns	ns
ESM-E0.2 vs ESM-E0.5	ns	ns	ns
ESM-E0.2 vs ESM-E0.9	ns	ns	ns
ESM-E0.5 vs ESM-E0.9	ns	ns	ns

Figure 2.19. Young's modulus evaluated at different test speed.
Samples: ESMstrip, ESM-A0.5, ESM-A0.9. ESM-A1.8, ESM-E0.2, ESM-E0.5 and ESM-E0.9. All values are expressed as mean ± σ for n=6. (*$p<0.05$, **$p<0.01$, (***$p<0.001$ ns: no significant difference)

2.4.7 Fluid handling properties

The porosity of a material is vital in the cornea wound healing process as it influences other characteristics of the biomaterials such as moisture retention, permeability and strength (Foulks, 2014; Du, Huang and Feng, 2017 and Devi et al, 2012). Table 2.10 shows that the manually obtained membrane, ESMstrip, has the lowest porosity profile of 56.54 %. On the contrary, EDTA-extracted membranes, ESM-E0.9, were found to have the highest porosity measurement of 69.38 percent. Despite these findings, there is no statistically significant difference between the three types of extracted membranes ($p>0.05$) when compared directly.

At the 1-hour and 24-hour timepoints, the fluid absorption capacity of the extracted membranes was evaluated. According to the findings (Table 2.12), no significant differences were found when comparing the two timepoints of the ESMstrip, ESM-A0.5, ESM-A0.9, ESM-A1.8, ESM-E0.2, ESM-E0.5 and ESM-E0.9 samples. The fluid absorption capacity of the ESMstrip, on the other hand, was lower than that of the ESM-A0.5, ESM-A0.9, ESM-A1.8, ESM-E0.2, ESM-E0.5 and ESM-E0.9 samples. Among the membranes extracted with acetic acid, ESM-A1.8 has the lowest fluid adsorption while ESM-A0.5 was found to have the highest porosity.

2.4.8 Thermal properties

The thermal behaviour of the extracted membranes was examined by TGA experiments. The percentage weight loss for each type of membrane was deduced from the TGA curve and the results are summarised in Table 2.10 and 2.11. Overall, the percentage weight loss of ESMstrip was highest (72.58%) than that of the ESM-A0.5 (58.71%), ESM-A0.9 (59.22%), ESM-A1.8 (57.23) and ESM-E0.2 (62.46%), ESM-E0.5 (55.63%) and ESM-E0.9 (51.47%) samples. However, ESMstrip was not significantly different from the other samples except ESM-E0.5 ($p>0.05$) and ESM-E0.9 ($p<0.01$). It has been reported that differences in the thermal stabilities of the membranes are dependent on the structure and chemical composition (Du, Huang and Feng, 2017, Roy et al, 2010 and Jia et al, 2012) and, as such, the obtained data validates the results obtained for the fluid handling properties above.

Table 2.10. Porosity, fluid adsorption and weight loss% of different extracted membranes.

Samples	Porosity (%)	Fluid adsorption (%)		Weight loss (%)
		1h	24h	
ESMstrip	56.54 ± 8.26	232.24 ± 33.23	229.97 ± 27.53	72.58 ± 3.27
ESM-A0.5	63.06 ± 11.42	291.49 ± 34.50	284.88 ± 20.53	58.71 ± 2.58
ESM-A0.9	61.55 ± 14.46	304.15 ± 52.94	306.80 ± 63.85	59.22 ± 1.63
ESM-A1.8	58.11 ± 4.57	266.69 ± 25.94	268.47 ± 35.75	57.23 ± 271
ESM-E0.2	59.02 ± 8.30	274.37 ± 33.40	251.49 ± 34.50	62.46 ± 1.05
ESM-E0.5	58.33 ± 5.28	270.77± 13.85	272.42 ± 24.49	55.63 ± 3.42
ESM-E0.9	69.38 ± 3.85	317.98 ± 29.28	335.45 ± 34.77	51.47 ± 1.98

All values are expressed as mean ± σ for n=3

Table 2.11 Porosity, fluid adsorption and weight loss% of different extracted membranes.

Immersion time (hours)	Porosity,	Fluid adsorption (%)		Weight loss (%)
		1h	24h	
ESM strip vs ESM-A0.5	ns	***	***	ns
ESM strip vs ESM-A0.9	ns	***	***	ns
ESM strip vs ESM-A1.8	ns	***	***	ns
ESM strip vs ESM-E0.2	ns	***	***	ns
ESM strip vs ESM-E0.5	ns	***	***	*
ESM strip vs ESM-E0.9	ns	***	***	**
ESM-A0.5 vs ESM-A0.9	ns	*	**	ns
ESM-A0.5 vs ESM-A1.8	ns	**	ns	ns
ESM-A0.5 vs ESM-E0.2	ns	***	***	ns
ESM-A0.5 vs ESM-E0.5	ns	*	*	ns
ESM-A0.5 vs ESM-E0.9	ns	***	***	ns
ESM-A0.9 vs ESM-A1.8	ns	***	***	ns
ESM-A0.9 vs ESM-E0.2	ns	***	***	ns
ESM-A0.9 vs ESM-E0.5	ns	***	***	ns
ESM-A0.9 vs ESM-E0.9	ns	**	**	ns
ESM-A1.8 vs ESM-E0.2	ns	ns	ns	ns
ESM-A1.8 vs ESM-E0.5	ns	ns	ns	ns
ESM-A1.8 vs ESM-E0.9	ns	***	***	ns
ESM-E0.2 vs ESM-E0.5	ns	ns	ns	ns
ESM-E0.2 vs ESM-E0.9	ns	***	***	ns
ESM-E0.5 vs ESM-E0.9	ns	***	***	ns

All values are expressed as mean ± σ for n=3. ;(*p<0.05, **p<0.01, (***p<0.001 ns: no significant difference). 2-way ANOVA with Bonferroni's multiple comparison post-test (p >0.05).

2.4.9 Wettability

The wettability properties of the extracted membranes were assessed by measuring the contact angle. Figure 2.20 and Table 2.12 show contact angle measurements for ESM samples. No significant differences in contact angle values were observed among inner side (LESMstrip, LESM-A0.5, LESM-A0.9 LESM-A1.8, LESM-E0.2, LESM-E0.5, LESM-E0.9, $p>0.05$) and outer side (OESMstrip, OESM-A0.5, OESM-A0.9, OESM-A1.8, OESM-E0.2, OESM-E0.5 and OESM-E0.9, $p>0.05$) of each extracted membrane. Noticeably, significant differences between the outer and the inner sides were observed (Table 2.12). This shows that the outer layer ESM extracted manually and solvent immersion method with acetic acid and EDTA, have low hydrophilicity.

These values demonstrate the hydrophilicity of the extracted membrane, and this characteristic could contribute to the adhesion and spreading of cells on the membrane surface as previously suggested Wang et al, 2017. It is assumed that the low hydrophilicity of the outer side of the membrane is attributed to its interwoven fibrous structure and rough surface. In contrast, the relatively smooth surface and dense structure of the inner side, the limiting membrane, may contribute to its high hydrophilic behaviour. Above all, no significant difference among the respective inner and outer sides of the extracted membrane ($p>0.05$) were observed and these results can be seen to be in a good agreement with previous published studies (Banerjee et al, 2010, Wang et al, 2017, Liang et al, 2014 and Chen et al, 2019).

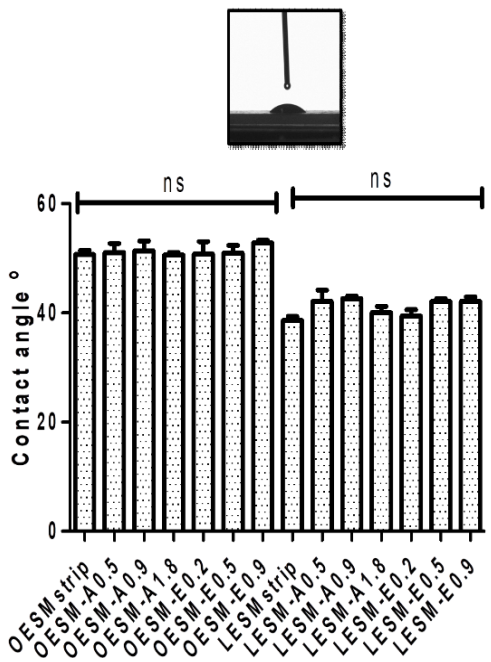

Table 2.12. Results of 2-way ANOVA with Bonferroni's multiple comparison post-test (p >0.05).

Samples	Contact angle /°	Samples	Contact angle /°	Samples	Contact angle /°
OESMstrip vs LESMstrip	ns	OESM-A0.9 vs LESMstrip	***	OESM-E0.5 vs LESM-A0.5	***
OESMstrip vs LESM-A0.5	ns	OESM-A0.9 vs LESM-A0.5	**	OESM-E0.5 vs LESM-A0.9	***
OESMstrip vs LESM-A0.9	ns	OESM-A0.9 vs LESM-A0.9	**	OESM-E0.5 vs LESM-A1.8	**
OESMstrip vs LESM-A1.8	ns	OESM-A0.9 vs LESM-A1.8	***	OESM-E0.5 vs LESM-E0.2	**
OESMstrip vs LESM-E0.2	ns	OESM-A0.9 vs LESM-E0.2	***	OESM-E0.5 vs LESM-E0.5	***
OESMstrip vs LESM-E0.5	ns	OESM-A0.9 vs LESM-E0.5	**	OESM-E0.5 vs LESM-E0.9	***
OESMstrip vs LESM-E0.9	***	OESM-A0.9 vs LESM-E0.9	**	OESM-E0.9 vs LESMstrip	***
OESM-A0.5 vs LESMstrip	**	OESM-A1.8 vs LESMstrip	***	OESM-E0.9 vs LESM-A0.5	***
OESM-A0.5 vs LESM-A0.5	ns	OESM-A1.8 vs LESM-A0.5	**	OESM-E0.9 vs LESM-A0.9	***
OESM-A0.5 vs LESM-A0.9	ns	OESM-A1.8 vs LESM-A0.9	*	OESM-E0.9 vs LESM-A1.8	***
OESM-A0.5 vs LESM-A1.8	ns	OESM-A1.8 vs LESM-A1.8	***	OESM-E0.9 vs LESM-E0.2	***
OESM-A0.5 vs LESM-E0.2	ns	OESM-A1.8 vs LESM-E0.2	***	OESM-E0.9 vs LESM-E0.5	ns
OESM-A0.5 vs LESM-E0.5	ns	OESM-A1.8 vs LESM-E0.5	**	OESM-E0.9 vs LESM-E0.9	ns
OESM-A0.5 vs LESM-E0.9	***	OESM-A1.8 vs LESM-E0.9	**	OESM-E0.2 vs LESM-A0.9	ns
OESM-E0.2 vs LESMstrip	***	OESM-E0.2 vs LESM-A0.5	**	OESM-E0.2 vs LESM-A1.8	***

Figure 2.20. Contact angles of extracted membranes.

1-way ANOVA with Bonferroni's Multiple Comparison post Test ($p<0.05$). All values are expressed as mean ± σ for n=6 ns: no significant difference among the inner side (LESMstrip, LESM-A0.5, LESM-A0.9 LESM-A1.8, LESM-E0.2, LESM-E0.5, LESM-E0.9) ($p>0.050$) and outer side (OESMstrip, OESM-A0.5, OESM-A0.9, OESM-A1.8, OESM-E0.2, OESM-E0.5 and OESM-E0.9) ($p>0.05$). (*$p<0.05$, **$p<0.01$, ***$p<0.001$)

2.4.10 Characterisation of ESMs obtained from the optimised protocol.

In exploring the ideal protocol for the extraction of eggshell membrane (ESM), ESM isolated with 0.5M of acetic acid or 0.9M was selected. The physical/mechanical characteristics of ESM-A0.5 and ESM-E0.9 have demonstrated that the ESM produced with the optimised protocol are promising biomaterials for cornea wound healing application. According the physical and biological characteristics of ESM-A0.5 and ESM-E0.9 were invested.

2.4.10.1 Surface roughness

The surface characteristic of bandages for cornea wound healing application is a key factor in understanding its clinical performance such as the interaction of the biomaterial with the ocular surface i.e., biocompatibility (Bennett, 1992, Sweeney et al, 2000 and Talu and Talu, 2012). FESEM technique was employed to characterise the topography/surface roughness of OESMstrip, OESM-A0.5, OESM-E0.9, LESMstrip, LESM-A0.5 and LESM-E0.9. FESEM

images of the samples at magnification of 500x was utilised in the measurement of the surface roughness (Figure 2.21). A surface topography was extracted Fiji-ImageJ software for each of the samples (Figure 2.21 a, b, c, d, e, and f). The areas of the surface analysis for the inner and outer layers were 216.0 x 232.0 µm and 229.0 x 232.0 µm respectively. From Figure 2.21 a, b and c representing the surface plot for LESMstrip, LESM-A0.5 and LESM-E0.9 respectively,

the surfaces of the samples appear smooth with swells whereas, the surface of the outer layers OESMstrip (Figure 2.21d), OESM-A0.59 (Figure 2.21e), OESM-E0.9 (Figure 2.21f) have 'pine-like' structures (Yan et al, 2020, Kheirabadi et al., 2018, Zhang et al., 2016, Ray et al, 2018, Mann et al.,2006 and Zhou et al, 2010).

Furthermore, the surface roughness area value i.e., arithmetical mean deviation, Ra was extracted via Fiji-ImageJ software SurfCharJ 1q plugin to access the surface roughness profile of the samples. The surface roughness plots for each of the samples are in the Appendix (Figure A 1.0 a, b and c and Figure A 1.1 d, e and f). From the data (Figure 2.21g), the significant

difference was observed in the outer and inner layers ($p > 0.05$). this also proves that the extraction method did not affect the surface topography of the ESMs. However, comparing the Ra values of the inner to the outer layer, statistically they are difference ($p < 0.001$).

The evaluation of the surface roughness, Ra value (Figure 2.21 g) of outer layers samples indicated the acetic and EDTA treatments (OESM-A0.5 and OESM-E0.9) did not cause change in the surface compositions compared to the manual peeling (OESMstrip). The analysis revealed that the surface roughness of the outer layers was higher than the inner layers (Figure 2.21g). In biomaterial applications, surface roughness may impact cell adhesion and growth, this suggests that the low Ra values recorded for the inner layers are valuable (Chen et al., 2017, Zareidoost et al., 2012 and Biazar et al., 2011).

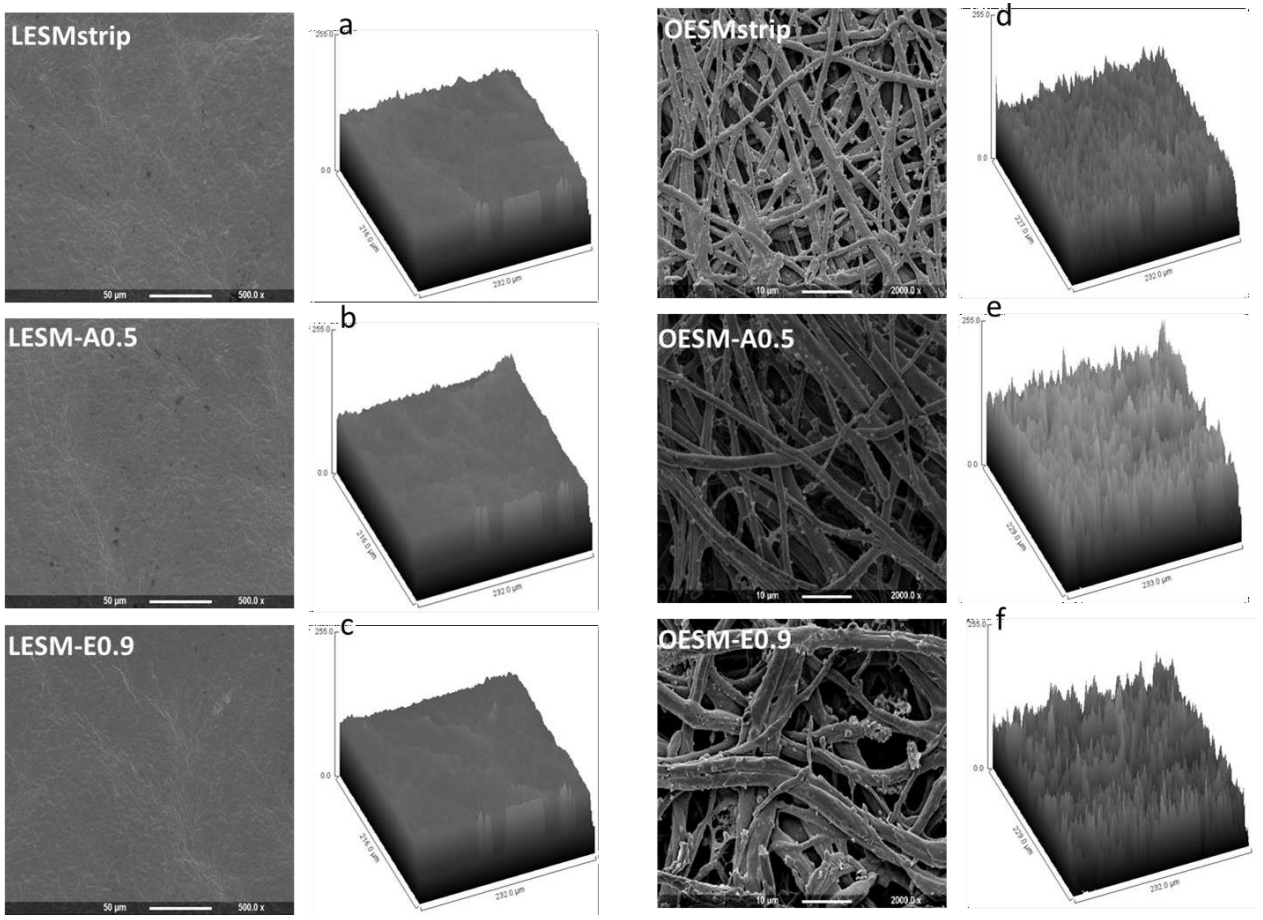

Figure 2.21. Surface roughness analysis of the outer side of the eggshell membrane
FESEM images of the OESMstrip, OESM-A0.5, OESM-E0.9, LESMstrip, LESM-A0.5 and LESM-E0.9. Magnification at 500x. The images a, b, c, d, e and f are surface topography of OESMstrip, OESM-A0.5, OESM-E0.9, LESMstrip, ESM-A0.5 and ESM-E0.9. generated via Fiji-ImageJ surface.

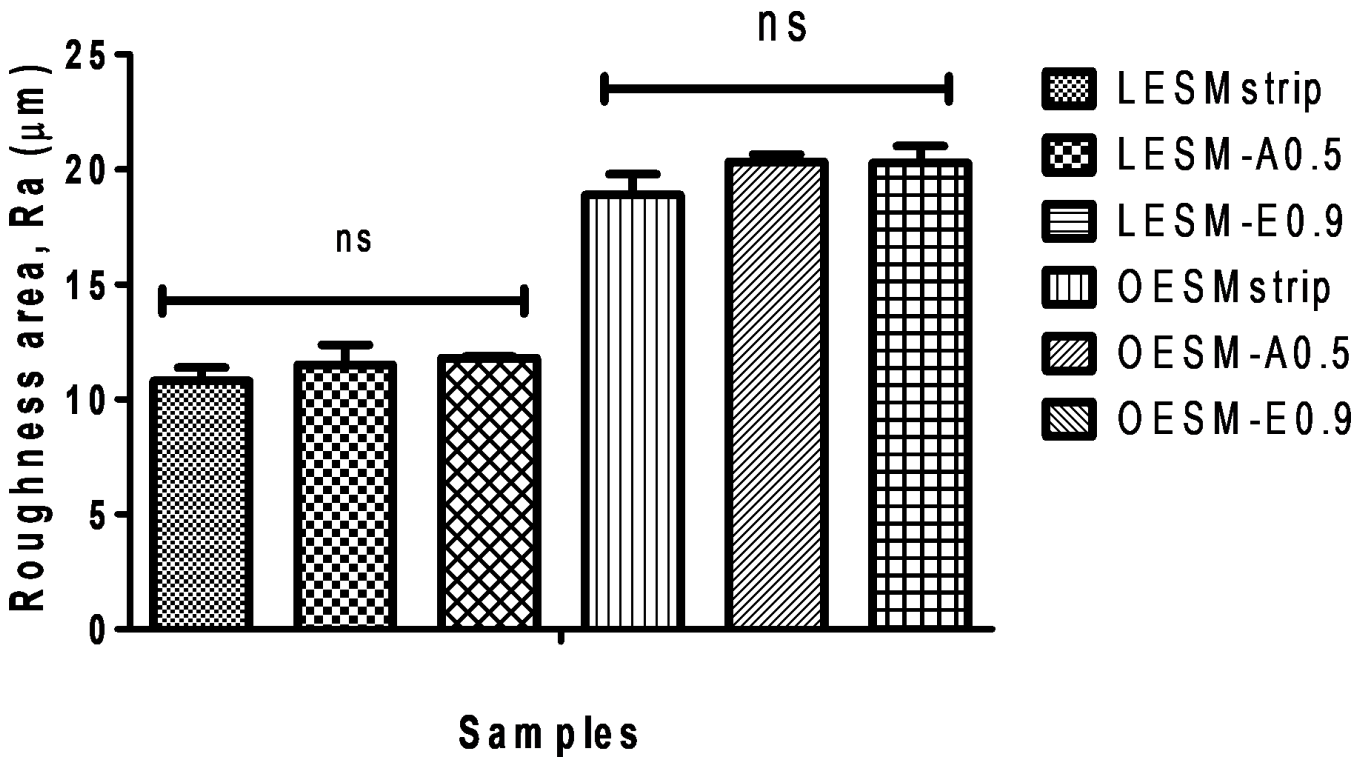

Figure 2.21. Surface roughness analysis

(g) A plot of arithmetical mean deviation, Ra (µm) recorded for inner layer LESMstrip, LESM-A0.5 and LESM-E0.9 and outer layers: OESMstrip, OESM-A0.5 and OESM-E0.9 and using FESEM at magnification of 500X on surface area of 216.0 X 232.0 µm and 229.0 X 232.0 µm respectively. The Ra values were calculated via Fiji-ImageJ software SurfCharJ 1q plugin. 1-way ANOVA with Bonferroni's multiple comparison post-test ($p > 0.05$). All values are expressed as mean ± σ for n=10. ns represents no significant difference, $p > 0.05$.

2.4.10.2 Fibre diameter

The FESEM images of the outer layer at 500x magnification are shown in Figure 2.22. They show a porous structure made up fibres with different diameters. Using the FESEM images, the fibre diameters of the OESMstrip, OESM-A0.5 and OESM-E0.9 were evaluated via Fiji-ImageJ Software. A total of 100 counts of fibre diameter measurements were obtained from a sign FESEM image of each ESM. OESMstrip, OESM-A0.5 and OESM-E0.9 show diameters ranging from 0.25 to 5 .75 µm, 0.936 to 8.97 µm and 1.02 to 8.88 µm respectively and they fall in, in line with reports by (Yan et al., 2020 and Torres et al., 2006). The fibre distribution plots of the samples were generated via OriginLab Origin 2021. Figure a, b and c represent the fibre diameter distribution for OESMstrip, OESM-A0.5 and OESM-E0.9 respectively. Further analysis was implemented by comparing the average fibre diameter of OESMstrip to the OESM-A0.5 and OESM-E0.9 (Figure 2.22d). Statistically, the average fibre diameter of the OESMstrip which is the inner eggshell membrane is smaller than the outer eggshell membranes of OESM-A0.5 and OESM-E0.9 ($p < 0.001$). This agrees with the theoretical statement by Torres et al. that the fibre diameters of the inner shell membrane are smaller than the outer shell embrace (Torres et al., 2010).

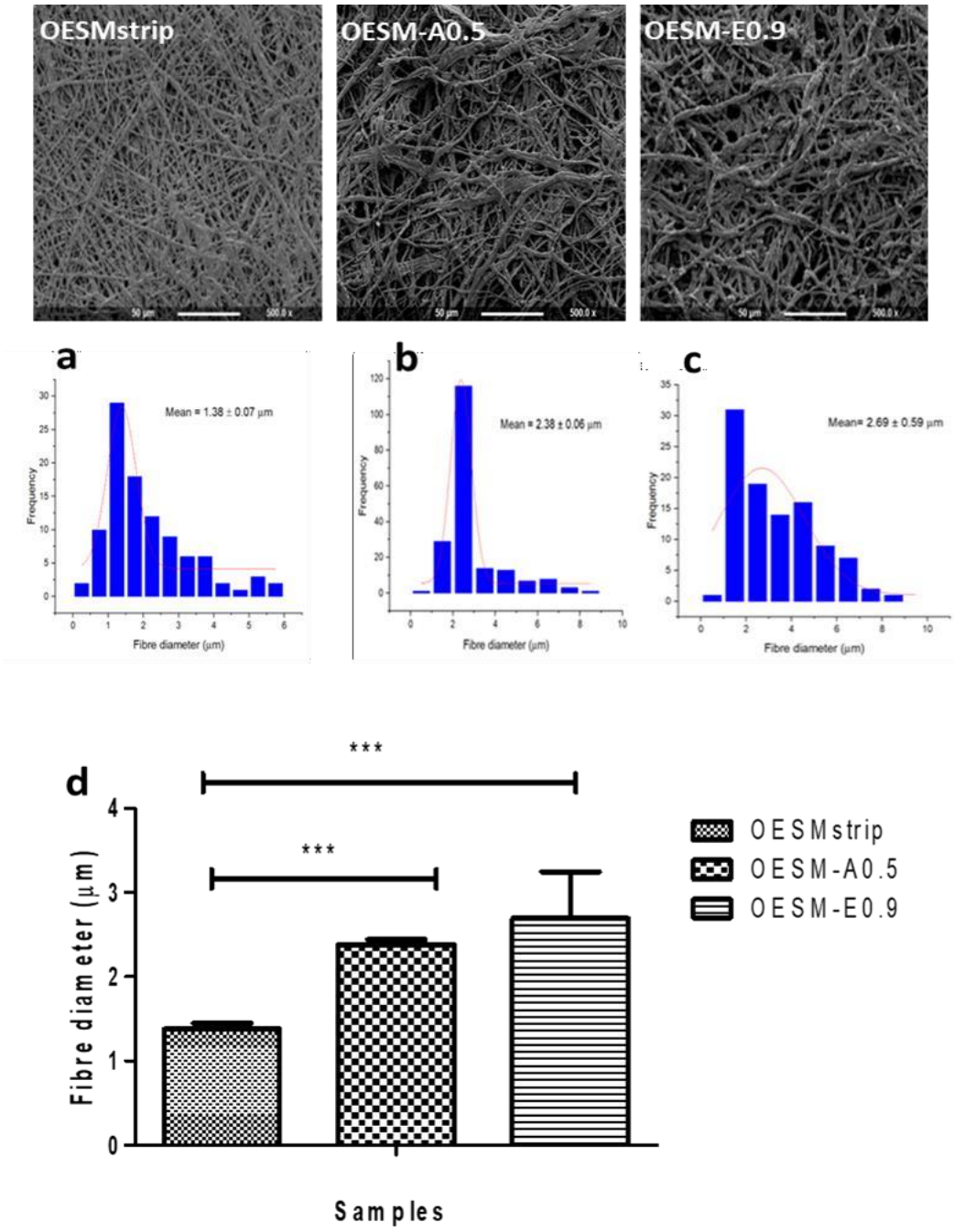

Figure 2.22. Structural analysis of the fibrous network of ESM.
FESEM images at 500x magnification of the outer layer (fibrous network) of ESM, OESMstrip, OESM-A0.5 and OESM-E0.9. 'a, b and c' represent the fibre diameter distribution (n= 100 counts) for OESMstrip, OESM-A0.5 and OESM-E0.9 respectively. 'd' is the results for the comparison of the average fibre diameter of the OESMstrip to OESM-A0.5 and OESM-E0.9. They are significantly different, ***p <0.001. All values are expressed as mean ± σ for n=100 (1-way ANOVA with Bonferroni's multiple comparison post-test (p>0.05).

2.4.10.3 In vitro cytotoxicity

Swelling profile is one of the important characteristics that determine fluid retention, erosion and hydrophilic of a material with potential application for an ocular wound dressing (Tsai et al, 2006, Roy et al, 2010 and Chau et al, 2012). In this study, the swelling profiles of ESMstrip, ESM-A0.5 and ESM-E0.9 were assessed, and the results summarised in Figure 2.23. In the first 2 minutes, all three membranes swelled rapidly, however the swelling capacities of the ESM-A0.5 and ESM-E0.9 were significantly higher (p,0.01 and p<0.001, respectively) than that of the ESMstrip sample. After 10 minutes, the swelling capacities of all the extracted membranes remained relatively constant. It can be noted that the swelling prolife of the ESMstrip was significantly lower than the ESM-A0.5 (p<0.05) and ESM-E0.9 (p<0.001) samples. In contrast, no significant difference was observed between the ESM-A0.5 and the ESM-E0.9 (p>0.05) samples.

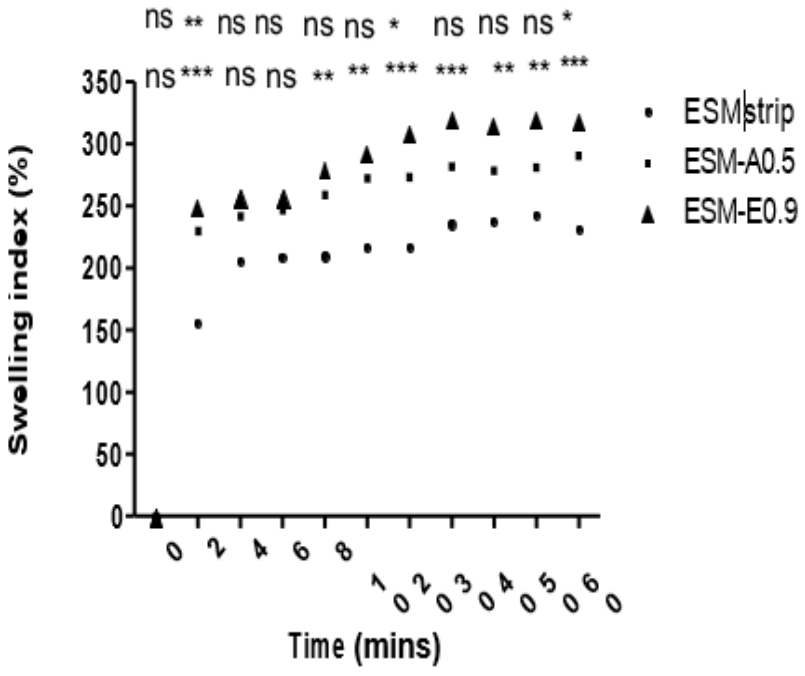

Figure 2.23. Swelling profiles of the extracted membranes.
One way ANOVA with Bonferroni's Multiple Comparison post Test (p>0.05). With reference to the ESMstrip significant difference were observed in the swelling index compared to the ESM-A0.5 and ESM-E0.9. There's no significant difference between ESM-A0.5 AND ESM-E0.9. All values are expressed as mean ± σ for n=6. (*p<0.05; **p<0.01; ***p<0.001; ns: no significant difference).

2.4.10.4 Water drying profile

The membrane water desorption profiles for ESMstrip, ESM-A0.5 and ESM-E0.9, are shown in Figure 2.24, which qualitatively shows a similar trend to the swelling profiles, with ESM-E0.9 having the highest swelling due to fluid retention, followed by ESM-A0.5 and ESMstrip. It is also interesting to note that at a decreasing time, a similar pattern can be observed i.e., a period of constant water weight followed by a steady decrease, which is consistent with the CA data. The sharp decline is also consistent with the logarithmic decay behaviour observed in polymer-based membranes (Alves-Lim, Letizia, Degl'Innocenti, Dawson, Lin, 2020; Majsztrik PW, Satterfield, Bocarsly, and Benziger, 2007; Majsztrik PW, Satterfield, Bocarsly, and Benziger, 2007). The sharp weight loss in the first 3 minutes is possibly due to evaporation of the excess surface water.

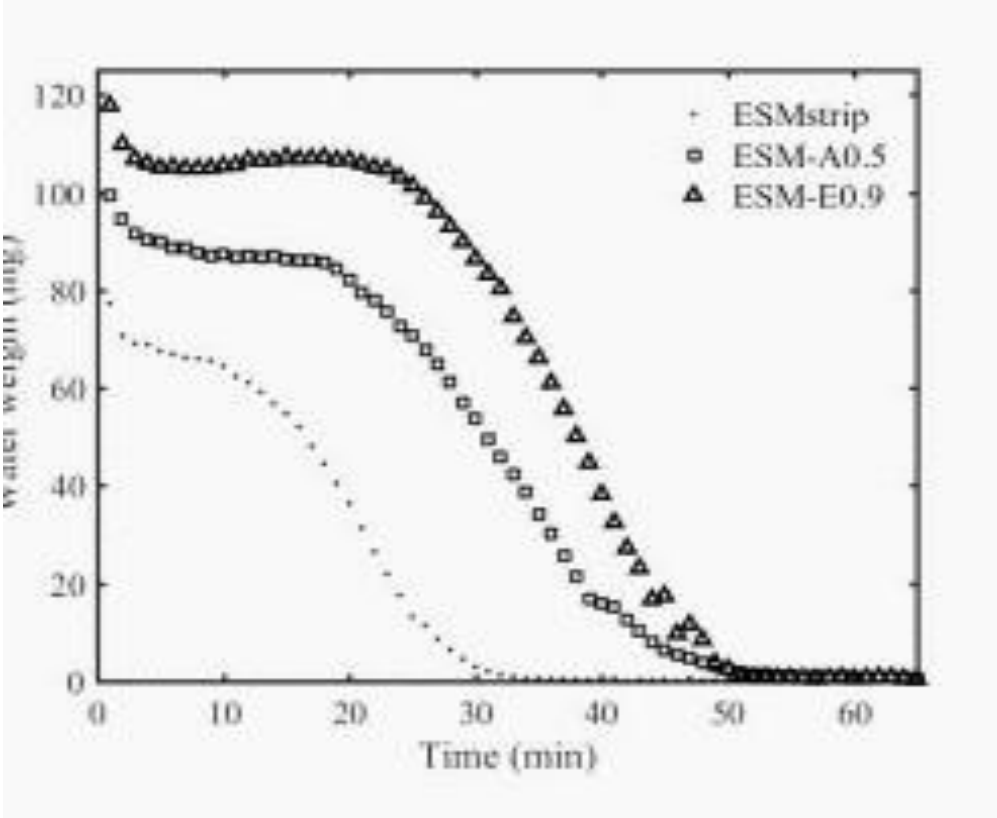

Figure 2.24. Desorption profiles for ESMstrip, ESM-A0.5 and ESM-E0.9.
This a plot of water weight (mg) of ESMstrip, ESM-A0.5 and ESM-E0.9 against time (minutes).

2.4.10.5 In vitro cytotoxicity

An ideal membrane must be nontoxic to healthy tissue (O'Berien, 2011). It is important to sterilize the membrane efficiently before use. The sterilization method might have influence on the membrane's mechanical and biological characteristics. The effects of five sterilization methods, namely, 100 IU/ml penicillin-100 µg/ml streptomycin solution for 24 hours, exposure to ultraviolet UV radiation for 2 hours, penicillin- streptomycin before UV radiation, UV radiation before penicillin- streptomycin and soaking in 70% v/v ethanol for 24 hours for complete evaporation of the ethanol on the burst strength of the outer layer of the ESM was evaluated. In order to ascertain the optimal sterilisation method for cytotoxicity study, OESM-A0.5 was selected, sterilised with 5 different methods and characterised mechanically by measuring their burst strength.

From the results as presented in Figure 2.25, no significant difference was observed comparing the burst strength obtained for the 5 different methods: 100 IU/ml penicillin-100 µg/ml streptomycin solution for 24 hours, exposure to ultraviolet UV radiation for 2 hours, penicillin-streptomycin before UV radiation, UV radiation before penicillin-streptomycin and soaking in 70% v/v ethanol for 24 hours for complete evaporation of the ethanol to the unsterile OESM-A0.5 sample, the control ($p > 0.05$).). This preliminary study showed that the five-sterilization method did not significantly affect the mechanical characteristic of the membrane.

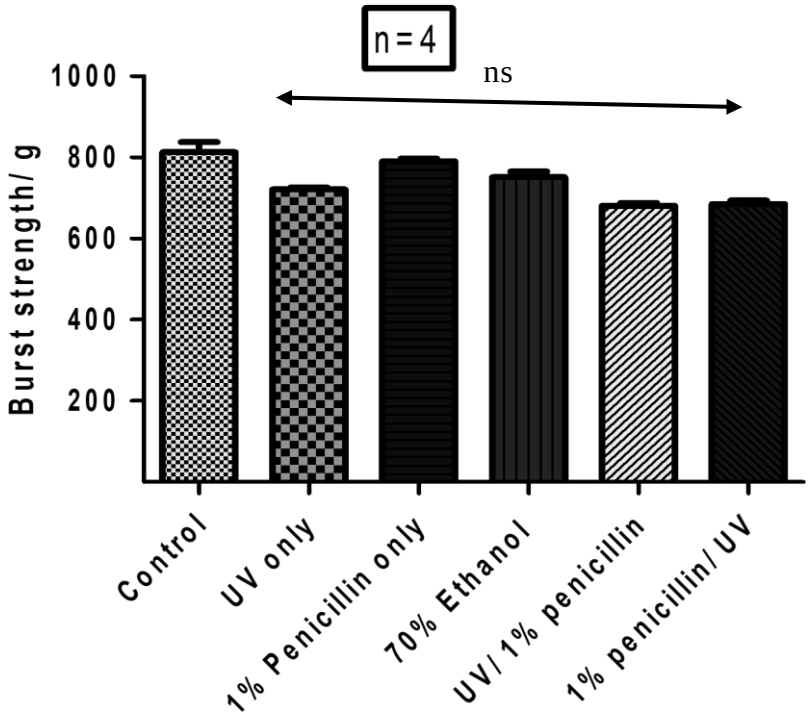

Figure 2.25. Burst strength measurements for the sterilisation methods.
OESM-A0.5 samples were sterilised using 100 IU/ml penicillin-100 μg/ml streptomycin solution for 24 hours, exposure to ultraviolet UV radiation for 2 hours, penicillin- streptomycin before UV radiation, UV radiation before penicillin- streptomycin or soaking in 70% v/v ethanol for 24 hours. The control represents untreated/unsterilised OESM-A0.5 sample. The burst strength was measured using a film support rig attached to a TA. XT instrument (Stable Micro Systems Ltd, Surrey, UK). All values are expressed as mean ± σ for n=4, ns= no significant difference ($p>0.05$). 1-way ANOVA with Bonferroni's multiple comparison post-test ($p >0.05$).

Mitochondrial activity and cell death of the iHCE and C-MSC cells were measured using the MTS and LDH assays, respectively, following *in vitro* culture on the different ESM samples for up to 7 days. As can be seen in Figures 2.26 and 2.27, a notable effect of the inner sides of ESM samples (i.e., LESMstrip, LESM-A0.5 and LESM-E0.9) on the metabolic activities of both cell lines were observed than during culture on the outer side membrane samples (i.e., OESMstrip, OESM-A0.5, OESM-E0.9). In the context of the iHCE cells (Figure 2.26), after 24 hours of culture, no significant difference was observed in each membrane type as compared to the control (TCP). Moreover, on day 3 of culture, no significant differences were observed in cells cultured on LESM-E0.0. However, significant differences were recorded for LESMstrip ($p<0.001$), LESM-A0.5 ($p<0.05$), OESMstrip (($p<0.05$), OESM-A0.5 and OESM-E0.9. The metabolic activities of all the samples increased after day 3 except for the LESMstrip and OESMstrip samples.

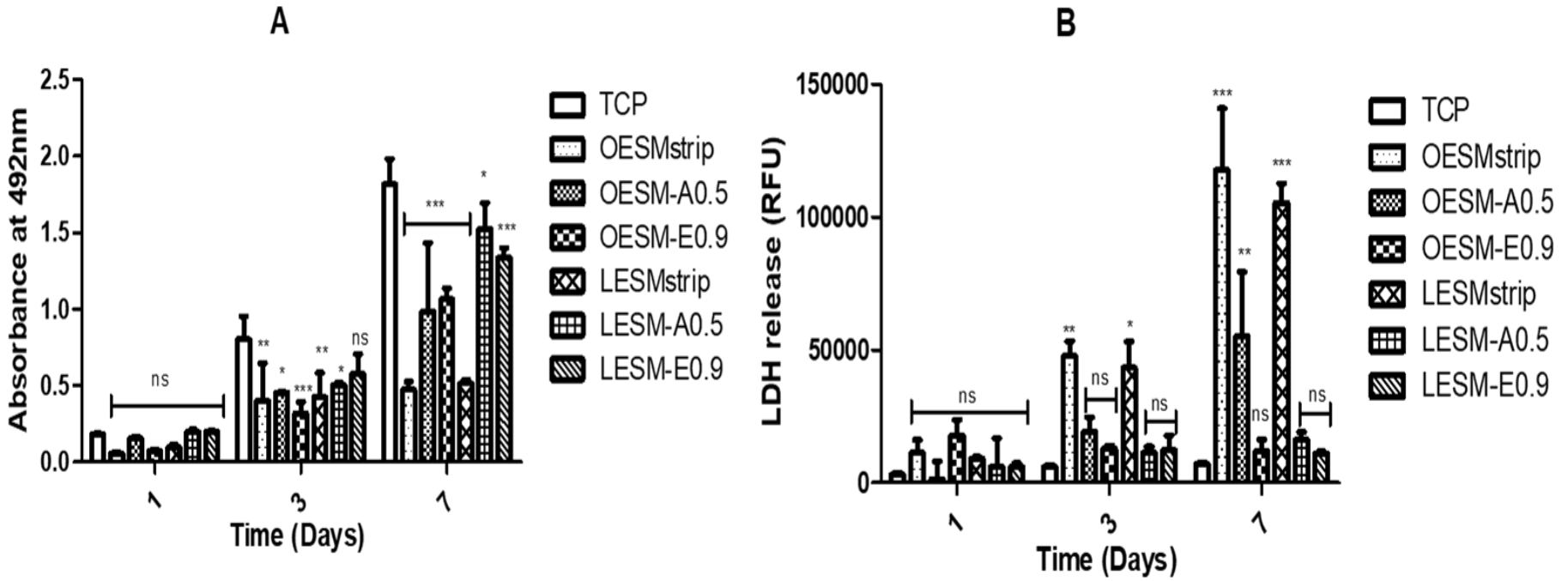

Figure 2.26. Cell metabolic activity and LDH release of iHCE cells cultured on tissue culture plate.
The inner and outer sides of extracted membranes at 204 cells per well density over 7 days. 2-way ANOVA with Bonferroni's Multiple Comparison posttest ($p<0.05$) was applied using TCP as the control. Data are represented as mean σ (n=3). (*$p<0.05$; **$p<0.01$; ***$p<0.001$; ns: no significant difference). (A)Comparison of iHCE cell metabolic activity cultured on different membranes/sides (B)Comparison of iHCE LDH release and cytotoxicity cultured on different membranes/sides.

Lactate dehydrogenase (LDH) is released by cells following a compromised cell membrane i.e., cell death and, as such, the collated LDH results correlate to the mitochondrial activity/MTS data. Figure 2.27 compares the effect of the inner and outer side of the membranes on C-MSC cell function: in short, no statistically different observations could be made between the samples and the control following 24 hours of cell incubation ($p > 0.05$). Intriguingly, a linear increase in the mitochondrial functions of cells attached to ESM were observed over the 7 days and suggest that the cell may be growing in a non-exponential manner but, more importantly, not being subjected to apoptosis and/or necrotic cell death.

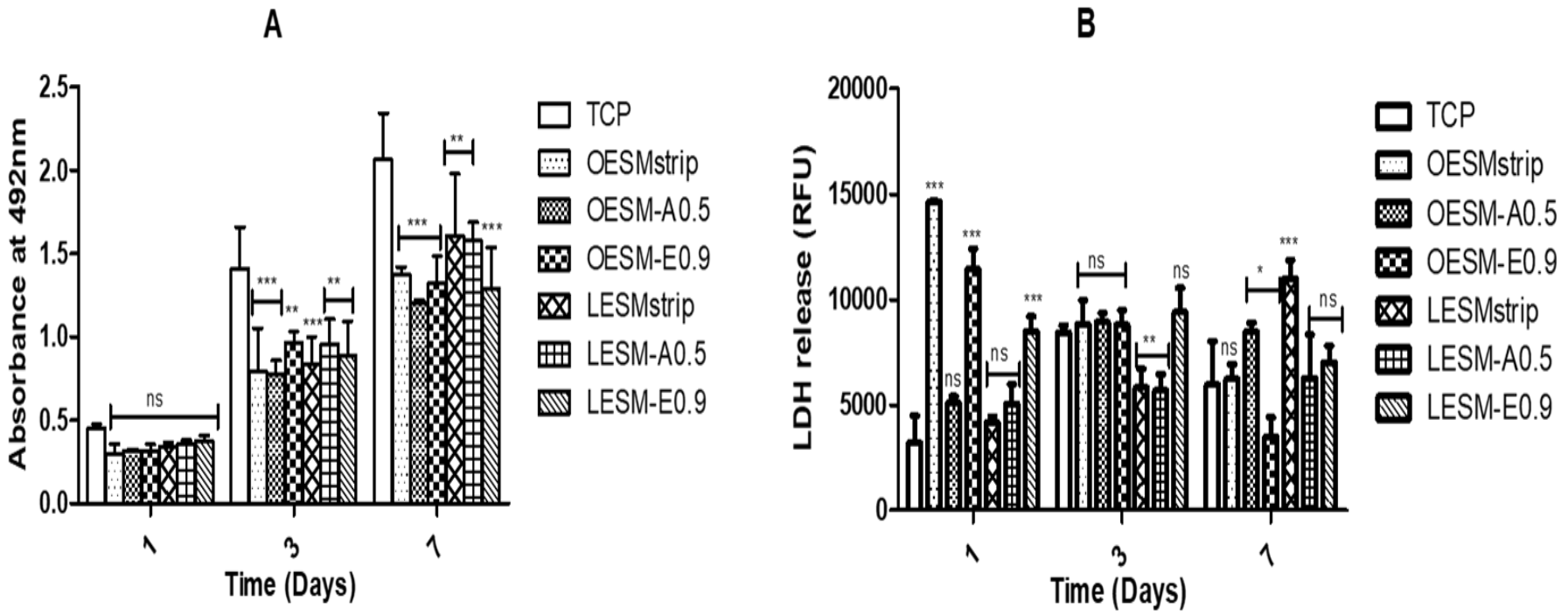

Figure 2.27. Cell metabolic activity and LDH release of MSC-C cells cultured on tissue culture plate.
The inner and outer sides of extracted membranes at 104 cells per well density over 7 days. 2- way ANOVA with Bonferroni's Multiple Comparison post Test ($p<0.05$) was applied using TCP as the control. Data are represented as mean σ (n=3). (*$p<0.05$; **$p<0.01$; ***$p<0.001$; ns: no significant difference). (A)Comparison of MSC-C cell metabolic activity cultured on different membranes/surfaces(B)Comparison of MSC-C LDH release and cytotoxicity cultured on different membranes/surfaces.

Figure 2.28 summarises the attachment and spreading of iHCE and C-MSC cells on OESMstrip, OESM-A0.5, OESM-E0.9, LESMstrip, LESM-A0.5 and LESM-E0.9 samples. It appears that due to the relatively increase in surface area (or smooth topography) of the surface of the inner side of ESM (i.e., LESMstrip, LESM-A0.5 and LESM-E0.9), a great number of cells adhered compared to the contrasting outer side samples (i.e., OESMstrip, OESM-A0.5, OESM-E0.9).This characteristic may seemingly corroborate the observed biocompatibility and biological properties of the cells in terms of degree of attachment, spreading and proliferation of the cells on the ESMs (Mohammadzadeh et al, 2019 and Shafaie et al, 2017).

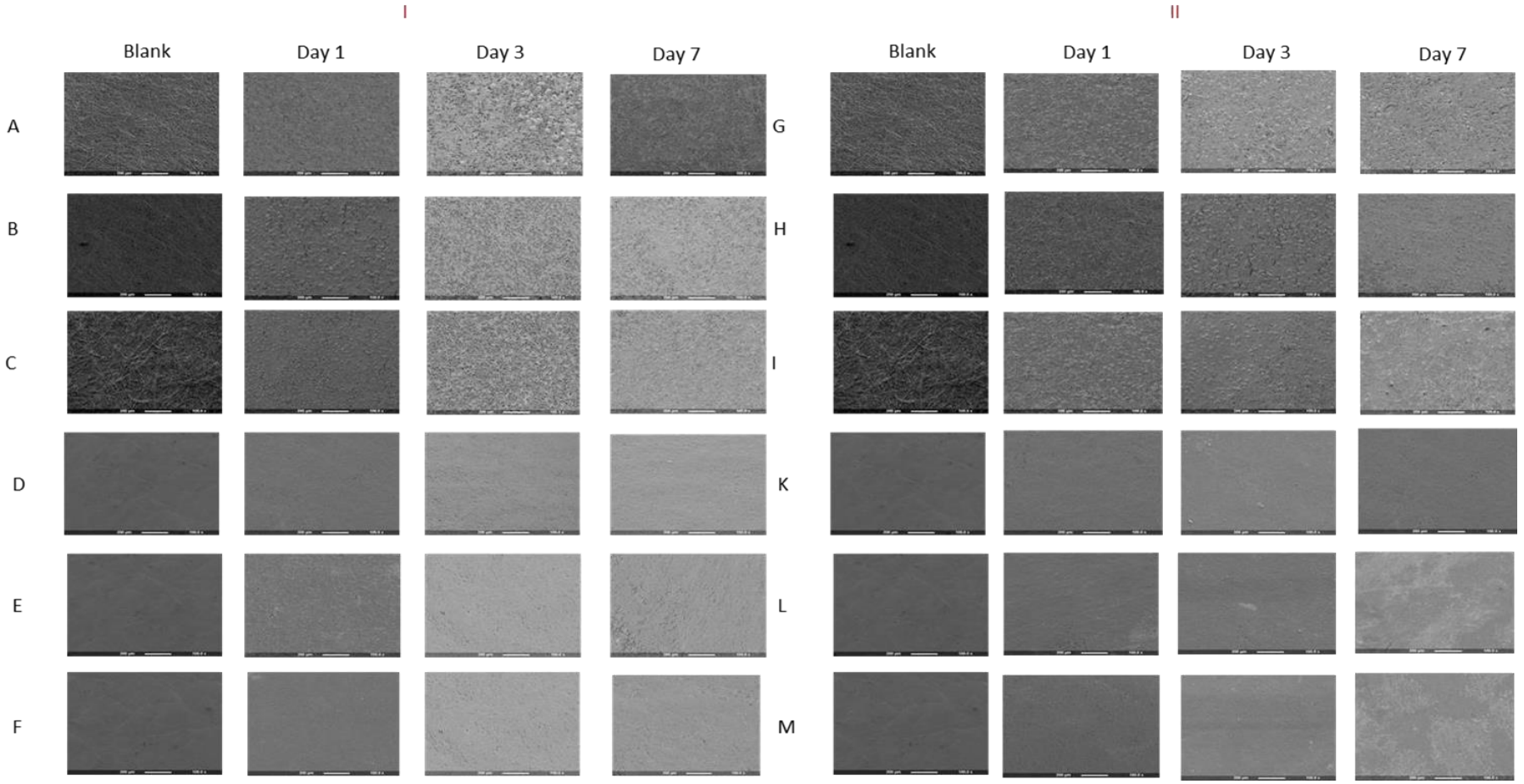

Figure 2.28. SEM images showing (I) the attachment and spreading of iHCE cells ESM samples.
A= OESMstrip, B= OESM-A0.5, C= OESM-E0-9, D=LESMstrip, E= LESM-A0.5 and F= LESM-E0.9. The iHCE cells were cultured for 1. 3 and 7 days. (II)the attachment and spreading of MSC-C cells on G= OESMstrip, H= OESM-A0.5, I=OESM-E0-9, J=LESMstrip, K= LESM-A0.5 and L= LESM-E0.9. The MSC cells were cultured for 1. 3 and 7days. Magnification: 100x

2.4.10.6 Angiogenic profile

Angiogenesis plays a vital role in wound healing and the presence of pro-and anti-angiogenic factors can therefore influence the response and regulation of blood vessel formation (Zadpoor, 2015, Honnegowda et al, 2016, Semenza, 2002 and Shibuya, 2011). In order to assess the angiogenic profile of the ESM, the CAM assay was employed. Figures 2.29A and 2.29B summarise the results obtained from the CAM assay where no treatment, filter paper loaded PBS control, VEGF-a key mediator angiogenic agent, LESMstrip, LESM-A0.5, LESM-E0.9, OESMstrip, OESM-A0.5 and OESM-E0.9 were used and compared to each other. After 10 days of incubation within the CAM, samples were imaged, and the number of branching vessels were determined using AngioQaunt software. According to the results (Figure 2.29B), the VEGF-loaded sample had the most vessel branches ($p<0.001$), while the inner side of the manually peeled ESM, LESMstrip sample had the fewest ($p<0.05$). In contrast, the no-treatment CAM, the PBS control, LESM-A0.5, LESM-E0.9, OESMstrip, OESM-A0.5, and OESM-E0.9 samples did not significantly increase angiogenesis. No data has been reported on the angiogenic potential of ESM to date and, as such, further studies may need to be employed to confirm the behaviour and/or mechanism behind these results. However, it is importantly to note that no detrimental effect had been observed with the ESM samples within the CAM assay. In the context of a biomaterial, having pro- and/or angiogenic capability may be considered as a positive or negative characteristics e.g., minimal blood vessels for optical applications (i.e., transparency) whereas increased blood vessels would be advantageous for a dermal wound dressing.

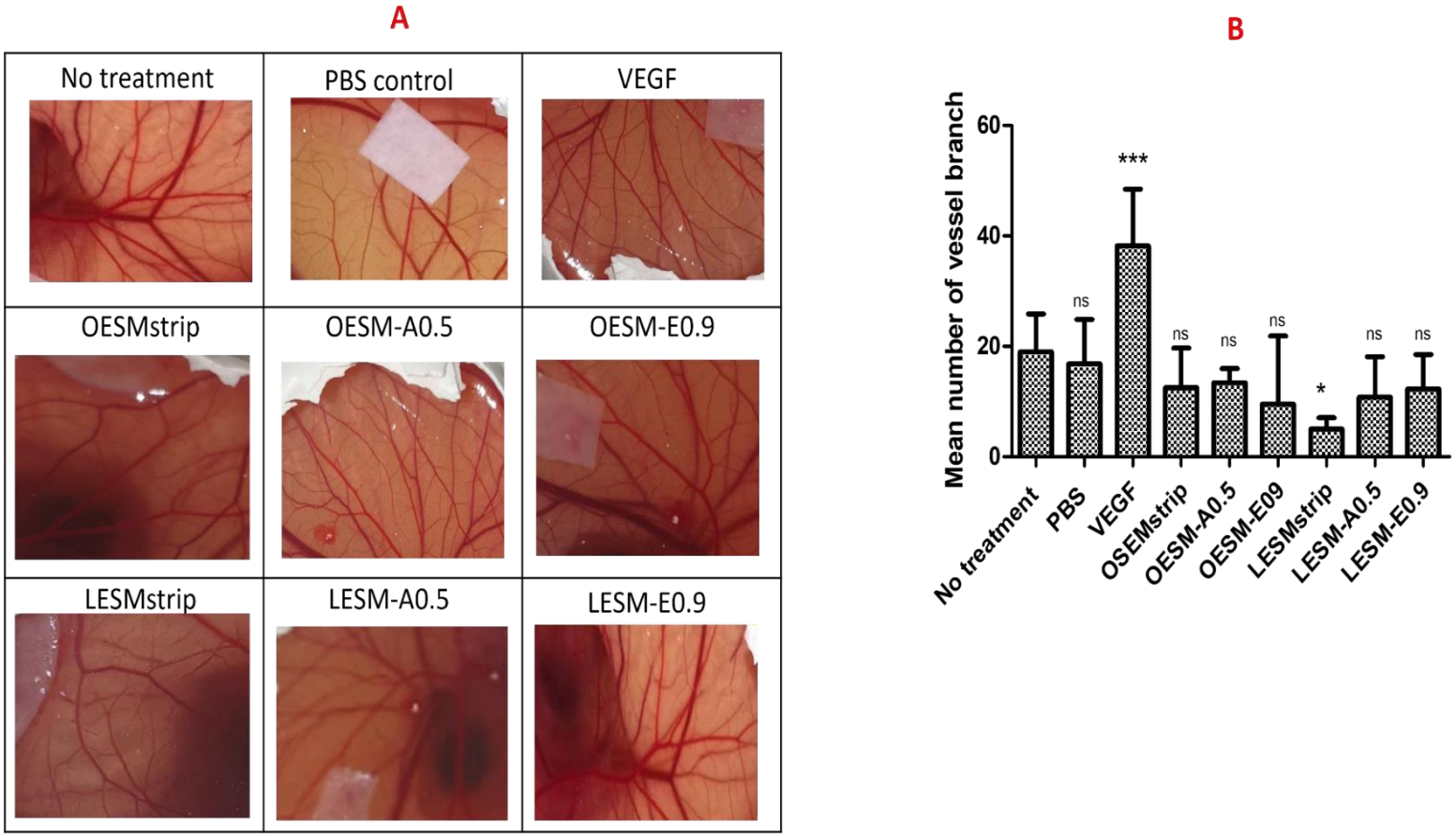

Figure 2.29. Angiogenic profile results
(A) Photographs of the CAM assays, after 10 days of incubation at 37 °C, the presence of extracted ESM samples and controls. VEGF: vascular endothelial growth factor (B) Graph of number blood vessel branches measured using AngioQaunt software expressed as mean ± σ.
* corresponds to $p<0.05$, *** corresponds to $p<0.001$, ns: no significant difference. 1-way ANOVA with Bonferroni's multiple comparison post-test ($p>0.05$).

2.5 CONCLUSION

In this study, two successfully optimised protocols: extraction with 0.5 acetic acid and 0.9M EDTA that can be used to extract the intact membrane from the eggshell without comprising its innate structure or physico-biological characteristics were identified. Accordingly, each specific protocol results in the isolation of an ESM that has defined properties which include membrane thickness, structural arrangement, surface roughness, porosity, swelling profiles, hydrophilicity, elemental composition and transparency. Biocompatibility of these ESMs: LESMstrip, LESM-A0.5, LESM-E0.9, OESMstrip, OESM-A0.5, and OESM-E0.9 were also assessed using cell culture and demonstrated minimal adverse effects- in some instances, increasing cell attachment, spreading and proliferation of the cells. Taken together, these results demonstrate that the ESM could be exploited in a number of regenerative medical and/or biotechnological applications such as a wound dressing substitute or as a culture substrate for the drug discovery pipeline.

2.6 REFERENCES

AHLBORN G, SHELDON B. Identifying the Components in Eggshell Membrane Responsible for Reducing the Heat Resistance of Bacterial Pathogens. Journal of Food Protection. 2006,69(4):729-738.

Ahmed A, Boateng J. Calcium alginate-based antimicrobial film dressings for potential healing of infected foot ulcers. Therapeutic Delivery. 2018,9(3):185-204.

Ahmed T, Suso H, Hincke M. Experimental datasets on processed eggshell membrane powder for wound healing. Data in Brief. 2019, 26:104457.

Ahmed T, Suso H, Maqbool A, Hincke M. Processed eggshell membrane powder: Bioinspiration for an innovative wound healing product. Materials Science and Engineering: C. 2019, 95:192-203.

Alves-Lima DF, Letizia R, Degl'Innocenti R, Dawson R, Lin H. Quantitative video-rate hydration imaging of Nafion proton exchange membranes with terahertz radiation. Journal of Power Sources. 2020. 450:227665

Baláž M. Eggshell membrane biomaterial as a platform for applications in materials science. Acta Biomaterialia. 2014,10(9):3827-3843.

Banerjee A, Panda S, Sidhantha M, Chakrabarti S, Chaudhuri B, Bhattacharjee S. Utilisation of eggshell membrane as an adsorbent for carbon dioxide. International Journal of Global Warming. 2010,2(3):252.

Bellairs R, Boyde A. Scanning electron microscopy of the shell membranes of the hen's egg. Zeitschrift fr Zellforschung und Mikroskopische Anatomie. 1969,96(2):237-249.

Boonprasert P, Tangboriboon N. Electromechanical-Conductive Natural Rubber Doped Eggshell and Eggshell Membrane for Drug Delivery and Actuator Applications. Materials Science Forum. 2018, 934:43-49.

Carmeliet P. VEGF as a Key Mediator of Angiogenesis in Cancer. Oncology. 2005,69(3):4-10.

Cavanagh H. Ocular Surface Disease. Cornea. 2002,21(6):634.

Chau D, Brown S, Mather M, Hutter V, Tint N, Dua H et al. Tissue transglutaminase (TG-2) modified amniotic membrane: a novel scaffold for biomedical applications. Biomedical Materials. 2012,7(4):045011.

Chau, D. Y. S., A. R. Dennis, Lin, H., Zeitler, JA, Tunnacliffe, A. 2016. Determination of water content in dehydrated mammalian cells using terahertz pulse imaging: a feasibility study. Current Pharmaceutical Biotechnology 17(2): 200–207.

Chen L, Kang J, Sukigara S. Preparation and characterization of polyurethane/soluble eggshell membrane nanofibers. Bio-Medical Materials and Engineering. 2014,24(6):1979-1989.

Chen X, Zhu L, Wen W, Lu L, Luo B, Zhou C. Biomimetic mineralisation of eggshell membrane featuring natural nanofiber network structure for improving its osteogenic activity. Colloids and Surfaces B: Biointerfaces. 2019, 179:299-308.

Chi Y, Zhao Y. Characterization of Collagen from Eggshell Membrane. Biotechnology (Faisalabad). 2009,8(2):254-258.

Colatrella N. Amniotic Membrane Therapy in Ocular Surface Disease: Introduction. Journal of Dry Eye Disease. 2019,2(1):e1.

Coover D. The use of egg membrane in ophthalmic surgery. The ophthalmic record. 1899, 8:222-224.

Devi P, Banerjee S, Chowdhury S, Kumar G. Eggshell membrane: a natural biotemplate to synthesize fluorescent gold nanoparticles. RSC Advances. 2012,2(30):11578.

Du L, Huang M, Feng J. Immobilization of α-amylase on eggshell membrane and Ag-nanoparticle-decorated eggshell membrane for the biotransformation of starch. Starch - Stärke. 2017,69(9-10):1600352.

Dua H. Variation and limitations of the amniotic membrane. Acta Ophthalmologica. 2014, 92:0-0.

Foulks G. Understanding Ocular Surface Disease From Uncommon to Extremely Common Afflictions. The Ocular Surface. 2014,12(4):233.

Foulks G. Understanding Ocular Surface Disease From Uncommon to Extremely Common Afflictions. The Ocular Surface. 2014,12(4):233.

Ghaee A, Nourmohammadi J, Danesh P. Novel chitosan-sulfonated chitosan-polycaprolactone-calcium phosphate nanocomposite scaffold. Carbohydrate Polymers. 2017, 157:695-703.

Gocek I, Adanur S. Effect of Processing parameters on polypropylene Film Properties. Modern Engineering Research. 2012,2(5):3056-3060.

Guarderas F, Leavell Y, Sengupta T, Zhukova M, Megraw T. Assessment of Chicken-Egg Membrane as a Dressing for Wound Healing. Advances in Skin and Wound Care. 2016,29(3):131-134.

Honnegowda T, Kumar P, Padmanabha Udupa E, Sharan A, Singh R, Prasad H et al. A comparative study to evaluate the effect of limited access dressing (LAD) on burn wound healing. International Wound Journal. 2015,13(5):791-798.

Hsieh S, Chou H, Hsieh C, Wu D, Kuo C, Lin F. Hydrogen peroxide treatment of eggshell membrane to control porosity. Food Chemistry. 2013,141(3):2117-2121.

Jamshidi Gohari R, Halakoo E, Lau W, Kassim M, Matsuura T, Ismail A. Novel polyethersulfone (PES)/hydrous manganese dioxide (HMO) mixed matrix membranes with improved anti-fouling properties for oily wastewater treatment process. RSC Adv. 2014,4(34):17587-17596.

Jia J, Liu G, Guo Z, Yu J, Duan Y. Preparation and Characterization of Soluble Eggshell Membrane Protein/PLGA Electrospun Nanofibers for Guided Tissue Regeneration Membrane. Journal of Nanomaterials. 2012, 2012:1-7.

Liang M, Su R, Qi W, Yu Y, Wang L, He Z. Synthesis of well-dispersed Ag nanoparticles on eggshell membrane for catalytic reduction of 4-nitrophenol. Journal of Materials Science. 2013,49(4):1639-1647.

Litwiniuk M, Grzela T. Amniotic membrane: New concepts for an old dressing. Wound Repair and Regeneration. 2014,22(4):451-456.

Maharajan V, Shanmuganathan V, Currie A, Hopkinson A, Powell-Richards A, Dua H. Amniotic membrane transplantation for ocular surface reconstruction: indications and outcomes. Clinical and Experimental Ophthalmology. 2007,0(0)

Majsztrik PW, Satterfield MB, Bocarsly AB, Benziger JB. Water sorption, desorption and transport in Nafion membranes. Journal of Membrane Science.301(1):93-106

Mallakpour S, Madani M. Synthesis, structural characterization, and tensile properties of fructose functionalized multi-walled carbon nanotubes/chitosan nanocomposite films. Journal of Plastic Film and Sheeting. 2015,32(1):56-73.

Manolova Y, Stoycheva Z, Yordanov Y, Grupcheva C. Amniotic membrane transplantation – Analysis of structural characteristics in amniotic membrane transplant and corneal ulcers. Scripta Scientifica Medica. 2017,49(1):12.

Mohammadzadeh L, Rahbarghazi R, Salehi R, Mahkam M. A novel egg-shell membrane-based hybrid nanofibrous scaffold for cutaneous tissue engineering. Journal of Biological Engineering. 2019,13(1).

Morooka H, Nagaoka C, Nishimura D, Ito H, Morooka H. Effects of Processed Fabric with Eggshell Membrane on Human Skin Properties. FIBER. 2009,65(7):184-190.

Murube J. Early Clinical Use of Amniotic Membrane in Medicine and Ophthalmology. The Ocular Surface. 2006,4(3):114-119.

Niemisto A, Dunmire V, Yli-Harja O, Wei Zhang, Shmulevich I. Robust quantification of in vitro angiogenesis through image analysis. IEEE Transactions on Medical Imaging. 2005,24(4):549-553.

Niemisto A, Dunmire V, Yli-Harja O, Wei Zhang, Shmulevich I. Robust quantification of in vitro angiogenesis through image analysis. IEEE Transactions on Medical Imaging. 2005,24(4):549-553.

Ohto-Fujita E, Konno T, Shimizu M, Ishihara K, Sugitate T, Miyake J et al. Hydrolyzed eggshell membrane immobilized on phosphorylcholine polymer supplies extracellular matrix environment for human dermal fibroblasts. Cell and Tissue Research. 2011,345(1):177-190.

Parodi B, Russo E, Gatti P, Cafaggi S, Bignardi G. Development and In Vitro Evaluation of Buccoadhesive Tablets Using a New Model Substrate for Bioadhesion Measures: The Eggshell Membrane. Drug Development and Industrial Pharmacy. 1999,25(3):289-295.

Rahman I, Said D, Maharajan V, Dua H. Amniotic membrane in ophthalmology: indications and limitations. Eye. 2009,23(10):1954-1961.

Rolando M, Barabino S, Bentivoglio G, Mingari C, Calabria G. Treatment of Ocular Surface Inflammation in Keratoconjunctivitis Sicca by Means of a Silicon-Hydrogel Bandage Contact Lens Dressed with Amniotic Membrane. The Ocular Surface. 2005,3:S107.

Roy N, Saha N, Kitano T, Saha P. Development and Characterization of Novel Medicated Hydrogels for Wound Dressing. Soft Materials. 2010,8(2):130-148.

Semenza G. HIF-1 and tumor progression: pathophysiology and therapeutics. Trends in Molecular Medicine. 2[C0056002,8(4):S62-S67.

Shafaie S, Hutter V, Brown M, Cook M, Chau D. Influence of surface geometry on the culture of human cell lines: A comparative study using flat, round-bottom and v-shaped 96 well plates. PLOS ONE. 2017,12(10):e0186799.

Shibuya M. Vascular Endothelial Growth Factor (VEGF) and Its Receptor (VEGFR) Signaling in Angiogenesis: A Crucial Target for Anti- and Pro-Angiogenic Therapies. Genes and Cancer. 2011,2(12):1097-1105.

Sidney, L.E., et al., Effect of culture medium on propagation and phenotype of corneal stroma–derived stem cells. Cytotherapy, 2015. 17(12): p. 1706-1722.

Strnková J, Nedomová Š, Kumbár V, Trnka J. Tensile Strength of the Eggshell Membranes. Acta Universitatis Agriculturae et Silviculturae Mendelianae Brunensis. 2016,64(1):159-164.

Tang J, Han L, Yu Y, Kang J, Zhang Y. A label-free immunoassay using eggshell membrane as matrix and poly (diallyl dimethylammonium chloride) as light-scattering enhancer. Luminescence. 2011,26(6):634-639.

Tighsazzadeh M, Mitchell J, Boateng J. Development and evaluation of performance characteristics of timolol-loaded composite ocular films as potential delivery platforms for treatment of glaucoma. International Journal of Pharmaceutics. 2019, 566:111-125.

Torres F, Troncoso O, Piaggio F, Hijar A. Structure–property relationships of a biopolymer network: The eggshell membrane. Acta Biomaterialia. 2010,6(9):3687-3693.

Tsai W, Yang J, Lai C, Cheng Y, Lin C, Yeh C. Characterization and adsorption properties of eggshells and eggshell membrane. Bioresource Technology. 2006,97(3):488-493.

Vega-Estrada A, Alio J. Keratoconus Corneal Posterior Surface Characterization According to the Degree of Visual Limitation. Cornea. 2019,38(6):730-736.

Vynckier AK, Lin H, Zeitler JA, Willart JF, Bongaers E, Voorspoels J, et al. Calendering as a direct shaping tool for the continuous production of fixed-dose combination products via co-extrusion. Eur J Pharm Biopharm. 2015,96: 125–31.

Wang D, Li Y, Liu L, Liu J, Bao M, Yang N et al. Traits of eggshells and shell membranes of translucent eggs. Poultry Science. 2017,96(5):1514.

Whittaker J, Balu R, Choudhury N, Dutta N. Biomimetic protein-based elastomeric hydrogels for biomedical applications. Polymer International. 2014,63(9):1545-1557.

WONG LIONG J, FRANK J, BAILEY S. Visualization of Eggshell Membranes and Their Interaction with Salmonella enteritidis Using Confocal Scanning Laser Microscopy. Journal of Food Protection. 1997,60(9):1022-1028.

WU B. Biosensors for determination of glucose with glucose oxidase immobilized on an eggshell membrane. Talanta. 2004,

Zadpoor A. Mechanics of Biological Tissues and Biomaterials: Current Trends. Materials. 2015,8(7):4505-4511.

Zidan G, Rupenthal I, Greene C, Seyfoddin A. Medicated ocular bandages and corneal health: potential excipients and active pharmaceutical ingredients. Pharmaceutical Development and Technology. 2017,23(3):255-260.

CHAPTER 3:
MICROPARTICLES FABRICATION & OPTIMISATION

3.0 CHAPTER 3: MICROPARTICLES FABRICATION & OPTIMISATION

3.1 INTRODUCTION

In corneal wound healing, the current approaches to accelerate wound closure is the use of ocular bandages and a topically administered drug via eye drops. In reality, the use of eye drops suffers from poor bioavailability thereby the necessity for repeated application, and poor patient compliance that may lead to corneal wound healing complications and poor clinical outcomes (Zidan et al., 2018).

In this chapter, microparticles (MP), a control drug delivery system was used to overcome some of the problems associated with conventional therapy (Ankit, Rishabha and Pramod, 2011, Tamboli et al., 2012, Alagusundaram et al., 2009 and Chau et al., 2010). The fabrication of MP depends on the choice of suitable polymeric materials to act as encapsulant. An ideal polymeric material must be non-toxic, biodegradable, and biocompatible (Giri et al., 2013). In this work, PLGA was chosen for MP fabrication as it possesses the suitable properties, i.e., its readily available and approved by regulatory authorities (i.e., FDA) for clinical use in humans (Tamboli, Mishra and Mitra, 2012).

Comparative studies have shown that the solvent evaporation technique for MP fabrication, a simple method requiring only glassware and a magnetic stirrer is economical, convenient, robust and reproducible technique for MP fabrication (Prior et al., 2000, Lai and Tsiang, 2005 and Khaled et al., 2010). This technique can therefore be used to provide preliminary information regarding the factors that influence the production of MP during scale up (Bodmeier and McGinity, 1987 and Prior et al., 2000). The process factors involved in this method are known to affect the physical properties of the MP produced, such as particle size and dispersity (Freitas, Merkle, Gandee, 2005).

The performance of MP is dependent on the particle size, impacting duration of drug release and

mode of application, e.g., topical vs injectable (Ferreira et al., 2012 and Yadav and Jat, 2013).

Researchers have been able to identify several process factors that influence the formulation of MP by changing one variable at a time to achieve the desired particle sizes (Steinberg and Hunter, 1984). However, this optimisation method is inefficient, and thus costly, and a systematic approach based on design of experiments (DOE) may be beneficial (Steinberg and Hunter, 1984 and Montgomery, 1999). The significance of optimization methodology and DOE in research and development has been demonstrated in several studies (Steinberg and Hunter, 1984, Coates, 1988, Montgomery, 1999 and Kemala, Budianto and Soegiyono,2012). DOE is a systematic technique used to determine the relationship between factors affecting a method and the response produced by the process. The information allows the researcher to identify and select the factors and levels which have significant effects on the final response/output. One such DOE methodology is Taguchi design (Coates, 1988).

Taguchi design is a statistical tool used to optimize factors with complex interrelationship. This design ascertains that not all factors that cause variability can be controlled. The design evaluates and identifies the controllable factors that reduce the effect of the uncontrollable factors (noise factors) (Coates, 1988, Montgomery, 1999 and Nair, Hansen and Shi,2000). Furthermore, for Taguchi design, several factors can be analysed at the same time with few experimental runs. Taguchi design uses an orthogonal array (OA) to estimate the effects of factors on the response mean and variation. An OA means the design is balanced so that factor levels are weighted equally. Hence, each factor can be assessed independently of all the other factors, and the effect of one factor does not affect the estimation of a different factor. This makes it more economical and efficient than conventional experimental methods (for example the ‘one-factor-at-a time' method) (Steinberg and Hunter, 1984, Nair, Hansen and Shi,2000, Packianather, Drake, and Rowlands, 2000, Kim, Kim, and Kim, 2005, Yang, Mather and Fotheringham, 2011 and Huang, Hung and Yang, 2016).

Additionally, Taguchi design uses signal-to-noise (S/N) ratio, a statistical measure of performance to evaluate the data for the responses. This S/N ratio serves a purpose of identifying the correct factors and their optimal levels. The main goal of the experiment is to find the best settings of control factors involved to maximize the S/N ratio (Nair, Hansen and Shi, 2000). Three available standard types of S/N ratios may be chosen depending on the desired performance response: smaller the better (for making the response as small as possible), nominal the best (for reducing variability around a target) and larger the better (for making the response as large as possible) (Phadke, 1989).

The steps of the Taguchi design generally involve (Torkaman, Soltanieh and Kazemian, 2010 and Krishnamoorthy and Mahalingam, 2015):

1. Identifying the aim of the project
2. Identifying the characteristic and its measurement method
3. Determining the factors that may affect the quality characteristics and their levels
4. Selecting the suitable orthogonal arrays and assigning the factors at their levels to the orthogonal array
5. Conducting the experiment described by the trials in the orthogonal array.
6. Analysing the experiment data using signal to noise ratio, response plot and analysis of the variance (ANOVA) to evaluate and identify which factors are statistically significant and finding the optimum levels of factor and
7. Verifying the ideal design factors through confirmation experiment.

In this chapter, the use of Taguchi OA designs to explore the effect of process factors on particle size using single o/w evaporation technique to obtain a drug delivery for ocular application is investigated. Furthermore, the various characterizations of the protein loaded MP produced with the optimised formulation model are outlined.

3.2 MATERIALS

PLGA copolymers with lactic: glycolic acid ratios of 1:1 (MW: 29-38 kDa) were purchased from Evonik (Darmstadt, Germany). PVA samples: 98 % hydrolysed (MW: 13-23 kDa), 99+ % hydrolysed (MW:146-186 kDa), 99+ % hydrolysed (MW: 89-98 kDa), phosphate buffer saline (PBS), albumin–fluorescein isothiocyanate conjugate (FITC-BSA), lysozyme (LZM), QuantiPro Bicinchoninic Assay (BCA) and lysozyme detection kits were obtained from Sigma-Aldrich (Poole, Dorset, UK). Anhydrous dichloromethane (≥99.8 % with 50-150 ppm amylene as stabiliser) and ethyl acetate (≥ 99.5 %) were purchased from Fisher Scientific (Loughborough, Leicester, UK).

3.3 METHODS

3.3.1 Design of experiment

Taguchi OA design was employed in this study to explore the effect of 10 processing factors on particle size using the solvent evaporation technique. These factors were: concentration of PVA, molecular weight of PVA, concentration of PLGA, type of solvent (i.e., DCM, EAc), concentration of PVA in the hardening bath, stirring speed, ratio of organic/aqueous phases, vortexing speed, duration of speed and time for solvent evaporation. The aim was to generate a formulation model to produce 10–50 μm (Prior et al., 2000, Lai and Tsiang, 2005 and Khaled et al., 2010. PLGA MP which has been suggested to be to most suitable for topical and ocular applications. PLGA copolymers with lactide: glycolide ratios of 50:50 was utilized in this research due to the proposed end-point therapeutic application.

3.3.1.1. Selection of factors and levels

In a typical solvent evaporation technique, an extensive number of processing factors can influence the MP size (response). In this study, ten factors (concentration of PLGA, type of solvent, molecular weight of PVA, concentration of PVA in primary emulsion, vortexing speed, vortexing duration, organic/aqueous phase ratio, concentration of PVA in hardening bath, stirring speed and duration of solvent evaporation) deemed experimentally controllable that influence particle size were identified by assessing relevant literature. Bible et al., (2009) identified polymer concentration, vortexing speed and duration, speed of hardening bath and PVA concentration as possible important factors which affect particle size. Vyslouzil et al., (2014) conducted the study of the influence of a stirring speed (600, 1000 rpm), PVA concentration (0.1%, 1% w/v) and organic solvent (DCM, EAc) during the formulation of drug loaded PLGA microspheres. Sharna, Madan and Lin (2016) included homogenization speed, evaporation time, surfactant concentration, organic/aqueous phase ratio, PLGA polymer type and concentration as process factors for the formation of paclitaxel loaded PLGA nanoparticles using modified solvent evaporation method.

3.3.1.2 Taguchi OA design of experiments

Two types of Taguchi OA designs were implemented to develop a model for optimal PLGA MP formulation to produce a particle size in the range 10–50 μm. Taguchi design was employed to study only the main factor effects. Taguchi L12 (2^{10}) OA design (12, 2 and 10) represent the number of experiments, levels, and factors respectively) was initially employed to study ten factors at two levels: low and high (Table 3.1). The levels of the factors were selected based on an established protocol by Bible *et al.* (2009).

Table 3.1. 10 factors and associated levels used in L12 design

Factor	Name	Units	Levels	
			Low	High
A	Conc. of PLGA	%w/v	10	20
B	Solvent type	-	DCM	EAc
C	MW of PVA	Da	Low	High
D	Conc. of PVA in primary emulsion	%w/v	0.3	1.2
E	Vortexing speed	scale	5	8
F	Vortexing duration	Seconds	45	90
G	Organic/aqueous phase ratio	v/v	1:1	1:3
H	Conc. of PVA in Hardening Bath	%w/v	0.3	1.2
J	Stirring speed	rmp	400	900
K	Solvent evaporation duration	hours	18	24

The results produced by the L12 OA design were fed into the second design: the factors selection for Taguchi L18 (21) (3^7) OA design (18 = the number of experiments, 2 and 3 = levels, and 1 and 7 = the factors) were guided by the analyses of a half-normal plot, Pareto chart and response plot generated for the L12 OA design. In the L18 OA design, the number of factors was reduced to 8 and the number of levels for 7 factors were increased to 3: low, medium and high (Table 3.2).

Table 3.2. 8 factors and associated levels used in L18 design

Factor	Name	Units	Levels		
			Low	Medium	High
A	MW of PVA	Da	13,000	89,000	
B	Conc. of PLGA	%w/v	15	20	30
C	Conc. Of PVA in primary emulsion	%w/v	0.8	1.2	2.0
D	Organic/aqueous phase ratio	v/v	1:0.75	1:1	1:2
E	Vortexing speed	scale	3	5	9
F	Vortexing duration	seconds	60	90	120
G	Stirring speed	rmp	100	400	1200
H	Solvent evaporation duration	hours	20	24	48

The L12 OA and L18 OA data generated by design-expert software version 10 (Stat-Ease, Inc., USA) are presented in Tables 3.3 and 3.4 respectively. Each row in these tables represents a formulation run with the level of the factors. The "X50" particle size value representing the median particle diameter was taken as the response. All runs were performed in triplicate.

Table 3.3. Combination of parameter levels of L12 OA design

Run	A (%w/v)	B	C (Da)	D (%w/v)	E (scale)	F (sec)	G (v/v)	H (%w/v)	J (rpm)	K (h)
1	10	DCM	low	0.3	5	45	1:1	0.3	400	18
2	10	DCM	low	0.3	5	90	1:3	1.2	900	24
3	20	EAc	low	1.2	5	90	1:1	0.3	400	24
4	20	EAc	high	0.3	5	45	1:1	1.2	900	18
5	20	DCM	high	1.2	5	45	1:3	1.2	400	24
6	10	EAc	low	1.2	8	45	1:3	1.2	400	18
7	20	DCM	low	1.2	8	90	1:1	1.2	900	18
8	20	DCM	high	0.3	8	90	1:3	0.3	400	18
9	10	EAc	high	1.2	5	90	1:3	0.3	900	18
10	20	EAc	low	0.3	8	45	1:3	0.3	900	24
11	10	DCM	high	1.2	8	45	1:1	0.3	900	24
12	10	EAc	high	0.3	8	90	1:1	1.2	400	24

Note. Low = Mw: 13–23 kDa, High = Mw: 146–186 kDa

Table 3.4. Combination of parameter levels of L18 OA design

Run	A (Da)	B (%w/v)	C (%w/v)	D (v/v)	E	F (sec.)	G (rmp)	H (hrs)
1	13000	15	1.2	1:1	5	90	400	24
2	89000	30	0.8	1:2	5	120	200	24
3	13000	20	2.0	1:2	3	60	400	24
4	89000	20	2.0	1:0.75	5	120	400	20
5	89000	15	1.2	1:0.75	3	120	1200	24
6	13000	30	1.2	1:2	5	60	1200	20
7	89000	15	2.0	1:1	5	60	200	48
8	13000	30	0.8	1:1	3	120	400	48
9	13000	20	1.2	1:1	9	120	200	20
10	13000	30	2.0	1:0.75	9	90	200	24
11	13000	15	2.0	1:2	9	120	1200	48
12	89000	20	1.2	1:2	3	90	200	48
13	89000	30	1.2	1:0.75	9	60	400	48
14	13000	15	0.8	1:0.75	3	60	200	20
15	89000	15	0.8	1:2	9	90	400	20
16	89000	20	0.8	1:1	9	60	1200	24
17	89000	30	2.0	1:1	3	90	1200	20
18	13000	20	0.8	1:0.75	5	90	1200	48

3.3.2 Microparticle fabrication

3.3.2.1 Blank PLGA Microparticles

PLGA MP were fabricated using a single o/w emulsion technique (Figure 3.1). For the L12 design, 12 formulation runs were applied to produce MP of different sizes. Accordingly, 0.5 or 1.0 g of PLGA were weighed and dissolved in 5 ml of DCM or EAc in a glass vial and incubated overnight at 19 ˚C to form a PLGA solution. 3.0 or 12.0 g of either 13 or 146 kDa PVA were completely dissolved in 1 L deionized water heated at 90 ˚C using an IKA heated magnetic stirrer (RCT basic, UK) at 800 rpm, followed by filtration.

A hardening bath was formed by transferring 200 ml of filtered 0.3 or 1.2% w/v PVA solution into a 250 ml glass beaker with a magnetic stirrer bar. 5 or 15 ml of the filtered 0.3 or 1.2% w/v PVA solution was added to the 10 or 20% w/v PLGA solution and shaken with Vortex-Genie1 2 at a scale of 5 or 8 for 45 or 90 s (Scientific Industries, lnc, NY, USA) to form an o/w emulsion. The o/w emulsion was then added slowly to the hardening bath and stirred at either 400 or 900 rpm for 18 or 24 h for complete evaporation of the organic solvent and hardening of the MP. The MP were harvested using Whatman-grade 1 filter paper under vacuum. MP were then washed three times with distilled water before being transferred to glass vials for freeze drying (MechaTech Systems Ltd, Bristol, UK) for 24 h.

The PLGA MP in the L18 design were fabricated with the same single o/w emulsion technique (Figure 3.1) and 18 different formulation runs were used. PVA solution at different concentrations was prepared by completely dissolving 8.0, 12.0 or 20.0 g of either 13 or 89 kDa PVA in 1 L deionized water. In order to form the o/w emulsion, 0.75, 1.0 or 1.5 g of PLGA were dissolved in 5 ml of EAc and added to either 3.75, 5 or 10 ml of 0.8, 1.2 or 2.0% w/v PVA solution. The solution was emulsified for 60, 90 or 120 s at a scale of either 3, 5 or 9. The o/w emulsion was homogenized into the hardening bath consisting of 200 ml of 0.3% w/v PVA (MW 13 kDa). The emulsion was stirred at either 100, 400 or 1200 rpm for 20, 24 or 48 h to

ensure complete organic solvent evaporation. The prepared MP were collected, washed, and freeze-dried for 24 h.

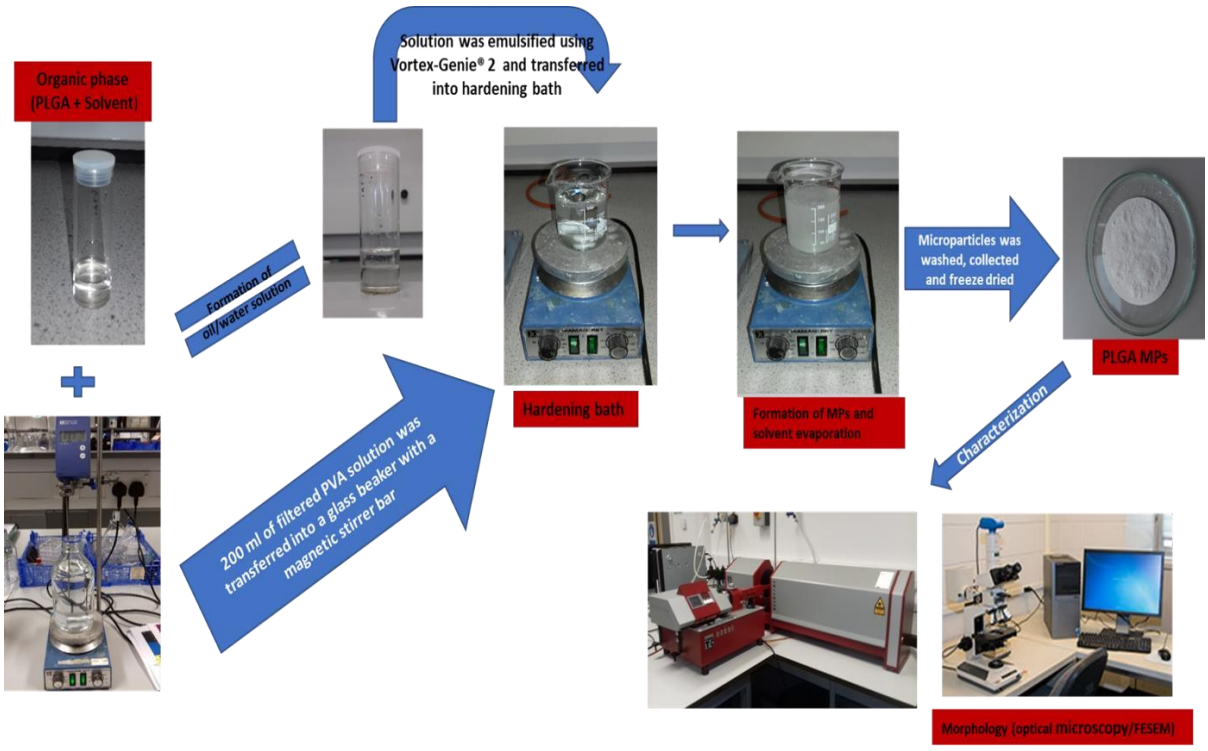

Figure 3.1. Photograph of single o/w emulsion technique.
Single o/w emulsion method displaying the various steps in creating microparticles (Bible et al., 2009 and Mensah et al., 2018).

3.3.2.2 Protein-loaded Microparticles

The model formulation produced by the initial Taguchi method was exploited in the fabrication of protein loaded PLGA MP. FITC-BSA was used as the model protein drug and conducted to validate the optimal locations of the factor levels and to investigate the effect of incorporated drugs on the particle size distribution. For the purpose of confirming the retention of protein activity after the fabrication of the MP and the release of the protein, LZM was encapsulated in MP. Briefly, 5, 10 or 20 mg FITC-BSA or 20 mg LZM was dissolved in 5 ml of ethyl acetate in which 1 g of PLGA polymer was completely pre-dissolved. A primary emulsion of the protein /PLGA/EAc and PVA solution was formed and vortexed to create the microparticles. Thereafter, the emulsion was added to a hardening bath for allow for complete

evaporation (24 h). The hardening bath was completely covered with aluminium foil to exclude light. The supernatant was collected before the filtering, washing, and freeze-drying of the generated particles. The protein loaded MP produced were termed as FBM-1, FBM-2, FBM-3 and LZM-MP representing 5, 10 or 20 mg FITC-BSA and 20 mg LZM loaded in the MP respectively.

3.3.3 Characterization

3.3.3.1 Particle size measurements

3.3.3.1.1 Optimisation of instrument parameters

The MP with the smallest and largest particle size produced from the Taguchi L12 (2^{10}) OA design was employed to define the instrument parameters. Using an optical microscopy, Meiji EMT microscope (Meiji Techno, Somerset, UK), approximately 5 mg of the MP were homogenously dispersed on a microscope slide and images were taken using GX CAM digital camera at 4x magnification. The particle sizes were analysed using *ImageJ*® software. Six individual measurements of ferret diameters (µm) were taken for each MP produced. The MP with the smallest (from Run 3) and largest (from run 4) particle sizes were selected and subsequently used in the dry dispersion laser diffraction (DDLD) and wet dispersion laser diffraction (WDLD).

The WDLD particle size analysis of run 3 and 4 were carried using a SymPatec HELOS combined with QUIXEL cuvette (Germany) fitted with R5 (4.5 to 875 µm). Saturated liquid dispersants (PVA) were prepared by sonication using the factors defined in Table 3.5. Approximately 5 mg of the MP were added the 20 ml of dispersant and at equilibrium of 60 seconds, three individual measurements of the particle size distribution (X10:10th percentile, X50:50th percentile and X90: 90th percentile) and volume mean diameter (VMD) were taken for each MP sample.

The particle size distribution of run 3 and 4 were measured by LD using a SymPatec HELOS equipped with a RODOS/ASPIROS dry dispenser (Germany) and R5 (4.5 to 875 µm). About

5 mg of each sample was placed in an ASPIROS glass vial, and the measurement was set to trigger when the optical concentration (C_{opt}) surpassed 0.1 % and stop when the C_{opt} fell below 0.2 % for 5 s (or 5 s real time). the time base was 50 ms and the primary pressure was manually set using the adjustment valve in the range 0.2-6.0 bar for run 4 and 0.2-4.5 bar for run 3. Three measurements were taken at each pressure setting using freshly loaded MP. The particle size distribution (volume mean diameter, X10, X50, X90) were analysed in WINDOX 5 software (SymPatec, Germany). A graph of particle size (X50) against the pressure was generated to identify the pressure at which the particle size-primary pressure profile reaches a plateau.

Table 3.5. A summary of laser diffraction (LD) parameters used in PLGA MP size analysis

Run	Dispersant (%, w/v)	Sonication time (mins)	Stir setting	Sweeps (rmp)	Equilibration time (s)
4	1.0% PVA	15	3	2500	60
7	1.0% PVA	5	3	2000	60

3.3.3.1.2 Particle size/polydispersity analysis of blank and protein loaded MP.

The optimised DDLD obtained was used to measure the particle size distribution of the Taguchi OA designs and the protein loaded MP. All measurements were performed using the R5 (4.5 to 875 µm) and R3 (0.5 to 175 µm) lens for L12 and L18 designs, respectively. The particle size analyses of the FITC-BSA and LZM loaded MP were evaluated using the DDLD method for the L18 design. The particles were dispersed under a 4-bar pressure. About 5 mg of each sample was placed in an ASPIROS glass vial. The particle size distribution (VMD, X10, X50, X90) were analysed with WINDOX 5 software (SymPatec, Germany). The particle size distributions were applied to determine the polydispersity (PDI) of the blank and protein loaded MP. The PDI was calculated using the equation 3.1 below:

$$\text{PDI} = \frac{X90 - X10}{X50} \qquad \text{Equation 3.1}$$

3.3.3.2 Surface morphology

Surface morphology and shape of the MP fabricated by formulation runs and the protein loaded MP were obtained using a scanning electron microscope (JOEL JCM-5700, USA). The dried MP samples were deposited onto adhesive carbon tabs (Agar Scientific G3357N), which were pre-mounted onto aluminum stubs (Agar Scientific JEOL stubs G306). The samples were gold sputtered for 60 s to attain a thickness of approximately 30 nm (Quorum SC7620). The morphologies of the MP samples were analysed at magnifications of 500X.

3.3.3.3 Protocol validation

The method and protein assay (Micro-QuantiPro™ BCA Assay) used in the protein loading and release profiles were validated by measuring the following parameters: linearity, limit of detection (LOD) and limit of quantification (LOQ). The buffers used in the study were water and PBS for entrapment/loading and *in vitro* release profiles respectively. For linearity study, calibration curves were constructed for concentration range of 0-20 µg/ml and 0.5-20 µg/ml of FITC-BSA in water and PBS, respectively. Considering the calibration curves for LZM in water and PBS, 0.5-20 µg/ml and 1.0-20 µg/ml concentration ranges were used, respectively. The LODs and LOQs of each protein in water or PBS were evaluated using the standard deviation of the y-intercepts (σ) and the slope (S) of the calibration curve (equation 3.2 and equation 3.3) (Mondal, Pal and Ghosal, 2009).

$$LOD = 3.3\ \frac{\sigma}{S} \qquad \text{Equation 3.2}$$

$$LOQ = 10\ \frac{\sigma}{S} \qquad \text{Equation 3.3}$$

3.3.3.4 Percentage yield, protein entrapment and loading

The percentage yield (Y%) of the protein loaded MP were deduced from equation 3.4. Practical yield is the weight of MP obtained after encapsulation and theoretical yield equals to the total weight of the PLGA polymer and weight of the protein added. Encapsulation efficiency (EE%) and loading capacity (LC%) were evaluated, through the indirect method of determining the amount of FITC-BSA or LZM in the supernatant (water and free unentrapped protein), using Micro-QuantiPro™ BCA Assay Kit (Sigma-Aldrich, Poole, Dorset, UK). The amount of protein not encapsulated was obtained and thereafter, a mass balance calculation was performed to determine the amount of FITC-BSA or LZM loaded into the MP. The EE% and LC% were determined by the equation 3.5 and 3.6 below:

$$Y\% = \frac{Practical\ \ yield}{theoritical\ \ \ yield} x\ 100 \qquad \text{Equation 3.4}$$

$$EE\% = \frac{total\ protein\ \ added - free\ \ \ unentrapped\ \ \ protein}{total\ \text{protein}\ \ added} \qquad \text{Equation 3.5}$$

$$LC\% = \frac{amount\ \ of\ protein\ \ \ entrapped}{total\ \ microparticle\ \ \ weight} \qquad \text{Equation 3.6}$$

3.3.3.5 *In vitro* release profile

The *in vitro* protein release was determined using a method described by Determan *et al.*, 2016 with slight modification (set up image shown in Figure 3.2). Briefly, 50 mg of FITC- BSA or LZM loaded PLGA MP were suspended in 3 ml of PBS. The samples were placed in a water bath at 37 °C and continuously stirred at 100 rpm. Sample volumes of 3 ml were collected at different times within 28 days. Each time, fresh preheated PBS was reintroduced to maintain sink conditions. The FITC-BSA samples were centrifuged and the concentration of the protein in each sample was determined using Micro-QuantiPro™ BCA Assay kit. The QuantiPro working reagent was prepared by mixing 7.25 ml of Reagent QA, 7.25 ml of Reagent QB and 0.29 ml pf Copper (II) Sulphate reagent QC. 150 µl of the FITC-BSA samples were pipetted into a 96 wells plates and 150 µl of the QuantiPro working reagent was added. The plate was

covered with aluminum foil and incubated for 2 h in a water bath at 37 °C. The absorbance at 562 nm was measured using BioTeck micro plate reader and the protein concnetration was determined by using the calibration curve. LZM samples were collected for protein activity assay. All experiments were performed in triplicate.

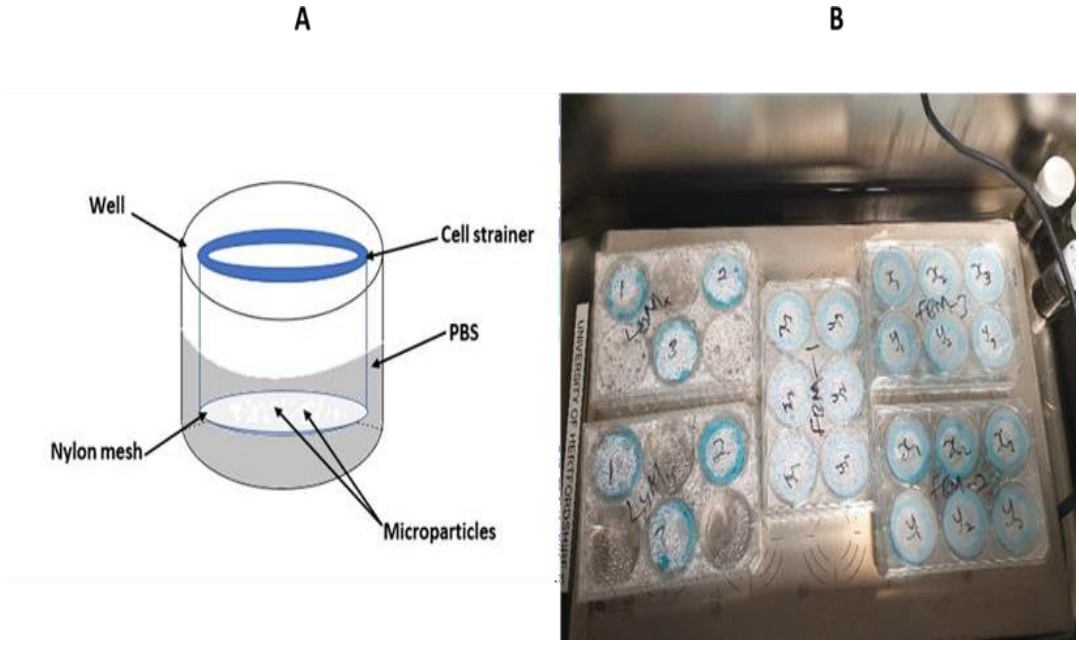

Figure 3.2. *In vitro* drug release study
(A) Schematic diagram of *in vitro* release study set up for FITC-BSA and LZM loaded microparticles. (B) Photographic image of release study set. 50 mg of the MP were weighed and placed in Falcon™ cell strainer with nylon mesh size of 40 µm with magnetic stirrer and placed 6 well plate. The MP were suspended in 3 ml of phosphate sulphur buffer (PBS, pH 7.4) and were placed in a water bath at 37 °C and continuously agitated at 100 rpm. At predetermined times within 28 days, the supernatant was collected, and fresh PBS was added to maintain sink condition.

3.3.3.6 Protein activity

The lysozyme activity tests were conducted using Sigma-Aldrich lysozyme detection kit (Poole, Dorset, UK). A cell suspension was prepared by dissolving *Micrococcus lysodeikticus* cells in 66 mM phosphate buffer (Reaction buffer). In a 96 well plate, 190 µl of the cell suspensions were added and equilibrated at 25 °C using BioTeck microplate reader. The absorbance at 450 nm (A_{450}) of the cell suspensions used were in the range of 0.6 – 0.7 before the addition of 40 µl of the reaction buffer, and LZM samples obtained from the *in vitro* release set up in the 28 days period (Figure 3.2). Similarly, the A_{450} of these selected concentrations

were measured. The plate was mixed by immersion and the measurements of the decrease in A_{450} were carried over a period of 0-6 mins at 1 min interval. The change in the activity of the concentration of lysozyme released on day 0, 1, 4, 7, 10, 14 and 28 were determined.

3.3.4 Statistical analysis

The experimental design results were statistically analysed using Design-Expert software version 10.0.5.0 (Stat-ease- Inc., Minneapolis). Response and interaction plots were generated to examine the effect of factor levels on the mean response (particle size). Half-normal plots and Pareto charts were generated to guide the selection of factors for the final optimal model. The data were assessed by ANOVA combined with Fisher's statistical test (F- test) to determine whether a chosen factor had a significant effect on the desired value ($p < 0.05$). The S/N ratio formula below (i.e., smaller-the-better) was used to evaluate the response values. All data presented were expressed as mean and standard deviation.

$$\text{S/N ratio} = -10 * \log(\Sigma \frac{Y2}{n}) \qquad \text{Equation 3.7}$$

3.4 RESULTS & DISCUSSIONS

3.4.1 Experimental design

The solvent evaporation method has been used widely to encapsulate drugs in polymer matrices to form delivery systems and involves many processing factors which are known to affect the physical properties of MP produced, such as particle size (Prior et al., 200, Lai and Tsiang, 2005 and Khaled et al., 2010). The MP size is important in determining the drug release profile and mode of application (Freitas, Merkle and Gander, 2004 and Bidone et al., 2009). Therefore, there is a need for careful selection of the process factors in order to formulate the most appropriate MP size. The optimization of the method by treating one factor at a time is impractical. As such, this study employed the use of a Taguchi orthogonal arrays design of experiment protocol to assess the optimal conditions required for the fabrication of 10–50 μm sized MP and to identify the factors that deemed to most significantly influence PLGA MP size. This design assumes that there is no interrelationship between any two factors. However, clear evidence of interaction was observed between concentration of PLGA and solvent type, although this interaction had no effect on the particle size. This is because in each formulation run the PLGA polymer was dissolved in a constant volume (5 ml) of solvent type stated in the run.

3.4.1.1 L12 OA design

The Taguchi design DOE approach was explored to identify the process factors in the solvent evaporation technique with the most significant effects on PLGA MP size and to generate a predictive model. L12 OA design was used as the first optimization step in the DOE. The factors and their levels for the L12 OA design (Table 3.1) were selected based on previous studies using the solvent evaporation method for MP fabrication (Bible et al., 2009, Torkaman, Soltanieh and Kazemian, 2010 and Vyslouszil et al., 2014). From the design, ten factors at two levels were investigated, namely, concentration of PLGA (A), solvent type (B), MW of PVA

(C), concentration of PVA in primary emulsion (D), vortexing speed (E), vortexing duration (F), organic/aqueous phase ratio (G), concentration of PVA in hardening bath (H), stirring speed of the hardening bath (J), and solvent evaporation duration (K), with particle size as a response. This design resulted in 12 formulation runs (36 runs in total, three replicates for each run). PLGA MP were then successfully fabricated using the 10 factors combinations.

Table 3.6 shows the factor levels combinations computed by design-expert software for and the median particle size measurement by laser diffraction using a SymPatec HELOS equipped with a RODOS/ASPIROS dry dispenser (Germany). The rows represent the formulation runs and the column represents the factors. All the level settings in each formulation run appeared an equal number of times: for each factor, low level and high level appeared 6 times. The data with the average median particle size ranging from 54.39 to 200.37 μm was produced for the design. The data had a mean of 103.42 ± 41.55 μm. None of the runs produced MP within the goal range of 10-50 μm. Nonetheless, Run 3 (54.39 μm) created MP with smallest median particle size closed to the upper range value.

MP with smallest median diameter (run 3) were obtained from an organic phase comprising of EAc and 20 % w/v PLGA polymer, and an aqueous phase of low molecular weight of 1.2 % w/v PVA which were combined at a ratio of 1:1 to form a primary emulsion by a vortexing with speed at scale 5 for 90 s. The emulsion was introduced to a hardening bath of 0.3 % w/v PVA at a speed off 400 rpm and the MP created were hardened at complete solvent evaporation for 24 h (Run 3). The largest particle size was registered with 10 % w/v PLGA concentration, DCM, 0.3 % w/v (low MW) PVA in primary emulsion, vortexing speed at scale 5, vortexing duration of 45 s, 1:1 organic/aqueous phase ratio, 0.3 % w/v PVA in hardening bath, 400 rpm stirring speed and 18 h evaporation duration (Run 1).

Table 3.6. Results produced for combination of parameter levels of L12 OA design

Run	A (%w/v)	B	C (Da)	D (%w/v)	E (scale)	F (sec.)	G (v/v)	H (%w/v)	J (rmp)	K (hrs)	Mean ± σ (µm)	S/N ratio
1	10	DCM	low	0.3	5	45	1:1	0.3	400	18	200.37 ± 2.82	-3.84
2	10	DCM	low	0.3	5	90	1:3	1.2	900	24	100.7 ± 12.12	-3.34
3	20	EAc	low	1.2	5	90	1:1	0.3	400	24	54.39 ± 4.37	-2.89
4	20	EAc	high	0.3	5	45	1:1	1.2	900	18	162.12 ± 4.83	-3.68
5	20	DCM	high	1.2	5	45	1:3	1.2	400	24	104.63 ± 0.85	-3.37
6	10	EAc	low	1.2	8	45	1:3	1.2	400	18	97.27± 0.46	-3.31
7	20	DCM	low	1.2	8	90	1:1	1.2	900	18	60.30 ± 1.29	-2.97
8	20	DCM	high	0.3	8	90	1:3	0.3	400	18	102.16 ± 7.19	-3.35
9	10	EAc	high	1.2	5	90	1:3	0.3	900	18	97.03 ± 0.08	-3.31
10	20	EAc	low	0.3	8	45	1:3	0.3	900	24	61.99 ± 16.27	-2.99
11	10	DCM	high	1.2	8	45	1:1	0.3	900	24	105.07 ± 1.73	-3.37
12	10	EAc	high	0.3	8	90	1:1	1.2	400	24	95.04± 1.89	-3.30

3.4.1.2 Statistical data analysis for L12 OA design

S/N ratio was computed for each of the formulation run with the smaller-the-better particle size characteristic (Table 3.6). High S/N ratio value was recorded for formulation Run 3 (-2.89). The L12 OA design results were statistically analysed using design-expert software (version 10). This software is able to screen each factor with respect to their influence on the particle size characteristic. A half-normal plot is one of the tools used in this software by identifying the important factors and any interactions. This plot uses the magnitude of the estimated effects for the main factors and any interactions in order to evaluate the important and unimportant factors and order the factors from the most important down to the least important. Important factors have their estimated effects completely removed from zero, while unimportant factors have near-zero effects (Determen et al., 2004). From Figure 3.3, the p factors located at the far right of the error lines are the important factors and factor F (vortexing speed) can be considered to have the maximum independent effect on particle size. Concentration of PVA in hardening bath and the interaction between the concentration of PLGA and solvent types that are lined up on the error line are unimportant, have zero or near zero effect on the particle size and excluded from the model. In Figure 3.3, the orange colour represents the factor that has a positive effect, and the blue represents factor with negative effect on the mean particle size.

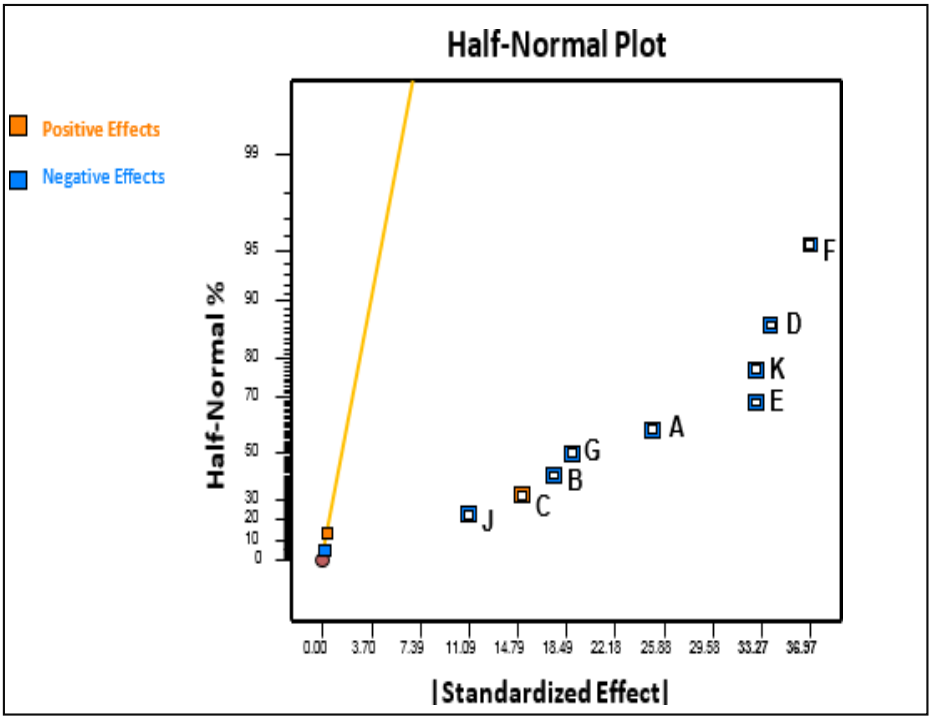

Figure 3.3. Half-normal % probability versus standardized effects plot after selection of factors for the model.

The yellow line represents the error line. Positive effects represent factors with positive standardized values and negative effects signify factors with negative standardized values. Plot generated for L12 OA design factors: vortexing duration (F), concentration of PVA in emulsion (D), solvent evaporation duration (K), vortexing speed (E), concentration of PLGA (A), aqueous/organic phase ratio(G), solvent type (B), molecular weight of PVA (C) and stirring speed (J).

In addition, a Pareto chart was created to identify the magnitude of the chosen p factors' effects for the model (Figure 3.4). The bars above the t- critical value (the reference line) with white represent the important factors that can possibly be included in the model and the bars below the reference line is unimportant. The white column seen inside the bars indicates that the factors have significant effect on the mean particle size. F-test was carried out on the experimental data. The ANOVA for the selected model summarised in Table 3.3 showed that the model F value of 7880.15 was significant and that there was only 0.01 % likelihood the variations among the mean particle size of the factors is due to noise. Furthermore, a p-value of less than 0.05 indicates that the model terms are significant at the probability level of 95 %. All the parameters chosen for the model have very significant effects on the microparticle size. From Table 3.3, vortexing speed had the maximum contribution (21.60 %) and the least was stirring speed for the hardening process (1.95 %). This evaluation is confirmed in the data presented in the Pareto chart (Figure 3.4).

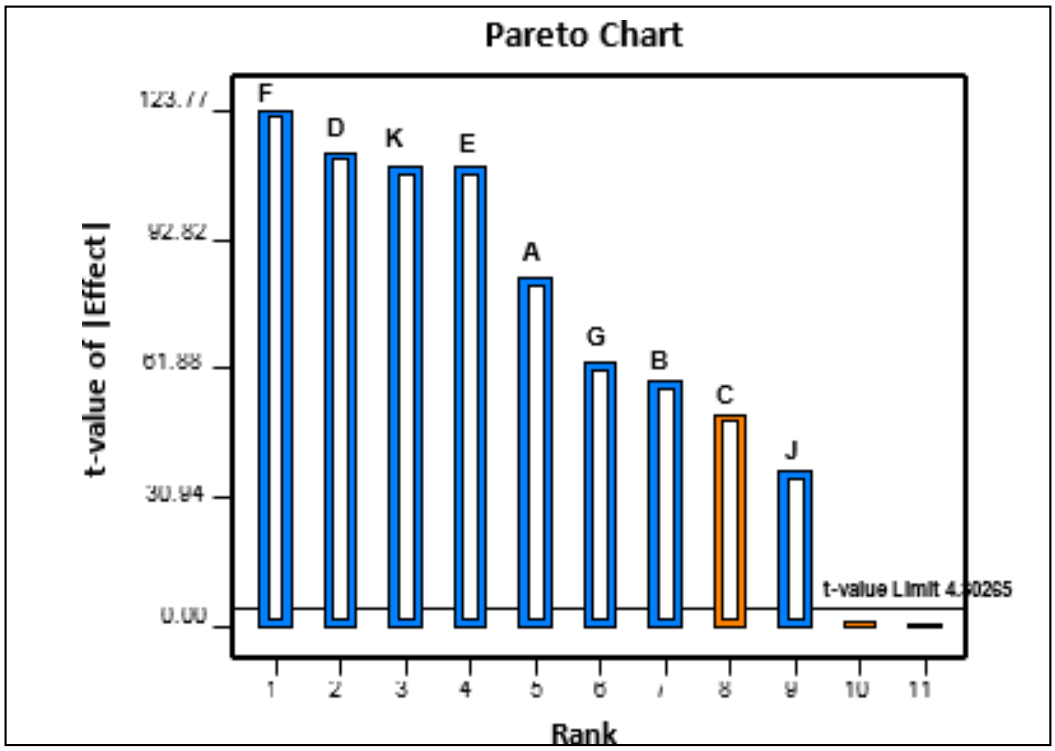

Figure 3.4. Graph of t-value of absolute effects verses rank.
This is an ordered bar chart, which shows the magnitude of the chosen factors for the model. The bars above the t-value (the reference line) with white represent the significant effects and the bars below the reference line are the insignificant ones. Data generated for L12 OA design factors: vortexing duration (F), concentration of PVA in emulsion (D), solvent evaporation duration (K), vortexing speed (E), concentration of PLGA (A), aqueous/organic phase ratio(G), solvent type (B), molecular weight of PVA (C) and stirring speed for hardening process(J).

The ANOVA for the selected model summarised in Table 3.7 showed that the model F value of 7880.15 was significant and that there was only 0.01 % likelihood the variations among the mean particle size of the factors is due to noise. Furthermore, a p-value of less than 0.05 indicates that the model terms are significant at the probability level of 95 %. All the parameters chosen for the model have very significant effects on the microparticle size. From Table 3.7, vortexing speed had the maximum contribution (21.60 %) and the least was stirring speed for the hardening process (1.95 %). This evaluation is confirmed in the data presented in the Pareto chart (Figure 3.4).

Table 3.7. ANOVA for L12 OA design

Source	Sum of Squares	Degree of freedom (df)	Mean Square	F Value	p-value Prob. > F	% Contribution
Model	18986.23	9	2109.58	7880.15	0.0001	-
A	1872.25	1	1872.25	6993.62	0.0001	9.86
B	925.59	1	925.59	3457.45	0.0003	4.87
C	690.54	1	690.54	2579.44	0.0004	3.64
D	3457.47	1	3457.47	12915.06	< 0.0001	18.21
E	3247.56	1	3247.56	12130.96	< 0.0001	17.10
F	4100.71	1	4100.71	15317.84	< 0.0001	21.60
G	1073.71	1	1073.71	4010.75	0.0002	5.66
J	370.19	1	370.19	1382.79	0.0007	1.95
K	3248.22	1	3248.22	12133.42	< 0.0001	17.11
Residual	0.5354	2	0.2677	-	-	-
Corr. Total	18986.76	11	-	-	-	-

Additionally, a diagnostic analysis was performed by generating the response plots for the 10 factors to evaluate the influence of each factor's levels on the mean particle size of all runs (103.4 μm) (Figure 3.5). The plots illustrate the average of each particle size for each level of each factor and display the factor with the largest effect. From the plots, the concentration of PVA in hardening bath (H) has negligible effect on the mean particle size. However, the remaining factors show significant effects on the mean particle size as already evaluated by AVOVA and the Pareto chart. As shown in Figure 3.5, increasing the vortexing duration (F) produced a small particle size. An extended duration of vortexing may allow for better dispersal

of the oil phase to form fine droplets which then harden to form MP (Pang et, 2014 and Zahn 1975). The effective creation of a primary emulsion and the stability of the droplets during the emulsification depends on the presence of surfactant, in this case PVA, at the interface between the aqueous and organic phases, lowering interfacial tension and providing a barrier to coalescence (Torkaman, Soltanieh and Kazemian, 2010, Vyslouzil et al., 2014 and Tan et al., 2015). Increasing the PVA concentration in the primary emulsion (D) from 0.3% w/v to 1.2% w/v resulted in a decrease in the mean particle size (Figure 3.5). As shown in the Figure, an increase in the solvent evaporation duration (K) resulted in a decrease in mean particle size. It is possible that at the low-level solvent removal from the droplet is incomplete, and that a longer duration allows for removal of any residual solvent expanding the polymer network. Vortexing speed (E) was a parameter of primary importance in the homogenization step because energy is required to disperse the organic phase in the aqueous phase (Pang et al., 2014). The results showed that the mean particle size was inversely proportional to the vortexing speed, increase in vortexing speed decreased the MP size because the emulsion was dispersed into smaller droplets at a higher scale. This observation is line with the studies of Sharma, Madan and Lin (2016). The response plot for PLGA concentration (A) in the Figure clearly shows that particle size decreased at higher PLGA concentration and may be as a consequence of PLGA surface activity. In this study two organic/aqueous phase ratios (G) were evaluated (1:1 and 1:3). The higher continuous phase volume may allow for a greater distance between dispersed oil droplets, reducing the rate of collision and coalescence. As observed in Figure 3.5, microparticles prepared with solvent type (B), EAc were characterized by their smaller particle size and most likely due to the result of increased water solubility. The response plot for MW of PVA (C) shows that increasing the molecular weight increases the microparticle size and may be attributed to the increased viscosity of the solution resisting deformation due to shear during emulsification (Wagh and Apar, 2014).

Stirring speed is one of the parameters that is well documented to have significant effect on particle size (Bible et al., 2009, Vyslouzil et al., 2014, Sharma, Madan and Lin, 2016, Quintanar-Guerrero, Fessi, Allemann and Doelker, 1996, Mondal, Samanta, Pal, and Ghosal, 2008, Valizadeh, Jelvehgari, Nokhodchi and Rezaour, 2010). Increasing stirring speed produces microparticle with small sizes by improved dispersal of the oil phase, where the stirrer imparts shear onto the emulsion droplets, reducing their size. This observation is confirmed in this study. In the effect of stirring speed (J) plot, the particle size decreased with increased in stirring speed from 400 rpm to 900 rpm.

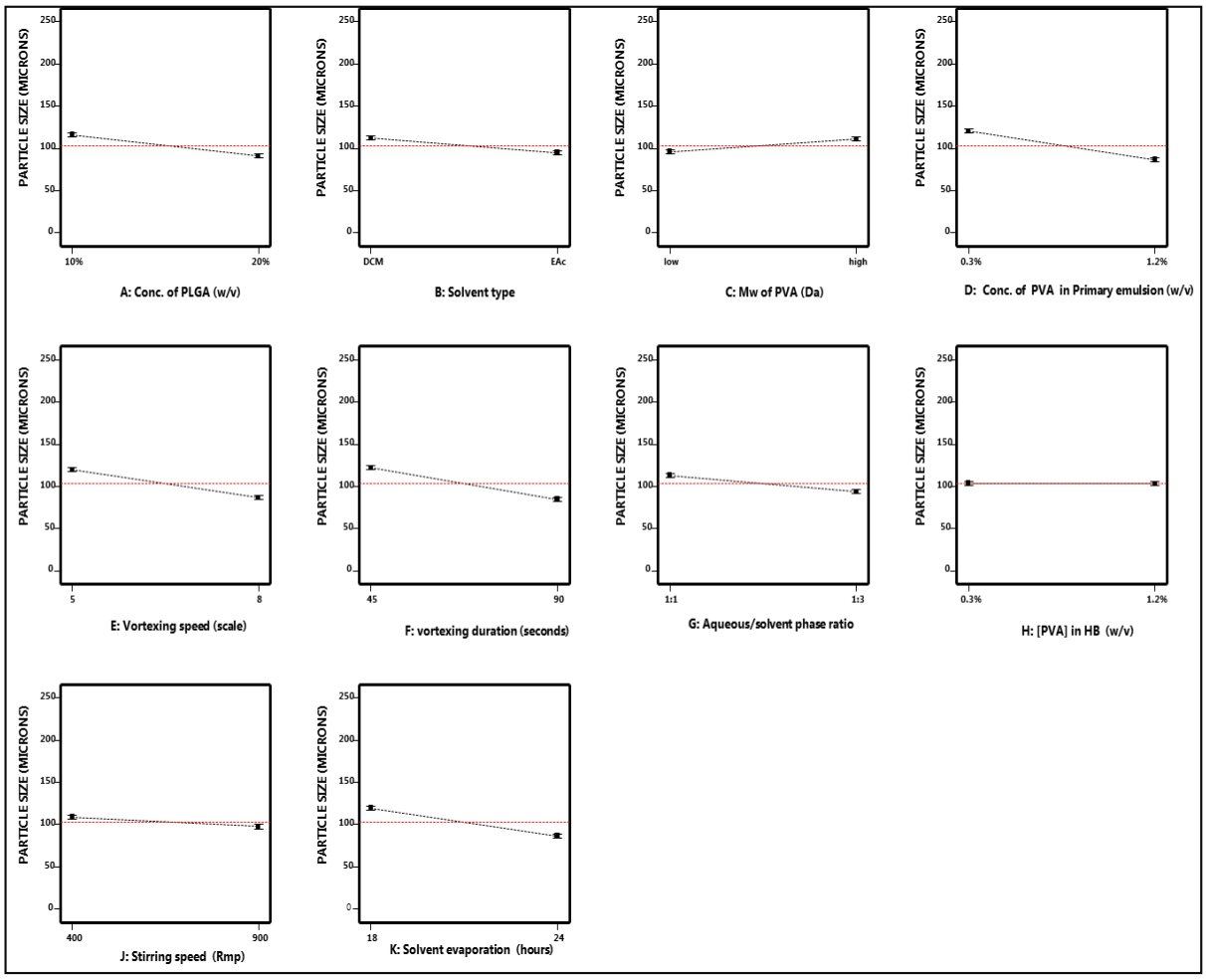

Figure 3.5. Response (main effects) plots.
The plots for the average effects of the 10 process factors (A, B, C, D, E, F, G, H, J and K) on the mean particle size for the L12 OA design. The vertical axis shows the mean particle size (µm), and the horizontal axis shows two levels (low and high) of the process factors. The red dashed line represents the value of the total mean of the particle size.

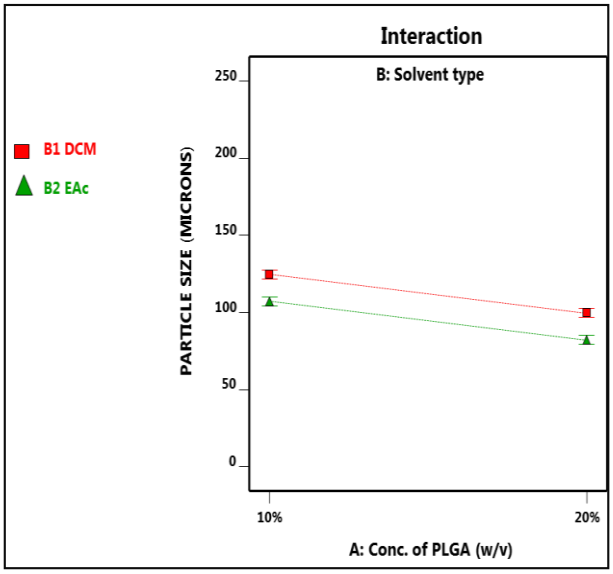

Figure 3.6. Interaction graph plot.
This plot displays the effect of concentration of PLGA (w/v) and solvent type on for mean particle size (µm).

3.4.1.3 L18 OA design

The L12 OA design identified 9 important factors, namely: concentration of PLGA, solvent type, MW of PVA, concentration of PVA in primary emulsion, vortexing speed, vortexing duration, organic/aqueous phase ratio, stirring speed of the hardening process and solvent evaporation duration that significantly influence the particle size of MP as such can be controlled. These results were fed into a second design, L18 OA design to further ascertain how these factors determine the particle size of MP by introducing a third level for each of the important factors excluding factor C (i.e., solvent type). Eight factors: MW of PVA (A), concentration of PLGA (B), concentration of PVA in primary emulsion (C), organic/aqueous phase ratio (D), vortexing speed (E), vortexing duration (F), stirring speed of the hardening process (G) and solvent evaporation duration (H) were considered for the L18 OA design. The factor levels as seen in Table 3.1 were based on formulation Run 3 as this generated the smallest particle size closed to the target range. The solvent type (EAc and PVA) concentration in the hardening process (0.3 % w/v) were kept constants for all the formulation runs.

Table 3.8 shows the L18 design generated by the design-expert software and the particle size obtained for each formulation run. A data of 18 formulation runs with 8 factors was constructed, in each of the factor's column, the levels low, medium or high occurred 9 times. The 16 formulation runs within this design produced particle size range of 23.51- 73.13 μm and a mean particle size of 48.32 μm. Runs 14 and 17 failed completely and no MP were created. These formulation runs failed using scale 3 as the vortexing speed to homogenize the o/w emulsion. Looking at Table 3.8 most of the MP created from this design have particle size within the target range apart from Run 3 (60.84 μm), Run 5 (73.13 μm), Run 8 (67.04 μm),
Run 10 (60.25 μm) and Run 12 (55.38 μm). MP formulated with Runs 3, 5, 8 and 10 had large particle size by using vortexing speed at the low level (scale 3). The goal of the study was to generate the smallest particle size within the range 10-50 μm, the smallest particle size 23.51 μm (PDI = 1.09 ± 0.01) was achieved by formulation Run 16.

Table 3.8. Results produced for combination of parameter levels of L18 OA design

Run	A (Da)	B (%w/v)	C (%w/v)	D (v/v)	E	F (sec.)	G (rmp)	H (hrs)	Mean ± σ (µm)	S/N ratio
1	13000	15	1.2	1:1	5	90	400	24	49.76 ± 2.65	-2.83
2	89000	30	0.8	1:2	5	120	200	24	45.48 ± 2.41	-2.76
3	13000	20	2.0	1:2	3	60	400	24	60.84 ± 4.22	-2.97
4	89000	20	2.0	1:0.75	5	120	400	20	41.12 ± 1.50	-2.69
5	89000	15	1.2	1:0.75	3	120	1200	24	73.13 ± 0.52	-3.11
6	13000	30	1.2	1:2	5	60	1200	20	44.94 ± 1.20	-2.75
7	89000	15	2.0	1:1	5	60	200	48	25.83 ± 0.65	-2.35
8	13000	30	0.8	1:1	3	120	400	48	67.09 ± 4.67	-3.04
9	13000	20	1.2	1:1	9	120	200	20	24.01 ± 1.27	-2.30
10	13000	30	2.0	1:0.75	9	90	200	24	50.81 ± 3.15	-2.84
11	13000	15	2.0	1:2	9	120	1200	48	28.10 ± 1.26	-2.41
12	89000	20	1.2	1:2	3	90	200	48	60.25 ± 6.09	-2.97
13	89000	30	1.2	1:0.75	9	60	400	48	55.38 ± 1.07	-2.91
14	13000	15	0.8	1:0.75	3	60	200	20	*	*
15	89000	15	0.8	1:2	9	90	400	20	47.46 ± 5.39	-2.79
16	89000	20	0.8	1:1	9	60	1200	24	23.51 ± 0.81	-2.29
17	89000	30	2.0	1:1	3	90	1200	20	*	*
18	13000	20	0.8	1:0.75	5	90	1200	48	40.38 ± 7.43	-2.68

3.4.1.4 Statistical data analysis for L18 OA design.

Table 3.8 summarises the S/N ratio evaluated for each of the formulation runs. The largest value based on the smaller-the-better analysis was produced by Run 16 (-2.29). Figure 3.7 displays the half-normal plot generated by the design-expert software to assess which of the factors are important and which are unimportant. The factors: vortexing speed, concentration of PLGA, organic/aqueous phase ratio, stirring speed, concentration of PVA in primary emulsion, vortexing duration and solvent evaporation duration are seen at the far right of the error line. The factor MW of PVA is located on the error line. The ANOVA for the selected factors: concentration of PLGA, concentration of PVA in primary emulsion, organic/aqueous phase ratio, vortexing speed, vortexing duration, stirring speed of the hardening process and solvent evaporation duration is summarized in Table 3.9 and it shows all factors selected for the model have significant effects on the particle size ($p > 0.05$). A high value of F (12261.0) was obtained for the model (1.68 %). The sum of squares shows that 32.79 % of the total variance is established by the vortexing speed. The factor with the least contribution is solvent evaporation duration.

Table 3.9. ANOVA for L18 OA design

Source	Sum of Squares	df	Mean Square	F Value	p-value Prob. > F	% Contribution
Model	3504.60	14	250.33	12261.00	0.0071	
B-B	336.50	2	168.25	8240.73	0.0078	9.60
C-C	83.86	2	41.93	2053.66	0.0156	2.39
D-D	249.47	2	124.74	6109.56	0.0090	7.12
E-E	1149.15	2	574.58	28142.50	0.0042	32.79
F-F	62.67	2	31.34	1534.89	0.0180	1.79
G-G	193.63	2	96.82	4742.02	0.0103	5.53
H-H	58.75	2	29.38	1438.86	0.0186	1.68
Residual	0.0204	1	0.0204	-	-	-
Corr. Total	3504.62	15	-	-	-	-

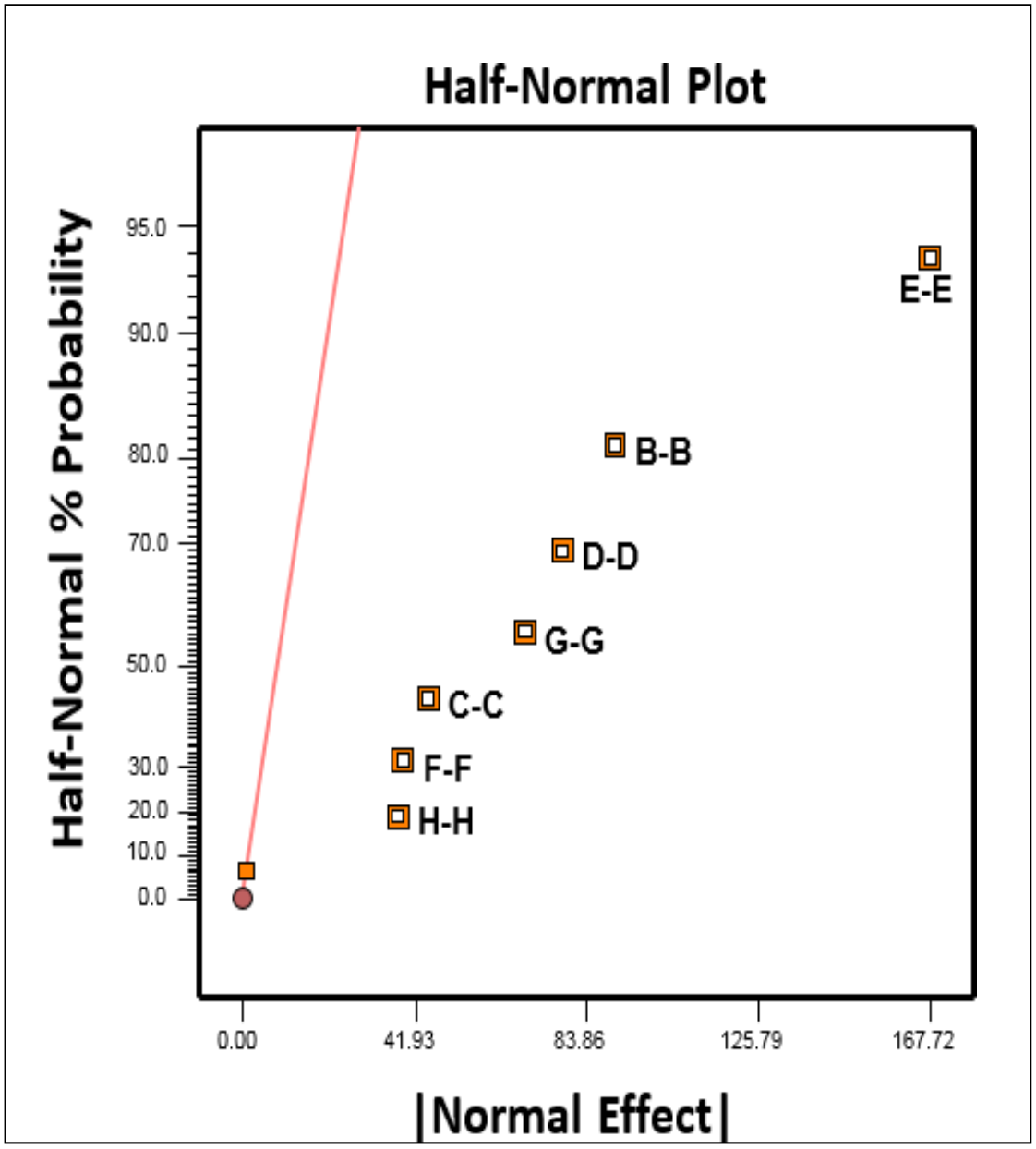

Figure 3.7. Half-normal % probability versus normal effects plot.
After selection of factors for the model, this plot was generated to identify the important and unimportant factors. Pink line represents error line. Data generated for L18 OA design factors: vortexing speed (E), concentration of PLGA (B), aqueous/organic phase ratio (D), stirring speed (G), concentration of PVA in emulsion (C), vortexing duration (F) and solvent evaporation duration (H).

Figure 3.8 shows the response plots for the average factor levels of the L18 design. No influence is observed for the two levels of the MW of PVA. The concentration of PLGA response shows medium level (20 % w/v) having the largest influence on the mean particle size followed by the low level (15 % w/v) and then the high level (30 % w/v). The plot for the concentration of PVA in primary emulsions displays 2.0 % w/v (high level) with the most significant effect and the 1.2 % w/v (medium level) with the least. The medium level (1:1) for the organic/aqueous phase ratio increased the mean particle size while the high level (1:3) and low level (1:0.75) decreased the response accordingly. As the level increases in the vortexing speed factor, the effect on the mean particle size increases. In the plot for vortexing duration, the low level (60 s) and the high level (120 s) have an equal and larger influence on the mean particle size. Stirring speed and solvent evaporation duration have the same pattern for levels influence on the mean particle size i.e., low > high > medium implies a reduction in the effect.

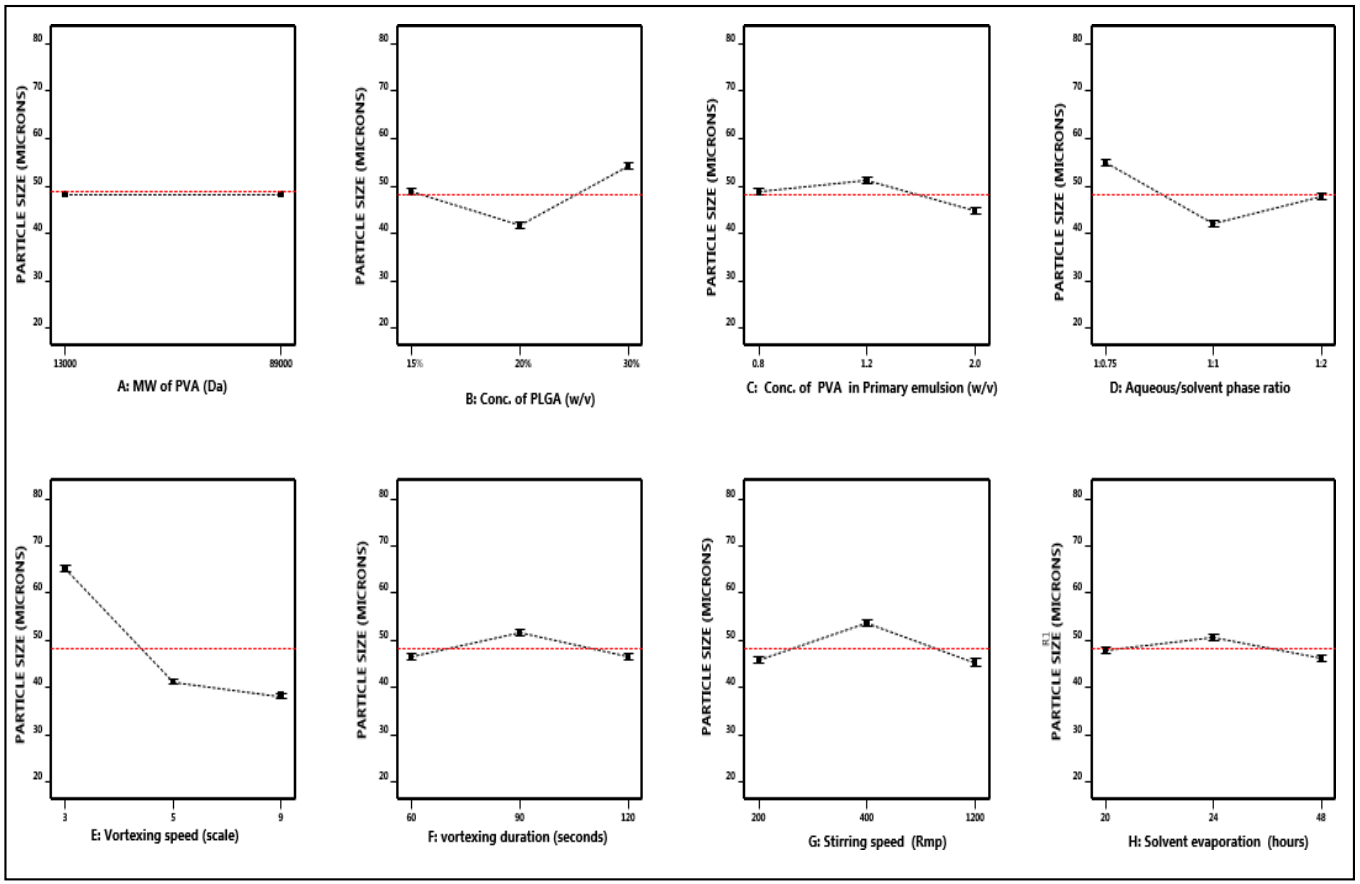

Figure 3.8. Response plots for the average effects of the 8 process factors.
The response plots for the 8 process factors (A, B, C, D, E, F, G and H) on the mean particle size for the L18 OA design. The vertical axis shows the mean particle size (μm), and the horizontal axis shows three levels (low, medium and high) of the process factors. The red dashed line represents the value of the total mean of the particle size.

The optimal model formulation was identified to be Run 16 from the L18 OA design. The mean particle size was found to be 23.51 µm which falls into the required range of 10 – 50 µm. The factors and the associated level for the optimal model formulation are molecular weight of PVA= 89,00Da (high), concentration of PLGA = 20 w/v % (medium), organic/aqueous phase ratio= 1:1 (medium), vortexing speed = 9 (high), vortexing duration= 60 seconds (low), stirring speed for hardening process = 1200 rpm (high) and solvent evaporation duration = 24 h (medium).

3.4.2 Characterization

3.4.2.1 Optimization of instruments parameters for particle size analysis

One key step in Taguchi design of experiment is the selection of the characteristic and the instrument to assess it (Torkaman, Soltanieh and Kazemian, 2010 and Krishnamoorthy and Mahalingam, 2015). The particle size of the MP created in this study was evaluated using dry dispersion laser diffraction method via SymPatec HELOS equipped with a RODOS/ASPIROS dry dispenser (Germany). In laser diffraction technique, it is vital to achieve an optimal dispersion to inhibit agglomeration and to ensure the reproducibility of results (Jaffari et al, 2013). To determine the optimal parameters, imaging particle size analysis was combined with the dry dispersion laser diffraction (DDLD) and wet dispersion laser diffraction (WDLD) methods. The WDLD was used so as to observe the particles in liquid and identify any agglomerate.

The initial step in the optimisation procedure was selecting the MP with small and large particles size to establish optimal measurement conditions for the different range of MP sizes. The particle size analysis was assessed with imaging The optical microscopic images confirmed that the MP were made up of particles with range of sizes (Figure 3.9). Agglomerates were observed in each of the MP. The median and average of the Feret's diameter of MP produced in each run were obtained from *ImageJ*© software (Table 3.10). The MP with smallest particle size of 23.59 ± 1.70 µm (median) was produced by formulation Run 3 and the

largest size of 239.97 µm from Run 4, which were used to optimize particle size measurement techniques over the range of possible particle sizes present.

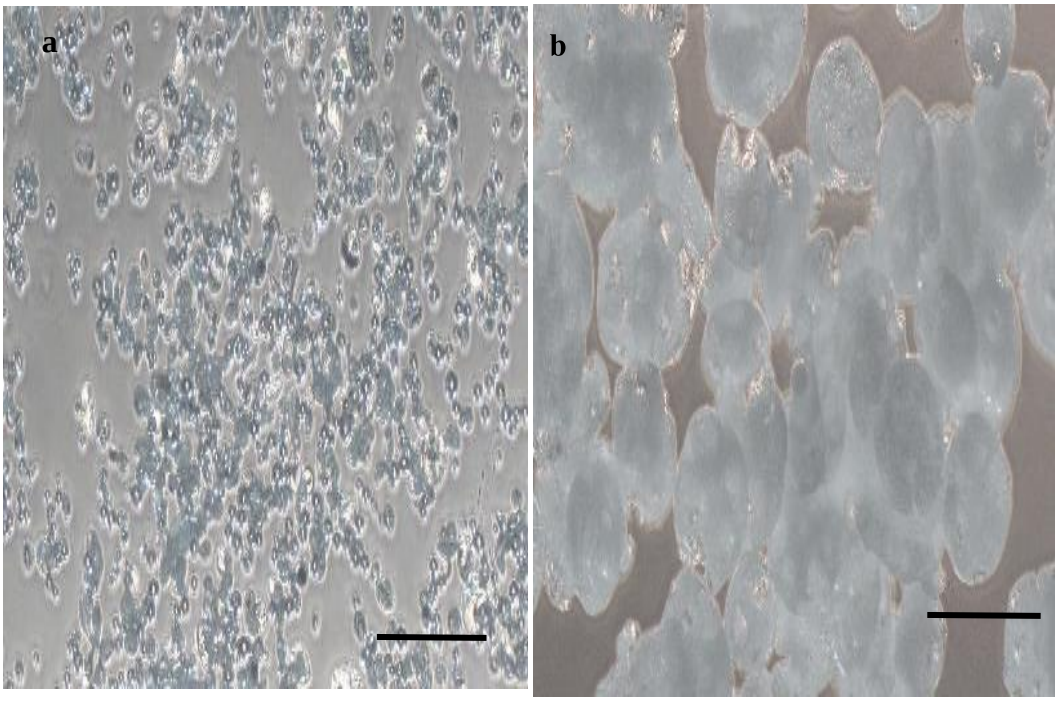

Figure 3.9. Optical microscopic images of Run 3 (a) and Run 4 (b) at 4x magnification (scale bar = 100 µm)

Table 3.10. Summary of Feret diameter (µm) of Microparticles measured with *ImageJ*© software (mean ± σ, n=6)

Run	Median diameter (µm)	Average diameter (µm)
1	39.89 ± 0.91	47.01 ± 1.42
2	47.12 ± 3.60	50.86 ± 5.54
3	23.59 ± 2.86	28.67 ± 1.70
4	239.97 ± 8.24	296.47 ± 21.19
5	53.04 ± 5.20	52.81 ± 1.38
6	37.37 ± 8.27	39.37 ± 2.38
7	27.85 ± 5.18	29.58 ± 1.79
8	50.31 ± 3.09	49.82 ± 2.03
9	125.21 ± 17.17	100.53 ± 8.69
10	55.49 ± 9.28	69.67 ± 3.94
11	138.67 ± 16.49	169.55 ± 0.49
12	23.81 ± 3.23	32.43 ± 6.89

The particle size obtained from the wet dispersion method were measured to determine the fully dispersed particle size in liquid medium independent of the DDLD method but has the limitation that swelling/dissolution may be observed. The X50 values for Run 3 and 4 were 21.41 ± 0.30 and 103.28 ± 0.15 µm respectively. The effect of primary pressure on the particle size distribution following DDLD. Figure 3.10 represents the particle size-primary pressure profiles for Run 3 and Run 4. In both graphs, the MP showed reduction in particle size as the pressure increased until a plateau size was attained. The particle size obtained at the plateaued pressure (4.0 Bar) was compared to the particle size measured using WDLD (Table 3.11). The sonication time and the ultrasound frequency were varied in the WDLD technique. These variation factors are essential in the optimisation (Jaffari et al, 2013) The finding (Table 3.11) shows that PSD were similar, and this confirms that the samples were well dispersed in the DDLD method. Subsequently, the optimal parameters for the DDLD were utilized to assess the DOE MP samples (i.e., samples obtained in L12 OA design and L18 OA design).

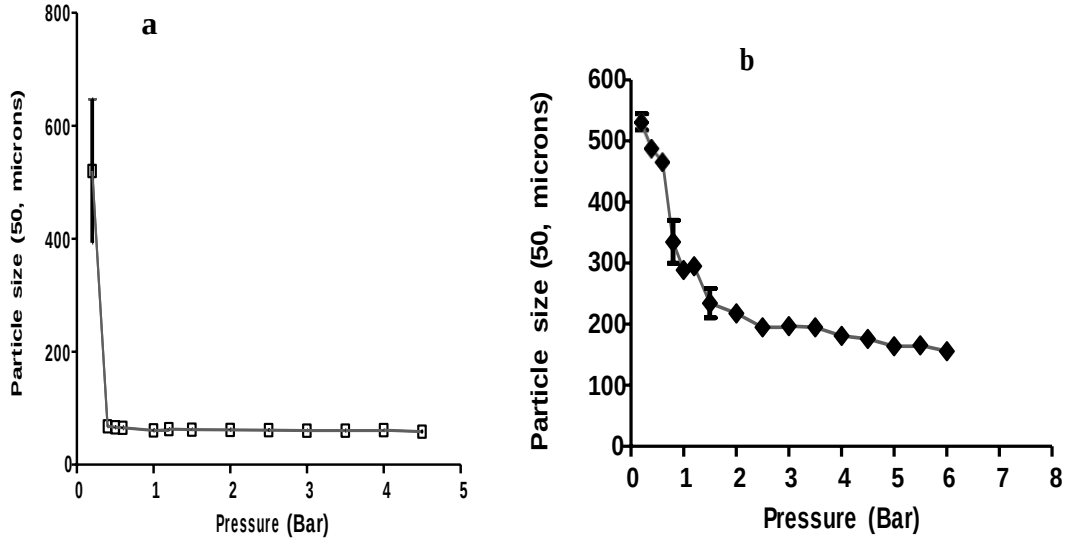

Figure 3.10. The particle size (X50) vs pressure of Run 3 (a) and Run 4 (b) MP measured by SymPatec HELOS/RODOS DDLD (mean ± σ, n=3)

Table 3.11. Particle size (X10, X50, X90, VMD) of Run 3 and 4 assessed by dry dispersion laser diffraction at 4.0 Bar primary pressure and wet dispersion laser diffraction (mean ± σ, n=3)

Run	3_{WDLD}	3_{DDLD}	4_{WDLD}	4_{DDLD}
X10	10.16 ± 0.22	12.12 ± 0.15	29.80 ± 0.13	69.68 ± 0.37
X50	21.41 ± 0.30	22.39 ± 0.26	103.28 ± 0.15	183.35 ± 5.76
X90	37.43 ± 1.02	36.69 ± 1.24	218.95 ± 0.85	295.32 ± 11.02
VMD	24.56 ± 0.39	26.78 ± 0.85	116.67 ± 0.89	181.62 ± 6.36

3.4.2.2 Particle size/ polydispersity analysis of blank and protein loaded MP

The particle size distributions of the L12 OA design and L18 OA design runs were measured using the DDLD technique. The cumulative size distribution curves of the selected run 3 from L12 OA design and the run 16 from L18 OA design are shown in Figures 3.11a and 3.11b respectively. The curve of run 3 showed a bimodal distribution due to the population of fine and large particles (Figure 3.11a) and that of run 16 showed a narrow distribution. FITC-BSA (FBM-1, FBM-2, FBM-3) and LZM loaded PLGA MP were successfully generated using the

factors deduced from the optimal model formulation (run 16). The cumulative size distributions of the FBM-1, FBM-2, FBM-3 and LZM-MP MP are displayed in Figures 3.11 c, d, e and f respectively and the curves in these MP are narrow with small shoulders due to very fine particles. The values of the particle size distribution and the PDI of the blank MP and the protein loaded are summarised in Table 3.12. Comparatively, the average particle size and the PDI of the loaded MP are not significantly different from the blank MP ($p > 0.05$ by t-test). The increase in the concentration of FITC-BSA had no significant effect on the particle size and PDI (Table 3.12).

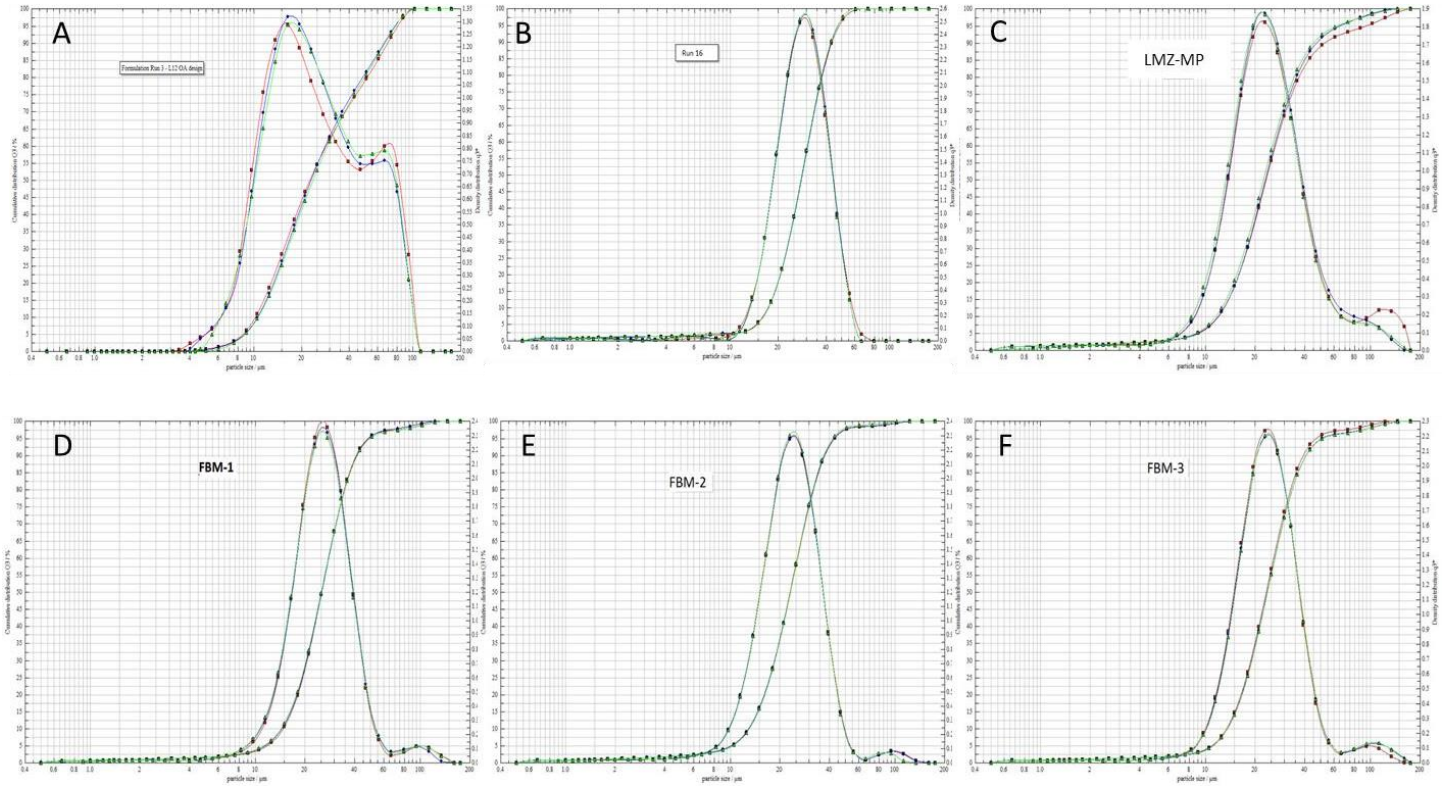

Figure 3.11. Cumulative size distribution of PLGA MP fabricated with ethyl acetate as organic solvent:
(A) formulation Run 3 from L12 OA design and (B) formulation Run 16 from L18 OA design identified as the optimal formulation with lowest particle size, (C) Lysozyme loaded MP, (D) FITC-BSA loaded MP: 5 mg, (E) FITC-BSA loaded MP: 10 mg and (E) FITC-BSA loaded MP: 20 mg. (n = 3).

Table 3.12. Particle size distribution (X10, X50, X90) and polydispersity index of samples assessed by DDLD at 4.0 Bar (mean ± σ, n=3)

MP sample	Particle size distribution (µm)			Polydispersity index (PDI)
	X10	X50	X90	
L12 OA design (Run 3)	11.96 ± 1.23	54.39 ± 4.37	92.67 ± 2.56	1.48 ± 0.56
L18 OA design (Run16)	12.31 ± 0.68	23.51 ± 0.81	37.93 ± 1.24	1.09 ± 0.01
FBM-1	13.11 ± 1.87	24.25 ± 1.71	45.44 ± 5.28	1.35 ±0.39
FBM-2	11.47 ± 2.02	21.67 ± 2.04	45.02 ± 10.25	1.58 ± 0.72
FBM-3	12.76 ± 0.93	24.5 ± 1.12	50.53 ± 13.60	1.53 ± 0.52
LZM-MP	11.49 ± 0.02	24.45 ± 0.01	41.53 ± 0.06	1.45 ± 0.04

3.4.2.3 Scanning electronic microscopy

SEM images were taken to visualise the surface morphology of the MP formulation Run 16 selected from L18 OA design as the optimal model formulation for this study (Figure 3.11 A and B). The SEM imaging was further utilized to study the morphologies of the protein loaded MP prepared with 3 different concentrations of FITC-BSA (5, 10 and 20 mg) and LZM loaded MP. The SEM images of the MP samples are shown in Figure 3.11 (C, D, E and F). The images show that each sample are made of a range of spherical-like microparticles and these confirm the particle size measurements.

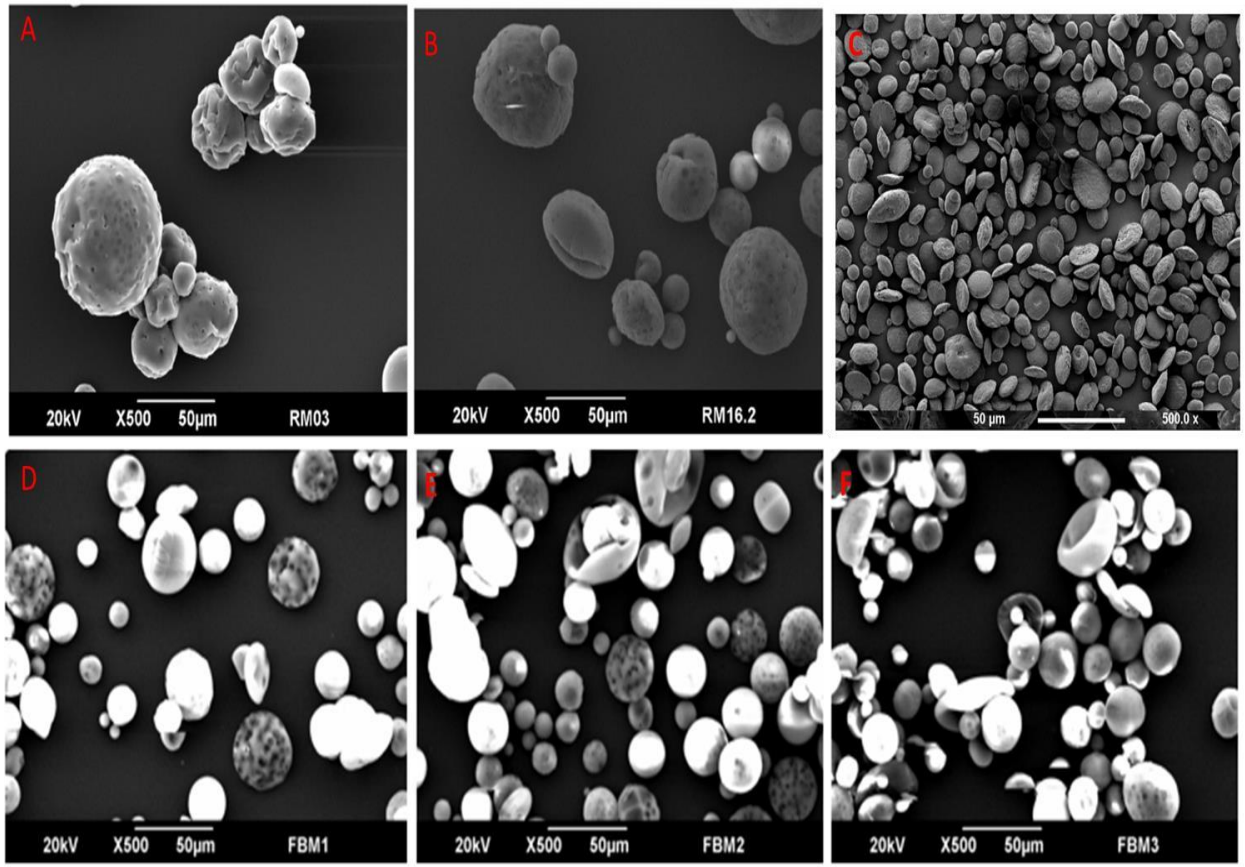

Figure 3.12. SEM images of PLGA MP.
Formulated by (A) run 3 from L12 OA design, (B) run 16 from L18 OA design, (C) Lysozyme loaded MP, (D) FITC-BSA loaded MP: 5 mg, (E) FITC-BSA loaded MP: 10 mg and (E) FITC-BSA loaded MP: 20 mg.

3.4.2.4 Analysis of the % Yield, LC%, EE% and the in vitro release profiles

Calibration curves were constructed for FITC-BSA and LZM in water and PBS in different ranges. The statistical data and the equation of linear regression are presented in Table 3.13. The linearity of the calibration curves for FITC-BSA in water, FITC-BSA in PBS, LZM in water and LZM in PBS were validated by high values of correlation coefficient, R^2 =0.9982, 0.9929, 0.9964 and 0.9913 respectively. The LOD and the LOQ are shown in Table4.13.

Table 3.13. Statistical data for calibration curves for FITC-BSA and LZM

Parameters	FTIC-BSA in water	FITC-BSA in PBS	LZM in water	LZM in PBS
Linearity (ug/ml)	0-20	0.5-20	0.5-20	1.0-20
Regression equation	Y= 0.021x + 0.0382	Y= 0.022x + 0.042	Y=0.021x + 0.041	Y=0.021x + 0.035
Correlation coefficient (R^2)	0.9982	0.9929	0.9964	0.9913
Slope	0.021	0.022	0.021	0.0211
Intercept	0.038	0.042	0.041	0.035
σ of slope	0.00023	0.0045	0.000071	0.00014
σ of intercept	0.0001	0.00009	0.0006	0.0004
LOD (ug/ml)	0.0181	0.0144	0.0993	0.0553
LOQ (ug/ml)	0.0548	0.0426	0.3009	0.1676

The results of the average yield % (Table 3.14) increased with increased amount of FTIC-BSA. 20 mg of LZM produced a high average yield %. In Table 3.14, the average EE% results showed that the EE increased with increased number of proteins. All the proteins had a fairly high average EE% (64.35 – 78.07%). As shown Table 3.14, high average LC% of 17.18 and 15.94 % of FBM-3 and LZM-MP and the amount of protein used was 20 mg. FBM-1, MP formulated with 5 mg FITC-BSA gave the lowest average LC (5.02%).

Table 3.14. Yield%, encapsulation efficiency and loading capacity for FITC-BSA and LZM loaded PLGA MP

Batch	Amount of drug/ mg	Yield %	EE%	LC%
FBM-1	5	64.35 ± 4.99	52.38 ± 7.06	5.02 ± 0.23
FBM-2	10	64.66 ± 4.65	55.42 ± 4.44	8.1 ± 1.91
FBM-3	20	67.89 ± 2.51	58.69 ± 1.15	17.18 ± 0.41
LZM-MP	20	78.07 ± 0.67	62.34 ± 6.02	15.94 ± 1.64

3.5.1.1 *In vitro* release analysis

Herein, the robustness and predictive ability of the Taguchi OA design of experiment methodology in the fabrications of the FITC-BSA-loaded MP was assessed. FITC-BSA, ~66 KDa, is a stable, globular and relatively non-reactive protein that is often used as a model protein in drug MP development studies.

The *in vitro* release profile of the entrapped FITC-BSA and LZM from FBM-1/FBM-2/FBM-3 and LZM-MP respectively are summarised in Figure 3.13. From the results, about 11.74%, 36.92%, and 27.05% of FITC-BSA were released from FBM-1, FBM-2 and FBM-3 respectively and 27.56% of LZM was released from LZM-MP after 18 hours. At 7 days, about 65.01%, 81.844%, 85.86% and 86.09 % of the protein loaded were released from FBM-1/FBM-2/FBM-3 and LZM-MP respectively. It can be observed at 11 days that, about 70.80 %, 86.32 %, 94.13 % and 92.06% of the respective proteins were released from FBM-1, FBM-2, FBM-3 and LZM-MP respectively. Finally, at day 28, about 70.93 %, 86.34%, 94.35 % and 92.06 % of the loaded proteins were released from FBM-1, FBM-2, FBM-3 and LZM-MP respectively. The generated MP exhibited good, sustained release profiles. The maximum release after 28 days was found in FBM-3 and LZM-MP. It shows that the release profile of the protein was dependent on the amount of the protein loaded.

This aspect further validates the DOE technique as a feasible predictive tool for pharmaceutical formulation-especially in the context of biological entrapment e.g., growth factors, antibodies, biologicals.

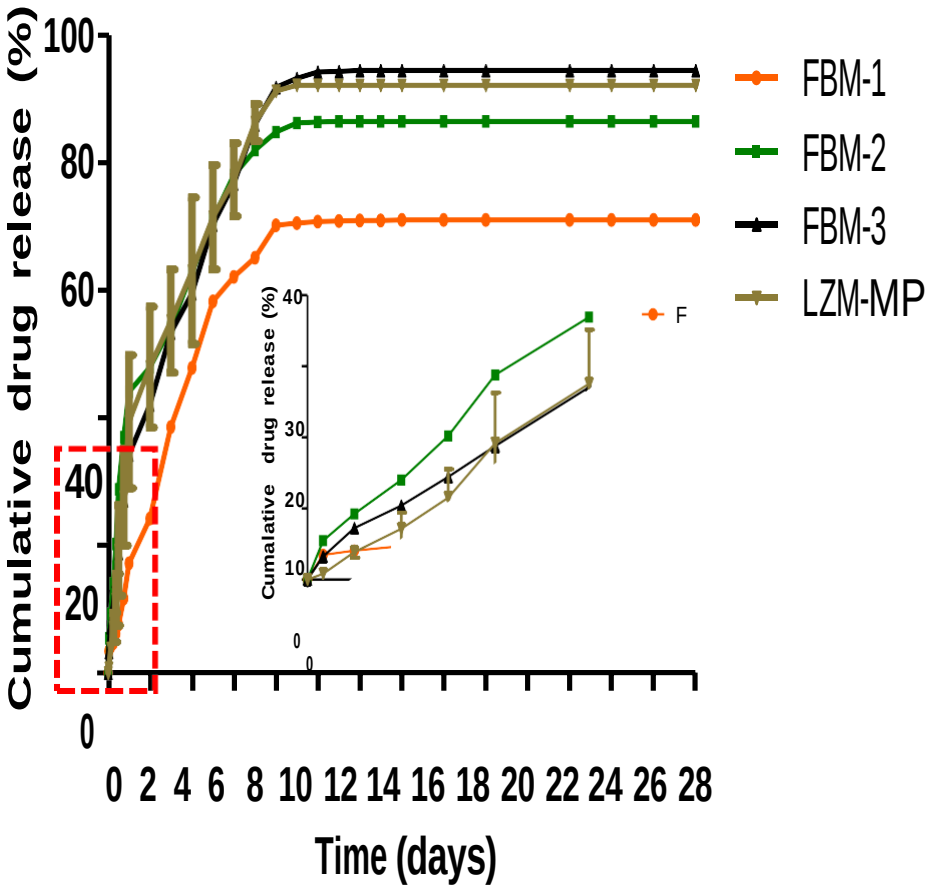

Figure 3.13. Invitro release profile of FITC-BSA and LZM loaded microparticles. Insert (release profile for 20 hrs) (mean ± σ, n=3).

3.4.2.5 Protein activity

the activity of the protein incorporated was determined by utilising lysozyme loaded microparticles (LZM). The absorbance of *Micrococcus lysodeikticus* cells incubated with the lysozyme was measured. The absorbance of *Micrococcus lysodeikticus* cells incubated with the lysozyme releases on days 0, 1, 4, 7, 10, 14 and 28 was monitored at 450 nm using Sigma-Aldrich lysozyme detection kit. From Figure 3.14, linearity of the change in the activity of lysozyme decreases as a function of time. At day 0, no change in activity is observed. At days 10, 14 and 28, low amount of lysozyme is released therefore the change of activity is less pronounced. However, on day 1, day 4, and day 7 the change in activity is more pronounced due to the significant amount of lysozyme released.

From the results (Figure 3.14), the activity of the protein was dependent on the amount of protein released and the kinetic of the change in activity of the protein agreed with the release data.

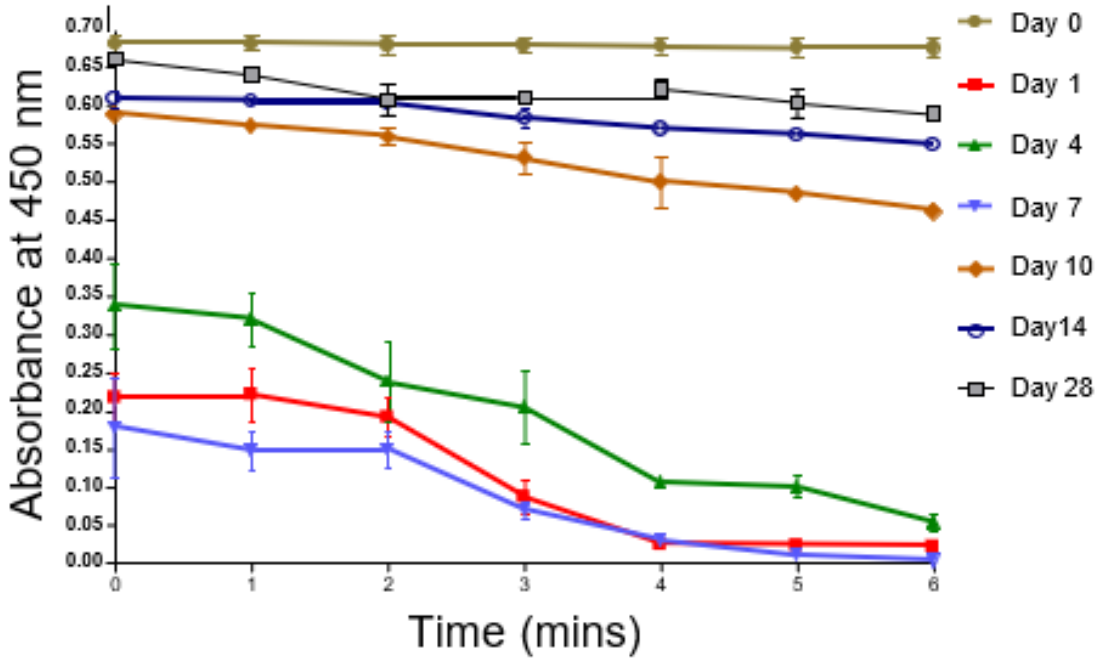

Figure 3.14. Kinetics of the change in activity of lysozyme treated *micrococcus lysodeikticus* cells.

3.5 CONCLUSION

In this study, Taguchi OA design proved to be a valuable tool in the optimization of several processing parameters in solvent evaporation technique with complex interrelationship with few experiments. The design was efficient for identifying the parameters which had significant effect on MP size More precisely, vortexing speed, concentration of PLGA, organic/aqueous phase ratio, stirring speed, concentration of PVA in primary emulsion, vortexing duration were significant whereas the molecular weight of PVA and concentration of PVA in hardening bath were proven to be not important parameters with regard to PLGA microparticle size. The optimal model formulation was established as molecular weight of PVA = 89,00 Da, concentration of PLGA = 20 w/v %, organic/aqueous phase ratio = 1:1, vortexing speed = 9, vortexing duration= 60 s, stirring speed for hardening process = 1200 rpm and solvent evaporation duration = 24 h. These optimum levels of the parameters were useful in the fabrication of PLGA microparticles with the minimum particle size of 23.51 μm. A model drug (FITC-BSA) was successfully incorporated into the optimised microparticles, which had no statistically significant impact on size and the activity.

3.6 REFERENCES

Airavind Chakrapan, M. (2006). Processing and characterization of polymer microparticles for controlled drug delivery systems. Ph.d. The ohio state university.

Bible, E., Chau, D., Alexander, M., Price, J., Shakesheff, K. and Modo, M. (2009). Attachment of stem cells to scaffold particles for intra-cerebral transplantation. Nature Protocols, 4(10), pp.1440-1453.

Bodmeier, R. and McGinity, J. (1988). Solvent selection in the preparation of poly(dl-lactide) microspheres prepared by the solvent evaporation method. International Journal of Pharmaceutics, 43(1-2), pp.179-186.

Bourke, S., Al-Khalili, M., Briggs, T., Michniak, B., Kohn, J. and Poole-Warren, L. (2003). A photo-crosslinked poly(vinyl alcohol) hydrogel growth factor release vehicle for wound healing applications. AAPS PharmSci, 5(4), pp.101-111.

Chang-Lin, J., Attar, M., Acheampong, A., Robinson, M., Whitcup, S., Kuppermann, B. and Welty, D. (2011). Pharmacokinetics and Pharmacodynamics of a Sustained-Release Dexamethasone Intravitreal Implant. Investigative Opthalmology and Visual Science, 52(1), p.80.

Chang-Lin, J., Burke, J., Peng, Q., Lin, T., Orilla, W., Ghosn, C., Zhang, K., Kuppermann, B., Robinson, M., Whitcup, S. and Welty, D. (2011). Pharmacokinetics of a Sustained-Release Dexamethasone Intravitreal Implant in Vitrectomized and Nonvitrectomized Eyes. Investigative Opthalmology and Visual Science, 52(7), p.4605.

Chau, D., Tint, N., Collighan, R., Griffin, M., Dua, H., Shakesheff, K. and Rose, F., 2010. The visualisation of vitreous using surface modified poly(lactic-co-glycolic acid) microparticles. British Journal of Ophthalmology, 94(5), pp.648-653.

Coates, N. (1988). Determinants of Japan's business success: Some Japanese executives. Academy of Management Executive, 2(1), pp.69-72.

Giri, T., Choudhary, C., Ajazuddin, Alexander, A., Badwaik, H. and Tripathi, D. (2013). Prospects of pharmaceuticals and biopharmaceuticals loaded microparticles prepared by double emulsion technique for controlled delivery. Saudi Pharmaceutical Journal, 21(2), pp.125-141.

Hickey, T., Kreutzer, D., Burgess, D. and Moussy, F. (2002). Dexamethasone/PLGA microspheres for continuous delivery of an anti-inflammatory drug for implanTablemedical devices. Biomaterials, 23(7), pp.1649-1656.

Kemala, T., Budianto, E. and Soegiyono, B. (2012). Preparation and characterization of microspheres based on blend of poly (lactic acid) and poly(ε-caprolactone) with poly (vinyl alcohol) as emulsifier. Arabian Journal of Chemistry, 5(1), pp.103-108.

Kerr, D. (1987). Microparticulate Drug Delivery Systems as an Adjunct to Cancer Treatment. Cancer Drug Delivery, 4(1), pp.55-61.

Kim, K., Kim, S. and Kim, H. (2005). Applying the Taguchi method to the optimization for the synthesis of TiO2 nanoparticles by hydrolysis of TEOT in micelles. Colloids and Surfaces A: Physicochemical and Engineering Aspects, 254(1-3), pp.99-105.

Krishnamoorthy, K. and Mahalingam, M. (2015). Fabrication and optimization of camptothecin loaded Eudragit S 100 nanoparticles by Taguchi L4 orthogonal array design. International Journal of Pharmaceutical Investigation, 5(3), p.147.

Lai, M. and Tsiang, R. (2005). Microencapsulation of acetaminophen into poly(L-lactide) by three different emulsion solvent-evaporation methods. Journal of Microencapsulation, 22(3), pp.261-274.

Montgomery, D. (1999). Experimental Design for Product and Process Design and Development. Journal of the Royal Statistical Society: Series D (The Statistician), 48(2), pp.159-177.

Mori, Y., Yoshida, H. and Masuda, H. (2012). Particle Size Analysis by Laser Diffraction Method Using Reference Particles. Advanced Materials Research, 508, pp.33-37.

Mori, Y., Yoshida, H. and Masuda, H. (2012). Particle Size Analysis by Laser Diffraction Method Using Reference Particles. Advanced Materials Research, 508, pp.33-37.

Nair, V., Hansen, M. and Shi, J. (2000). statistics in Advanced Manufacturing. Journal of the American Statistical Association, 95(451), pp.1002-1005.

Nihant, N., Schugens, C., Grandfils, C., Jerome, R. and Teyssie, P. (1995). Polylactide Microparticles Prepared by Double Emulsion-Evaporation. Journal of Colloid and Interface Science, 173(1), pp.55-65.

Gaudana, R., Ananthula, H., Parenky, A. and Mitra, A., 2010. Ocular Drug Delivery. The AAPS Journal, 12(3), pp.348-360.

ISO. 2022. ISO 13320:2009. [online] Available at: <https://www.iso.org/standard/44929.html> [Accessed 31 June 2021].

Keck, C. and Müller, R., 2008. Size analysis of submicron particles by laser diffractometry—90% of the published measurements are false. International Journal of Pharmaceutics, 355(1-2), pp.150-163.

Le Bourlais, C., Acar, L., Zia, H., Sado, P., Needham, T. and Leverge, R., 1998. Ophthalmic drug delivery systems—Recent advances. Progress in Retinal and Eye Research, 17(1), pp.33-58.

Patel, A., 2013. Ocular drug delivery systems: An overview. World Journal of Pharmacology, 2(2), p.47.

Zidan, G., Rupenthal, I., Greene, C. and Seyfoddin, A., 2017. Medicated ocular bandages and corneal health: potential excipients and active pharmaceutical ingredients. Pharmaceutical Development and Technology, 23(3), pp.255-260.

Weng, Y., Liu, J., Jin, S., Guo, W., Liang, X. and Hu, Z., 2017. Nanotechnology-based strategies for treatment of ocular disease. Acta Pharmaceutica Sinica B, 7(3), pp.281-291.

Jaffari, S., Forbes, B., Collins, E., Barlow, D., Martin, G. and Murnane, D., 2013. Rapid characterisation of the inherent dispersibility of respirable powders using dry dispersion laser diffraction. International Journal of Pharmaceutics, 447(1-2), pp.124-131.

Patil, S., Papadimitrakopoulos, F. and Burgess, D. (2004). Dexamethasone-Loaded Poly(Lactic-Co-Glycolic) Acid Microspheres/Poly(Vinyl Alcohol) Hydrogel Composite Coatings for Inflammation Control. Diabetes Technology and Therapeutics, 6(6), pp.887-897.

Peppas, N. (1989). Ophthalmic drug delivery: Pharmaceutical, technological and clinical aspects. Journal of Controlled Release, 8(3), pp.275-276.

Ross, A. (1973). Particle detection and shape discrimination using a laser diffraction method. Optics and Laser Technology, 5(1), p.13.

CHAPTER 4:
Generation of drug loaded PLGA microparticle bandage

4.0 CHAPTER 4: GENERATION OF DRUG LOADED PLGA MICROPARTICLE BANDAGE

4.1 INTRODUCTION

Millions are estimated to suffer from cornea wounds yearly and these wounds invariably bring, aside from the obvious heath issues, potential emotional and financial implications to patients. Cornea is a part of the eye that is exposed to the outside environment and its position make it vulnerable to a variety of injuries and insults. Cornea wound healing is a major clinical issue (Ljubimov and Saghizadeh, 2015, Sheha et al., 2019 and. Fernández-Pérez et al., 2020). Corneal wound healing is a complex process involving cell death, migration, proliferation, differentiation, and extracellular matrix (ECM) remodelling (Mathews et, al.,2018 and Singh et al., 2013). Corneal healing mechanisms exist to aid in the proper repair and preservation of corneal structure following an injury (Cursiefen et al.,2007). When these fail, there are therapeutic advances that aim to reduce long-term complications. Corneal opacity can be caused by an abnormal regulation of the healing mechanisms. It's critical to reduce inflammation and promote epithelial wound healing for a scar-free corneal recovery with no vision problems. Current treatments for corneal wound healing include human amniotic membrane (HAM) bandages, bandage contact lenses (BCL), and collagen shields, as well as the use of therapeutic eye drops on a regular basis. Each of the treatment mentioned has advantages and limitations in terms of ease of raw material acquisition, manufacture, biocompatibility, drug loading, release kinetics, suitability and storage (Zarrintaj et al., 2018; Chau et al, 2012 and Bian et al., 2017). Despite the need for a convenient and cost-effective strategy for corneal wound healing, such as in conditions where extensive topical treatment with eye drops is required, there is still no drug-eluting corneal bandage on the market aside medicated AM bandages which is expensive. However, a well-designed drug incorporated bandage will offer a safe, patient-friendly and efficient solution to many chronic patients that

are having trouble adhering to the regular administration of ophthalmic medication by the use of eye drops or in critical cases where frequent administration of therapeutics is required.

As discussed in chapter 1 and chapter 2, ESM, a protein-rich fibrous natural biomaterial similar to native ECM. ESM is inexpensive, nontoxic, and it can easily be modified. Over the years, ESM has been demonstrated to be an ideal biomaterial for wound healing. Choi et al, (2021) found acid-treated ESM could promote skin regeneration and wound healing. Guarderas et al (2016) considered ESM as a dressing to aid the closure of wound in the early stages of wound healing. Furthermore, Yang, Chuang, Yang and Tsay (2003), showed that ESM could provide wound protection and pain relief over split-thickness graft donor sites.

An ideal bandage for cornea wound healing must encourage promote healing, non-toxic to surrounding tissues, have the appropriate physical /mechanical characteristics conforms to the shape of the wounds, be easily removal and cost effective. Collectively, literature and the findings from chapter 2 confirm ESM as a promising biomaterial for wound healing bandages. (Benson et al., 2012 andMine et al., 2003). Likewise, the large surface area of the ESM allows it to act as an adsorbent of drugs or microparticles to enhance tissue regeneration through sustained drug release (Chai et al., 2013) (Benson et al., 2012) (Yang et al., 2003).

As discussed in chapter 1 and 3, MP is a drug delivery system that can be used to address the limitations of eye drops. The major problem with eye drops is poor bioavailability and ophthalmic adverse effects including wound-healing complications. Polymer based microparticulate systems are often used in therapeutic applications as controlled and sustained release carriers for drugs and growth factors to improve the bioavailability and efficiency. The combination of drug loaded MP and ESM can be a convenient and cost-effective strategy for ocular/cornea wound healing. For successful drug delivery using drug incorporated bandage, certain parameters have to be adjusted to overcome critical challenges during the design, manufacturing and storage processes. It is crucial to consider the drug loading, physical and

surface properties such as shape, thickness, transparency, modulus and wettability. Moreover, content stability of wound bandage is of importance during preservation and storage.

The aim of study in this chapter was to formulate and evaluate a potential novel bandage comprising of drug loaded PLGA MP and ESM for ophthalmic wound healing applications. The physiochemical and mechanical properties of the MP-loaded ESM based bandages were evaluated using fluid content analysis, fluid contact angle test, visual tests and UV/Visible spectrophotometry for transparency, SEM, FTIR and texture analyses. A combination of in vitro/ in vivo tests i.e., Franz cells, CAM assay and rat corneal wound model were employed in assessing the biocompatibility, release profiles, toxicity, pro-angiogenic and wound healing responses of the bandage.

4.2 MATERIALS

PLGA copolymers with lactic: glycolic acid ratios of 1:1 (MW: 29-38 kDa) were purchased from Evonik (Darmstadt, Germany). 99+ % hydrolysed PVA (MW: 89-98 kDa), PBS, FITC-BSA, QuantiPro Bicinchoninic Assay (BCA) kit and VEGF were obtained from Sigma-Aldrich (Poole, Dorset, UK. Ethyl acetate (≥ 99.5 % and acetic acid, ≥ 99% were purchased from Fisher Scientific (Loughborough, Leicester, UK). Free-range, brown, chicken eggs (British Blacktail, gallus galuus) were purchased from a local supermarket (Waitrose, London, UK). Fertilized hens' eggs were purchased from Henry Stewart and Co Ltd (Norfolk, UK). was purchased from Fisher Scientific (Loughborough, Leicester, UK). Ethylenediaminetetraacetic acid (EDTA) was supplied by Agar Scientific (Stansted, Essex, UK). The Visking Dialysis Tubing membrane, a regenerated cellulose membrane (MW:12-14 kDa, dry thickness: 20 µm) was purchased from Medicell membrane Ltd (Greenwich, London, UK). All other reagents and chemicals were obtained from Merck (Poole, Dorset, UK) unless otherwise stated. Fresh porcine eyes were kindly donated by Royal Veterinary Collage (Hertfordshire, Hatfield, UK).

4.3 METHODS

4.3.1 Preparation of drug-loaded microparticle ESM

Fresh eggs were carefully washed in DI water before being submerged in 0.5 M acetic acid for 44 hours (ESM-A0.5) or 0.9 M EDTA for 20 hours at room temperature (19 °C) (ESM-E0.9). The extracted membranes were collected and thoroughly washed in DI to remove the albumen and yolk after the calcium carbonate shell had completely dissolved (Mensah et al, 2021). The ESM was manually removed from the eggshell using tweezers as a control (ESMstrip). To avoid dehydration, all extracted ESM samples were fully immersed in PBS and stored in a refrigerator (4 °C) before use.

The drug-loaded MP were generated using the in house developed method (Mensah et al, 2019). Briefly, 20 mg FITC-BSA (model drug) or 20 µg VEGF was dissolved in 5 ml of ethyl acetate in which 1 g of PLGA polymer was completely pre-dissolved. A primary emulsion of FITC-BSA or VEGF/PLGA/EAc and PVA solutions were formed and vortexed to create the MP. Following that, the emulsion was added to a hardening bath to allow for complete evaporation (24 h). The hardening bath was completely covered with aluminium foil to exclude light. The supernatant was collected before the formulated MP were filtered, washed, and freeze-dried.

To prepare the FITC-BSA loaded MP (FBM), or VEGF loaded MP (VM) OESMs, 50 mg of the generated MP were immersed in 1 ml of aqueous 0.2 M NaOH, alkaline-catalyzed hydrolysis for 30 seconds (Figure 4.1). The modified MP were washed three times to remove the NaOH residue (Amoyav and Ofra, 2019). The MP were loaded onto the outer layer (fibrous side) of 3 x 3 cm^2 membranes. Using a spatula, the MP were spread on the outer layer of the ESM samples (Figure 4.1). The generated FBM loaded OESMs samples (FBM-OESMstrip, FBM-OESM-A0.5 and FBM-OESM-E0.9) and VM loaded OESMs samples (VM-OESMstrip, VM-OESM-A0.5 and VM-OESM-E0.9) were washed to remove excess MP, freeze-dried at

room temperature (19 °C) and stored at 4 °C for characterisation. The residue from the washing process was filtered, and the MP collected was air-dried and weighed to determine the quantity of MP loaded on the ESMs.

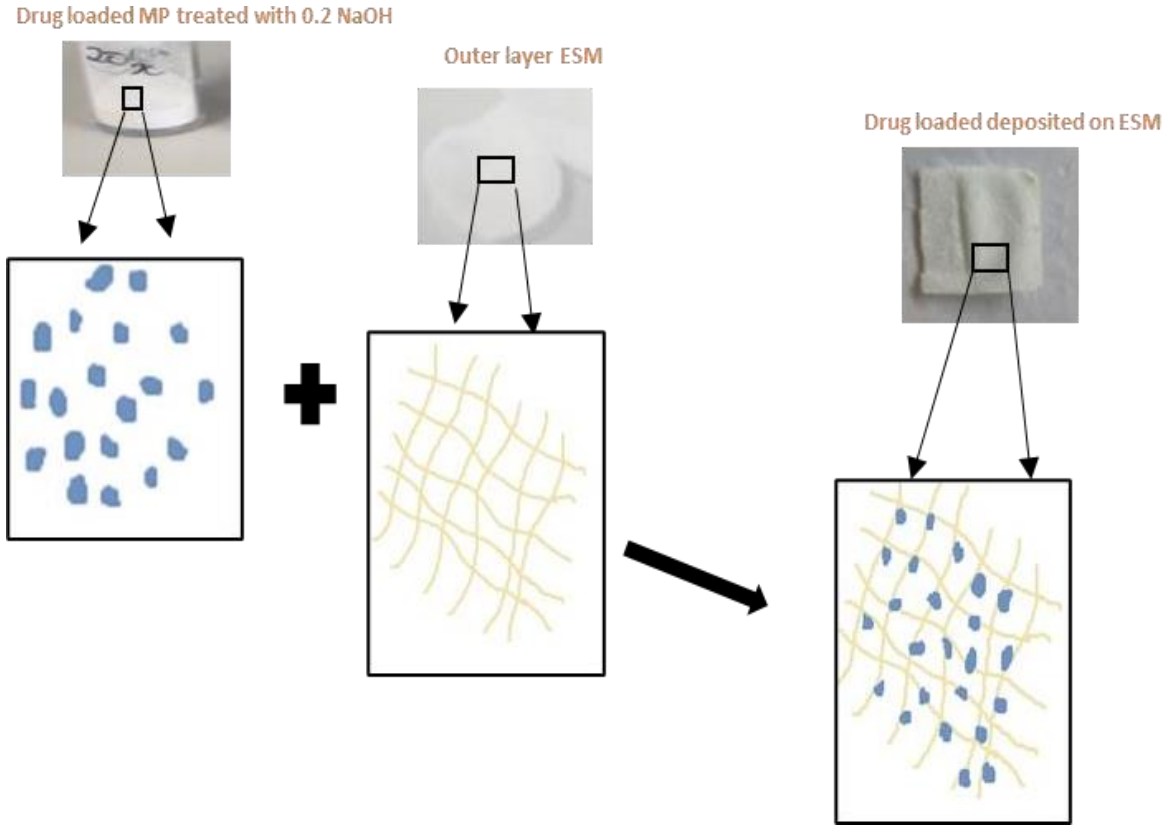

Figure 4.1. Schematic diagram of the fabrication of drug loaded microparticle ESM using the chemical treatment method: alkaline-catalysed hydrolysis.
They were immersed in 0.2 M NaOH for 30 minutes, the MP were washed three times to remove excess NaOH. The modified MP were then spread on the ESM, washed, air- dried at room temperature (19 °C) and stored at 4 °C. The microparticles were loaded onto the outer layer (fibrous side) of the membranes.

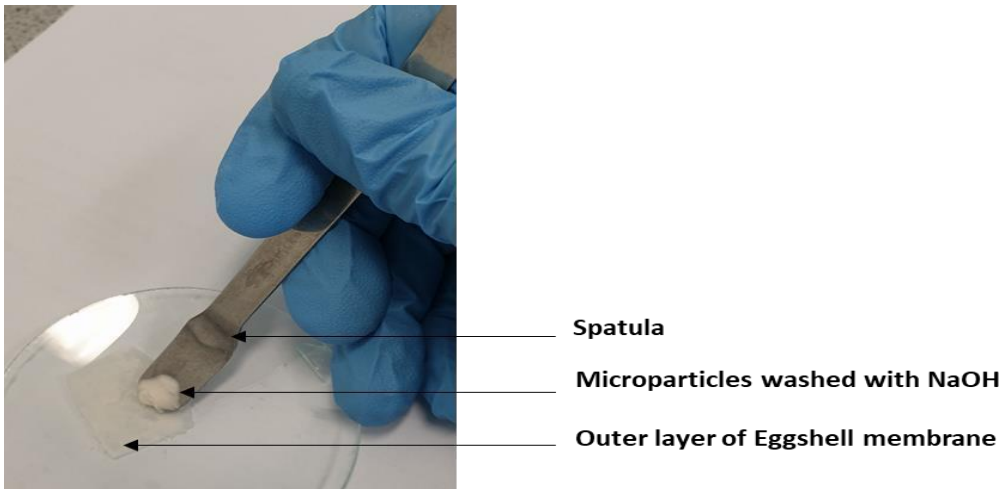

Figure 4.2. Photograph of the preparation of the drug loaded microparticles ESM.
The microparticles was washed with NaOH before spreading on the membrane.

4.3.2 Evaluation of the Loading method

Prior to loading the drug loaded microparticles to the outer layers of the ESMs, a preliminary structural study was performed using both the outer and inner layers of the ESMs. Briefly, 50 mg blank PLGA MP were fabricated and treated with 0.2 NaOH. The modified MP were loaded onto the inner layers: LESMstrip, LESM-A0.5 and LESM-E0.9 and outer layers: OESMstrip, OESM-A0.5 and OESM-E0.9, washed and air-dried. The quantity of MP not loaded were determined. The structures of the samples (blank MP-LESMstrip, blank MP-LESM-A0.5, blank MP-LESM-E0.9, blank MP-OESMstrip, blank MP-OESM-A0.5 and blank MP-OESM-E0.9) were studied using FESEM at a magnification of 100x and 500x for the inner and outer layers respectively.

4.3.3 Stability test

The tensile properties of the blank MP ESM samples (ultimate tensile strength, elongation at break and Young's modulus) were analysed using a tensile grip attached to Texture Analyser TA. XT (StableMicro Systems Ltd, Surrey UK) with a 5 Kg load cell at 10 mm/sec. Samples were wet with PBS and dabbed with paper towel before the tests. The samples were cut into bone shape of height-25mm and weight – 10 mm. Before being carefully placed in between the

two grips and screwed tightly together, each test membrane was supported by standard sandpaper to increase friction and prevent slipping in between the grips during the analyses (Mensah et al, 2021). Data were recorded when the force equaled the trigger force and analyse with Texture Exponent Software 32 program. The sample: blank MP-OESMstrip, blank MP-OESM-A0.5 and blank MP-OESM-E0.9 used were air-dried or freeze- dried. On day zero, some of the dried samples were stored at room temperature for an hour before testing and the remaining samples were stored at two different temperatures (4° C and -20° C) 60 days (Figure 4.3). The tensile properties were measured on day 30 and day 60. The ultimate tensile strength and elongation at break were generated from the TA machine and Young's modulus was calculated using equation 4.1 as stated below (Ahmed and Boateng, 2018).

$$Young's\ modulus\ (MPa) = \frac{Slope}{(Membrane\ \ thickness\ \ x\ speed\ \ (mm/sec))} x100 \qquad \text{Equation 4.1}$$

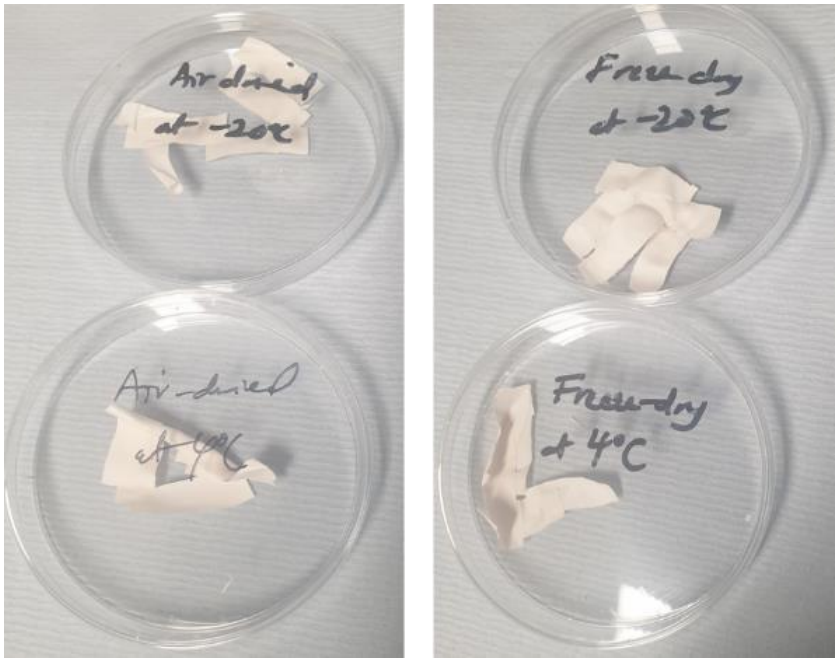

Figure 4.3. Photographic images of the air-dried and freeze-dried FITC-BSA loaded Microparticles eggshell membrane for 60 days storage at 4° C and -20° C.

On day 30 and 60, the tensile properties were measured using Texture Analyser TA. XT (StableMicro Systems Ltd, Surrey UK).

4.3.4 Thickness measurements

The thickness of the FBM-loaded OESMs and blank MP OESMs were measured by sandwiching them between two known-thickness microscopic slides. The total thickness of the samples was measured to the nearest 0.01 mm using a Moore and Wright Outside micrometre (Zoro, Leicester, UK). Each sample's thickness was measured at six random locations, and the average values were reported as the membrane thickness (Mensah et al, 2021).

4.3.5 Characterization

4.3.5.1 Surface Morphology

Freshly made FBM-OESMstrip, FBM-OESM-A0.5 and FBM-OESM-E0.9 were fixed for 24 hours at 4 °C in 3 % (w/v) glutaraldehyde in 0.1 M cacodylate buffer. The fixed membranes were then dehydrated for 2 minutes in a series of graded ethyl alcohol solutions: 1 x 70%, 1 x 90%, and 3 x 100%. The membranes were then critical point dried by immersing them in HMDS for 2 minutes. The dried membranes were adhered to 12 mm carbon tabs (Agar Scientific, Stansted, UK) that were pre-mounted onto 0.5 aluminium spectrum stubs (Agar Scientific, UK) before being sputter-coated with gold/palladium (Polaron E500, Quorum Technology, UK). The morphological characteristics of the FITC-BSA MP and the FITC-BSA MP loaded ESMs were measured using Philips XL30 FESEM (UK) at an operating voltage of 5 kV, spot size 3. The samples were examined at a magnification of 500x. The fibre diameters of the drug-loaded ESMs in the FESEM images were evaluated via Fiji-ImageJ software and OriginLab Origin 2021. Using the FESEM images at Magnification of 500x generated for FBM-OESMstrip, FBM-OESM-A0.5 and FBM-OESM-E0.9, the surface roughness was examined. Surface topography and surface roughness plots were generated using Fiji-ImageJ software. Based on the surface topography and profile plots, the surface roughness (Arithmetical mean deviation, Ra) was deduced via SurfCharJ-1q plugin in the Fiji-ImageJ software.

4.3.5.2 Transparency tests

To determine the transparency qualities of FBM-OESMstrip, FBM-OESM-A0.5 and FBM-OESM-E0.9, the samples were soaked in PBS for 24 hours to equilibrate, and the wet samples were placed over a standardised waterproof test card. The images of the samples were taken with a Samsung Galaxy S9 plus cell phone's 12 MP Super Speed Dual Pixel AF sensor camera (OIS, FOV: 77, Dual Aperture: F1.5 mode/ F2.4 mode) (Chau et al, 2012; Mensah et al, 2021). Further transparency of the samples was examined by measuring light transmittance through wet samples with a T80 UV-VIS spectrophotometer (PG instrument Ltd., Leicester, UK) over a wavelength range of 400 to 1000 nm (method adopted form Mensah et al, 2021).

4.3.5.3. Fourier-transform infrared spectroscopy

PerkinElmer FTIR operating in the Attenuated Total Reflectance mode (SensIR Technologies, UK) was used to determine the elements and functional groups of the FBM-OESMstrip, FBM-OESM-A0.5 and FBM-OESM-E0.9. The samples were scanned in the infrared range 600–4000 cm^{-1} and measured at 19 °C. Before analysing the samples, the spectrometer was calibrated by taking a background spectrum.

4.3.5.4 Porosity

A previously reported liquid displacement method was employed to determine the porosity of the FBM-OESMstrip, FBM-OESM-A0.5 and FBM-OESM-E0.9 (Ahmed and Boateng,2018; Mensah et al. 2021). In brief, the samples were air dried for 24 hours at room temperature (~19 °C) and weighed. The dried samples were then immersed in 5 ml of PBS for 24 hours at 34 ℃ before being weighed after patting the surfaces with a paper towel. The total pore volume was calculated using the average thickness (mm) and diameter of the FBM-loaded ESM samples (equation 4.2). The porosity was calculated as shown in equation 4.3 below (n=3).

$$V_o = (\pi x \frac{D}{2})^2 \, x \, H \qquad \text{Equation 4.2}$$

$$\varepsilon \, (\%) x \frac{W_w \, x \, W_d}{\rho \, x \, V_o} \, x \, 100 \qquad \text{Equation 4.3}$$

Where, V_o is the total pore volume, D is the diameter, π is the pi value of 3.14, H is the thickness, W_w and W_d are the wet and dry weights of the samples, ε is the porosity and ρ is the density of PBS.

4.3.5.5 Contact angle measurement

The contact angle of a PBS solution droplet (~2.0 µL) was measured using an optical contact angle meter (200 CAM, KSV Instruments Ltd, Finland) to assess the surface wettability of FBM-OESMstrip, FBM-OESM-A0.5 and FBM-OESM-E0.9 at room temperature (~19 °C). Each value of the contact angle was calculated as an average of three different readings taken under the same conditions.

4.3.6 *In vitro* release study with diffusion cell

4.3.6.1 Standard calibration curve

Calibration curve was constructed for concentration range of 1-20 µg/ml FITC-BSA in PBS prepared from a stock solution of 1 mg/ml. The fluorescein intensities of the FITC-BSA concentrations were measured using BioTeck micro plate reader The LOD and LOQ of the protein in PBS were evaluated from the calibration curve.

4.3.6.2 Extraction of porcine vitreous humour

A small incision was made on the lateral side of the *porcine* eye *(ex-vivo)* with a scalpel to extract the vitreous humour. Vitreous humour was gently *separated* onto a Petri dish, and non-vitreous parts attached to it, such as the iris and lens, were separated further. Extracted vitreous was stored in sterile containers at 2-8 °C. The isolated vitreous was used in the *in vitro* eye model within 12 hours of the extraction.

4.3.6.3 *In vitro* eye model

The drug release profile of the fabricated MP-ESMs was examined using an *invitro* Franz diffusion cell eye model generated by Shafaie et al, 2018. The bespoke Franz cell used consisted of three compartments: a donor chamber, a middle chamber containing porcine

vitreous humour and a receptor chamber (Figure 4.4i). The middle chamber was filled with vitreous, and the top and bottom were covered a cellulose dialysis membrane. Subsequently, the donor and receptor chambers were attached. The set up was occluded with parafilm to prevent evaporation. The FBM-OESMstrip, FBM-OESM-A0.5 and FBM-OESM-E0.9 were trimmed into circular discs of diameter 10 mm sufficient to cover the diffusion area of the donor chamber. The samples were soaked in PBS for at least 2 hours before cutting into the desire size. Each membrane sample was mounted between the donor chamber and middle chamber with drug loaded side (outer layer) facing upwards. For the study of free FBM (control), the 30 mg of sample was introduced directly onto the cellulose dialysis membrane at the top. Using a syringe, 3 ml of PBS was introduced into the receptor chamber with magnetic stirrer and allowed to equilibrate at 34 °C (natural temperature of the eye) for 30 minutes (Figure 4.4ii). 1 ml of the PBS was introduced into the donor chamber. FITC-BSA sample volume of 3 ml were collected though the sampling port of the cell at different times within 14 days. The FITC-BSA samples were centrifuged and the concentration of the protein in each sample was determined using Micro-QuantiPro™ BCA Assay kit. Each time an equal volume of fresh preheated PBS was reintroduced into the receptor chamber to main sink conditions. Air bubbles formed were removed by carefully tilting the Franz cell for the bubbles to escape through the sampling port. The cumulative percentage released was calculated, and the mean values and standard deviations were reported.

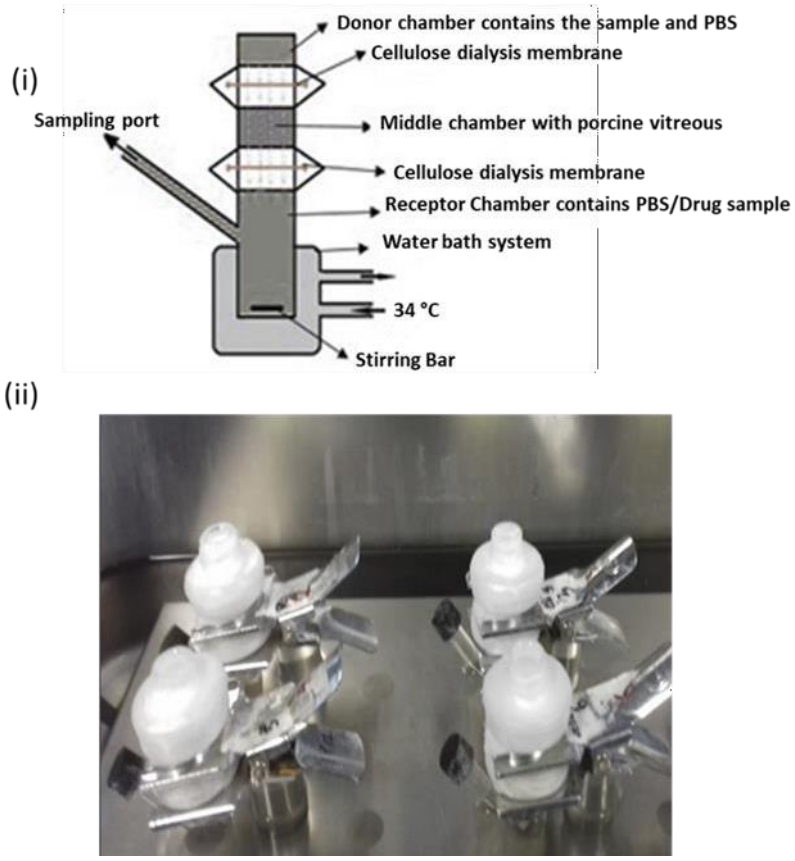

Figure 4.4. *In vitro* drug release study
(i) Schematic diagram of novel in vitro Franz diffusion cell eye model. FBM-OESMstrip, FBM-OESM-A0.5 or FBM-OESM-E0.9 mounted in the Franz cell eye model to evaluate the release s PBS: Phosphate buffer saline (ii) Photography of Franz diffusion cells in water bath at 34°C.

4.3.7 *In ovo* Chick Chorioallantoic membrane assay

An *in ovo* CAM assay was used to determine the toxicity and biocompatibility of the drug loaded MP-ESMs. Fertilized Dekalb White chicken eggs (Henry Stewart and Co Ltd, Norfolk, UK) were incubated for four days in a Brinsea Eco incubator at 37 °C and 80 % relative humidity. On the fourth day, 5 ml of egg white was extracted with a blunt 18-gauge needle through a hole to reduce the volume space within the egg and result in a lower/detachment of the CAM from the top portion of the eggshell. In each egg, a 2 x 2 cm square window opening was cut and covered with a transparent low adhesion tape. The eggs were incubated for an extra day. Blank MP-OESMstrip, blank MP-OESM-A0.5, blank MP-OESM-E0.9, VM-OESMstrip, VM-OESM-A0.5 and VM-OESM-E0.9 samples immersed in PBS were sterilised under UV irradiation in laminar cell culture for 24 hours. On the 5th day, the pre- sterilised samples were

placed on the CAM. The sides without the MP were placed directly on the CAM. Additionally, 3 x 3 mm Whatman #1 filter paper squares, blank MP, VEGF loaded MP and VEGF were sterilized using 70% ethanol. The filter papers socked with VEGF loaded MP 20 L were placed on the CAM. Using a 100 mm micro spatula, 20 µg of blank MP, 20 µg of VEGF loaded MP and 2 µg of VEGF were carefully loaded on the filter papers previously placed on the CAM. All samples were placed on the CAM under sterile conditions. The windows of the eggs were sealed and kept in the incubator for an additional 5 days and monitored daily. The seal was removed on the tenth day, and photographs were obtained using a GX CAM digital camera at X1 magnification. The AngioQaunt programme (MATLAB, UK) was used to quantify, analyse, and characterise blood vessels (Niemisto et al, 2005). The counting of the various vessels in each CAM were random and triplicated.

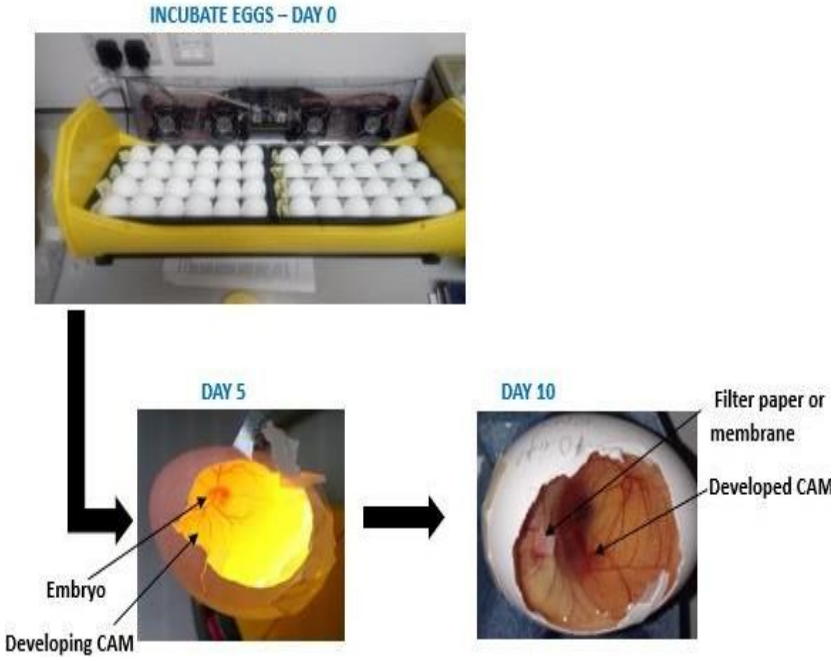

Figure 4.5. Angiogenic study
Fertilized eggs were incubated for 10 days to access the developed CAM in order to observe and compare the pro-angiogenic responses and release of the test samples introduced onto the CAM on day 5.

4.3.8 *In vivo* experiments

A preliminary study of the cornea wound healing characteristics of the inner sides of ESM samples: ESMstrip, ESM-A0.5 and ESM-E0.9 generated using the optimised protocol were assessed using an *in vivo* rat model. Researchers from the Department of Ophthalmology, Dankook University College of Medicine, Dankook University, Cheonan, Republic of Korea, performed the procedures. All animal care and use were done in accordance with the guidelines for using animals in ophthalmic research. A schematic representation of the *in vivo* rat corneal wound healing model is presented in Figure 4.6a. Six-week-old male Sprague Dawley (SD) rats were given cornea wound using mechanical and chemical method (Figure 4.6b). The rats were sedated with ketamine and xylazine before the procedures. In giving a mechanic wound, a biopsy punch (3.5 mm diameter) dipped in 30% ethanol was used applied on the cornea for 40 seconds. The cornea tissue was mechanically scraped with a mico-forcep. The ocular surface was rinsed with 5 ml PBS (Gabriella, 2019). For chemical wound, 3.5 mm paper disc soaked in 1n NaOH was applied on the rat cornea for 30 seconds. The ocular surface was rinsed with 10 ml PBS for 2 minutes (Gabriella, 2019). The wounds given by both methods were covered with AM (positive control), ESMstrip, ESM-A0.5, and ESM-E0.9. The inner layer of the samples was placed directly on the cornea wound. The membranes' periphery was sutured to the corneal edge to ensure that it stayed in place for the observation. Eyelids were also sutured to prevent further injury from scratching. As a control, a corneal incision without a membrane was utilised. The rat was given Alfaxan for observation at 24-hour. Fluorescein staining was used to examine wound closure and photographs were taken to evaluate the percentage of wound closures.

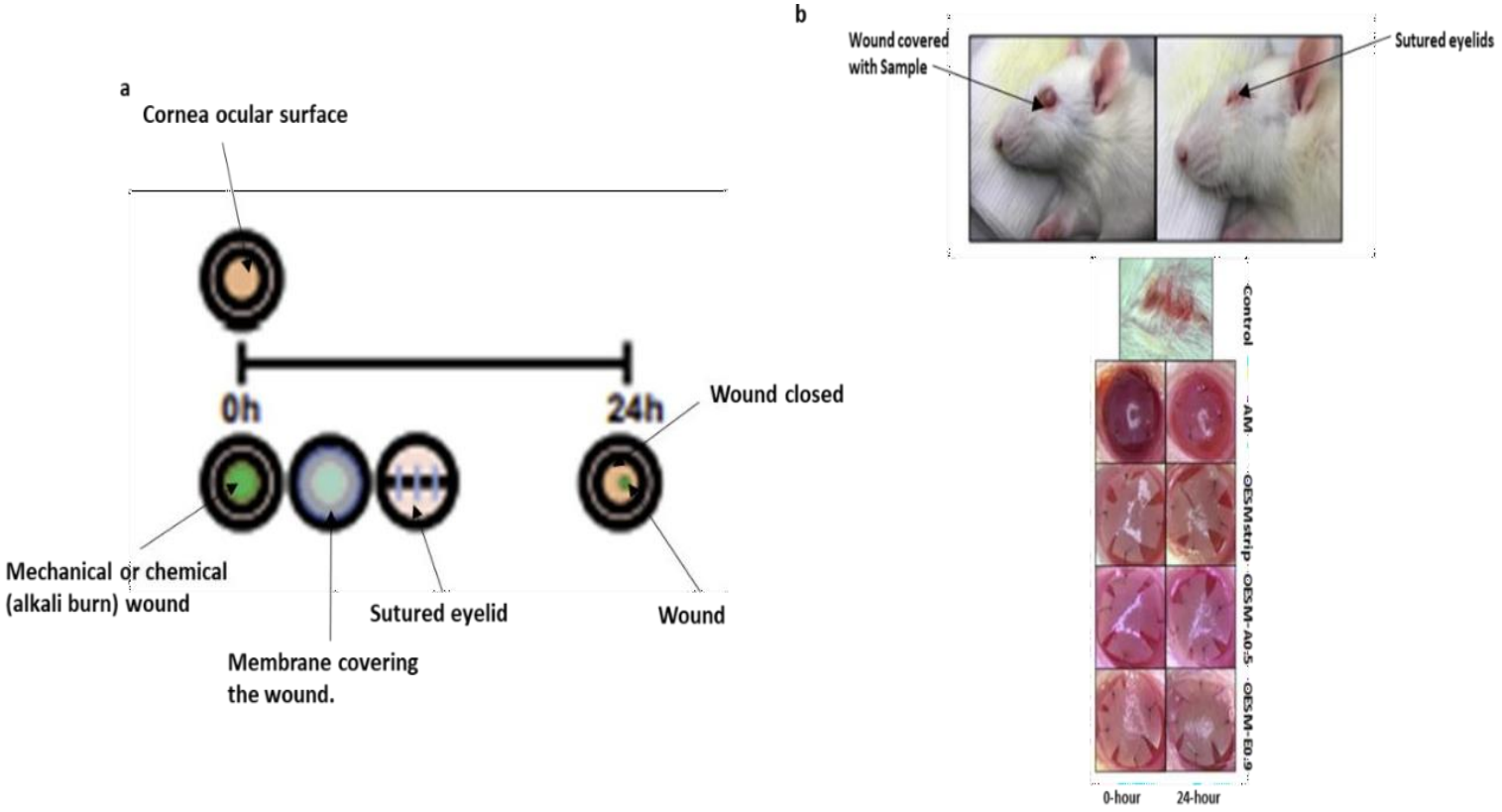

Figure 4.6. In vivo corneal wound healing model

(a) Schematic representation of In vivo corneal wound healing model using 6 weeks old male σ rats. A 3.5 mm wound was made on the cornea, and the following treatments were used: control (no membrane), AM, LESMstrip, LESM-A0.5, and LESM-E0.9. The percentage of wound closure was calculated for observation at 0 and 24 hours. (b) Photograph of the procedure was used. At 0 and 24 hours, the cornea wound was closely

4.3.9 Statistical analysis

Data are shown as mean ± SD (standard deviation) and compared using 1-way and 2-way ANOVA with Tukey's, Dunnett's Multiple Comparison Test and Bonferroni post-hoc test respectively. Statistical significance is indicated with (*) which represents a $p < 0.05$, (**) which represents a $p < 0.01$, and (***) which represents a $p < 0.001$. No statistical significance is indicated by $p > 0.05$. GraphPad software 9.0, Fiji-ImageJ and OriginLab Origin 2021 software were utilised in analysing the data.

4.4 RESULTS & DISCUSSION

The treatment for corneal wound healing normally calls for the combination of ocular bandages and concurrent application of topical drugs. Adherence to regular admiration of ophthalmic medicine is a major issue, henceforth there is a need to develop a 2 in 1 ocular bandage for convenient and cost-effective strategy for ocular wound healing. A drug incorporated bandage is useful in the treatment of ocular/corneal diseases. Its main indications are to relieve the pain, protect the ocular surface, promote corneal healing and epithelial regeneration and deliver ophthalmic drugs on the ocular surface (Zidan, Rupenthal, greene and Seyfoddin, 2017). It is crucial to consider these physical and surface properties such as thickness, transparency, modulus, wettability, water content, oxygen permeability and maximise drug loading capacity when developing the bandage. In this chapter, a drug loaded microparticles (MP) was loaded into ESM in order to produce cheap, effective and rapid wound bandage for patients. The generated bandage was characterised by evaluating the physical, mechanical and the biological properties.

4.4.1 Drug incorporated Microparticles eggshell membrane

The optimal protocol for generating ESM and drug loaded MP developed in chapter 2 and chapter 3 of the thesis were utilised to generate ESMs and FITC-BSA (model drug) incorporated microparticles. Drug incorporated microparticles ESMs were generated using chemical treatment method. Chemical modification is basically the simplest technique through surface hydrolysis with an alkali or aminolysis. This method introduces hydrophilic carboxylic acids (-COOH) and hydroxyl (-OH) or amine groups through the cleavage of ester bonds which can be used to bind bioactive molecules such as collagen and chitosan (Zhu et al, 2004, croll et al, 2004, Mohd Sabee1, Kamalaldin, Yahaya and Abdul Hamid, 2016 and Soo-ling, Jaafar, Abdul hamid and Yahaya, 2018). The ESMs were extracted using manual peeling, immersion in 0.5M acetic acid and immersion in 0.9 M EDTA methods. Using the optimised single o/w

emulsion method, 10 – 50 µm MP were formulated with or without model drugs: FITC-BSA and VEGF. In order to ascertain the side of the ESM to load the drug loaded MP, blank MP ESMs were generated. The MP were treated using 0.2 M NaOH, washed and the modified MP were spread on the outer and inner layers of the ESMs. The modified MP were washed after the treatment to remove any NaOH residue. The modified MP were successfully loaded into the ESMs by using a spatula. The generated ESMs were washed, air dried and stored. A

preliminary study was performed to select the ideal side of the ESM to load the MP. Blank MP-OESMstrip, blank MP-OESM-A0.5, blank MP-OESM-E0.9, blank MP-LESMstrip, blank MP-LESM-A0.5, and blank MP-LESM-E0.9 were generated by loading the MP on both sides of the membrane. The amount of MP loaded into the membranes were deduced and from the results (Table 4.1), less than 10% of the MP were incorporated into the inner sides of the membrane (blank MP-LESMstrip, blank MP-LESM-A0.5, and blank MP-LESM-E0.9). On the other hand, the outer layer samples: Blank MP-OESMstrip, blank MP-OESM-A0.5, blank MP-OESM-E0.9 contained more than 65% MP.

Table 4.1. Percentage unloaded modified MP for the MP-ESM samples.

Sample	Percentage of unloaded MP (%)
Blank MP-LESMstrip	91.13
Blank MP-LESM-A0.5	93.28
Blank MP-LESM-E0.9	90.62
Blank MP-OESMstrip	33.78
Blank MP-OESM-A0.5	26.44
Blank MP-OESM-E0.9	30.17

Likewise, the structural morphology of the samples was studies via FESEM and compared with blank ESMs. From the results no reasonable difference was observed between the blank LESMstrip, LESM-A0.5, and LESM-E0.9 and the MP loaded samples blank MP-LESMstrip, blank MP-LESM-A0.5, and blank MP-LESM-E0.9 (Figure 4.7 A). The failure may be due to the continuous and slender nature of the limiting membrane of the ESMs. In contrast, spherical shaped MP were attached to the fibres in the Blank MP-OESMstrip, blank MP-OESM-A0.5, blank MP-OESM-E0.9 (Figure 4.7 B). This confirmed that the MPs were successfully loaded into the fibrous network of the membrane. The highly interconnected, porous and large surface area of the outer side of ESM allow the inner shell membrane of the ESMstrip, and outer shell membrane of the ESM-A0.5 and ESM-E0.9 act as an adsorbent of MPs (Yi et al, 2004 and Mensah et al, 2021). The major component of the chicken ESM is collagen protein and Nakono et al (2016) pointed out that the main chemical composition are amino acids. Thereby, lots of the amino functional groups on the ESMs are available to interact with free –COOH and –OH groups on the PLGA MP surface.

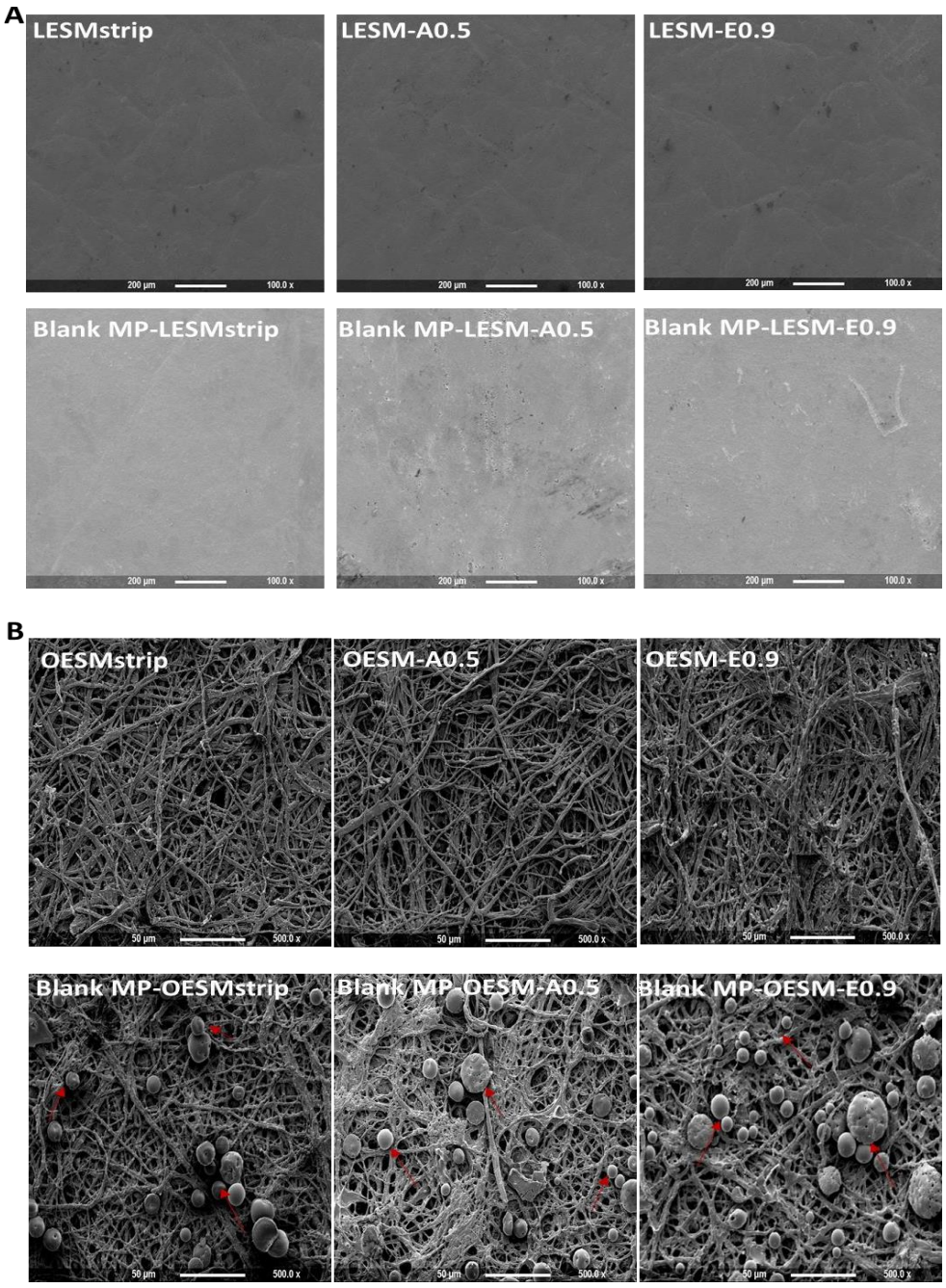

Figure 4.7. Surface Morphology analysis of the limiting membrane.
FESEM images of the LESMstrip, LESM-A0.5, LESM-E0.9, blank MP-LESMstrip, blank MP-LESM-A0.5 and blank MP-LESM-E0.09 at Magnification at 100x. (B) (A)FESEM images of the OESMstrip, OESM-A0.5, OESM-E0.9, blank MP-OESMstrip, blank MP-OESM-A0.5 and blank MP-OESM-E0.09. Red arrows point to microparticles (MP) attached to fibres of ESM. Magnification at 500x.

4.4.2 Stability of drug-loaded microparticles ESM in different drying/storage conditions

Prior to selecting an effective drying and storage temperature for the bandages produced, the stability of the drying and storage temperature on the mechanical property of the bandages was measured. Blank MP-OESMstrip, blank MP-OESM-A0.5, blank MP-OESM-E0.9, blank MP-LESMstrip, blank MP-LESM-A0.5, and blank MP-LESM-E0.9 were generated, air dried at room temperature or freeze-dried. The dried samples tensile properties were measured Ultimate tensile strength, elongation at break and Young's modulus were measured. The samples were stored at two different temperatures 4 and -20 C for 60 days. On day 30 and 60, the mechanical properties were determined. The thickness measurements of the membranes used are represented in table 4.2. No clear changes, $p>0.05$ were observed in the mechanical property of the air-dried and freeze-dried samples on day 0 (Figure 4.8). The results indicated that storage temperatures (4 and -20 °C) and the storage time (30 and 60 days) did not affect ($p>0.05$) the mechanical properties in terms of the ultimate tensile strength and young's modulus of the dried samples (Figure 4.8A and Figure 4.8C).

The elongation at break of the air-dried and freeze-dried samples during the storage period did not change with the exception of the freeze-dried ESM stored at 4 °C on the 30th day vs freeze-dried ESM stored at -20 °C on the 60th day ($p<0.05$), freeze-dried ESM stored at -20 °C on the 30th day vs freeze-dried ESM stored at 4 °C on the 60th day ($p<0.05$) and freeze-dried ESM stored at -20 °C on the 30th day vs freeze-dried ESM stored at -20 °C on the 60th day ($p<0.01$). From the findings, both drying methods caused no structural changes-denaturing of proteins, however several studies have revealed that freeze-drying collagenised scaffolds improves the mechanical property for long tern storage < 2 years (Zeng et al, 2013, Lowe et al, 2016, Sancho, Vazquez and De Juan-Pardo, 2014). According to Lee (1983), cold storge is an optimal condition for long term storage for native collagens. At low temperatures, the protein structures are intact.

.

Table 4.2. Thickness measurements of microparticles loaded membranes

Sample	Thickness (mm)
	Mean
Blank MP-OESMstrip	0.103 ± 0.010
Blank MP-OESM-A0.5	0.126 ± 0.008
Blank MP-OESM-E0.9	0.131 ± 0.014

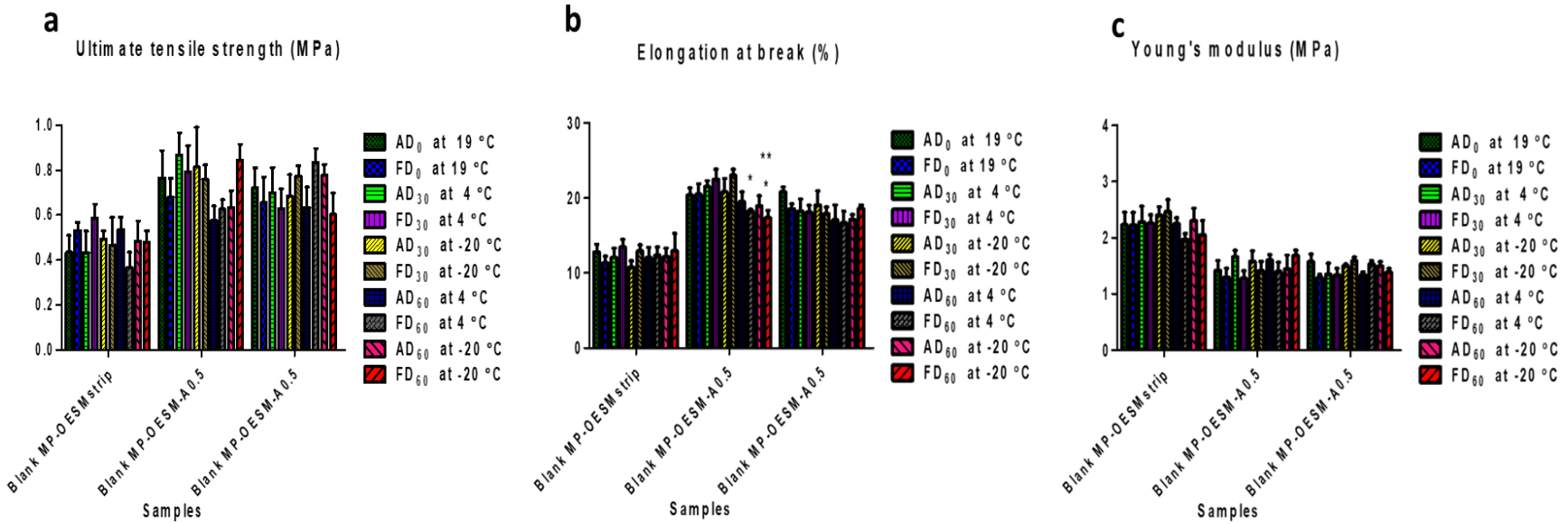

Figure 4.8. Mechanical properties for stability test.

The ultimate tensile strength, elongation at break and young's modulus at test speed of 10 mm/sec for Blank MP-OESMstrip, Blank MP-OESM-A0.5, Black-MP-OESM-A0.9. air-dried and freeze-dried at stored for 30/60days at 4 °C and -20 °C. AD_0 = air dried on day 0; FD_0 = freeze-dried on day 0; AD_{30} = air dried on day 30; FD_{30}= freeze-dried on day 30; AD_{60} = air dried on day 60 and FD_{60} = freeze-dried on day 60. * Corresponds to $p<0.05$ (FD_{30} at 4 °C vs FD_{60} at -20 °C and FD_{30} at -20 °C vs FD_{60} at 4 °C; ** corresponds to $p<0.01$ (FD_{30} at -20 °C vs FD_{60} at -20 °C).

4.4.3 Surface Morphological analysis of drug loaded MP-ESM

The morphology of the FITC-BSA loaded MP (FBM) and FITC-BSA MP incorporated OESMs was analysed and compared to blank OESMs (section 2.4.10) and FITC-BSA MP sample (Figure 4.9). The images showed the presence of MP adhered to the nanofibers in the ESM. The results revealed that the MP were successfully incorporated into the ESM. The MP attached to the fibres in the ESM have similar spherical-like shape as the MP.

Subsequently, the particle size of the MP and fibre diameters of the FITC-BSA MP loaded OESMs were evaluated via Fiji-ImageJ software and their respective distribution plots (Figure 4.9 a, b, c and d) were generated with OriginLab Origin 2021. From the data (Figure 4.9 a), FITC-BSA MP with particles size ranging from 2.56 to 57.5 µm (mean particle size of 17.09 ± 0.25 µm) were loaded into the ESMs.

The fibre diameters of the FBM-OESMstrip, FBM-OESM-A0.5 and FBM-OESM-E0.9 were evaluated as 0.28-4.75 µm, 0.84 – 8.97 µm and 1.26 – 6.87 µm respectively (figure 4.9 b, c and d). The fibre diameters of the MP loaded ESM were assessed and compared to the fibre diameters of blank ESMs. Figure 4.9 e displays the mean fibre diameter of the drug incorporated ESM and blank ESMs. From the results, no significance changes were observed in the MP loaded ESM (i.e., FBM-OESMstrip, FBM-OESM-A0.5 and FBM-OESM-E0.9) compared to their respective blank ESM, $p>0.05$ (i.e., OESMstrip, OESM-A0.5 and OESM-E0.9). This suggests that the introduction of the MP did not alter the fibrous structures.

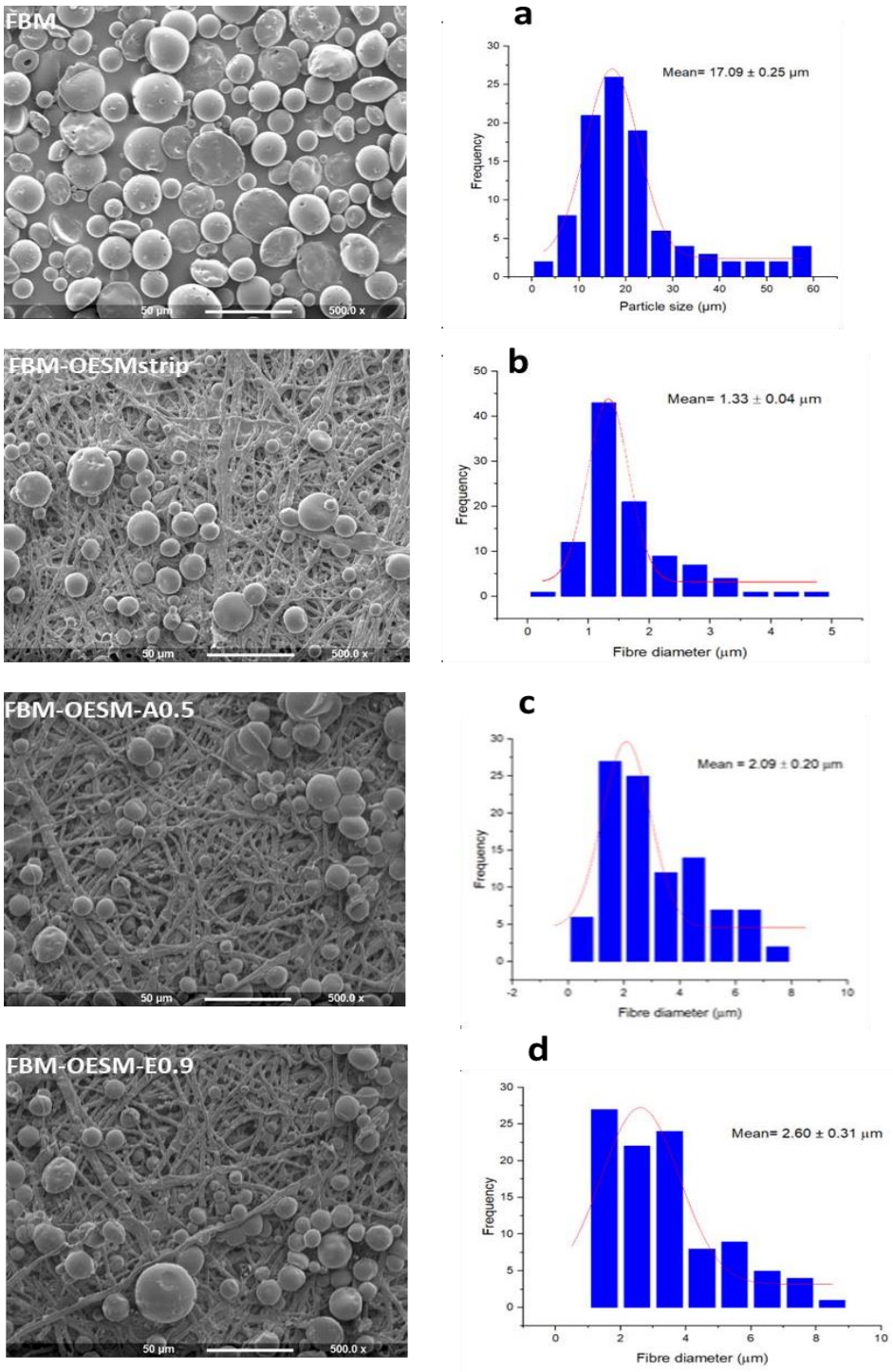

Figure 4.9. Structural analysis of FITC-BSA loaded Microparticles

FESEM images at 500X magnification of the FITC-BSA loaded Microparticles (FBM) and the FBM incorporated ESM i.e., FBM-OESMstrip, FBM-OESM-A0.5 and FBM-OESM-E0.9. 'a' present the particle size distribution plot for the FBM. 'b, c, d' represent the fibre diameter distribution (n= 100 counts) for OESMstrip, OESM-A0.5 and OESM-E0.9 respectively. All values are expressed as mean ± σ for n=100. FBM: FITC-BSA loaded microparticles

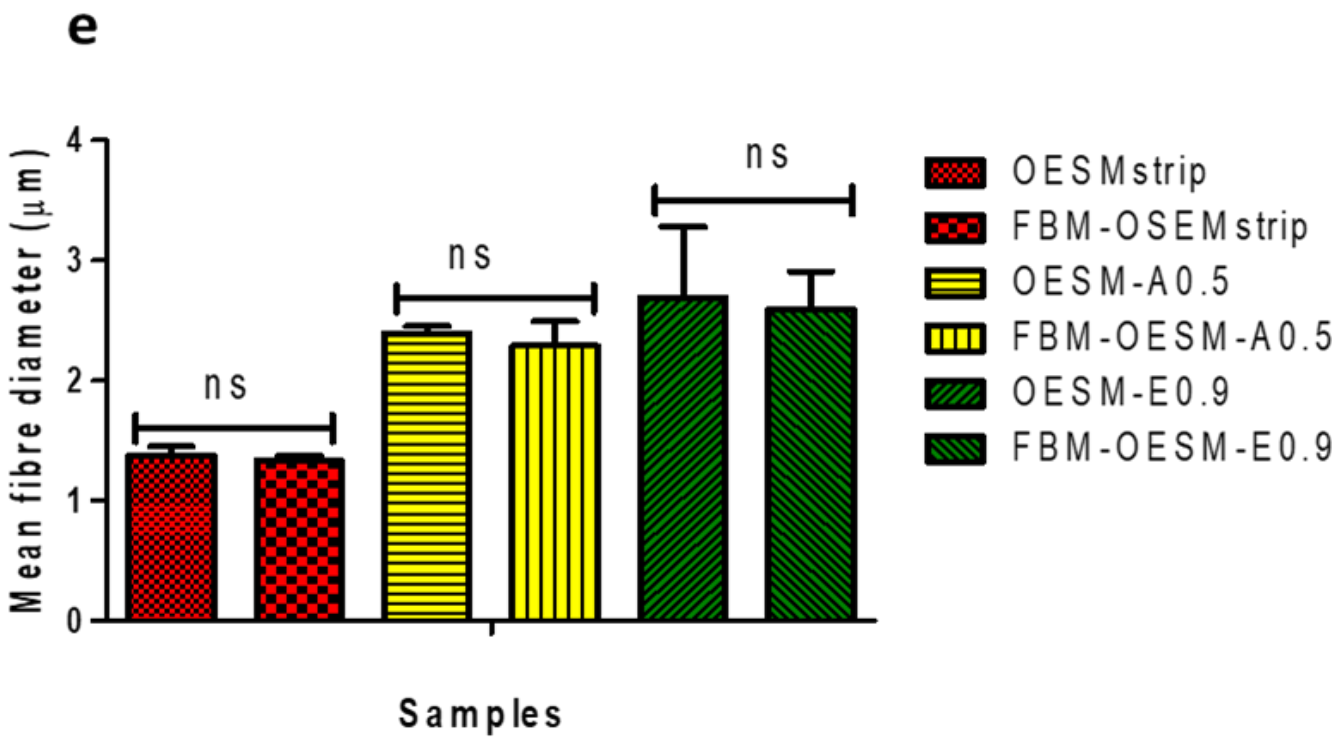

Figure 4.9e. Mean fibre diameter of FITC-BSA loaded Microparticles

. 'e' is the results for the comparison of the mean fibre diameter of the OESMstrip to OESM-A0.5 and OESM-E0.9 to FBM-OESMstrip, FBM-OESM-A0.5 and FBM-OESM-E0.9. No significance differences were observed (ns, $p>0.05$). All values are expressed as mean ± SD for n=100 (1-way ANOVA with Bonferroni's multiple comparison post-test ($p>0.05$). FBM: FITC-BSA loaded microparticles.

The surface roughness of the FITC-BSA MP loaded ESM samples were evaluated using the FESEM images at magnification of 500x. Figure 4.10a, b and c represent the surface topographies of FBM-OESMstrip, FBM-OESM-A0.5 and FBM-OESM-E0.9 respectively. The images were generated for the surface area of 229 x 330 μm^2 via Fiji-ImageJ software. The surface consists of pine-like surface identical to that of the blank outer layer ESM: OESMstrip, OESM-A0.5 and OESM-E0.9 outlined in section 2.4.10. Surface of the MP loaded ESM were further characterised by measuring the surface roughness area value i.e., arithmetical mean deviation, Ra. Prior to that, the surface roughness plots were generated via Fiji-ImageJ software (Appendix, Figure A 1.4 a, b and c). The Ra values obtained for FBM-OESMstrip, FBM-OESM-A0.5 and FBM-OESM-E0.9 were compared to the corresponding Ra values of the blank ESMs: OESMstrip, OESM-A0.5 and OESM-E0.9 (figure 4.10d). Statistically, no differences were observed between the blank and the MP loaded ESMs ($p>0.05$). This indicates that the incorporation of FITC-BSA MP into the ESMs had no impact on the surface roughness

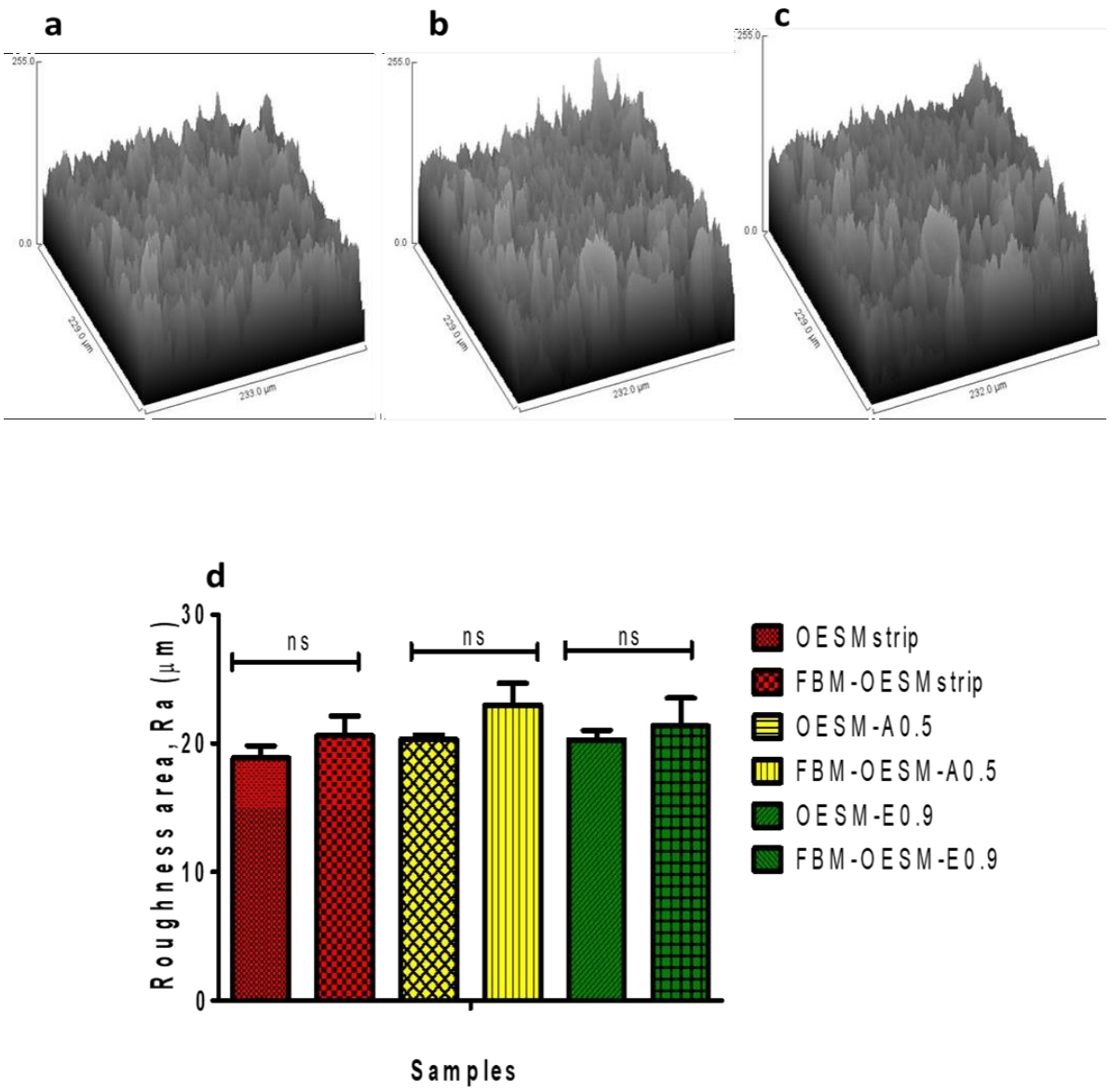

Figure 4.10. Surface roughness analysis

The images a, b and c are surface topography of FBM-OESMstrip, FBM-OESM-A0.5 and FBM-OESM-E0.9 generated via Fiji-ImageJ surface. Image d represents a plot of arithmetical mean deviation, Ra (µm) recorded for outer layers: OESMstrip, OESM-A0.5 and OESM-E0.9 and drug loaded MP ESM: FBM-OESMstrip, FBM-OESM-A0.5 and FBM-OESM-E0.9. using FESEM at magnification of 500x on surface area 229.0 X 232.0 µm respectively. The Ra values were calculated via Fiji-ImageJ software SurfCharJ 1q plugin. 1-way ANOVA with Bonferroni's multiple comparison post-test ($p > 0.05$). All values are expressed as mean ± σ for n=10. ns represents no significant difference, $p>0.05$. FBM: FITC-BSA loaded microparticles

4.4 4 Chemical composition

FTIR was employed to characterize the PLGA MP, the ESMs and the incorporation of the MP in the ESMs (Figure 4.11). The PLGA MP spectrum displayed peaks such as the -CH2, -CH3 stretching vibrations (2946.72 - 3000 cm^{-1}), the carbonyl C=O stretching vibrations of esters (1746.53 cm^{-1}), asymmetrical stretching -CH2, -CH3 (1381.62 cm^{-1} and 1452.06 cm^{-1}) and the C–O stretching vibrations (1180.38 cm-1). The spectrum of blank OESM (Figure 4.11) displays the presence of peaks (in cm-1) at 3289 (stretching mode of O–H and N–H), 3060, 2932 and 2869 (asymmetric stretching vibrations of the C–H bonds present in =CH and =CH2 groups), 1646 (C=O stretch of amide), 1524 and 1240 (CN stretching/NH bending modes of amide), 1441 (stretching mode of C=C bond), 1066 (stretching mode of C–O bond) and 660 (stretching mode of C–S bond). Figure 4.11 illustrates that the FTIR spectra of the three ESM samples (FBM-OESMstrip, FBM-OESM-A0.5 and FBM-OESM-E0.9) containing the FITC-BSA loaded microparticles are similar. In the spectra some peaks came from the polymer CH2, -CH3 stretching vibrations (2946.72 - 3000 cm^{-1} and 1746.53 cm^{-1}) and these peaks from the ESM :1646 cm^{-1}, 1524 1441 and 1240 cm^{-1}. The reduction of the -OH peak may be due to the interaction of the amino group in the ESM and the ester group in the MP. This suggests that the FITC-BSA MP were successfully immobilised on the surface of the OESMstrip, OESM-A0.5 and OESM-E0.9.

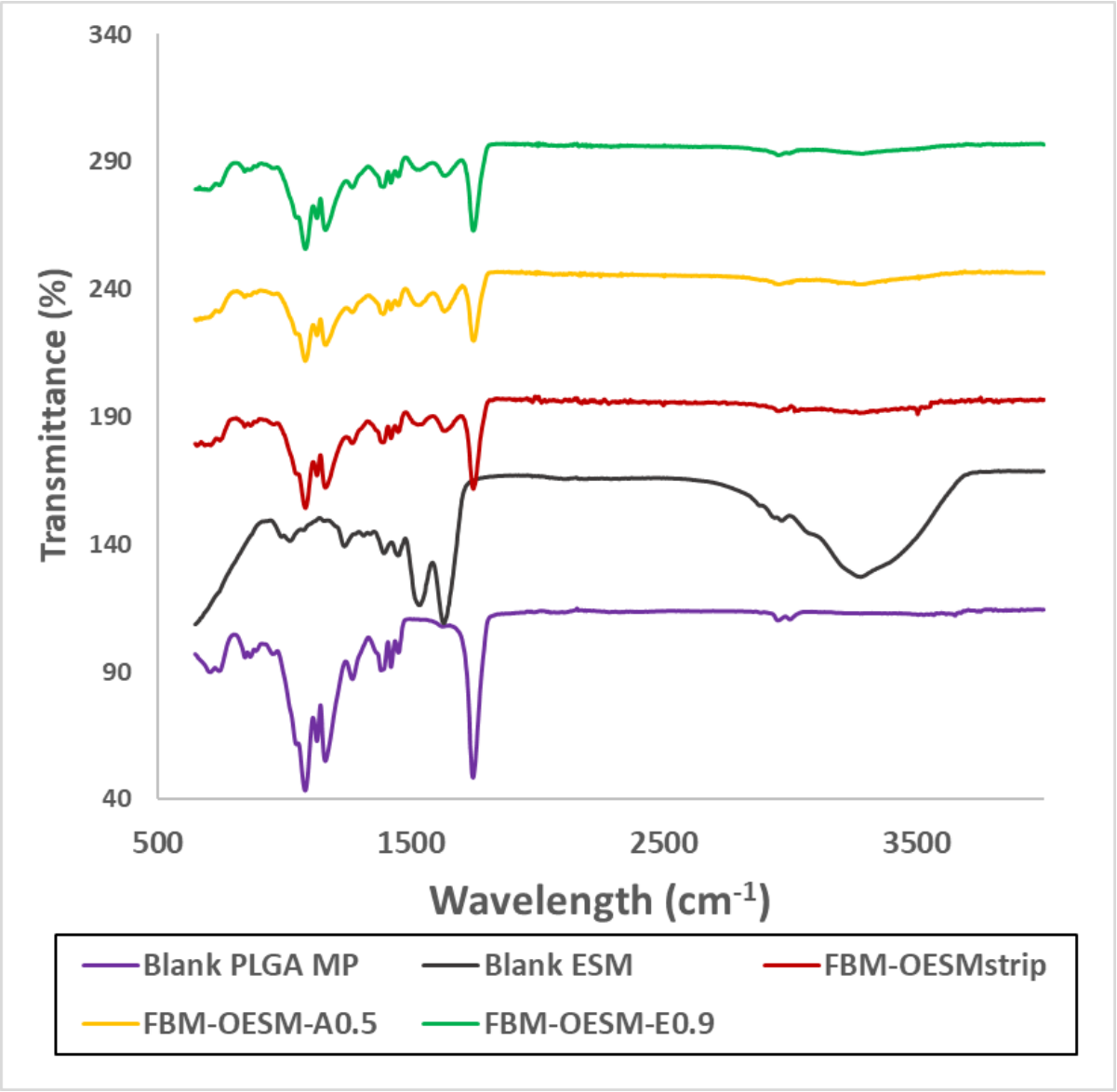

Figure 4.11. FTIR spectra of FITC-BSA loaded ESM
This diagram displays the FTIR spectra of PLGA MP blank OESM FBM-OESMstrip, FBM-OESM-A0.5 and FBM-OESM-E0.9. FBM: FITC-BSA loaded microparticles.

4.4.5 Visibility test

One of the prominent characteristics of the cornea is its transparency, which is an important criteria consideration when selecting a material for cornea wound healing (Ljubimov and Saghizadeh, 2015, Sheha et al., 2019). The transparency of wet blank ESMs and drug loaded MP ESMs was analysed using waterproof test card method (Figure 4.12i). The samples were placed on the card to determine the visibility of the test through the samples. The tests are obviously visible in all the samples however, the visibility in the FBM-OESMstrip, FBM-OESM-A0.5 and FBM-OESM-E0.9 is reduced as compared to the OESMstrip, OESM-A0.5 and OESM-E0.9. the reduction was due to the presence of drug loaded MP. Using UV-VIS spectrophotometer, the visibility of the samples was characterised by measuring the light transmittance. All the samples recorded light transmittance values above 70% (Figure 4.12ii), however the values of the MP loaded samples are below their corresponding neat ESMs. The reduction may be ascribed to the presence of the MP.

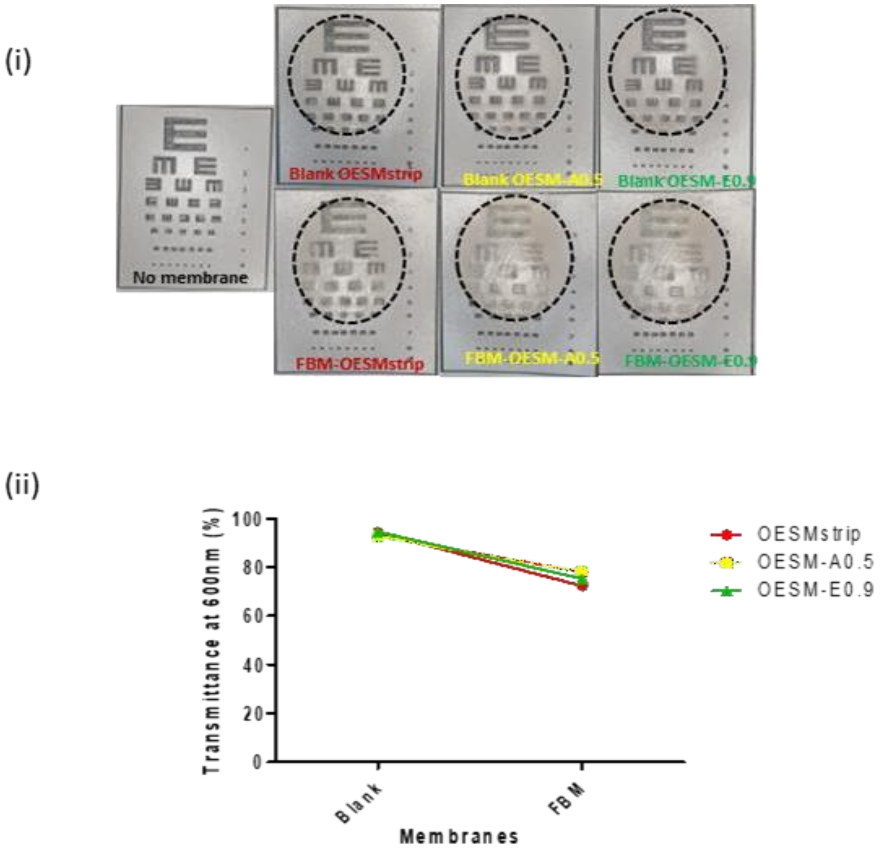

Figure 4.12. Transparency results.
(a) Images representing the visual transparency of the outer and inner sides of the ESM samples (b) UV light transmittance profiles of membranes (Blank OESMstrip, Blank OESM-A0.5, Blank OESM-E0.9, FBM-OESMstrip, FBM-OESM-A0.5 and FBM-OESM-E0.9) O: outer side membrane; FBM: FITC-BSA loaded MP. All values are expressed as mean ± σ for n=6. 1 way ANOVA with Tukey's Multiple Comparison post Test ($p<0.05$)

4.4.6 Porosity

Some of the main features of biomaterial for cornea wound healing applications are related to the porosity (Du, Huang and Feng, 2017). The fluid handling property of the drug loaded MP was assessed by measuring the porosity (Figure 4.13). The average porosity of the FITC-BSA loaded MP-ESM samples are significantly reduced as compared to the Blank OESM samples ($p < 0.001$). comparing the porosity of the drug loaded MP-ESM produced, the FBM-OESMstrip is significantly lower than the FBM-OESM-A0.5 and FBM-OESM-E0.9 ($p < 0.01$). In the case of FBM-OESM-A0.5 and FBM-OESM-E0.9, no significant difference was observed ($P > 0.05$).

Table 4.3. Thickness measurements of FITC- BSA loaded microparticles membranes

Sample	Thickness (mm)
	Mean
FBM-OESMstrip	0.098 ±0.009
FBM- OESM-A0.5	0.128 ±0.012
FBM-OESM-E0.9	0.127 ± 0.018

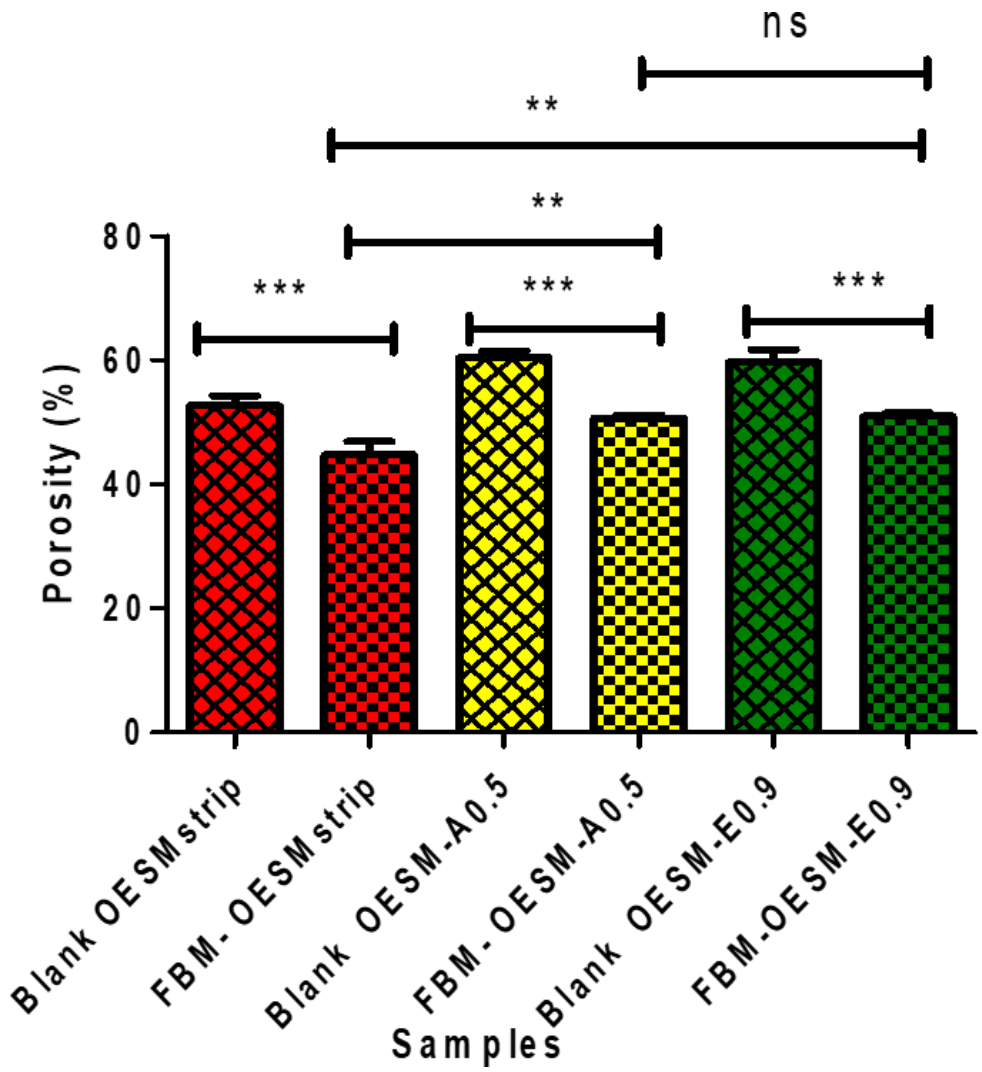

Figure 4.12. Porosity measurements drug loaded MP-ESM

Liquid displacement method was employed in measuring the porosity of the Blank OESMstrip, Blank OESM-A0.5, Blank OESM-E0.9, FBM-OESMstrip, FBM-OESM-A0.5 and FBM-OESM-E0.9. (*) which represents a $p < 0.05$, (**) which represents a $p < 0.01$, and (***) which represents a $p < 0.001$. No statistical significance (ns) is indicated by $p > 0.05$. All values are expressed as mean ± σ for n=3. 1-way ANOVA with Bonferroni's multiple comparison post-test ($p>0.05$). FBM: FITC-BSA loaded microparticles

4.4.7 Wettability test.

Wettability (hydrophilicity and hydrophobicity) of bandages n cornea wound healing plays a role in the interaction of the bandages and the cornea tissues. In this study, the wettable behaviour of the FITC-BSA loaded MP ESM samples was evaluated by determining the contact angle. (Figure 4.14). The contact angles of the blank ESMs are significantly lower than that of the FITC-BSA loaded MP-ESMs i.e., Blank OESMstrip vs FBM-OESMstrip, $p < 0.01$, Blank OESM-A0.5 vs FBM-OESM-A0.5, $p < 0.05$ and Blank OESM-E0.9 vs FBM-OESM-E0.9, $p < 0.01$. Additionally, no significant difference was observed the porosities of FBM-OESMstrip, FBM-OESM-A0.5 and FBM-OESM-E0.9 ($p>0.05$). The data (Figure 4.14) revealed that the contact angles of the FBM-OESMstrip, FBM-OESM-A0.5 and FBM-OESM-E0.9 increased significantly as compared to their respective blank samples OESMstrip, OESM-A0.5 and OESM-E0.9. This observation shows that the surfaces of FITC-BSA loaded MP ESMs have lower hydrophilicity than the blank ESMs. According to Hsieh et al, 2013, the contact angle measurement can be used to examine the surface roughness of materials. From this investigation, the modification of the ESMs by incorporating the FITC-BSA MP increased the roughness of the samples. Intriguingly, the qualitative measurement of the surface roughness obtained in section 4.4.3 (Figure 4.10) contract this observation as the roughness of the samples after the incorporation of MP did not significantly alter the surface roughness.

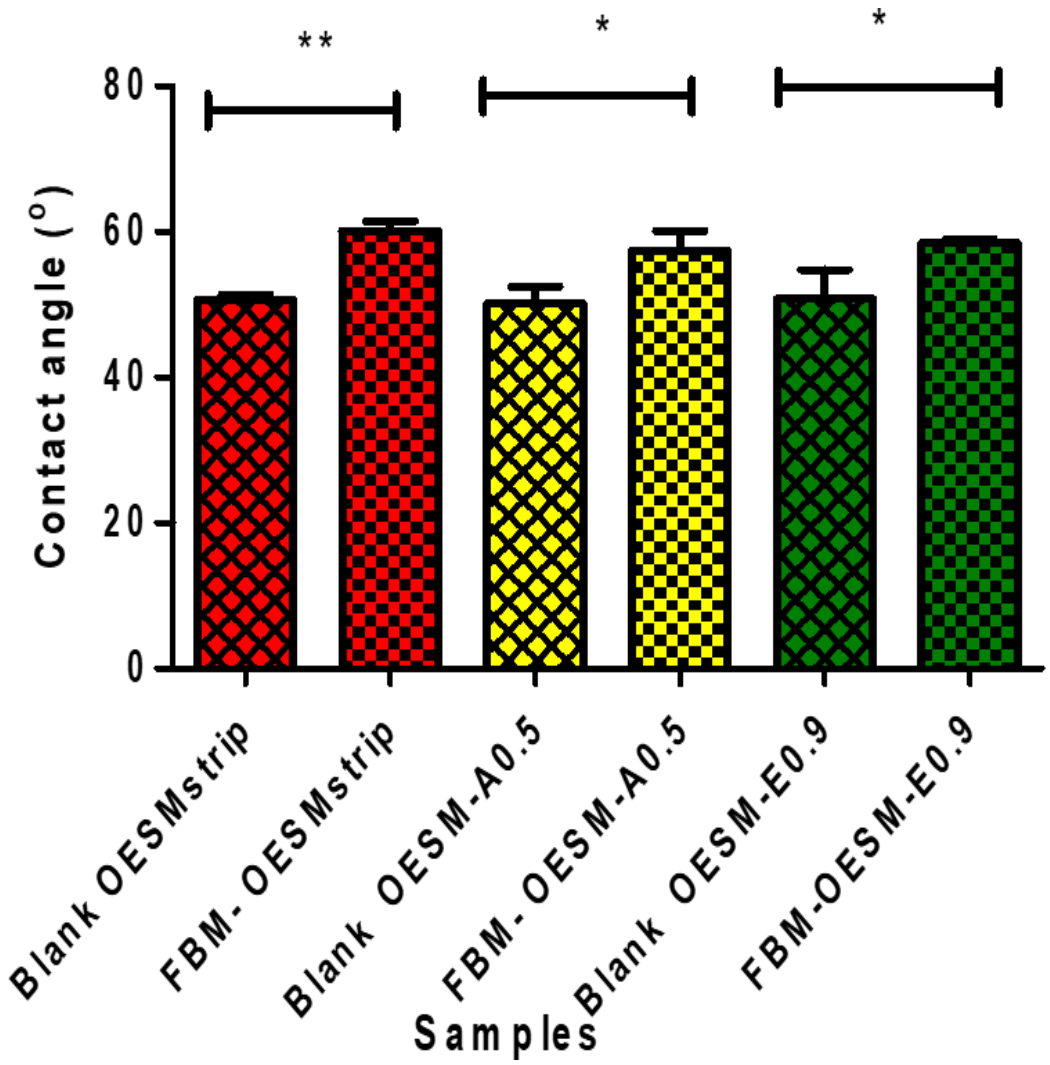

Figure 4.14. Wettability test

The contact angle of the blank and MP loaded ESM was measuring the sessile drop method. At 10 seconds, the contact angle of the PBS droplet on the samples were measured using CAM 200 optical contact angle meter ((KSV Instruments Ltd, Finland) at room temperature (19 °C). (*) which represents a $p < 0.05$, (**) which represents a $p < 0.01$, and (***) which represents a $p < 0.001$. No statistical significance (ns) is indicated by $p > 0.05$. All values are expressed as mean ± σ for n=3. 1-way ANOVA with Bonferroni's multiple comparison post-test ($p>0.05$). FBM: FITC-BSA loaded microparticles.

4.4.8 *In vitro drug* release studies

The application of ESM as a drug delivery reservoir was examined in this chapter. The release profile of the model drug, FITC-BSA encapsulated in the microparticles through ESMs were analysed using a novel *in vitro* France cell eye model constructed with a middle chamber containing porcine vitreous to stimulate the *in vivo* conditions of the eye (Shafaie et al, 2018).

4.4.8.1 FITC-BSA standard calibration curve

FTIC-BSA was dissolved in PBS in 7 different concentrations in a range of 1-20 µg/ml and the absorbance of each concentration was measured at 562 nm using BioTeck micro plate reader. The FITC-BSA calibration curve was generated subsequently (Figure 4.14). The limit of detection (LOD) and limit of quantification (LOQ) were evaluated using the standard deviation of the y-intercepts (σ) and the slope (S) of the calibration curve as 0.05786 µg/ml and 0.1753 µg/ml respectively.

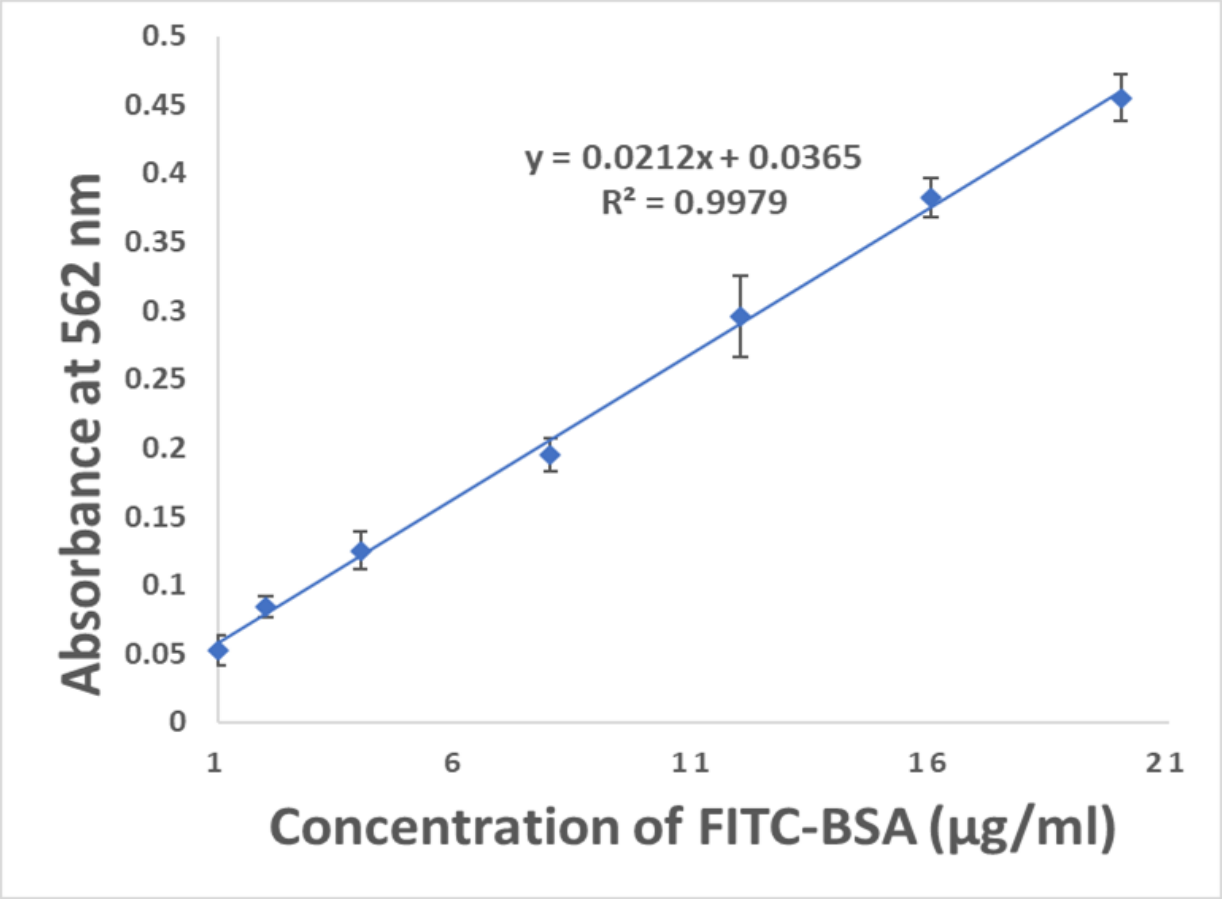

Figure 4.15. FITC-BSA standard calibration curve

A standard calibration curve of different FITC-BSA concentrations in PBS (µg/ml) vs absorbance at 562 nm were measuring using BioTeck micro plate reader. All values are expressed as mean ± σ for n=3

4.4.8.2 Drug release study

The *in vitro* % cumulative drug release profile fabricated membranes and Free PLGA microparticles (MP) were studied using a novel *in vitro* Franz cell model with porcine vitreous (Figure 4.16). (Figure 4.16). A higher percentage of FITC-BSA release was found in the control i.e., FITC-BSA loaded MP compared with the release from the MP loaded ESM i.e., FBM-OESMstrip, FBM-OESM-A0.5 and FBM-OESM-E0.9. From the results, FBM-OESMstrip and FBM-OESM-A0.5 provided the maximum release of the FITC-BSA ($p>0.05$, Table A1.0 in Appendix), followed by FBM-OESM-E0.9. The MP-ESMs showed a good, sustained release behaviour. The release of the drug from the ESMs were prolonged up to 10 days whereas in case of the control > 50% was release within 7 days. Sustained drug delivery directly into the corneal could circumvent patient compliance issues, the typical short residence time of ophthalmic drugs on the ocular surface, and the low efficacy of topical drugs (Bachu et al, 2018; Subrizi et al, 2019 and Ahkter et al, 2022).

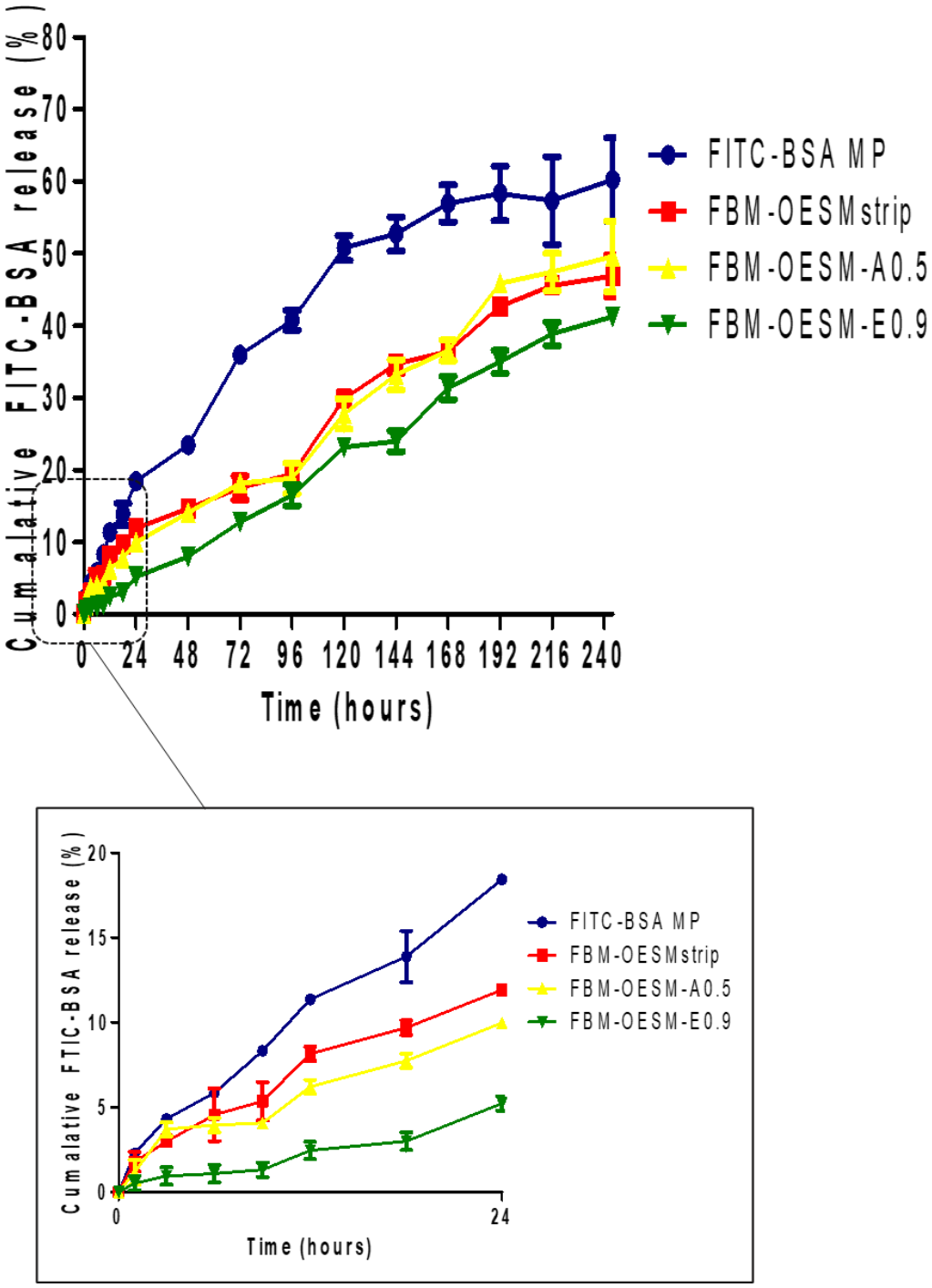

Figure 4.16. The % cumulative release of FITC-BSA release of FITC-BSA loaded microparticles (control) and MP ESMs.
Inert % cumulative release for the first 24 hours. All values are expressed as mean ± σ for n=3.
FBM: FITC-BSA loaded microparticles

4.4.9 *In ovo* Chorioallantoic membrane test

The angiogenic responses and biocompatibility of the drug loaded ESMs were suing using CAM assay. The results of the samples: no treatment, PBS, VEGF, VEGF loaded MP, Blank MP-OESMstrip, blank MP-OESM-A0.5, blank MP-OESM-E0.9, VM-OESMstrip, VM-OESM-A0.5 and VM-OESM-E0.9 are presented in Figure 4.17 A and Figure 4.17 b. On the 10th day, the samples were imaged, and the number of branching vessels were counted using AngioQaunt software). The statistical analysis of the study is summarised in Table A 1.1 in the Appendix. From the results, (Figure 4.17B), the VEGF (48.33 ± 17.89, $p<0.001$). All samples produced insignificant mean branch vessel counts ($p>0.05$) when compared to the control (no treatment, except VEGF ($p<0.001$), VEGF loaded MP ($p<0.05$) and VM-OESM-A0.5 ($p<0.05$).

In considering the mean branch vessels counts of VEGF vs the VEGF loaded MP samples, no significant difference was observed in VEGF vs VEGF loaded MP, VM-OESMstrip, VM-OESM-A0.5 and VM-OESM-E0.9 ($p>0.05$). Similarly, insignificant branch vessels count was obtained for VEGF loaded MP vs VM-OESMstrip, VM-OESM-A0.5 and VM-OESM-E0.9 ($p>0.05$). In regard to the blank ESMs and their respective VEGF loaded MP ESMs, the mean branch vessels count was significant in OESMstrip/VM-OESMstrip ($p<0.01$), OESM-A0.5/ VM-OESM-A0.5 ($p<0.01$) whereas the count in OESM-E0.9/ VM-OESM-E0.9 was insignificantly different ($p>0.05$). This result shows that the VEGF released from the VM-VM-OESM-A0.5 was significant enough to increase blood vessels formation.

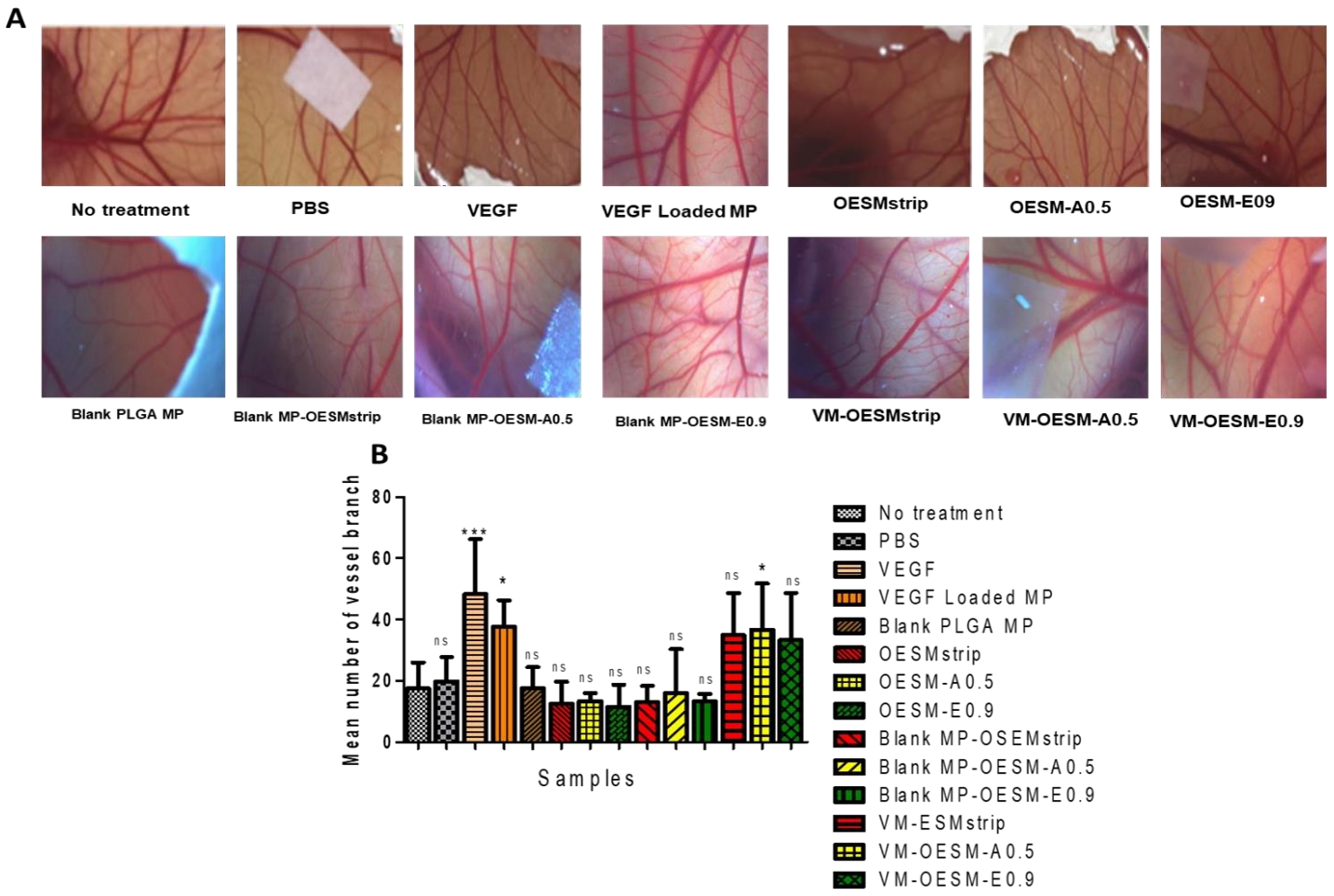

Figure 4.17. Angiogenic profile analysis

(A) Photographs of the CAM assays, after 10 days of incubation at 37°C, the presence of extracted ESM samples and controls.
(B) Plot indicating the number of blood vessel branches measured using AngioQaunt software expressed as mean ± σ. * corresponds to $p<0.05$; *** corresponds to $p<0.001$; ns: no significant difference. 1-way ANOVA with Bonferroni's multiple comparison post-test ($p>0.05$). VEGF: vascular endothelial growth factor FBM: FITC-BSA loaded microparticles VM: VEGF loaded microparticle

4.4.10 *In vivo* wound healing analysis

The cornea wound healing properties of the ESMs were assessed using *in vivo* rat cornea wound models. The results for the in *vivo* tests on six-week-old male Sprague Dawley (SD) *in vivo* rat eyes employing two separate cornea injury models, i.e., mechanical and chemical are displayed in Figure 4.18. The microscopic images of the bright field and blue lights observations are displayed in Figure 4.17a. The findings show that the chemical and mechanical wounds were successfully generated in the rats. Similar wound healing rate were observed in the ESM samples. After the 24-hour period, the signs of wounds in all the ESMs samples were more pronounced than the control (no treatment) and the amniotic membrane (AM). Figure 4.18b and c illustrate the percentage wound area evaluated for the various treatment under the two cornea injury models after 24 hours treatment with ESMs and AM (positive control) samples, and no treatment as a control. The results showed no significant therapeutic impact under these settings (ESMstrip, ESM-A0.5, ESM-E0-9) as compared to the control and AM. Moreover, no significant difference was observed between the two injury models i.e., mechanical and chemical wound healing ($p>0.05$). As this is a preliminary study, further investigation of the blank ESMs and drug loaded ESMs on cornea wound is required.

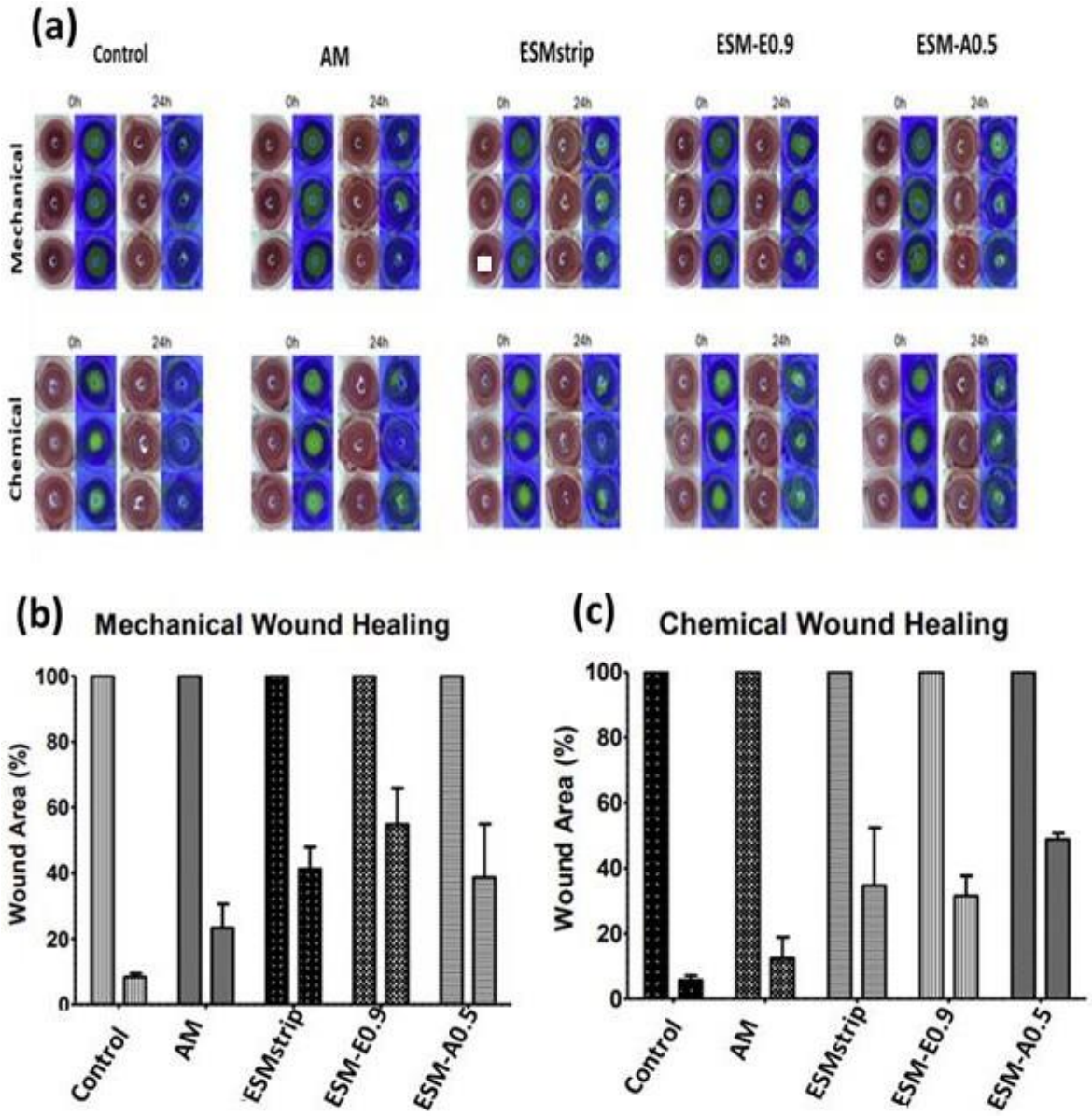

Figure 4.18. In vivo rat corneal wound healing analysis
(a)Microscopic images of the applications of amniotic membrane (AM) and ESMstrip, ESM-A0.5, ESM-E0.9 on SD rats in vivo mechanical and chemical wound healing models. The bright field observation is on the left and blue light observation on the right. (b) the graph of the percent wound area for mechanical wound healing and (c) percentage wound is for chemical wound healing. The ESMs samples (ESMstrip, ESM-A0.5, ESM-E0.9) yielded more significant wound area than the control and AM after 24 hours treatment.

4.5 CONCLUSION

Herein, intact and complete eggshell membranes (ESM) were successfully obtained using the in house optimised acetic and EDTA extraction methods. FITC-BSA loaded PLGA microparticles (MP) was fabricated and successfully deposited onto the outer layer of ESMs by a convenient surface adsorption and attachment technique. The stability test of the bandage showed that air drying or freeze-drying of the bandage and prolonged storage at 4 and -20 °C for 60 days do not compromise the mechanical properties. The 2 in 1 bandage consisting of the ESM and drug loaded MPs was characterised accordingly. The loaded MP was verified via FESEM and FTIR. The attachment process did not affect the morphology, fibre diameter, roughness and release profile of the FITC-BSA. Again, the presence of the loaded MPs did not compromise the transparency of the bandage. The bandage exhibited a good biocompatibility property and do not promote pro-angiogenesis. Although the bandage exhibited promising cornea wound healing properties, *in vivo* cornea wound healing will need to be undertaken to validate its effectiveness.

4.6 REFERENCES

Ahlborn, G, Sheldon, B. Identifying the components in eggshell membrane responsible for reducing the heat resistance of bacterial pathogens. J Food Prot 2006; 69: 729–738.

Ahmed, A, Boateng, J. Calcium alginate-based antimicrobial film dressings for potential healing of infected foot ulcers. Ther Deliv 2018; 9: 185–204.

Ahmed, T, Suso, H, Hincke, M. Experimental datasets on processed eggshell membrane powder for wound healing. Data Brief 2019; 26: 104457.

Ahmed, T, Suso, H, Maqbool, A, et al. Processed eggshell membrane powder: bioinspiration for an innovative wound healing product. Mater Sci Eng C Mater Biol Appl 2019; 95: 192–203.

Alves-Lima, DF, Letizia, R, Degl'Innocenti, R, et al. Quantitative video-rate hydration imaging of nafion proton exchange membranes with terahertz radiation. J Power Sour 2020; 450: 227665.

Amirsadeghi A, Khorram M and Hashemi S-S. Preparation of multilayer electrospun nanofibrous scaffolds containing soluble eggshell membrane as potential dermal substitute. J Biomed Mater Res A. Epub ahead of print 25 March 2021. DOI: 10.1002/jbm.a.37174.

Baláž, M. Eggshell membrane biomaterial as a platform for applications in materials science. Acta Biomater 2014; 10: 3827–3843.

Banerjee, A, Panda, S, Sidhantha, M, et al. Utilisation of eggshell membrane as an adsorbent for carbon dioxide. IJGW 2010; 2: 252.

Bellairs, R, Boyde, A. Scanning electron microscopy of the shell membranes of the hen's egg. Z Zellforsch Mikrosk Anat 1969; 96: 237–249.

Boonprasert, P, Tangboriboon, N. Electromechanical-conductive natural rubber doped eggshell and eggshell membrane for drug delivery and actuator applications. MSF 2018; 934: 43–49.

Carmeliet, P. VEGF as a key mediator of angiogenesis in cancer. Oncology 2005; 69: 4–10.

Cavanagh, H. Ocular surface disease. Cornea 2002; 21: 634.

Chau, D, Brown, S, Mather, M, et al. Tissue transglutaminase (TG-2) modified amniotic membrane: a novel scaffold for biomedical applications. Biomed Mater 2012; 7: 045011.

Chau, DYS, Dennis, AR, Lin, H, et al. Determination of water content in dehydrated mammalian cells using terahertz pulse imaging: a feasibility study. Curr Pharm Biotechnol 2015; 17: 200–207.

Chen, L, Kang, J, Sukigara, S. Preparation and characterization of polyurethane/soluble eggshell membrane nanofibers. Biomed Mater Eng 2014; 24: 1979–1989.

Chen, X, Zhu, L, Wen, W, et al. Biomimetic mineralisation of eggshell membrane featuring natural nanofiber network structure for improving its osteogenic activity. Colloids Surf B Biointerf 2019; 179: 299–308.

Chi, Y, Zhao, Y. Characterization of collagen from eggshell membrane. Biotechnology 2009; 8: 254–258.

Colatrella, N. Amniotic membrane therapy in ocular surface disease: introduction. JDED 2019; 2: 1–1.

Coover, D. The use of egg membrane in ophthalmic surgery. Ophthal Record 1899; 8: 222–224.

Devi, P, Banerjee, S, Chowdhury, S, et al. Eggshell membrane: a natural biotemplate to synthesize fluorescent gold nanoparticles. RSC Adv 2012; 2: 11578.

Du, L, Huang, M, Feng, J. Immobilization of α-amylase on eggshell membrane and Ag-nanoparticle-decorated eggshell membrane for the biotransformation of starch. Starch – Stärke 2017; 69: 1600352.

Dua, H. Variation and limitations of the amniotic membrane. Acta Ophthalmol 2014; 92(S253).

Farrar G, Barone J, Morgan A. Ovalbumin-based porous scaffolds for bone tissue regeneration. J Tissue Eng 2010; 2010: 209860.

Foulks, G. Understanding ocular surface disease from uncommon to extremely common afflictions. Ocul Surf 2014; 12: 233.

Ghaee, A, Nourmohammadi, J, Danesh, P. Novel chitosan-sulfonated chitosan-polycaprolactone-calcium phosphate nanocomposite scaffold. Carbohydr Polym 2017; 157: 695–703.

Gocek, I, Adanur, S. Effect of processing parameters on polypropylene film properties. Mod Eng Res 2012; 2: 3056–3060.

Gohari, RJ, Halakoo, E, Lau, W, et al. Novel polyethersulfone (PES)/hydrous manganese dioxide (HMO) mixed matrix membranes with improved anti-fouling properties for oily wastewater treatment process. RSC Adv 2014; 4: 17587–17596.

Google Scholar

Guarderas, F, Leavell, Y, Sengupta, T, et al. Assessment of chicken-egg membrane as a dressing for wound healing. Adv Skin Wound Care 2016; 29: 131–134.

Honnegowda, T, Kumar, P, Udupa, EP, et al. A comparative study to evaluate the effect of limited access dressing (LAD) on burn wound healing. Int Wound J 2016; 13: 791–798.

Hsieh, S, Chou, H, Hsieh, C, et al. Hydrogen peroxide treatment of eggshell membrane to control porosity. Food Chem 2013; 141: 2117–2121.

Jia J, Liu G, Guo Z, et al., Preparation and Characterization of Soluble Eggshell Membrane Protein/PLGA Electrospun Nanofibers for Guided Tissue Regeneration Membrane. Journal of Nanomaterials 2012: 2012; Article 282736.

Kheirabadi, E., Razavi, S., Khodaiyan, F. and Golmakani, M., 2018. Optimizing the Extraction of Acid-soluble Collagen Inside the Eggshell Membrane. Food Science and Technology Research, 24(3), pp.385-394.

Kim, E., Tripathy, N., Cho, S., Lee, D. and Khang, G., 2016. Collagen type IPLGA film as an efficient substratum for corneal endothelial cells regeneration. Journal of Tissue Engineering and Regenerative Medicine, 11(9), pp.2471-2478.

Knupp, C., Pinali, C., Lewis, P., Parfitt, G., Young, R., Meek, K. and Quantock, A., 2009. The Architecture of the Cornea and Structural Basis of Its Transparency. Advances in Protein Chemistry and Structural Biology, pp.25-49

Koide, M., Osaki, K., Konishi, J., Oyamada, K., Katakura, T., Takahashi, A. and Yoshizato, K., 1993. A new type of biomaterial for artificial skin: Dehydrothermally cross-linked composites of fibrillar and denatured collagens. Journal of Biomedical Materials Research, 27(1), pp.79-87.

Koizumi, N., Inatomi, T., Sotozono, C., Fullwood, N., Quantock, A. and Kinoshita, S., 2000. Growth factor mRNA and protein in preserved human amniotic membrane. Current Eye Research, 20(3), pp.173-177.

Lai, J., Wang, T., Li, Y. and Tu, I., 2012. Synthesis, characterization and ocular biocompatibility of potential keratoprosthetic hydrogels based on photopolymerized poly(2-hydroxyethyl methacrylate)-co-poly(acrylic acid). J. Mater. Chem., 22(5), pp.1812-1823.

Li, E., Donati, S., Lindsley, K., Krzystolik, M. and Virgili, G., 2020. Treatment regimens for administration of anti-vascular endothelial growth factor agents for neovascular age-related macular degeneration. Cochrane Database of Systematic Reviews,

Li, F., Carlsson, D., Lohmann, C., Suuronen, E., Vascotto, S., Kobuch, K., Sheardown, H., Munger, R., Nakamura, M. and Griffith, M., 2004. Cellular and nerve regeneration within a biosynthetic extracellular matrix for corneal transplantation. American Journal of Ophthalmology, 138(2), p.318.

Li, X., Cai, Z., Ahn, D. and Huang, X., 2019. Development of an antibacterial nanobiomaterial for wound-care based on the absorption of AgNPs on the eggshell membrane. Colloids and Surfaces B: Biointerfaces, 183, p.110449.

Liang, M, Su, R, Qi, W, et al. Synthesis of well-dispersed Ag nanoparticles on eggshell membrane for catalytic reduction of 4-nitrophenol. J Mater Sci 2014; 49: 1639–1647.

LIFSHITZ, A., BAKER, R. and NAYLOR, H., 1964. The Relative Importance of Chicken Egg Exterior Structures in Resisting Bacterial Penetration. Journal of Food Science, 29(1), pp.94-99.

Liong, JW, Frank, J, Bailey, S. Visualization of eggshell membranes and their interaction with Salmonella enteritidis using confocal scanning laser microscopy. J Food Prot 1997; 60: 1022–1028.

Litwiniuk, M, Grzela, T. Amniotic membrane: new concepts for an old dressing. Wound Repair Regen 2014; 22: 451–456.

Ljubimov, A. and Saghizadeh, M., 2015. Progress in corneal wound healing. Progress in Retinal and Eye Research, 49, pp.17-45.

M.M Katz S.I. Detection of specific collagen types in normal and keratoconus corneas. Investig. Ophthalmol. Vis. Sci. 1981;20:738–750

Ma, D., Lai, J., Cheng, H., Tsai, C. and Yeh, L., 2010. Carbodiimide crosslinked amniotic membranes for cultivation of limbal epithelial cells. Biomaterials, 31(25), pp.6647-6658.

Maeda, K. and Sasaki, Y., 1982. An experience of hen-egg membrane as a biological dressing. Burns, 8(5), pp.313-316.

Maharajan, V., Shanmuganathan, V., Currie, A., Hopkinson, A., PowellRichards, A. and Dua, H., 2007. Amniotic membrane transplantation for ocular surface reconstruction: indications and outcomes. Clinical and Experimental Ophthalmology, 0(0), p.070130044246003

Majsztrik, PW, Satterfield, MB, Bocarsly, AB, et al. Water sorption, desorption and transport in nafion membranes. J Membr Sci 2007; 301: 93–106.

Malhotra, C. and Jain, A., 2014. Human amniotic membrane transplantation: Different modalities of its use in ophthalmology. World Journal of Transplantation, 4(2), p.111.

Mallakpour, S, Madani, M. Synthesis, structural characterization, and tensile properties of fructose functionalized multi-walled carbon nanotubes/chitosan nanocomposite films. J Plast Film Sheet 2016; 32: 56–73.

Mann, K., Maček, B. and Olsen, J., 2006. Proteomic analysis of the acid-soluble organic matrix of the chicken calcified eggshell layer. PROTEOMICS, 6(13), pp.3801-3810.

Manolova, Y, Stoycheva, Z, Yordanov, Y, et al. Amniotic membrane transplantation – analysis of structural characteristics in amniotic membrane transplant and corneal ulcers. SSM 2017; 49: 12.

Marshall KM, Kanczler JM, Oreffo RO. Evolving applications of the egg: chorioallantoic membrane assay and ex vivo organotypic culture of materials for bone tissue engineering. J Tissue Eng 2020; 11. DOI: 10.1177/2041731420942734.

Marusina, A., Merleev, A., Luna, J., Olney, L., Haigh, N., Yoon, D., Guo, C., Ovadia, E., Shimoda, M., Luxardi, G., Boddu, S., Lal, N., Takada, Y., Lam, K., Liu, R., Isseroff, R., Le, S., Nolta, J., Kloxin, A. and Maverakis, E., 2019.

Mohammadzadeh L, Rahbarghazi R, Salehi R, et al. A novel egg-shell membrane-based hybrid nanofibrous scaffold for cutaneous tissue engineering. Journal of Biological Engineering 2019; 13: Article 79.

Morooka, H, Nagaoka, C, Nishimura, D, et al. Effects of processed fabric with eggshell membrane on. Sen-i Gakkaishi 2009; 65: 184–190.

Murube, J. Early clinical use of amniotic membrane in medicine and ophthalmology. Ocular Surf 2006; 4: 114–119.

Niemisto, A, Dunmire, V, Yli-Harja, O, et al. Robust quantification of in vitro angiogenesis through image analysis. IEEE Trans Med Imag 2005; 24: 549–553.

Ohto-Fujita, E, Konno, T, Shimizu, M, et al. Hydrolyzed eggshell membrane immobilized on phosphorylcholine polymer supplies extracellular matrix environment for human dermal fibroblasts. Cell Tissue Res 2011; 345: 177–190.

Parodi, B, Russo, E, Gatti, P, et al. Development and in vitro evaluation of buccoadhesive tablets using a new model substrate for bioadhesion measures: the eggshell membrane. Drug Dev Ind Pharm 1999; 25: 289–295.

Rahman, I, Said, D, Maharajan, V, et al. Amniotic membrane in ophthalmology: indications and limitations. Eye (Lond) 2009; 23: 1954–1961.

Rolando, M, Barabino, S, Bentivoglio, G, et al. Treatment of ocular surface inflammation in keratoconjunctivitis sicca by means of a silicon-hydrogel bandage contact lens dressed with amniotic membrane. Ocular Surf 2005; 3: S107.

Roy, N, Saha, N, Kitano, T, et al. Development and characterization of novel medicated hydrogels for wound dressing. Soft Mater 2010; 8: 130–148.

Semenza, G. HIF-1 and tumor progression: pathophysiology and therapeutics. Trends Mol Med 2002; 8: S62–S67.

Shafaie, S, Hutter, V, Brown, M, et al. Influence of surface geometry on the culture of human cell lines: a comparative study using flat, round-bottom and V-shaped 96 well plates. Plos One 2017; 12: e0186799.

Shibuya, M. Vascular endothelial growth factor (VEGF) and its receptor (VEGFR) signaling in angiogenesis: a crucial target for anti- and pro-angiogenic therapies. Genes Cancer 2011; 2: 1097–1105.

Sidney, LE, Branch, MJ, Dua, HS, et al. Effect of culture medium on propagation and phenotype of corneal stroma-derived stem cells. Cytotherapy 2015; 17: 1706–1722.

Strnková, J, Nedomová, Š, Kumbár, V, et al. Tensile strength of the eggshell membranes. Acta Univ Agric Silvic Mendelianae Brun 2016; 64: 159–164.

Tang, J, Han, L, Yu, Y, et al. A label-free immunoassay using eggshell membrane as matrix and poly(diallyldimethylammonium chloride) as light-scattering enhancer. Luminescence 2011; 26: 634–639.

Tighsazzadeh, M, Mitchell, J, Boateng, J. Development and evaluation of performance characteristics of timolol-loaded composite ocular films as potential delivery platforms for treatment of glaucoma. Int J Pharm 2019; 566: 111–125.

Torres, F, Troncoso, O, Piaggio, F, et al. Structure–property relationships of a biopolymer network: the eggshell membrane. Acta Biomater 2010; 6: 3687–3693.

Tsai, W, Yang, J, Lai, C, et al. Characterization and adsorption properties of eggshells and eggshell membrane. Bioresour Technol 2006; 97: 488–493.

Vynckier, AK, Lin, H, Zeitler, JA, et al. Calendering as a direct shaping tool for the continuous production of fixed-dose combination products via co-extrusion. Eur J Pharm Biopharm 2015; 96: 125–131.

Wang, D-H, Li, Y-J, Liu, L, et al. Traits of eggshells and shell membranes of translucent eggs. Poult Sci 2017; 96: 1514.

Whittaker, J, Balu, R, Choudhury, N, et al. Biomimetic protein-based elastomeric hydrogels for biomedical applications. Polym Int 2014; 63: 1545–1557.

Wu B, Zhang G, Shuang S, et al. Biosensors for determination of glucose with glucose oxidase immobilized on an eggshell membrane. Talanta 2004; 64: 546–553.

Zadpoor, A. Mechanics of biological tissues and biomaterials: current trends. Materials (Basel) 2015; 8: 4505–4511.

Zidan, G, Rupenthal, I, Greene, C, et al. Medicated ocular bandages and corneal health: potential excipients and active pharmaceutical ingredients. Pharm Dev Technol 2018; 23: 255–260.

CHAPTER 5:
GENERAL DISCUSSION

5.0 5.1 GENERAL DISCUSSION

The main objective of the thesis was to generate a 2 in 1 novel biomedical bandage consisting of ESM a 10-50 µm drug incorporated PLGA MP for ocular surface wound healing applications. The chapter 2 of the thesis entailed generating an optimum separation method to produce ESM with the desirable characteristics. Two dilute chemicals namely acetic acid and EDTA were employed in the experiment and compared to the peeling method. Three different concentration of the acetic acid (0.5M, 0.9M, 1.8M) and EDTA (0.2M, 0.5M, 0.9M) were varied against the duration of extraction. It was observed that higher the concentration, the shorter the extraction time. From the findings (Figure 2.10), the thickness of the ESMstrip is significantly smaller than that of the membrane samples extracted with acetic acid and EDTA ($p<0.01$). The limiting membrane, inner shell membrane and the outer shell membrane. The manually peeled membrane results in the isolation of a membrane composing of two layers, the limiting membrane and the inner shell membrane. Strnkova et al. (2016) measured the thickness of manually peeled ESM from hen, goose and Japanese quails by using a digital micrometer and obtained ranges of 22-170 µm, 33-110 µm and 40-90 µm, respectively (Alves-Lima et al., 2020). As such, these results obtained here are consistent with prior studies from existing literature.

In corneal wound healing, the transparency of the dressing or bandage is important so as to not compromise the functionality of the cornea. Again, it allows or the visualisation of the wound. (Sidney et al, 2015 & Niemisto et al, 2005). The transparency of the inner and the outer layers of the ESM was analysed using the simple visual method and light transmission. From the results in Figure 2.11 and Figure 2.12, it was confirmed that the inner layer of the ESM was more transparent than the outer layer. The inner layer appeared smooth while as the outer layer appeared rough and this agrees with the study by Bellairs and Boyde (1969). Nevertheless, both layers had light transmission values above 80% (Figure 2.21).

Using Field energy scanning electronic microscopy, the outer and inner surface morphology

was examined. The results confirmed the findings reported in literature that the structural characteristics of the two layers differs (Ahlborn and Sheldon, 2006, Marshalll, Kanezler and Oreffo, 2020 & Devi et al, 2012). According to the findings, the outer layer contains macroporous structures within networks of interwoven fibres (Figure 2.13), whereas the inner layer has a continuous dense structure (Figure 2.14). The fibres of the inner shell membrane, on the other hand, appear to be much thinner than those of the outer shell membrane. To profile remaining residues after the extraction process, EDS analyses were used to determine the elemental composition of the membranes. The data presented in Table 2.5 depicts that that the ESM membranes are made up of carbon (C), nitrogen (N), oxygen (O), and sulphur (S). Further, EDS analysis of the individual inner and outer sides of the extracted membranes revealed no calcium content, which is most likely due to the solvent treatment completely dissolving the $CaCO_3$ (i.e., acetic acid or EDTA). In summary, these findings show that the bulk elemental composition of both sides of the ESM is the same and that there is no stratified variation due to membrane thickness/distinct layering. This conforms to the conclusions by Tsai et (2006) and Du, Huang and Feng (2017) as both investigate the physical and chemical properties of ESM.

The extracted membranes were characterised using FTIR spectroscopy. The spectra of the inner and outer sides of each membrane are similar, as shown in Figure 2.15. In each spectrum, the characteristic bands associated with the structural unit of proteins are identified (Ahmed et al, 2019 & Balaz, 2014). This backs up the literature's claim that ESM fibres are mostly made up of proteins (Chi and Zhao, 2009, Ahmed et al, 2019, Wu et al, 2004, Chen, Kang and Sukigara, 2014, Tsang et al, 2011 & Farrar, Barone and Morgan, 2010). As a result, the FTIR spectra indicate that neither the acetic acid nor the EDTA extraction protocols modified the chemical composition of the ESM's (organic) structure. In regard to the acetic acid treatment method, a study by Torres-Man and Delgado-Me (2017) revealed that acetic acid is an ideal chemical solution for the separation of ESM because the changes in the chemical composition of ESM

was minimal and this corroborates to the results in chapter 2 of this thesis. In contrast, the ESM obtained from EDTA solution showed that the absorptions bands associated to the organic structures of ESM were altered.

The physical properties such as mechanical property has great influence on the functionality of a wound bandage (Parodi et al, 1999, Wang et al, 2017, and Wang, Armato and Wu, 2020). The mechanical properties in terms of the compression and tensile properties were assessed to help determine which extraction method produces the best ESM with the best properties for wound healing. It was discovered that the outer layer of the ESM required high forces to break and has slight expandable properties whereas the inner layer required less (Figure 2.16). The components and interactions in each side of the ESM samples influence the strength to burst and may be linked to their structural characteristics- as previously stated, the outer side of ESM is made up of fibres, whereas the inner side has significantly less (Ahmed et al, 2019, Wu et al, 2004 & Bellairs and Boyde, 1969). The combined analysis of the tensile properties in terms of the tensile strength, elongation at break and Young's modulus of the different layers of the ESM extracted with different extraction methods indicated that the mechanical behaviour of ESM is influenced by the distortion of the (alignment) proteins within the fibres of the membrane (Alves-Lima et al, 2020). The results obtained for the ESM samples contribute to the evidence that is reported in literature that ESM is a tough and stiff biomaterial (Parodi et al, 1999; Ahmed, Suso and Hincke, 2019; Gocekand Adanur, 2012). According to the results, the ESM obtained by 0.5 M acetic acid and 0.9 M EDTA have the desirable mechanical properties as biomaterial for corneal wound bandage.

The porosity of biomaterial is crucial to cornea wound healing as it affects other properties of the biomaterial such as moisture retention, permeability and strength (Foulks, 2014; Du, Huang and Feng, 2017 & Devi et al, 2012). The analysis as presented in Table 2.11 and Table 2.12 showed that the porosity of manually obtained ESM was higher than that of the acetic acid and

EDTA samples.The differences in pore size between the outer sides of ESMstrip and ESM-A0.5 and ESM-E0.9, the outer shell membrane, may be explained by the fact that ESMstriphas a smaller pore size as reported in literature (Ahmed, Suso and Hincke, 2019; Devi et al., 2012 & Hsieh et al., 2013).

Fluid absorption capacity of membranes was measured at 1- and 24-hour time points. Based on the results (Table 2.11), no significant differences were detected when comparing the two timepoints between ESMstrip, ESM-A0.5, and ESM-E0.9 samples. Despite this, fluid absorption capacity of the ESMstrip was noticeably higher than that of the ESM-A0.5 sample ($p<0.01$). In the comparison between the ESMstrip samples and the ESM-E0.9 samples, a similar pattern was observed. The fluid absorption capacities of ESM-A0.5 and ESM-E0.9 did not differ significantly ($p>0.05$). In TGA experiments, the thermal behaviour of the extracted membranes was examined (Table 2.11). It has been reported that thermal stabilities of membranes depend on their structure and chemical composition (Du, Huang and Feng, 2017, Roy et al, 2010 & Jia et al, 2012), and so the obtained data validates the results obtained for fluid handling properties above.

The wetting property of the extracted film was evaluated (Figure 2.20). The low hydrophilicity on the outer surface of the membrane is thought to be due to its interwoven fibrous structure and rough surface. On the other hand, the relatively smooth surface and dense structure of the inner, limiting membrane, may contribute to its highly hydrophilic character. Importantly, no significant difference was observed between the inner and outer surfaces of the extracted films ($p > 0.05$) and these results can be considered to be in good conformity with previously published findings (Banerjee et al., 2010, Wang et al., 2017, Liang et al. 2014 and Chen et al, 2019).

Physical/mechanical properties of ESMs isolated with optimised procedures are promising biomaterials for corneal wound healing application. The surface roughness of the inner layer and the outer layer of ESMstrip, ESM-A0.5 and ESM-E0.9 were measured using the FESEM methods. The results concur with the visual and morphological analyses previously deduced. The inner layer- limiting membrane appears smooth with round-like bulges structures whereas the outer layer – inner shell membrane for ESMstrip and outer shell membrane ESM-A0.5 and ESM-E0.9 appear like pine-like structure. Similarly, this observation was reported by Yan et al, 2020, Kheirabadi et al., 2018, Zhang et al., 2016, Mann et al., 2006 and Zhou et al, 2010. The quantification of the surface roughness in terms of the Ra (arithmetical mean deviation) values showed that the surface roughness of the outer layer was significantly higher than the inner layer. This observation may aid in selecting the side of the ESM to place directly on the cornea wound. Furthermore, some studies have suggested that bandages with rougher surfaces are susceptible to bacterial adhesion as the imperfections in the biomaterial is where the deposit are likely to form (Bruinsma et al, 2003 and Hosaka et al, 1983). In biomedical applications, surface roughness may affect cell adhesion and growth, this implies that the inner layer of ESM is valuable (Chen et al., 2017, Zareidoost et al., 2012 & Biazar et al., 2011). The fibre diameter of the outer layers of the ESMstrip, ESM-A0.5 and ESM-E0.9 were determined as 0.25 to 5 .75 µm, 0.936 to 8.97 µm and 1.02 to 8.88 µm respectively and they agree to the data by Yan et al., 2020 and Torres et al., 2006. This large variation in fibre diameter affects the transparency of the membrane (Hart et al., 1969 and Maurice et al., 1957).

The swelling profile of a biomaterial for ocular application is one of the most vital characteristics that determines fluid retention, erosion, and hydrophilicity (Tsai et al, 2006, Roy et al, 2010 & Chau et al, 2012). The swelling profiles of membranes obtained using the optimised methods ESM-A0.5 and ESM-E0.9 were evaluated and compared to a manually peeled sample, ESM strip, in this study (Figure 2.23). The ESM-A0.5 and ESM-E0.9 had

significantly higher swelling capacities ($p<0.01$ and $p<0.001$, respectively) than the ESMstrip sample. Additionally, the desorption profiles of the ESMstrip, ESM-A0.5 and ESM-E0.9 were analysed, and the results agreed with the swelling profiles (Figure 2.24).

O'Brien (2011) posits that an ideal membrane must be nontoxic to healthy tissue. It is critical to thoroughly sterilise the membrane before use. The sterilisation method may have an impact on the mechanical and biological properties of the membrane. Five sterilisation methods i.e., 100 IU/ml penicillin-100 μg/ml streptomycin solution for 24 hours, exposure to ultraviolet UV radiation for 2 hours, penicillin- streptomycin before UV radiation, UV radiation before penicillin- streptomycin and soaking in 70% v/v ethanol for 24 hours for complete evaporation of the ethanol were optimised. The mechanical properties-burst strength of the membrane was not significantly affected by the five-sterilization method (Figure 2.25). The *in vitro* cytotoxicity of the ES extracted with the different methods was evaluated using 3-(4,5-dimethylthiazol-2-yl)-5-(3-carboxymethoxyphenyl)-2-(4- sulfophenyl)-2H-tetrazolium (MTS) and Lactate dehydrogenase (LDH) assays. As presented in Figure 2.26 and Figure 2.27, the ESM samples were not toxic to Immortalised corneal epithelial cell line (iHCE) and Mesenchymal stem cell- corneal stromal (MSC-C) cells. The attachment and spreading of iHCE and C-MSC cells on the inner and outer layers and from Figure 2.28, it appears that a large number of cells adhered to the inner layer of the ESM surface due to the relatively increased surface area or low surface roughness as compared to the outer layer.

The human cornea is an avascular tissue in the body that keeps the eye clear for vision due to the lack of blood vessels (Cavanagh, 2002). In the context of a biomaterial, having pro-and anti-angiogenic characteristics can influence the performance of the cornea. Angiogenesis is important in wound healing, and the presence of pro- and anti-angiogenic factors can impact the response and regulation of blood vessel formation (Zadpoor, 2015, Honnegowda et al,

2016, Semenza, 2002 & Shibuya, 2011). The angiogenic capability of the ESMs were determined using Chorioallantoic membrane (CAM) assays. The results revealed that ESMs were nontoxic and in addition did not increase angiogenesis. To date, no data on ESM's angiogenic potential has been published, so more research may be required to confirm the behaviour and/or mechanism behind these findings.

As previously stated in chapter 1 and 2 of this thesis, the ESM can be explored as drug delivery device for microparticles (MP). In chapter 3, the aim of the study was to generate an optimised single o/w evaporation technique for the fabrication of drug loaded MP for ocular application. Solvent evaporation is used to encapsulate drugs in a polymer matrix to form a delivery system (Prior et al, 2006; Lai and Tsiang, 2005 and Khaled et al, 2010). Process variables influencing the physical properties of the manufactured MP are critical in determining drug release profiles and modes of application. The size of the MP is essential in defining the drug release profile and mode of application (Freitas, Merkle and Gander, 2004 and Bidone et al, 2009). As a result, careful selection of process factors is required in order to formulate the most appropriate MP size. A sub-study was performed using design of experiment (DOE) to determine the various factors that may affects the MP size using the solvent evaporation method.

By changing one variable at a time to achieve the desired particle sizes, researchers were able to identify several process factors that influence the formulation of MP (Steinberg and Hunter, 1984). Several studies have demonstrated the importance of optimization methodology and DOE in research and development (Steinberg and Hunter, 1984; Coates, 1988; Montgomery, 1999 and Kemala, Budianto and Soegiyono,2012). DOE is a method for determining the relationship between the factors that influence a method and the output of the process. The data enables the researcher to identify and choose the factors and levels that have a significant impact on the final response or output. Taguchi design of experiment was implemented in this

study.

Taguchi design is a statistical technique for optimising complex interrelationships. The design assesses and identifies the controllable factors that mitigate the impact of uncontrollable factors (noise factors) (Coates, 1988; Montgomery, 1999 and Nair, Hansen and Shi,2000). An orthogonal array (OA) is used in the Taguchi design to estimate the effects of factors on the response mean and variation. In addition, Taguchi design evaluates the data for the responses using the signal-to-noise (S/N) ratio, a statistical measure of performance. The experiment's main goal is to find the best control factor settings to maximise the S/N ratio (Nair, Hansen, and Shi, 2000).

The L12 OA design was employed as the first optimisation method to evaluate 10 factors namely concentration of PLGA, Solvent type, MW of PVA, concentration of PVA in primary emulsion, vortexing speed, vortexing duration, organic/aqueous phase ratio, concentration of PVA in hardening bath, stirring speed and solvent evaporation duration at two levels (low and high) The particle size of the MP was determined using the dry dispersion laser diffraction method on a SymPatec HELOS equipped with a RODOS/ ASPIROS dry dispenser (Germany). This design assumes that there is no interrelationship between any two factors. However, clear evidence of interaction was observed between concentration of PLGA and solvent type, although this interaction had no effect on the particle size. The mean particle size (response) for the 12 experiments were in a range of 54.39 – 200.37 μm as shown in Table 3.3. MP with the largest particle size (200.37 μm) were formulated with Run 1 when all the 10 parameters had been used in their lowest levels. The smallest mean particle size (54.39 ± 4.37 μm) was obtained from Run 3 in which the concentration of PLGA, solvent type, concentration of PVA primary emulsion, vortexing duration, and solvent evaporation duration were ‘high’ and the molecular weight of PVA, vortexing speed, organic/aqueous phase ratio, concentration of PVA

in hardening bath and stirring speed during the hardening process were at their low level. Form the results, formulation Run 3 produced the smallest particle size (54.39 μm) with the highest S/N ratio value (-2.89).

The L12 OA design results were statistically analysed using design-expert software (version 10). This software is able to screen each factor with respect to their influence on the particle size. A combination of two statistical tools i.e., Half normal plot and Pareto chart was used to identify the important factors as vortexing duration, concentration of PVA in emulsion, solvent evaporation duration, vortexing speed, concentration of PLGA, aqueous/organic phase ratio, solvent type, molecular weight of PVA and stirring speed, and the unimportant factors as concentration of PVA in hardening bath and interaction between concentration of PLGA and solvent type. (Figure 3.3 and Figure 3.4). All the parameters chosen for the model have very significant effects on the microparticle size. From Table 3.3, vortexing speed had the maximum contribution (21.60 %) and the least was stirring speed for the hardening process (1.95 %).

The response plots clearly show the effect of each factor on the mean particle size (Figure 3.5). Increasing the vortexing duration (F), as shown in Figure 3.5, resulted in small particle size. A longer duration of vortexing may allow for better dispersal of the oil phase, resulting in fine droplets that harden to form MP (Pang et, 2014 and Zahn 1975). The presence of a surfactant, in this case PVA, at the interface between the aqueous and organic phases, lowering interfacial tension and providing a barrier to coalescence, is required for the effective formation of a primary emulsion and the stability of the droplets during emulsification (Torkaman, Soltanieh and Kazemian, 2010; Vyslouzil et al, 2014 and Tan et al, 2015).

Energy is required to disperse the organic phase in the aqueous phase, vortexing speed (E) was a critical parameter in the homogenization step (Pang et al, 2014). The mean particle size was found to be inversely proportional to the vortexing speed; increasing the vortexing speed reduced the MP size because the emulsion was dispersed into smaller droplets on a larger scale.

This observation is consistent with Sharma, Madan, and Lin's research (2016). The response plot for MW PVA shows that increasing the molecular weight decreases the microparticle size, which could be due to the solution's increased viscosity resisting deformation due to shear during emulsification (Wagh and Apar, 2014). One of the parameters that has been shown to have a significant impact on particle size is stirring speed (Bible et al, 2009; Vyslouzil et al, 2014; Sharma, Madan and Lin, 2016; Quintanar-Guerrero, Fessi, Allemann and Doelker, 1996; Mondal, Samanta, Pal, and Ghosal, 2008; Valizadeh, Jelvehgari, Nokhodchi and Rezaour, 2010). By improving the dispersal of the oil phase, the stirrer imparts shear onto the emulsion droplets, reducing their size, increasing stirring speed produces microparticles with small sizes.

From the analysis of the L12 OA design, 9 factors were identified as important to be included in the formulation model. In the step, L18 OA design was employed 8 factors were used, compared to 9 factors in the L12 OA design. These factors were concentration of PLGA, concentration of primary emulsion, organic/aqueous phase ratio, vortexing speed, vortexing duration, stirring speed, solvent evaporation duration. The mean particle size range obtained for each of the 18 experimental runs was 23.51 to 73.13 m. The main factors affecting the particle size are vortexing speed, concentration of PLGA, organic/aqueous phase ratio, stirring speed, concentration of PVA in emulsion, vortexing duration and solvent evaporation duration. The optimal model formulation was identified to be Run 16 from the L18 OA design, with molecular weight of PVA = 89,000 Da, concentration of PLGA = 20 w/v %, organic/aqueous phase ratio = 1:1, vortexing speed = 9 (high), vortexing duration = 60 seconds (low), stirring speed for hardening process = 1200 rpm (low).

The optimal model formulation was utilized to generated FITC-BSA-loaded microparticles in order to evaluate the robustness and predictive ability of the Taguchi design. FITC-BSA (66 KDa) was used as it is a stable, globular, and non-reactive protein that is frequently used as a model protein in drug MP development studies (references). According to the data presented

in this study, no significant changes in size occur after sufficient entrapment of FITC-BSA within the MP (64.35% - 78.07% encapsulation efficiency), which is consistent with the Taguchi L18 OA assessment. The activity of the model drug was assessed by lysozyme loaded MP fabricated with the optimised method. As per the findings (Figure 3.14), the protein's activity was proportional to the amount of protein released, and the kinetics of the change in activity of the protein matched the release data.

In chapter 4, the aim was to develop and characterise a 2-in-1 biomedical bandage consisting of ESM and drug loaded MP for an effective and functional corneal wound healing application. The optimised method developed in chapter 2 and chapter 3 were employed to extract ESM and fabricated FITC-BSA loaded MPs respectively. A preliminary study was performed to determine the side to load the MPs. Accordingly, PLGA MPs were modified by alkaline hydrolysis with 0.2 M NaOH and then loaded into the inner or outer layer of ESMs. The results in Table 4.1 show that less than 10% of the MPs were loaded onto the layer whereas 65% were loaded onto the outer layer. The FESEM images of the MP loaded ESMs compared to the blank ESMs revealed that the MP were successfully attached to the fibres within the outer layer. In the case of the inner layer, no structural difference was observed between the blank and the MP loaded samples. The failure could be attributed to the structure of the inner layer (limiting membrane. No evidence in literature was identified to support this analysis.

A suitable drying method and storage temperature for the MP loaded ESM was identified by analysis different methods and temperatures. The influence of air-dried or freeze-dried ESMs stored at 4 or -20 °C for 60 days on the tensile properties was evaluated. The data (Figure 4.8 A, B and C) depicted no changes in the tensile strength if the ESMs dried with either of the methods. Additionally, neither the storage temperature nor storage durations caused structural changes in the ESMs. Several investigations have proven that freeze drying collage-based biomaterial improves the mechanical property for long term storage < 2 years (Zeng et al, 2013,

Lowe et al, 2016, Sancho, Vazquez and De Juan-Pardo, 2014). Study by Lee (1983) revealed that cold storage is an optimal condition for long term storage for native collagens and at low temperatures, the protein structures are intact.

FBM were successfully loaded into the outer layers of the ESMs generated by manually peeling, 0.5 M acetic acid and 0.9 M EDTA. The FBM loaded ESM (2 in 1 bandage) samples were freeze-dried at room temperature and stored at 4 °C for further characterisation. The surface morphology of the FBM and the 2 in 1 bandage were evaluated via FESEM and compared with FESEM images of the blank ESMs produced in section 2.4.10 in chapter 2. Figure 4.9 displayed that the FBM were adhered onto the fibres in the ESM and the MP in the bandage has similar shape and sizes as the FBM. This proved the attachment method did not alter the surface morphology of the MP. Using the FESEM images, the fibre diameters of the FBM loaded samples were evaluated via Fiji-ImageJ software and no significant changes were observed between the fibre diameters of the blank ESM and the FBM loaded ESM. Moreover, the surface roughness, Ra values of the of the 2 in 1 bandage was evaluated and compared to the blank. No changes were detected between the blank ESM and the 2 in 1 bandage and indicates that the incorporation of the FBM did not alter the surface roughness of the ESM.

Using Fourier transform infrared (FTIR) spectroscopy, the chemical composition of the generated 2 in 1 bandage was evaluated and the FTIR spectra (Figure 4.11) revealed that the FBM were successfully loaded into the ESM. Again, the major peaks of the natural ESM (i.e., 1646 cm^{-1}, 1524 1441 and 1240 cm^{-1}) and the PLGA polymer (i.e., 2946.72 - 3000 cm-1 & 1746.53 cm^{-1}) were identified in the spectra of the bandage. The transparency of the bandage was analysed, and the results demonstrated that the presence of the FBM in the bandage reduced the visibility of the test in the waterproof test card method (Figure 4.12i). The light

transmittance values of the bandages were lower than the blank ESM however they all recorded values above 80%.

The surface properties such as porosity and wettability of ocular bandage are vital parameters in the clinical performance in the ocular setting (Du, Huang and Feng, 2017). The porosity of the of bandage was lover when compared with the blank membrane (Figure 4.13). This revealed that the introduction of the MP reduced the pore size or volume in the blank ESM. The wettability of the 2 in 1 bandage was deduced by measuring the contact angle. The data in Figure 4.14 demonstrated the contact angle of the bandage was significantly increased implying a lower hydrophilicity as compared to the blank ESM. The release profile of the model drug, FITC-BSA, encapsulated in the MP loaded into the bandage was investigated using a novel *in vitro* France cell eye model with a middle chamber containing porcine vitreous generated by Shafaie et al (2018) to mimic *in vivo* eye conditions. From the data recorded (as seen in Figure 4.16), the bandages achieved sustained drug release up to 10 days.

A Chorioallantoic membrane (CAM) assay was used to assess the bioactivity and biocompatibility of the bandage. The angiogenic potential for ocuar bandge is a vital factor in s a key factor in biomaterials intended for corneal applications where neovascularization is deterred (Ziaei et al., 2018 and Stepp et al., 2014). VEGF loaded MP was loaded into ESM to determine the angiogenic profile of the bandage. The results confirmed that the bandage was no toxic, MP was successfully loaded into the bandage, and the bandage did not cause proangiogenic response. As mentioned in Chapter 2, the ESMs on the CAM had no impeding effect, so more research is needed to confirm the mechanism behind these results (Mensah et al, 2021). Minimal vascularization is advantageous in a biomaterial for corneal wound healing as the cornea is a transparent avascular tissue, excessive blood vessel formation will distort the ocular surface's clarity (Sridhar, 2018 & Delmonte and Kim, 2011).

The ESMs for corneal wound healing application were evaluated *in vivo* using a rat corneal model. In six-week-old male Sprague Dawley (SD) mice, chemical and mechanical wounds were created and treated with incision of the outer layer of the blank ESM samples and amniotic membrane (HAM) as a positive control (Figure 4.18). In conclusion, *in vivo* tests on rat eyes using two different cornea injury models, mechanical and chemical, revealed no significant therapeutic effect under these settings (ESMstrip, ESM-A0.5, ESM-E0-9) when compared to the control and HAM.

5.2 CONCLUSION

In this work, two successfully optimized protocols were described: isolation with 0.5 acetic acid and 0.9 M EDTA, which can be used to extract the intact membrane from the eggshell without disturbing its natural structure or physico-biological properties. The biocompatibility of the outer and inner sides of the eggshell membrane were also evaluated using cell culture and showed minimal side effects - in some cases, increased cell attachment, propagation and reproduction. A sub-study was performed in order to generate a technique to generate microparticles for the modification of the ESM. Taguchi OA design proved to be a valuable tool in the optimization of various processing parameters in the solvent evaporation technique with complex relationships with several experiments. The design was effective in determining parameters that had a significant impact on MP size. More precisely, vortexing speed, PLGA concentration, organic/aqueous phase ratio, mixing speed, PVA concentration in primary emulsion, vortexing time were important while molecular weight was important. It has been proven that the concentration of PVA and PVA in the curing bath are not important parameters for PLGA microparticle size. These optimum levels of parameters were useful in the fabrication of PLGA microparticles with a minimum particle size of 23.51 μm. A model drug was successfully incorporated into the optimized microparticles, A robust and complete eggshell membranes were successfully obtained using in-home optimized acetic and EDTA extraction methods. FITC-BSA loaded PLGA microparticles were fabricated and successfully embedded in the outer layer of ESMs with a suitable surface adsorption and attachment technique. Stability testing of the bandage showed that air-drying or freeze-drying of the bandage and prolonged storage at 4 and -20 °C for 60 days did not compromise mechanical properties. Attachment did not affect the morphology, fibre diameter, roughness, and release profile of FITC-BSA. These findings show that the ESM could be used in a variety of regenerative medical and/or biotechnological applications, such as wound dressing, or culture substrate for drug discovery.

5.3FUTURE WORK

The present research work aimed to extract and evaluate eggshell membrane (ESM), a novel biomaterial for ocular wound healing bandage. Furthermore, drug loaded microparticles were incorporated into the ESM to generate a 2 in 1 biomedical bandage. This allows for the release of ophthalmic formulations such as growth factors with the appropriate profile according to the demands of the healing process. The use of drug-incorporated for ocular application was first discovered in the late 1960s by Wichterle et al, however, the use of drug loaded bandages whose benefits have been proven has not been introduced into the market. Overall, the research showed the desirable properties of the drug incorporated microparticles ESM for ocular wound healing applications.

The research explored the idea of using eggshell membranes to make eye bandages, however at this initial screening stage, the eggs shell was extracted from full eggs obtained from the supermarkets. In subsequent replication of the experiment, we should consider recycling the eggshell waste from the food industry. As the eggshell obtained from the food industry come in fragments, a method has to be developed in combining the extracted ESM fragments into large size that can be manipulated for the desirable application.

The mechanical analysis of the ESM in the chapter two concurs with the evidence reported in literature that ESM is a tough and stiff material (Parodi et al, 1999; Ahmed, Suso and Hincke 2019 and Gocekand Adanur, 2012). In the near future, biological crosslinking between the fibres within the ESM through the use of enzymes such as transglutaminase can enhance the mechanical properties. Biological crosslinking of protein fibres has been identified to produce minimal toxicity (Chau et al, 2005 and Orban et al, 2004).

The angiogenic behaviour of the blank ESM and the drug loaded ESM bandage was assessed in chapter 2 and chapter 4 respectively. The angiogenic profile was measured using cost-effective Chorioallantoic membrane (CAM) assay. This assay was approved by the US Food

and Drug Administration (FDA) in 2006 as a pre-clinical evaluation of materials for wound healing application (Kohli et al, 2020). The analyses of the two materials revealed that the samples do not promote formation of new blood vessels. Due to absence of standardisation, a substantial amount of variation exits in this procedure. Furthermore, no data has been reported in literation on the angiogenic profile of ESM on CAM. It will be essential and interesting to repeat these experiments and assess the indebt histological assessment of the samples on CAM to further evaluate the angiogenic response. The CAM results can be beneficial to subsequent *in vivo* wound healing in animal model. In this research, the *in vivo* evaluation of the ESM using rat corneal wound healing model was inadequate and required further studies considering both layers of the membrane and the drug loaded bandage.

In this thesis, the stability of the drug loaded in the microparticles, and the components of the ESM was not examined. It is essential to evaluate the degradation of the samples as it is an important factor in the process of preservation. Other key properties such as ionic and oxygen permeability, and antibacterial should also be considered of the bandage. Further analysis to maximize the drug loading into the microparticle and the loading of the microparticles into the ESM needs to be studied as this factor is critical to a successful drug delivery. Additional drug release kinetic study is needed to substantiate the drug delivery ability of the ESM.

These ESM and 2 in 1 bandage can be explored in other research areas like skin and oral applications, and artificial cornea developments.

5.4 REFERENCES

Aagaard-Tillery KM, Silver R and Dalton J (2006). Immunology of normal pregnancy.Seminars in Fetal and Neonatal Medicine. 11(5): pp279–95

Ai-min, S.et al (2010) Preparation of starch-based nanoparticles through high-pressure homogenization and mini emulsion cross-linking: Influence of various process parameters on particle size and stability. Carbohydrate Polymers s 83: p1604–1610. DOI: 10.1016/j.carbpol.2010.10.011

Alagusundaram, M. et al., (2009) Microspheres as novel drug delivery system- a review. International Journal of ChemTech Research. 1(30): pp 526-534.

Alberton et al., (1996), Preparation and Characterisation of Poly (a dipic anhydride) Microspheres for Ocular Drug Delivery", Journal of Applied Polymer Science 62: p695—705.

Ankit, K., Rishabha, M. and Pramod, K.S. (2011) Recent Trends in Ocular Drug Delivery: A Short Review European Journal of Applied Sciences 3 (3): pp86-92

Azuara-Blanco A, Pillai CT, Dua HS (1999). Amniotic membrane transplantation for ocular surface reconstruction. Br J Ophthalmol 1999, 83: pp399–402.

Bachelder, E.M., et al., (2010). In vitro analysis of acetylated dextran microparticles as a potent delivery platform for vaccine adjuvants. Mol Pharm. 7(3): pp826–835. Doi:10.1021/mp900311x.

Balmayor, E.R. et al., (2009). Preparation and characterization of starch-poly-e-caprolactone microparticles incorporating bioactive agents for drug delivery and tissue engineering applications. Acta Biomaterialia 5: pp1035–1045

Barabino S, et al (2003). Role of amniotic membrane transplantation for conjunctival reconstruction in ocular-cicatricial pemphigoid. Ophthalmology, 110: pp 474–480.

Barcia et al., (2009) Downregulation of endotoxin-induced uveitis by intravitreal injection of polylactic-glycolic acid (PLGA) microspheres loaded with dexamethasone Experimental Eye Research v 89(2): pp238–245

Barcia, E., Herrero-Vanrell, R., Díez, A., Alvarez-Santiago, C., López, I. and Calonge, M., 2009. Downregulation of endotoxin-induced uveitis by intravitreal injection of polylactic-glycolic acid (PLGA) microspheres loaded with dexamethasone. Experimental Eye Research, 89(2), pp.238-245.

Berthold, A., Cremer, K., Kreuter, J. Collagen microparticles: carriers for glucocorticosteroids. Eur. J. Pharm. Biopharm., Stuttgart, 45: pp23-29

Bodmeier, R. and McGinity, J.W. (1987) The preparation and evaluation of drug-containing poly(DL-lactide) microspheres formed by the solvent evaporation method. Pharm Res.4(6): p465-71.

Capan, Y., Jiang, G., Giovagnoli, S., Na, K. and DeLuca, P. (2003). Preparation and characterization of poly(D,L-lactide-co-glycolide) microspheres for controlled release of human growth hormone. AAPS PharmSciTech, 4(2), pp.147-156.

Cavanagh, H., 2002. Ocular Surface Disease. Cornea, 21(6), p.634.

Chau, D., Brown, S., Mather, M., Hutter, V., Tint, N., Dua, H., Rose, F. and Ghaemmaghami, A. (2012). Tissue transglutaminase (TG-2) modified amniotic membrane: a novel scaffold for biomedical applications. Biomedical Materials, 7(4), p.045011.

Chau, D., Tint, N., Collighan, R., Griffin, M., Dua, H., Shakesheff, K. and Rose, F. (2010). The visualisation of vitreous using surface modified poly(lactic-co-glycolic acid) microparticles. British Journal of Ophthalmology, 94(5), pp.648-653.

Chella N, Yada K.K., and Vempati R. (2010) Preparation and Evaluation of Ethyl Cellulose Microspheres Containing Diclofenac Sodium by Novel W/O/O Emulsion Method, J. Pharm. Sci. and Res. 2(12): pp884-888

Ciolino J.B, Stefanescu C.F, Ross A.E. (2014)In vivo performance of a drug-eluting contact lens to treat glaucoma for a month. Biomaterials. 35(1): pp432-439.

Cornea. Healthline. https://www.healthline.com/human-body-maps/cornea#1. Accessed September 21, 2020.

Dalla Pozza G, (2005). Reconstruction of conjunctiva with amniotic membrane after excision of large conjunctival melanoma: a long-term study. Eur J Ophthalmol , 15: pp446–450.

Das M.K. and Rao K.R. (2007) Encapsulation of Zidovudine by Double emulsion solvent diffusion technique using ethyl cellulose. Indian J. Pharm. Sci., 69: pp244-250

Dua, H., Faraj, L., Said, D., Gray, T. and Lowe, J., 2013. Human Corneal Anatomy Redefined. Ophthalmology, 120(9), pp.1778-1785.

Dupps, W. and Wilson, S., 2006. Biomechanics and wound healing in the cornea. Experimental Eye Research, 83(4), pp.709-720.

Fernández-Pérez, J., Kador, K., Lynch, A. and Ahearne, M., 2020. Characterization of extracellular matrix modified poly(ε-caprolactone) electrospun scaffolds with differing fiber orientations for corneal stroma regeneration. Materials Science and Engineering: C, 108, p.110415.

Foulks, G., 2014. Old and New Methods of Evaluating the Ocular Surface. The Ocular Surface, 12(1), p.1.

Grinstaff, M., 2007. Designing hydrogel adhesives for corneal wound repair. Biomaterials, 28(35), pp.5205-5214.

Gukasyan, H.J., Hailu, S. and Karami, T.K. Ophthalmic Drug Discovery and Development.

Hyperbaric oxygen treatment of guinea pigs as a model for increased lens nuclear light scattering. (1992). *Experimental Eye Research*, 55, p.235.

ISSN 0169-409X, https://doi.org/10.1016/j.addr.2018.01.006.

Kwok, S., Shih, K., Bu, Y., Lo, A., Chan, T., Lai, J., Jhanji, V. and Tong, L., 2019. Systematic Review on Therapeutic Strategies to Minimize Corneal Stromal Scarring After Injury.

Litwiniuk, M. and Grzela, T., 2014. Amniotic membrane: New concepts for an old dressing. Wound Repair and Regeneration, 22(4), pp.451-456.

Mathews, P., Lindsley, K., Aldave, A. and Akpek, E., 2018. Etiology of Global Corneal Blindness and Current Practices of Corneal Transplantation: A Focused Review. Cornea, 37(9), pp.1198-1203.

Mohammed Ziaei, Carol Greene, Colin R. Green,Wound healing in the eye: Therapeutic prospects, Advanced Drug Delivery Reviews, Volume 126, 2018, Pages 162-176,

Niknejad H, Peirovi H, Jorjani M, Ahmadiani A, Ghanavi J, et al. (2008) Properties of the amniotic membrane for potential use in tissue engineering. Eur Cell Mater 15: 88-99.

Pezzullo, L., Streatfeild, J., Simkiss, P. and Shickle, D., 2018. The economic impact of sight loss and blindness in the UK adult population. BMC Health Services Research, 18(1).

Pharm Res 36, 69 (2019). https://doi.org/10.1007/s11095-019-2606-7

Shifali, A., Kumar, P. and Pandit, V., 2021. Recent trends in Ocular Drug Delivery System: A Review. Asian Journal Of Research in Pharmaceutical Science, 11(1), pp.71-80.

Slaughter, R., Watts, M., Vale, J., Grieve, J. and Schep, L., 2019. The clinical toxicology of sodium hypochlorite. Clinical Toxicology, 57(5), pp.303-311.

Spadea, L., 2015. Anterior Lamellar Keratoplasty in Keratoconus. Journal of Eye & Cataract Surgery, 01(01).

Torres-Man, A. and Delgado-Me, E., 2017. Influence of Separation Techniques with Acid Solutions on the Composition of Eggshell Membrane. International Journal of Poultry Science, 16(11), pp.451-456.

Who.int. 2022. Vision impairment and blindness. [online] Available at: <https://www.who.int/news-room/fact-sheets/detail/blindness-and-visual-impairment> [Accessed 7 June 2022].

Willmann D, Fu L, Melanson SW. Corneal Injury. [Updated 2022 May 2]. In: StatPearls [Internet]. Treasure Island (FL): StatPearls Publishing; 2022 Jan-. Available from: https://www.ncbi.nlm.nih.gov/books/NBK459283/

Yu, F., Yin, J., Xu, K. and Huang, J., 2010. Growth factors and corneal epithelial wound healing. Brain Research Bulletin, 81(2-3), pp.229-235.

Zidan, G., Rupenthal, I., Greene, C. and Seyfoddin, A., 2017. Medicated ocular bandages and corneal health: potential excipients and active pharmaceutical ingredients. Pharmaceutical Development and Technology, 23(3), pp.255-260.

APPENDIX

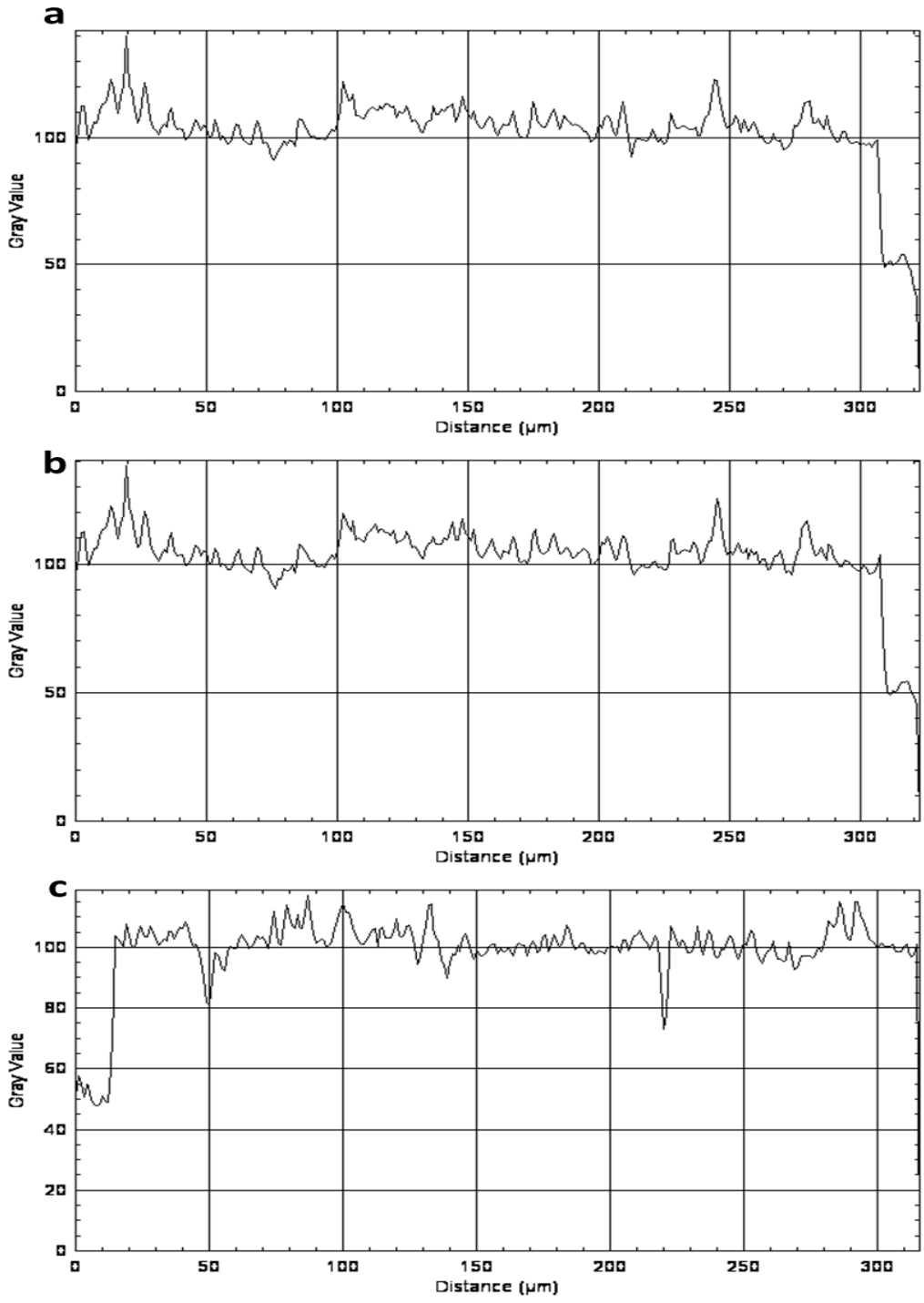

Figure A1.0. Surface roughness plot of LESMstrip, LESM-A0.5 and LESM-E0.9
The plots were generated from the Fiji-ImageJ software.

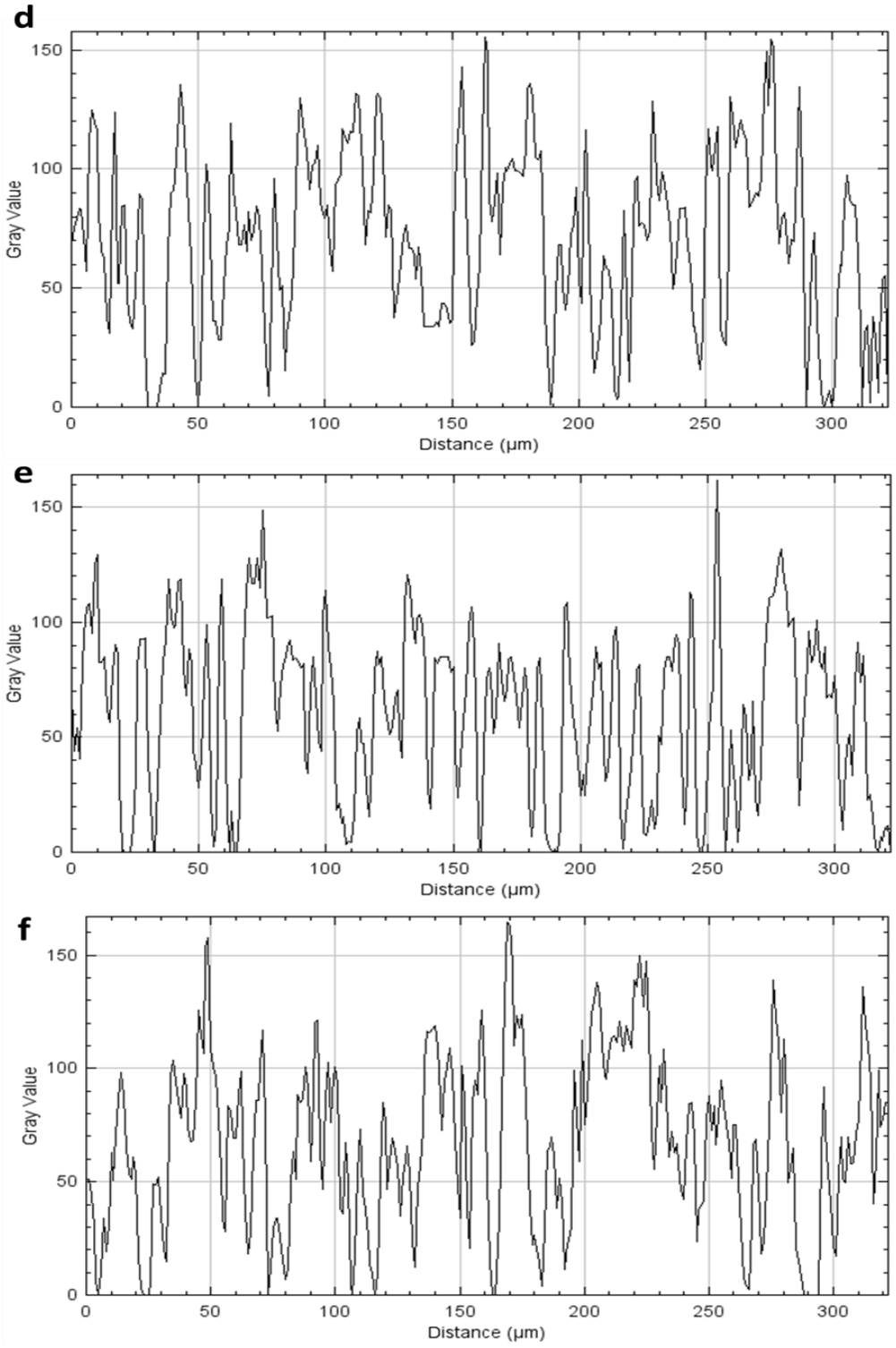

Figure A1.1. Surface roughness plot of OESMstrip, OESM-A0.5 and OESM-E0.9
The plots were generated from the Fiji-ImageJ software.

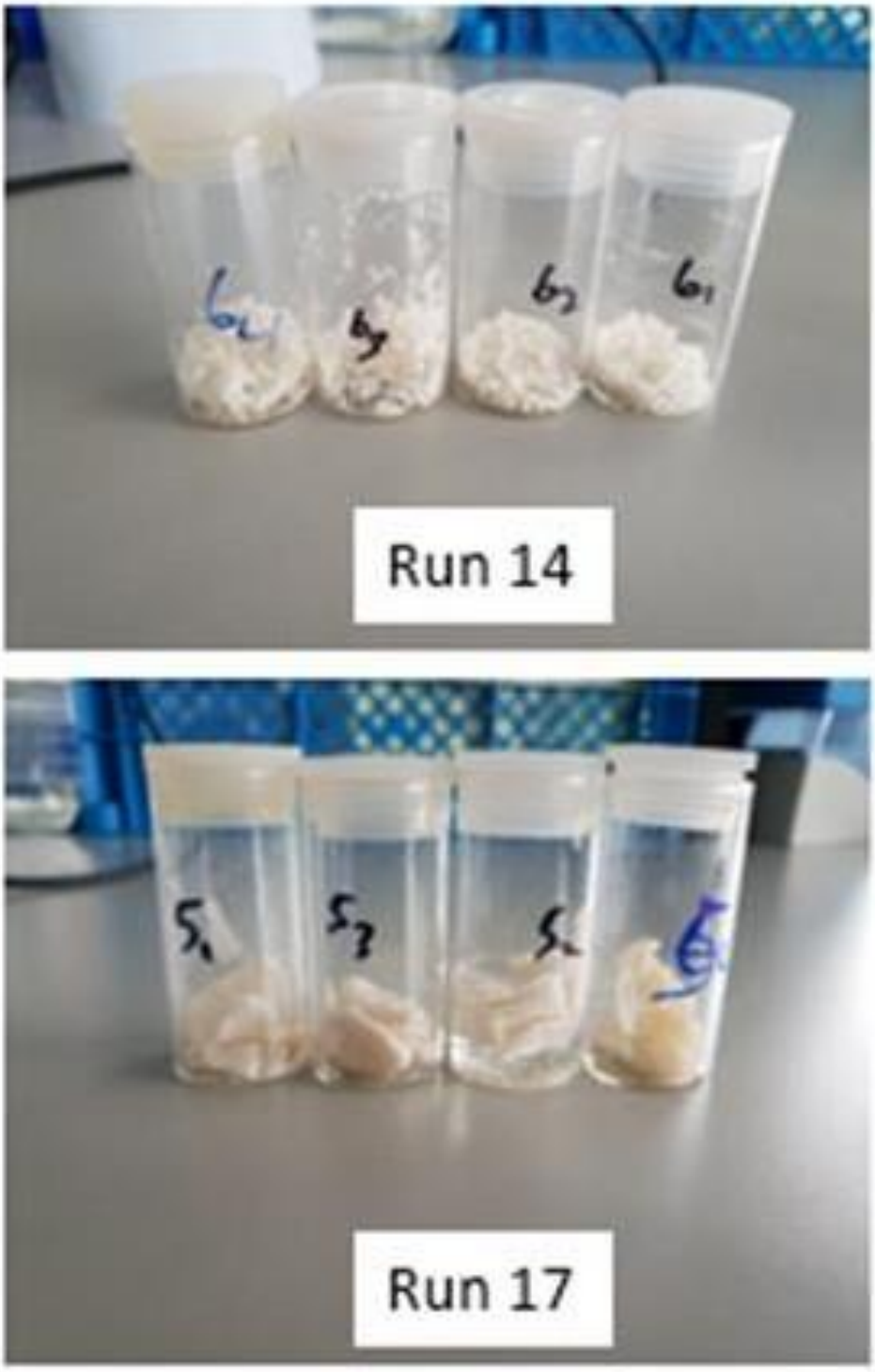

Figure A 2.0 Photograph of Run 14 and 17 from L12 OA design.
Runs 14 and 17 failed completely and no MP were created

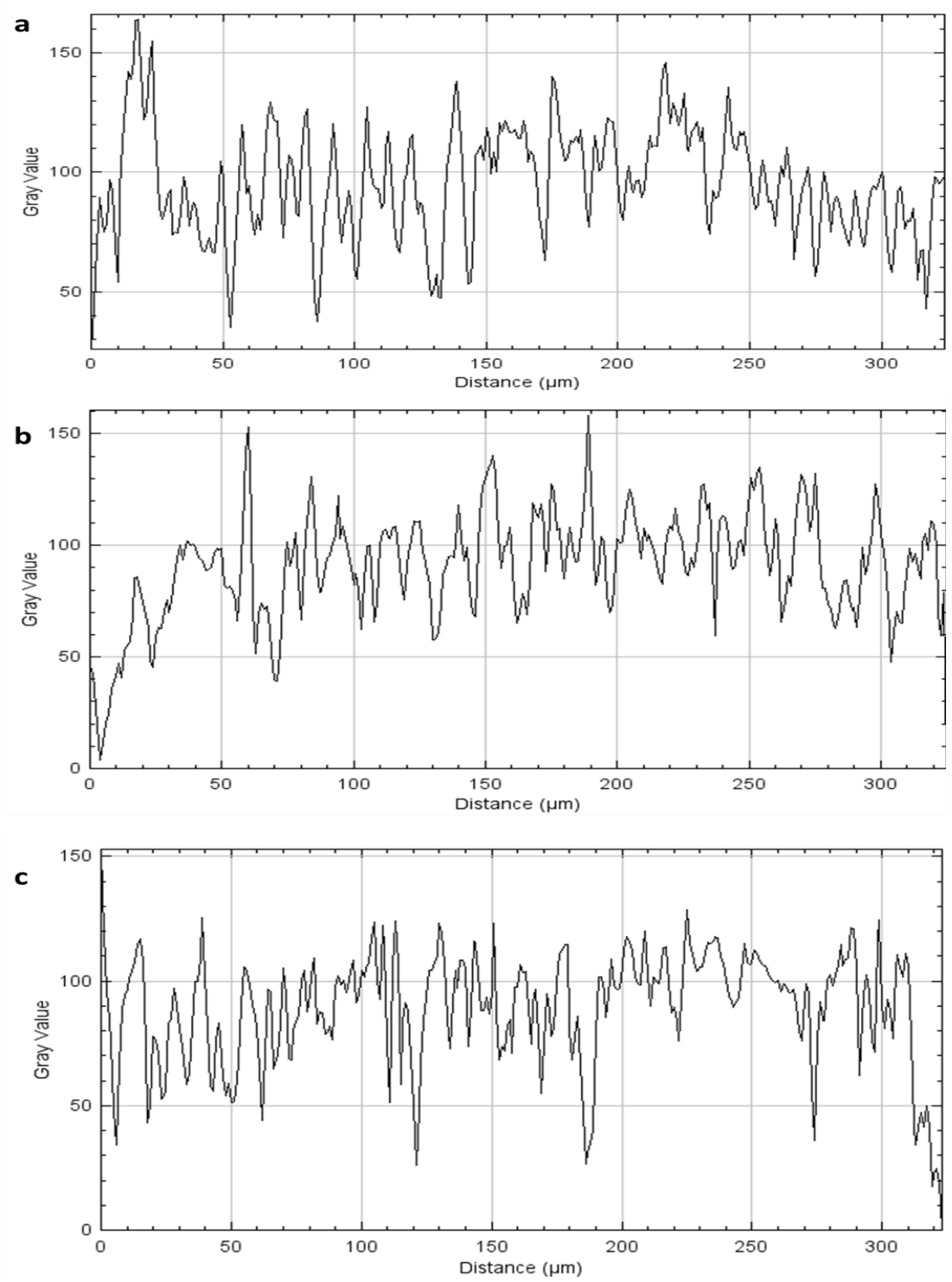

Figure A1.1. Surface roughness plot of FBM-OESMstrip, FBM-OESM-A0.5 and FBM_OESM-E0.9

The plots were generated via the Fiji-ImageJ software. FBM: FITC-BSA microparticles

Table A 1.0. Results of 1-way ANOVA with Bonferroni's multiple comparison post-test ($p < 0.05$)

Time/h	FITC-BSA MP vs FBM-OESMstrip	FITC-BSA MP vs FBM-OESM-A0.5	FITC-BSA MP vs FBM-OESM-E0.9
0.0000	ns	ns	ns
1.000	ns	ns	ns
3.000	ns	ns	ns
6.000	ns	ns	**
9.000	ns	*	***
12.00	ns	**	***
18.00	*	***	***
24.00	***	***	***
48.00	***	***	***
72.00	***	***	***
96.00	***	***	***
120.0	***	***	***
144.0	***	***	***
168.0	***	***	***
192.0	***	***	***
216.0	***	***	***
244.0	***	***	***

Time/h	FBM-OESMstrip vs FBM-OESM-E0.9	FBM-OESM-A0.5 vs FBM-OESM-E0.9	FBM-OESM-A0.5 vs FBM-OESM-E0.9
0.0000	ns	ns	ns
1.000	ns	ns	ns
3.000	ns	ns	ns
6.000	ns	ns	ns
9.000	ns	*	ns
12.00	ns	***	ns
18.00	ns	***	**
24.00	ns	***	**
48.00	ns	***	***
72.00	ns	**	**
96.00	ns	ns	ns
120.0	ns	***	*
144.0	ns	***	***
168.0	ns	**	**
192.0	ns	***	***
216.0	ns	***	***
244.0	ns	***	***

Table A 2.0. Results of 1-way ANOVA with Bonferroni's multiple comparison post-test ($p < 0.05$)

PBS vs VEGF	**
PBS vs VEGF Loaded MP	ns
PBS vs Blank PLGA MP	ns
PBS vs OESMstrip	ns
PBS vs OESM-A0.5	ns
PBS vs OESM-E0.9	ns
PBS vs Blank MP-OSEMstrip	ns
PBS vs Blank MP-OESM-A0.5	ns
PBS vs Blank MP-OESM-E0.9	ns
PBS vs VM-ESMstrip	ns
PBS vs VM-OESM-A0.5	ns
PBS vs VM-OESM-E0.9	ns
VEGF vs VEGF Loaded MP	ns
VEGF vs Blank PLGA MP	***
VEGF vs OESMstrip	***
VEGF vs OESM-A0.5	***
VEGF vs OESM-E0.9	***
VEGF vs Blank MP-OSEMstrip	***
VEGF vs Blank MP-OESM-A0.5	***
VEGF vs Blank MP-OESM-E0.9	***
VEGF vs VM-ESMstrip	ns
VEGF vs VM-OESM-A0.5	ns
VEGF vs VM-OESM-E0.9	ns
VEGF Loaded MP vs Blank PLGA MP	ns
VEGF Loaded MP vs OESMstrip	**
VEGF Loaded MP vs OESM-A0.5	*
VEGF Loaded MP vs OESM-E0.9	**
VEGF Loaded MP vs Blank MP-OSEMstrip	*
VEGF Loaded MP vs Blank MP-OESM-A0.5	ns
VEGF Loaded MP vs Blank MP-OESM-E0.9	*
VEGF Loaded MP vs VM-ESMstrip	ns
VEGF Loaded MP vs VM-OESM-A0.5	ns
VEGF Loaded MP vs VM-OESM-E0.9	ns
Blank PLGA MP vs OESMstrip	ns
Blank PLGA MP vs OESM-A0.5	ns
Blank PLGA MP vs OESM-E0.9	ns
Blank PLGA MP vs Blank MP-OSEMstrip	ns
Blank PLGA MP vs Blank MP-OESM-A0.5	ns
Blank PLGA MP vs Blank MP-OESM-E0.9	ns
Blank PLGA MP vs VM-ESMstrip	ns
Blank PLGA MP vs VM-OESM-A0.5	ns
Blank PLGA MP vs VM-OESM-E0.9	ns
OESMstrip vs OESM-A0.5	ns
OESMstrip vs OESM-E0.9	ns

OESMstrip vs Blank MP-OSEMstrip	ns
OESMstrip vs Blank MP-OESM-A0.5	ns
OESMstrip vs Blank MP-OESM-E0.9	ns
OESMstrip vs VM-ESMstrip	*
OESMstrip vs VM-OESM-A0.5	*
OESMstrip vs VM-OESM-E0.9	ns
OESM-A0.5 vs OESM-E0.9	ns
OESM-A0.5 vs Blank MP-OSEMstrip	ns
OESM-A0.5 vs Blank MP-OESM-A0.5	ns
OESM-A0.5 vs Blank MP-OESM-E0.9	ns
OESM-A0.5 vs VM-ESMstrip	ns
OESM-A0.5 vs VM-OESM-A0.5	*
OESM-A0.5 vs VM-OESM-E0.9	ns
OESM-E0.9 vs Blank MP-OSEMstrip	ns
OESM-E0.9 vs Blank MP-OESM-A0.5	ns
OESM-E0.9 vs Blank MP-OESM-E0.9	ns
OESM-E0.9 vs VM-ESMstrip	*
OESM-E0.9 vs VM-OESM-A0.5	**
OESM-E0.9 vs VM-OESM-E0.9	ns
Blank MP-OSEMstrip vs Blank MP-OESM-A0.5	ns
Blank MP-OSEMstrip vs Blank MP-OESM-E0.9	ns
Blank MP-OSEMstrip vs VM-ESMstrip	ns
Blank MP-OSEMstrip vs VM-OESM-A0.5	*
Blank MP-OSEMstrip vs VM-OESM-E0.9	ns
Blank MP-OESM-A0.5 vs Blank MP-OESM-E0.9	ns
Blank MP-OESM-A0.5 vs VM-ESMstrip	ns
Blank MP-OESM-A0.5 vs VM-OESM-A0.5	ns
Blank MP-OESM-A0.5 vs VM-OESM-E0.9	ns
Blank MP-OESM-E0.9 vs VM-ESMstrip	ns
Blank MP-OESM-E0.9 vs VM-OESM-A0.5	*
Blank MP-OESM-E0.9 vs VM-OESM-E0.9	ns
VM-ESMstrip vs VM-OESM-A0.5	ns
VM-ESMstrip vs VM-OESM-E0.9	ns
VM-OESM-A0.5 vs VM-OESM-E0.9	ns